Mechanics of hydrogel films : swelling-induced instabilities, finite-size effects, and contactless rheology to indentation-induced dehydration

Caroline Kopecz-Muller

université de BORDEAUX

ESPCI PARIS | PSL

THÈSE PRÉSENTÉE
POUR OBTENIR LE GRADE DE

DOCTEURE
DE L'UNIVERSITÉ DE BORDEAUX

ECOLE DOCTORALE SCIENCES PHYSIQUES ET DE L'INGÉNIEUR
LASERS, MATIÈRE, NANOSCIENCES

Par **Caroline KOPECZ-MULLER**

Mecanique de films d'hydrogels : instabilités induites par le gonflement, effets de taille finie, de la rhéologie sans contact à une déshydratation induite par indentation

Mechanics of hydrogel films: swelling-induced instabilities, finite-size effects, and contactless rheology to indentation-induced dehydration

Sous la direction de : **Thomas SALEZ**
Co-directeur : **Joshua D. MCGRAW**

Soutenue le 5 mars 2024

Membres du jury :

Mme. Camille Duprat	Professeure	Ecole Polytechnique	Rapportrice
M. M. Grae Worster	Professor	Cambridge University	Rapporteur
Mme Elisabeth Charlaix	Professeure	Université Grenoble Alpes	Examinatrice
M. Julien Dervaux	Chargé de Recherche	Université Paris Cité	Examinateur
M. Carlos Drummond	Directeur de Recherche	Université de Bordeaux	Président du jury
M. Thomas Salez	Chargé de Recherche	Université de Bordeaux	Directeur
M. Joshua D. McGraw	Chargé de Recherche	ESPCI Paris	Co-directeur

Contents

List of Figures

List of Symbols

A_{pat}	Amplitude of surface instability
$\mathcal{A}$	Amplitude of the modulated signal
A_ω	Amplitude spectral density of the cantilever
$a_{\mathrm{in}}, a_{\mathrm{out}}, a_{\mathrm{mod}}$	Electric signals amplitudes
a_{canti}	Cantilever oscillation amplitude
A, B	Displacement potentials
$a_1, a_2, b_1, b_2, b_3, b_4$	Integration constants
b	y-intercept in fitting the SFA linear regime
b_{ind}	Indentation
c_{PNIPAM}	PNIPAM concentration of the solution
c	Solvent concentration
c_0	Solvent concentration at equilibrium
DS	Deflection sensitivity
$\mathcal{D}_{\mathrm{pe}}$	Effective diffusion coefficient
D	Glass-to-glass distance in SFA
E	Young's modulus
E^*	Reduced Young modulus
F	Force applied on the sphere
$\mathcal{F}$	Flux term in thin-film equation
f_0, f_1	Cantilever resonance frequencies, without and with a colloid attached
G	Shear modulus
G_{Gibbs}	Gibbs free energy
$\mathcal{G}$	Green's function
H	Gel-probe initial distance
H_{c}	Critical distance
h_0	Sphere or *cube* oscillation amplitude
i	Imaginary number such as $i^2 = -1$
I	Light intensity
$\boldsymbol{J}$	Solvent flux
K	Spring stiffness
$\mathcal{K}_{\tau_0,\nu}$	Integration kernel
k	Effective permeability
k_{B}	Boltzmann constant
k_{canti}	Cantilever stiffness
$l_{\mathrm{cap}}^{\mathrm{dry}}, l_{\mathrm{cap}}^{\mathrm{wet}}$	Elastocapillary length based on dry/wet mechanical properties
m_{canti}	Cantilever effective mass
m_{sphere}	Colloid mass

M_{Hertz}	Estimated contact point
$\mathcal{M}$	Matrix to invert
n_w, n_g	Optical indexes of water and glass
$\mathcal{OP}$	Non-linear operator
P	Pressure
p	Extra pressure field in the fluid phase with respect to the atmospheric pressure
q	Laplace variable
Q_0, Q_1	Quality factors of the cantilever spectrum, without and with a colloid attached
R	Sphere radius
$\mathcal{R}$	Reflectance
$\mathcal{RHS}$	Right-hand-side
r	Radial coordinate
r_{wg}, r_{gw}	Fresnel coefficients at the water-glass interface
s	Hankel variable
S_{R}	Swelling ratio
$\mathcal{T}$	Transmission function
T	Temperature
t	Time
$\boldsymbol{u}$	Displacement field
$U_{\text{IN}}, U_{\text{OUT}}, U_{\text{MOD}}$	Electric sinusoidal signals
$u_{\text{in}}, u_{\text{out}}$	Mean value of electric signals
$\mathbf{v}$	Velocity field
v_r	Radial component of the velocity field
V	Command approach velocity
$\mathcal{V}$	Unknown vector
w	Surface deformation of a semi-infinite medium
w_τ	Surface deformation of a finite-thickness layer
x	Horizontal coordinate
$\hat{X}$	X variable expressed in reciprocal spaces
$\tilde{X}$	X variable under dimensionless form
X^*	Complexe variable such as $X(t) = \text{Re}\,[X^*]$
z	Vertical axis
z_{cube}	Vertical position of the piezo *cube*
z_{piezo}	Vertical position of the AFM piezo
Z_{canti}	Deflection of the cantilever
$\alpha_1, \alpha_2, \alpha_3$	Fitting parameters
β	Dimensionless variable such as $\beta = \sqrt{1 + 1/\chi}$
δ	SFA spring compression
γ	Surface tension
ϵ_0	Dimensionless ratio between viscous stresses and substrate elasticity
$\boldsymbol{\epsilon}$	Strain tensor
ζ	Dimensionless variable such as $\zeta = s\tau$
η	Solvent viscosity
θ	Azimuth
κ_0	Dimensionless ratio between viscous stresses and spring elasticity
λ_{pat}	Wavelength of surface instability

λ	Wavelength of light
Λ	Compressibility factor
μ	Chemical potential
μ_0	Chemical potential at equilibrium
ν	Poisson ratio
ρ	Fluid density
$\boldsymbol{\sigma}$	Stress tensor
τ	Gel thickness
τ_0	Dimensionless gel thickness
ϕ	Phase shift
$\Phi_\mathrm{w}, \Phi_\mathrm{s}, \Phi_\mathrm{p}$	Volume fraction of water, solvent, and polymer
χ_wp	Flory mixing parameter, between water and polymer
χ	Dimensionless diffusive variable such as $\chi = \mathcal{D}_\mathrm{pe} s^2/q$
Ω	Molecular volume of the solvent
ω_c	Critical angular frequency
ω	Angular frequency
ω_spin	Angular velocity of spin coating
ω_0	Angular resonance frequency of the cantilever

Introduction

Soft and squishy matter is ubiquitous in nature at many size scales. Some emblematic examples are living systems, such as bacteria and sea sponges, while others are inert matter such as clay and mud. Others examples are found in common man-made objects, such as dish sponges, or even in complex synthetic materials, such as foams or polymeric networks. Examples are illustrated in Fig. 1. From a physicist's point of view, such systems are poroelastic materials. They have the abilities to deform and recover their initial shape as a signature of elasticity, to absorb a solvent and to host fluid flows as a signature of porosity. From this perspective, reticulated polymer hydrogels are fascinating systems that exhibit particularly well a poroelastic signature. In particular, the ability of poly-N-isopropylacrylamide (PNIPAM) to swell by a factor 4 in water at room temperature [1] has been largely exploited in science. The resulting hydrogel exhibits a transition in temperature, from a hydrophilic behavior at room temperature to a hydrophobic one for higher temperatures. When grafted on a substrate [2], the latter temperature-responsive polymer has found applications in the design of microfluidic valves [3, 4], in biomedical fields such as single-cell trapping [5] for medical analysis, or drug delivery [6], and finally in cellular culture [7, 8], exploiting PNIPAM bio-compatibility.

Despite the increasing interest for polymer hydrogels and their scientific applications, their fundamental mechanical behavior still constitutes a partly covered subject in the literature. The first works on poroelastic matter were conducted by Biot [10], in the context of soil sedimentation mechanics. While the effects of viscoelasticity [11–13] have been recently under investigation, poroelasticity remains to address in more detail [14–17]. The intrinsic complexity of these types of composite materials generates poroelastic and/or elastohydrodynamic couplings, thus, their mechanical response depends on their interaction with the environment. Moreover, polymer hydrogels are formed upon swelling, and constitute a mixture of different species characterized by certain affinities [18]. If the mechanics of swelling has been addressed for polymer gels [19–21], and the one of drying is well documented for complex liquid droplets [22–25] and films [26–29], the literature on gel-deswelling mechanics is less present. Furthermore,

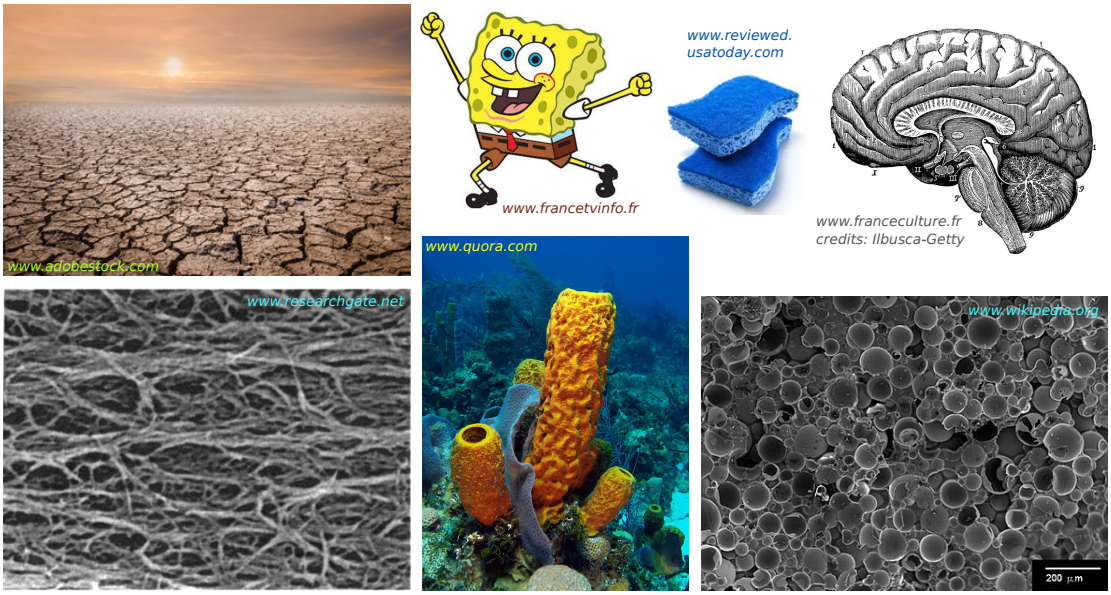

FIG. 1. **Examples of soft and porous systems.** *A picture of cracked mud in Ireland; Bob the sponge, dish sponges; a drawing of a human brain; a SEM picture of a polymer network; sea sponges; a SEM picture of a synthetic foam. The SEM picture of the polymer network was originally published in [9].*

the swelling-deswelling process presents asymmetric aspects [19, 20, 30].

In the present thesis, we study both theoretically and experimentally the mechanical behavior of poroelastic materials when immersed into a solvent. The manuscript is organized as follows. A first preliminary Chapter presents the overall context of the thesis, from basics of fluid mechanics, continuum mechanics and polymer physics up to the specific scientific background of this work. In the second Chapter, we report elastic instabilities that can occur at the surface of hydrogels upon swelling and drying. We exhibit a new morphology that is not reported in the literature, to the best of our knowledge. In the third Chapter, we establish the theoretical background of the poroelastic mechanical response to a point force. We compute the resulting deformation profile over time for a permeable poroelastic medium, both in the semi-infinite and the finite-thickness cases. In the fourth Chapter, we apply the latter theory to the case of a gel gently indented by an oscillating sphere in lubrication conditions. We compare our theoretical results to preliminary experiments performed on a PNIPAM hydrogel with an Atomic Force Microscopy (AFM) based system. We show that such types of experimental setups are well-designed to probe fragile and soft materials in a non-contact mode without risk to damage the sample. However the porosity of the swollen hydrogel appears as a subtle feature of the mechanical response, and can be described as an effective compressibility. The last Chapter is dedicated to the investigation of PNIPAM hydrogel thin films by Surface Forces Apparatus (SFA) in approach mode. We highlight several regimes of mechanical response, from a small-deformation regime to the dehydration-induced glass transition of the indented polymer film. Overall, we show through different situations that the poroelastic response is characterized by a transition from the behavior of a purely elastic and incompressible material to the one of a purely elastic and compressible material.

Chapter 1

General introduction and concepts

In this preliminary Chapter, we introduce first the basic concepts of continuum mechanics, fluid mechanics and polymer physics that we will use in the thesis. Then, in Sec. 1.5 we highlight the specific scientific context that led to the work reported in the thesis.

1.1 Flows in confined environments

1.1.1 Poiseuille flows

Fluid mechanics describes how fluids are transported in various contexts. The fundamental theory to describe such ubiquitous phenomena was developed between 1820 and 1850 by Claude-Louis Navier and Georges Gabriel Stokes. They gave their names to the so-called Navier-Stokes equations, which express the mass conservation and the momentum balance, for Newtonian fluids [31]. Let us consider such a fluid, of dynamic viscosity η and density ρ. The Navier-Stokes equations are partial differential equations on the pressure and velocity fields p and $\boldsymbol{v}$, respectively. By denoting the time t, the Navier-Stokes equations are expressed in an Eulerian system of coordinates (x, y, z), as:

$$\frac{\partial \rho}{\partial t} + \boldsymbol{\nabla} \cdot (\rho \boldsymbol{v}) = 0, \tag{1.1a}$$

$$\rho \left[\frac{\partial \boldsymbol{v}}{\partial t} + \boldsymbol{v} \cdot \boldsymbol{\nabla} (\boldsymbol{v}) \right] = -\boldsymbol{\nabla} p + \eta \boldsymbol{\nabla}^2 \boldsymbol{v} + \boldsymbol{f}, \tag{1.1b}$$

with $\boldsymbol{f}$ the external volumic forces, such as gravity: $\boldsymbol{f} = \rho \boldsymbol{g}$. The Navier-Stokes equations may be applied for instance to a compressible fluid, such as ambient air, which defines the domain of aerodynamics. Or, for instance, the Navier-Stokes equations can be used to describe incompressible fluids, such as water, which is the case in this thesis. When the fluid is incompressible, the fluid density ρ is constant. Thus, the mass conservation reads:

$$\boldsymbol{\nabla} \cdot \boldsymbol{v} = 0. \tag{1.2}$$

A common practice in fluid mechanics is to introduce dimensionless quantities, that compare different terms of the Navier-Stokes equations. The Reynolds number compares the inertia term with the viscous stress term [32]. We introduce a typical scale of flow velocity V_0 and a typical length scale H_0 over which the velocity varies. The Reynolds

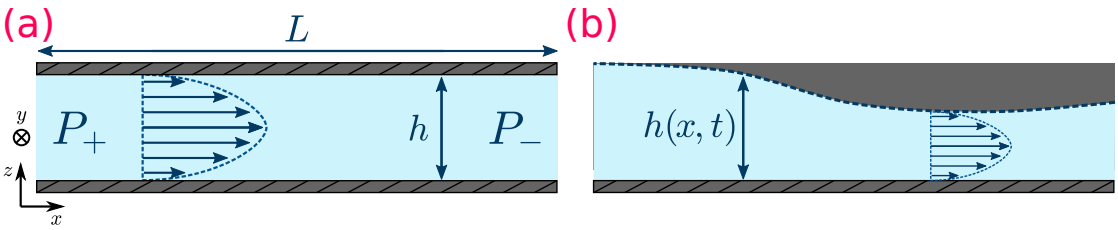

FIG. 1.1. **Poiseuille velocity profiles in a pipe.** *(a): A fluid flows in a straight pipe of length L and height h in between two rigid boundaries, driven by an extra pressure applied at the entrance of the pipe. The resulting velocity profile is parabolic, and called a Poiseuille profile. (b): A thin liquid film flows over a rigid boundary, squeezed towards it by an object. The height profile of the film is denoted $h(x,t)$. The same velocity Poiseuille profile can be observed in the film.*

number is defined as:

$$\mathrm{Re} \sim \frac{\rho||\boldsymbol{v}\cdot\boldsymbol{\nabla}(\boldsymbol{v})||}{\eta||\boldsymbol{\nabla}^2\boldsymbol{v}||}, \tag{1.3a}$$

$$= \frac{\rho V_0 H_0}{\eta}. \tag{1.3b}$$

The value of the Reynolds number predicts the flow regime: for small Re, the flow is dominated by viscous forces, while for large Re, the flow is dominated by fluid inertia. However, the transition value depends on the geometry and the fluid density. The so-called transition to turbulence is still a research area today.

To describe flows in confined geometries, in the present thesis, we work with small values of the Reynolds number, in the range $\mathrm{Re} = 10^{-10} - 10^{-5}$. Thus, we neglect the convective term. Let us introduce a simplified geometry that is representative of the fluid mechanics problems encountered in this thesis. We consider a two-dimensional straight pipe, of length L and height h, at the entrance of which a constant extra pressure is applied, as schematized in Fig. 1.1(a). The velocity field rapidly reaches a steady state, thus the temporal derivative of the velocity field can be neglected. In the absence of external body forces, the incompressible Navier-Stokes equations reduce to the incompressible Stokes equations:

$$\boldsymbol{\nabla}\cdot\boldsymbol{v} = 0. \tag{1.4a}$$

$$-\boldsymbol{\nabla}p + \eta\boldsymbol{\nabla}^2\boldsymbol{v} = 0. \tag{1.4b}$$

In this situation, the vertical component of the velocity field is null, thus $\boldsymbol{v} = v_x\boldsymbol{e_x}$. The incompressible Stokes equations (1.4) become then:

$$\frac{\partial v_x}{\partial x} = 0, \tag{1.5a}$$

$$\frac{\partial p}{\partial x} = \eta\frac{\partial^2 v_x}{\partial z^2}, \tag{1.5b}$$

$$\frac{\partial p}{\partial z} = 0. \tag{1.5c}$$

Thus, the mass conservation and the momentum balance equations, respectively Eqs. 1.4a and (1.4b), impose that the velocity v_x is a constant along the horizontal direction x, and that the pressure field p is a constant along the vertical direction z, respectively, as shown by Eqs. (1.5a) and (1.5c). Then, the velocity profile $v_x(z)$ can be computed by

solving Eq. (1.5b). In the simple situation presented here, we assume that the fluid does not slip on the rigid walls, which reads:

$$v_x(z=0) = v_x(z=h) = 0. \tag{1.6}$$

We note that taking into account slippage at the walls may be relevant in more complex situations, such as flows of polymer solutions [33–35] or flows on hydrophobic surfaces [36, 37]. Here, the chosen no-slip boundary condition leads to the computation of a parabolic velocity profile, as:

$$v_x(z) = \frac{1}{2\eta}\frac{\partial p}{\partial x} z\,(z-h)\,, \tag{1.7}$$

also known as Poiseuille velocity profile [38], that is often encountered in fluid mechanics problems at low Reynolds number [39]. For instance, in microfluidics the flows are contained into micrometric-to-millimetric channels, and are pressure-driven [40–44]: they are described by such a velocity profile. Besides, we stress that these techniques have found many applications over the past decades, from single-cell analysis [5, 45–47] to particle tracking [48–50], passing through medical diagnosis [51, 52]. In this thesis, we specifically study viscous flows that are confined in thin films.

1.1.2 Thin-film equation

The description of the fluid flow inside a thin film of liquid is similar to the one inside a straight pipe that we detailed before. As schematized in Fig. 1.1(b), we consider that a liquid film of thickness h is flowing onto a rigid boundary, yet the upper rigid boundary may move slowly, have a less trivial shape. Stokes equations as given in Eqs. (1.4) hold. We then introduce a hypothesis, which is that the vertical length scale is small compared to the horizontal one: $H_0 \ll L_0$. The latter hypothesis is called the lubrication condition [32], and implies that the vertical component of the velocity field is small compared to the horizontal one: $v_z \ll v_x$. Thus, at leading order in H_0/L_0, Stokes equations reduce to the same system of equations as for the Poiseuille flow, given in Eqs. (1.5). Then, the parabolic Poiseuille profile given in Eq. (1.7) is a solution for the velocity field. Now, when describing liquid thin films, a quantity of interest is the height profile of the film, $h(x)$, that can evolve along the x-axis. We then introduce the volumetric flux in the x direction, as :

$$Q_x = \int_0^l \mathrm{d}y \int_0^{h(x)} \mathrm{d}z\, v_x(z) = -\frac{l}{12\eta}\frac{\partial p}{\partial x} h^3(x), \tag{1.8}$$

where l is a length along the third direction of space, y, on which the system is invariant. Similarly, we introduce the volumetric flux in the z direction, that corresponds to the time derivative of the film thickness, integrated over the upper surface of the film, as:

$$Q_z = \int_0^L \mathrm{d}x \int_0^l \mathrm{d}y\, v_z(z) = \int_0^L \mathrm{d}x \int_0^l \mathrm{d}y\, \frac{\partial h}{\partial t} = l \int_0^L \mathrm{d}x\, \frac{\partial h}{\partial t}, \tag{1.9}$$

with L a horizontal length along which the film is flowing. Invoking the flux conservation for an incompressible liquid, the outgoing flux should equal the incoming one. Finally, we derive the thin-film equation [32, 53, 54], as:

$$\frac{\partial h}{\partial t} = \frac{1}{12\eta}\frac{\partial}{\partial x}\left[h^3 \frac{\partial p}{\partial x}\right]. \tag{1.10}$$

The thin-film equation is largely used to describe lubricated contacts and squeezed flows [55–57], from industrial applications to the modeling of landslides and faults in geophysics [58, 59], through droplet generation and trapping in microfluidics [60–63].

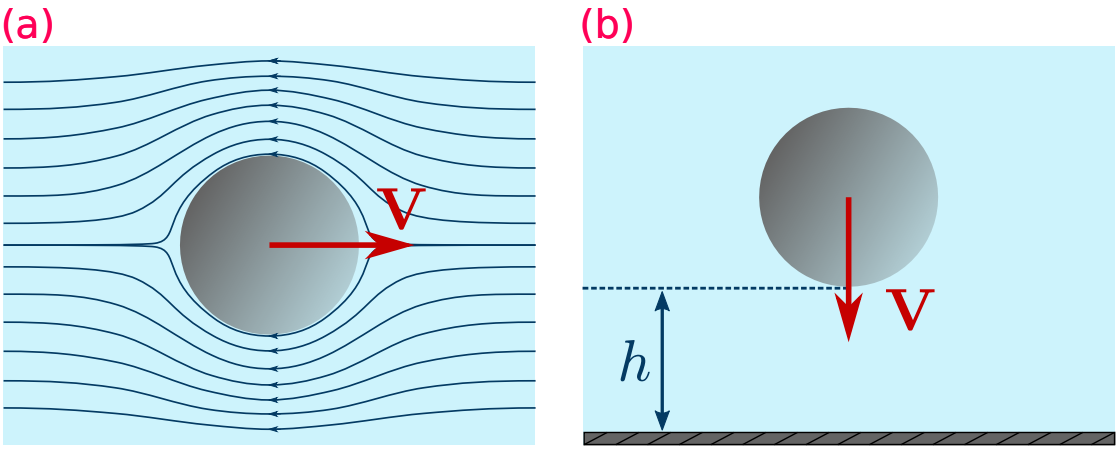

FIG. 1.2. **A spherical particle submitted to Stokes drag.** *(a): A particle of radius R is moving at a velocity $\boldsymbol{V}$ in a viscous fluid. The stream lines are drawn. (b): A particle of radius R is moving at a velocity $\boldsymbol{V}$ towards a rigid boundary. The distance to the wall is denoted h.*

1.1.3 Stokes drag

Let us now consider a spherical particle of radius R that is moving in a viscous and incompressible fluid, at velocity $\boldsymbol{V}$, as schematized in Fig. 1.2(a). The motion of the particle forces the surrounding fluid to bypass it, and the fluid resists, as a result of viscous stresses. Therefore, a drag force is applied by the fluid onto the particle. From Stokes equations 1.4, the so-called Stokes drag is computed in the frame of the particle, and reads:

$$\boldsymbol{F}_{\text{Stokes}} = -6\pi\eta R\boldsymbol{V}. \tag{1.11}$$

For a detailed demonstration, the reader can refer to a classical fluid mechanics book [55, 64, 65]. The latter force should be taken into account whenever a no-slip rigid sphere is in motion in a Newtonian fluid, when viscosity dominates over fluid inertia [66]. Furthermore, when the spherical particle approaches normally a flat rigid boundary, as schematized in Fig. 1.2(b), a region of fluid becomes squeezed in between the sphere and the walls. The escaping fluid is sheared between the particle and the wall. Therefore the drag force is modified [67], and its vertical component reads:

$$F_{\text{Stokes,confined}} = -6\pi\eta\frac{R^2}{h}V \quad \text{for} \quad h \ll R, \tag{1.12}$$

with h the distance from the bottom of the approaching sphere to the rigid wall. Finally, several works have so far investigated how the Stokes drag is modified when more complex physical effects are introduced, for instance by taking into account memory effects [68, 69], slippage [70], or for particles with a more complex shape [71].

1.1.4 Womersley number

We now consider that a sphere is immersed in a viscous fluid and has an oscillating motion, at an angular frequency ω. We can still consider that the Reynolds number is small, and then neglect in the Navier-Stokes equation the advection term $\rho\boldsymbol{v}\cdot\boldsymbol{\nabla}(\boldsymbol{v})$. Yet, the time-derivative term in Navier-Stokes equations, $\rho\partial_t\boldsymbol{v}$ is not zero any longer. The typical velocity scale of the sphere is again denoted V_0 and the typical length scale of velocity variation is denoted H_0. We introduce the Womersley number Wo, that was

originally introduced in the context of medical science, to study the pulsatile blood flow inside arteries [72, 73]. The Womersley number is defined by taking the square root of the ratio between the time-derivative term and the viscous term, as:

$$\mathrm{Wo} \sim \sqrt{\frac{\rho||\partial_t \boldsymbol{v}||}{\eta||\boldsymbol{\nabla}^2\boldsymbol{v}||}}, \tag{1.13a}$$

$$= \sqrt{\frac{\rho V_0 \omega}{\eta V_0/H_0^2}} = H_0\sqrt{\frac{\rho\omega}{\eta}}, \tag{1.13b}$$

where $\sqrt{\eta/(\rho\omega)}$ is the viscous penetration depth. Thus, the Womersley number compares the typical length scale of velocity variation H_0, to the viscous penetration depth. For low-Reynolds number unsteady problems, one should estimate the Womersley number, additionally to the Reynolds number. In the present thesis, we work with small Womersley numbers, in the range $\mathrm{Wo} = 10^{-4} - 10^{-2}$. When the Womersley number is small, the time-derivative term of inertia $\rho\partial_t\boldsymbol{v}$ can be neglected and the velocity field is considered to have reached a steady state.

1.2 Diffusion

1.2.1 Diffusion equation

If a drop of ink is dropped in a glass of water, one observes that the ink gradually spreads in the entire volume of water while the color fades at the same time. This phenomenon is called diffusion: the ink progressively diffuses in water. Diffusion happens for a drop of liquid in any miscible liquid as it would in gaseous media, and even for instance, for water penetrating a solid and hydrophilic medium as shown further in this thesis. Historically, the modern concept of diffusion was first described by the phenomenological Fick's law [74], which states that the diffusive transport of matter is oriented towards the lowest concentration. The mathematical form of Fick's law reads:

$$\boldsymbol{J} = -\mathcal{D}\boldsymbol{\nabla}c, \tag{1.14}$$

with $\boldsymbol{J}$ the diffusive flux of matter and c the concentration. The diffusion coefficient $\mathcal{D}$ quantifies the area explored by diffusion by unit of time. Moreover, the continuity equation given in Eq. (1.1a) ensures the conservation of matter, as:

$$\frac{\partial c}{\partial t} + \boldsymbol{\nabla}\cdot\boldsymbol{J} = 0. \tag{1.15}$$

Thus, a local variation of concentration with time is linked to a transport of matter. If additionally the diffusion coefficient $\mathcal{D}$ is constant with the concentration c, the two previous equations (1.14) and (1.15) lead to tho following linear diffusion equation:

$$\frac{\partial c}{\partial t} = \mathcal{D}\boldsymbol{\nabla}^2 c. \tag{1.16}$$

In the present paragraph, we established a diffusion equation for a concentration field. More generally, diffusive phenomena are encountered in many situations and for various fields (*e.g.* temperature), and obey to the same equation.

1.2.2 Resolution with a Green's function

In this subsection, we introduce the main ingredients of the classical path that is used to solve the diffusion equation written in Eq. (1.16). We take the opportunity of solving a simple standard diffusion equation to present the calculation method, whose scope is much more general. This method can be used to solve more complex systems of partial differential equations, as done in this thesis. The full calculation is detailed in Appendix D.1. We first introduce the following initial condition:

$$c\left(\boldsymbol{x},0\right)=c_0\delta^3\left(\boldsymbol{x}\right), \tag{1.17}$$

which together with Eq. (1.16) define the fundamental problem. The solution is called the fundamental solution, or Green's function, and reads:

$$\mathcal{G}\left(\boldsymbol{x},t\right)=\frac{c_0}{\sqrt{4\pi\mathcal{D}t}^3}\exp\left(-\frac{\boldsymbol{x}^2}{4\mathcal{D}t}\right). \tag{1.18}$$

By definition, the Green's function of a problem constituted of a system of linear partial differential equations, is the solution associated to a Dirac distribution as the the right hand side source term. Here in particular, the initial condition transforms the equation at $t=0$ into one with a Dirac distribution as the right hand side source term. Finally, by applying the superposition principle, or Duhamel's principle [75, 76], the solution to the diffusion equation (1.16) associated with any initial condition is computed by convolution to the Green's function $\mathcal{G}$, as:

$$c\left(\boldsymbol{x},t\right)=\iiint_{\mathbb{R}^3}\mathrm{d}^3\boldsymbol{x}\,\mathcal{G}\left(\boldsymbol{x}-\boldsymbol{y},t\right)c\left(\boldsymbol{y},0\right), \tag{1.19}$$

with $c\left(\boldsymbol{x},0\right)$ the initial condition. One can remark that a natural, dimensionless diffusive variable emerges, as $\chi=\mathcal{D}t/\boldsymbol{x}^2$. Indeed, the length explored by front of diffusion scales with $\sqrt{\mathcal{D}t}$, which defines the diffusive dynamics. For further reading on mathematical methods associated to diffusion problems, one can refer to the work of Crank [77].

1.2.3 Diffusion of a particle in a liquid

An example of application of the diffusion equation presented in the previous subsection is the diffusion of a solid sphere in a viscous liquid, that constitutes a classical problem. When moving, the particle is subjected to the Stokes drag, which slows down its motion in the liquid. On the contrary, the particle receives energy from thermal agitation, through the collisions of liquid molecules. At low Reynolds number, the Stokes-Einstein relation provides an expression of the diffusion coefficient of the particle [78–81], as:

$$\mathcal{D}=\frac{k_\mathrm{B}T}{6\pi\eta R}, \tag{1.20}$$

with R the radius of the particle, η the liquid viscosity, T the temperature and k_B the Boltzmann constant. Many works were conducted, based on the fundamental Stokes-Einstein relation, such as the experimental estimation of the Avogadro number by Jean Perrin [82], the establishment of the fluctuation-dissipation theorem [83, 84], that still constitute the basis of statistical physics today [85].

In the present section, we have considered a solid object that moves in a solvent by diffusion. In the next section, we rather take the opposite point of view, and consider a solvent that flows toward solid particles, to dilute them.

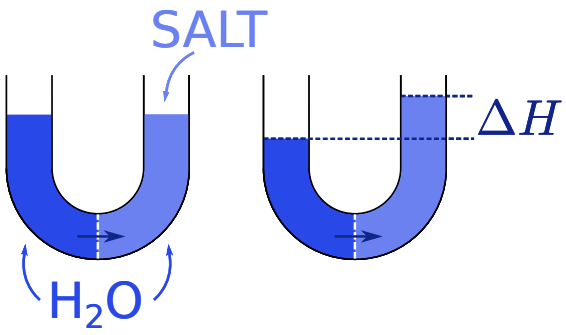

FIG. 1.3. **Intuitive definition of the osmotic pressure.** *A U-pipe is filled with water. Salt is added on the right side. A semi-permeable membrane placed in the middle allows water to flow but prevents salt to pass through. A water flow from left to right dilutes the salt, and results in a difference of height ΔH between the two sides.*

1.3 Osmosis

1.3.1 Definition of the osmotic pressure

Let us consider a U-pipe filled with pure water, as sketched on Fig. 1.3. A semi-permeable membrane is placed at the center of the tube, allowing only water to pass through. If now one adds salt on the right side, the water dilutes the salt and the salt diffuses in the water. Yet, the semi-permeable membrane prevents the salt to pass from right to left, resulting in a water flow from left to right. At equilibrium, the water height is different for the two sides of the tube. The height difference, noted ΔH, can be associated to a mechanical pressure difference in the fluid Δp, at both fluid surfaces. The osmotic pressure Π is defined as:

$$\Pi = -\Delta p = \rho g \Delta H, \tag{1.21}$$

with g the gravitational acceleration and ρ the mass density of water. In other words, the addition of a solute in a solvent creates a local increase of the osmotic pressure, compared to a pure solvent. Fluid flows are directed towards the highest osmotic pressure to dilute the solute. At equilibrium, all the water did not flow and some is left on the left side of the tube. Thus the osmotic pressure is higher (and homogeneous) in the right side on the tube compared to the left side. The difference in osmotic pressure is finally compensated by the mechanical pressure difference on the two free surfaces, as expressed by Eq. (1.21).

The latter situation provides an intuitive definition of the osmotic pressure. Considering the pure solvent as the reference state with a zero osmotic pressure, the latter increases with the concentration c of solute. This is materialized by Van't Hoff formula [18], which reads:

$$\Pi = c\mathcal{R}T, \tag{1.22}$$

with c the molar concentration, T the temperature and $\mathcal{R}$ the ideal gas constant. The Van't Hoff formula is derived from thermodynamics, considering that the activity of a solvent varies with the concentration of the added solute. In the next paragraph, we introduce a proper definition of the osmotic pressure, provided by thermodynamics.

First, still taking the pure solvent as the reference state, we consider the system after addition of a solute. We recall from thermodynamics the expression of an infinitesimal variation of Gibbs free energy [18, 86], which reads:

$$\mathrm{d}G_{\mathrm{Gibbs}} = -S\mathrm{d}T + V\mathrm{d}p + \Delta\mu\mathrm{d}N, \tag{1.23}$$

with S the entropy, V the volume, T the temperature, p the mechanical pressure and N the number of molecules of solute. The variation of chemical potential $\Delta\mu$ is expressed

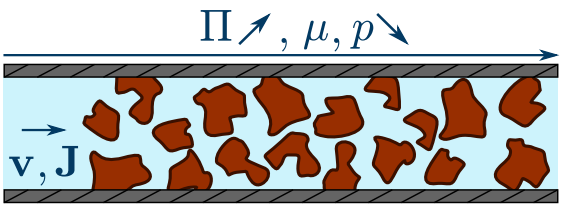

FIG. 1.4. **Darcy flow through a porous medium.** *A solvent flows through a porous medium at a velocity* $\boldsymbol{v}$*, or similarly with a molecular flux* $\boldsymbol{J}$*, following the decreasing mechanical pressures* p *or chemical potentials* μ*, or the increasing osmotic pressures* Π*.*

by comparison to the reference state, and defined from Eq. (1.23) at constant pressure and temperature, as:

$$\Delta\mu = \mu(p,T,c) - \mu^0(p,T) = \left.\frac{\partial G}{\partial N}\right|_{p,T}. \tag{1.24}$$

To reach an equilibrium, the solvent flows to dilute the solute. Assuming that the systems reaches an equilibrium when the Gibbs free energy is minimal, we deduce from Eq. 1.24 that the solvent flow decreases the difference of chemical potential $\Delta\mu$. In other words, the solvent flows towards the smallest chemical potentials. Then, by assuming the incompressibility of both the solvent and the solute, the molecular volume of the solvent Ω is defined by:

$$\mathrm{d}V = \Omega \mathrm{d}N. \tag{1.25}$$

Finally, the osmotic pressure Π is defined with the variation of chemical potential $\Delta\mu$, using the molecular volume Ω, as:

$$\Pi = -\frac{\Delta\mu}{\Omega} = -\frac{1}{\Omega}\left.\frac{\partial G_{\mathrm{Gibbs}}}{\partial N}\right|_{p,T} = -\left.\frac{\partial G_{\mathrm{Gibbs}}}{\partial V}\right|_{p,T}, \tag{1.26}$$

and the solvent flows towards the highest osmotic pressure.

1.3.2 Porosity

In this subsection, we rather consider the opposite situation, as schematized in Fig. 1.4, where a solvent flows through a composite medium, driven by an imposed mechanical pressure gradient. This situation can be represented by the local form of the Darcy's law [64, 87], which reads:

$$\boldsymbol{v} = -\frac{k}{\eta}\boldsymbol{\nabla} p, \tag{1.27}$$

with $\boldsymbol{v}$ the velocity field, η the fluid viscosity, p the pressure in the fluid and k the permeability of the medium. Equivalently, a flow through a porous medium can be described in terms of osmotic-pressure driving (directed towards the highest osmotic pressures), or chemical-potential driving (towards the lowest chemical potentials), as seen in the previous subsection. The Darcy's law is then also expressed as;

$$\boldsymbol{J} = -\frac{k}{\eta\Omega^2}\boldsymbol{\nabla}\mu, \tag{1.28}$$

with the instantaneous molecular flux $\boldsymbol{J}$, expressed as $\boldsymbol{J} = \boldsymbol{v}/\Omega$. Flows in porous media constitute a field of research that has found many applications in the investigation of soil mechanics [10, 88–92], and recently in the context of particles flowing in porous media [93] or near boundaries [94].

1.3.3 Polymer-solvent mixtures

When a solvent flows through a solid network, interactions between the solvent and the solid matrix may occur. In particular, a solvent is defined as "good" or "bad" for a polymer depending on theses interactions. Briefly, if the polymer dilutes in the available volume of solvent up to the extent of the chain size, the latter is considered as good, and otherwise, if the polymer collapses on itself the solvent is considered as bad [95]. When the solvent is pure water, the polymer is described as hydrophilic or hydrophobic. This statement is modeled by Flory-Huggins theory for solvent mixtures [18]. First, the Boltzmann formula provides the entropy per site of a thermodynamic system, as for the general so-called Shannon entropy, as:

$$S = -k_{\mathrm{B}} \sum_i p_i \ln p_i, \tag{1.29}$$

with p_i the probability associated to a state i of the system. In the case of a polymer-solvent mixture, two states are considered: the site is occupied either by a solvent molecule, either by a polymer one. We introduce the volume fractions of the polymer and solvent, as:

$$\Phi_{\mathrm{p}} = \frac{V_{\mathrm{p}}}{V} \quad \text{and} \quad \Phi_{\mathrm{s}} = \frac{V_{\mathrm{s}}}{V}, \tag{1.30}$$

with V_{p} and V_{s} the partial volume of polymer and solvent respectively, with $V_{\mathrm{p}} + V_{\mathrm{s}} = V$. The entropy per site reads:

$$S = -k_{\mathrm{B}} \left[\Phi_{\mathrm{p}} \ln\left(\Phi_{\mathrm{p}}\right) + \left(1 - \Phi_{\mathrm{p}}\right) \ln\left(1 - \Phi_{\mathrm{p}}\right) \right]. \tag{1.31}$$

The free energy is derived using the equation $F = U - TS$. An additional term of mixing is considered [86, 96], such as the the mixing free energy of the whole system reads:

$$F_{\mathrm{mix}} = \frac{k_{\mathrm{B}}T}{\Omega} V \left[\Phi_{\mathrm{p}} \ln\left(\Phi_{\mathrm{p}}\right) + \left(1 - \Phi_{\mathrm{p}}\right) \ln\left(1 - \Phi_{\mathrm{p}}\right) + \chi_{\mathrm{ps}} \Phi_{\mathrm{p}} \left(1 - \Phi_{\mathrm{p}}\right) \right], \tag{1.32}$$

with χ_{ps} the polymer-solvent interaction parameter, or Flory parameter, that quantifies the propensity of both species to demix. For instance, the quality of a solvent is quantified by the Flory parameter. Additionally, the stability of a liquid-liquid or a polymer-solvent mixture can be predicted using the Flory parameter. A mathematical study of the free energy F_{mix} as a function of the volume fraction of a species Φ determines whether the system is stable, depending on the value of the Flory parameter [97–102]. Furthermore, in the case of polymer solutions, the free energy of the system is expressed taking into account the number N_{p} of polymer segments connected by bounds. The free energy thus reads:

$$F_{\mathrm{mix,ps}} = \frac{k_{\mathrm{B}}T}{\Omega} V \left[\frac{\Phi_{\mathrm{p}}}{N_{\mathrm{p}}} \ln\left(\Phi_{\mathrm{p}}\right) + \left(1 - \Phi_{\mathrm{p}}\right) \ln\left(1 - \Phi_{\mathrm{p}}\right) + \chi_{\mathrm{ps}} \Phi_{\mathrm{p}} \left(1 - \Phi_{\mathrm{p}}\right) \right]. \tag{1.33}$$

By comparaison to the free energy in the case of liquid mixtures, as expressed in Eq. (1.32), the factor $1/N_{\mathrm{p}}$ in Eq. (1.33) accounts for the fact that N_{p} polymer segments are now bounded, which reduces the possibilities of arrangement. We note that Flory-Huggins theory has largely been applied to swelling polymers [100, 103, 104], and also to phase-separation in polymer mixtures [100, 105].

From Flory-Huggins mixing free energy, the isothermal elastic bulk modulus is defined as:

$$K_{\mathrm{el}} = -V \frac{\partial \Pi}{\partial V} = \Phi_{\mathrm{p}} \left. \frac{\partial \Pi}{\partial \Phi_{\mathrm{p}}} \right|_T. \tag{1.34}$$

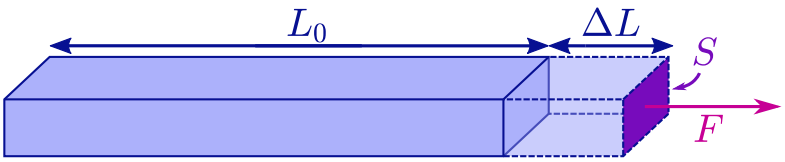

FIG. 1.5. **An elastic beam.** *A pulling force F is applied on a straight beam of section S and initial length L_0, causing an elongation ΔL.*

As a result, the elastic bulk modulus depends on the volume fraction of polymer, and thus of solvent, as $\Phi_s = 1 - \Phi_p$.

Elastomers are typically made of synthetic or natural polymers that are reticulated to form a network. When immersed in a favorable solvent, a polymeric matrix swells as predicted by Flory-Huggins theory [18], and forms a gel. In this thesis, we will work with a particularly hydrophilic polymer, that swells by several times its initial volume when brought in contact with water, driven by strong gradients of osmotic pressure. In such a case, the swollen hydrogel contains a large proportion of water molecules, likely to flow with any perturbation. According to Eq. (1.34), variations of elastic properties with the amount of solvent are expected [106, 107]. Having an idea for how the elastic modulus can be controlled on a physico-chemical basis, in the following we introduce basic concepts of elasticity theory that will be used in this thesis.

1.4 Elasticity

1.4.1 Hooke's law

The elasticity of a solid object characterizes how the latter can be deformed when submitted to a load, in a regime where it recovers perfectly its initial shape after release of the load. Let us consider a straight beam of section S and initial length L_0, as schematized in Fig. 1.5. A pulling force F is applied at one edge, normally to the section S and along the axis of the beam, resulting in an elongation ΔL. For simplicity, we consider here that the section S is not impacted by the stretching. The linear elasticity of the beam is modeled by Hookes's law as if it was a spring, as:

$$\frac{F}{S} = E\frac{\Delta L}{L_0}, \tag{1.35}$$

with E the Young's modulus of the material. In the one-dimensional case of an extended beam, we define the stress σ as the applied force per unit area, and the strain ϵ as the relative elongation, as:

$$\sigma = \frac{F}{S} \quad \text{and} \quad \epsilon = \frac{\Delta L}{L_0}, \tag{1.36}$$

and the Hooke's law can be written as:

$$\sigma = E\epsilon. \tag{1.37}$$

To generalize the linear-elasticity concept to three-dimensional objects, we first introduce the tensorial definition of the strain, as:

$$\boldsymbol{\epsilon} = \frac{1}{2}\left[\boldsymbol{\nabla u} + (\boldsymbol{\nabla u})^T\right], \tag{1.38}$$

with $\boldsymbol{u}$ being the spatial displacement field with respect to the undeformed reference state. Figure 1.6 schematizes how the strain tensor is established, in two dimensions for

simplicity. The displacement field $\boldsymbol{u}$ expresses the displacement upon deformation of a material point located at (x, z). An element of the strain tensor ϵ_{ij} expresses the variation of the i-component of the displacement field $\boldsymbol{u}$ with respect to the direction j. In the definition introduced in Eq. (1.38), the strain tensor is linear with respect to gradients of the displacement field. The latter definition is valid for small deformations [108], otherwise non-linear terms in the gradient of the displacement field are added. In the case of a solid presenting a linear and isotropic elasticity, the Hooke's law gives the stress-strain relationship:

$$\boldsymbol{\sigma} = 2G\left[\boldsymbol{\epsilon} + \frac{2\nu}{1-2\nu}\mathrm{Tr}\left(\boldsymbol{\epsilon}\right)\right], \tag{1.39}$$

with G the shear modulus [108]. The Poisson ratio ν characterizes the compressibility of the material, *i.e.* whether and how much volume is kept when a compression load is applied on the solid. For an elastic and incompressible solid, the Poisson ratio takes a particular value, which is $\nu = 0.5$. In this case, the total volume of the object is conserved in the deformed state, which is mathematically expressed from the strain tensor, as:

$$\mathrm{Tr}\left(\boldsymbol{\epsilon}\right) = 0, \tag{1.40}$$

with noting Tr the trace of a tensor, and the stress-strain relationship given in Eq. (1.39) becomes:

$$\boldsymbol{\sigma} = 2G\boldsymbol{\epsilon}. \tag{1.41}$$

For the case of the elastic beam presented at the beginning of this section, and schematized in Fig. 1.5, the Poisson ratio takes another particular value, which is $\nu = 0$. In that case, the strain in the direction of the pulling force does not affect the strains in the two other directions of space. Thus, the section of the beam is conserved in the deformed state, and the stress-strain relationship is identical to the one given in Eq. (1.41). Finally, the link between the Young's modulus E, the shear modulus G and the bulk modulus K is recalled, as:

$$E = 2G(1+\nu) = 3K(1-2\nu). \tag{1.42}$$

For further reading, one can refer to the following references [108, 109].

Finally, an equivalent of the Navier-Stokes equation for fluids, the motion of an elastic solid is described mathematically by Newton's second law, which reads:

$$\rho\frac{\partial \boldsymbol{u}}{\partial t} = \boldsymbol{\nabla}\cdot\boldsymbol{\sigma} + \boldsymbol{f} \tag{1.43}$$

with $\boldsymbol{f}$ the sum of external body forces per unit mass. In the particular case of a steady state, in the absence of external body force, Newton's second law becomes:

$$\boldsymbol{\nabla}\cdot\boldsymbol{\sigma} = 0, \tag{1.44}$$

which is also known as Navier's closure relation.

1.4.2 Towards poroelasticity

The present thesis studies the mechanics of swollen gels, which couples several of the themes presented until there. Upon swelling, solvent molecules penetrate inside the gel and diffuse through the polymer matrix. Therefore, when a load is applied to the gel, the solvent flows with time inside the polymeric network, and material deformations are time-dependent. This dynamic response arises because the elastic polymer chains are

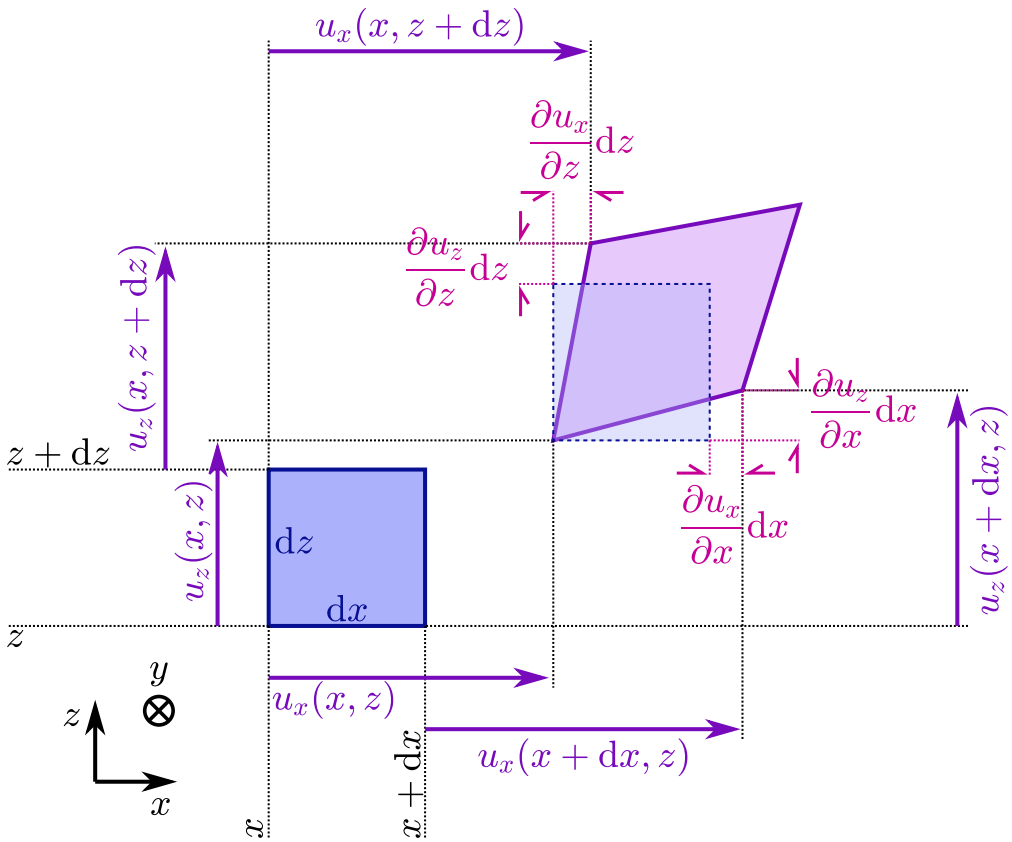

FIG. 1.6. **Two-dimensional displacement of an infinitesimal surface element upon deformation.** *Originally located at a position* (x, z)*, an infinitesimal surface element* $\mathrm{d}x\mathrm{d}z$ *is displaced by* $\boldsymbol{u}$ *upon a deformation. The strain tensor* $\boldsymbol{\epsilon}$ *is computed using the partial derivatives of the displacement field* $\boldsymbol{u}$*, using Eq.* (1.38)*.*

attached by reticulation, while the solvent motion is unbounded and implies viscous dissipation in the pores. Such a coupling mechanism is called poroelasticity. The question of poroelasticity was first addressed by Biot, in the context of soil-consolidation mechanics [10, 92]. Later, the framework of linear poroelasticity was established [15–17, 30, 91, 110–113]. Considering the gels as isotropic materials, the theory of elasticity presented in this subsection is coupled to Darcy's law (see Sec. 1.3.2), to describe solvent flows in elastic and porous media. As a result, a term of osmotic pressure is added to the expression of the stress as a function of strain, which thus reads:

$$\boldsymbol{\sigma} = 2G\left[\boldsymbol{\epsilon} + \frac{2\nu}{1-2\nu}\mathrm{Tr}\left(\boldsymbol{\epsilon}\right)\right] - \frac{\Delta\mu}{\Omega}\boldsymbol{I}. \tag{1.45}$$

Since Biot's first model, additional features have been added such as nonlinear elasticity [114, 115], viscoelasticity [116], or surface stresses [110, 117, 118], and instabilities have been considered [119].

Having presented basic notions of fluid mechanics, continuum mechanics and polymer physics, the next section sets the scientific context of this thesis. In particular, the first subsection is dedicated to the surface instabilities that arise at the surface of gels, upon swelling and drying. The second subsection focuses on soft-lubrication situations, encountered when a spherical particle moves close to a soft boundary.

1.5 Scientific context of the thesis

Besides the mechanisms of soil sedimentation, poroelasticity has also been an important ingredient in the context of the exploitation of soft-coating properties in fundamental science. Indeed, grafting polymer films onto rigid surfaces is largely used for various applications, from cellular culture [7, 120] and medicine [6] to microfluidic engineering [3, 5], through the building biomimetic systems [8, 121]. However, swollen polymer gels are fragile systems, and therefore are difficult to investigate without damage. Moreover, grafting to a substrate can constrain the swelling of hydrogel films and lead to surface patterning. Contactless methods appear as good candidates to probe the mechanical properties of such systems, yet the associated theoretical framework usually applies to flat substrates. Thus, in the following we present a few different types of surface instabilities that may occur upon swelling and drying, before focusing on different investigation modes of the mechanical properties of soft substrates.

1.5.1 Elastic and drying-induced instabilities

When a hydrophilic, reticulated polymer film is brought in contact with water, a hydrogel forms by swelling. However, when the polymer film is grafted onto a rigid support, the swelling of the hydrogel film is constrained in one direction, which leads to the formation of surface patterns. Volumetric expansion, associated with osmotic stress, is inhibited laterally by substrate attachment. The resulting geometrical incompatibility generates an in-plane compressive stress that can destabilize the flat surface of the hydrogel [122–125]. This nonlinear instability [126–128] renders the surface topography non-uniform, with sharp "creases" (localized regions of large strain/curvature [129]) separating smooth peaks [122, 130–132], as shown in Fig. 1.7(a). Creases were first noticed at the surface of reticulated gels of gelatine a century ago [133], and on swollen rubber in the 1960's [134]. Then, the works of Tanaka in the 1990's pioneered the research on the creasing instability [135, 136], and led to various numerical developments [130]. Later, the creasing instability has been largely reported at the surface of compressed elastomers [127, 129, 137–140], as well as on swelling gels[30, 122, 124, 133–136, 141, 142]. In particular, the characteristic wavelength λ_{crease} of the pattern observed at the surface of a swollen material is predicted by the works of Dervaux and Ben Amar [143], and reads:

$$\lambda_{\text{crease}} = \frac{4\pi\tau_{\text{dry}}}{\log\left(\frac{44.953\tau_{\text{dry}}}{d}\right)}, \tag{1.46}$$

with τ_{dry} being the initial dry thickness of the swelling film and d a regularization length, taking into account the mechanical properties of the material [144], such as the bulk elasticity, the surface tension between the material and the ambient air and the thickness of the material layer.

Besides, previous works showed that the deposition of a pre-stretched stiff film onto a soft material triggers the formation of wrinkles at the surface [125, 145], as schematized in Fig. 1.7(b). Wrinkles on bilayered systems have been first studied in details by Allen [146] in the engineering context of building materials, made of several layers with different mechanical properties. Later, wrinkles were observed on the treated surface of elastomers [145, 147–150] or on elastic films deposited on a bath of viscous fluid [151]. In such cases, the surface takes a sinusoidal form [131, 152–154], with a characteristic wavelength λ_{wrinkle} that is determined by the respective Young's moduli of both layers

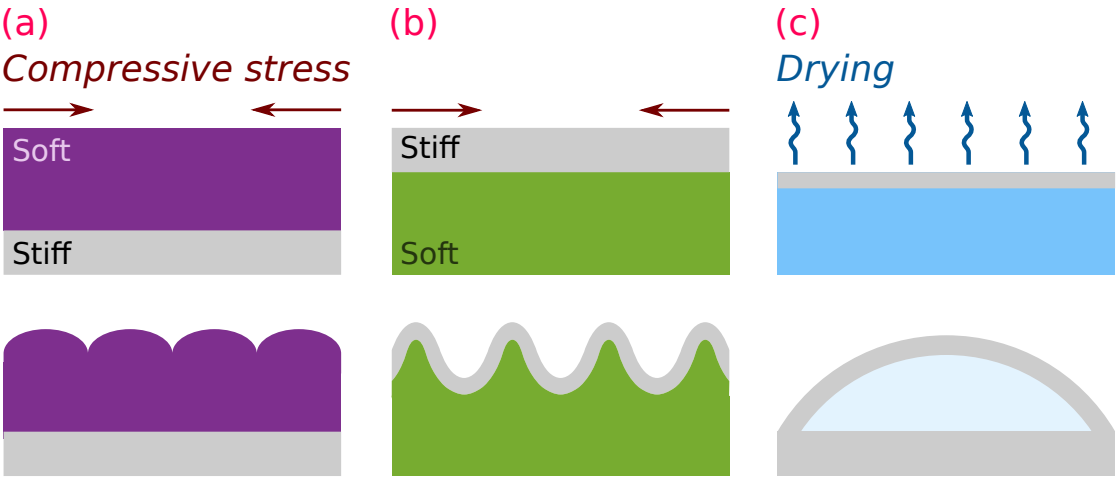

FIG. 1.7. **Creasing, wrinkling, and buckling instabilities.** *Summary of elastic instabilities that arise at the surface of elastomers, swelling gels, and drying droplets. (a): Creasing instability, observed on compressed elastomers and surface-attached swollen gels. (b): Wrinkling instability, observed on bilayered systems composed of a pre-stretched stiff and thin film deposited at the top of a soft and thick layer. (c): Buckling instability, observed on drying droplets of colloid or polymer solutions.*

and the thickness τ_{stiff} of the top stiff one. The wavelength reads:

$$\lambda_{\text{wrinkle}} = 2\pi\tau_{\text{stiff}} \left(\frac{E_{\text{stiff}}}{3E_{\text{soft}}} \right)^{1/3}, \tag{1.47}$$

with E_{stiff} the Young's modulus of the top, thin and stiff layer, and E_{soft} the one of the bottom, thick and soft layer.

A first theoretical prediction about the mechanism that triggers the apparition of surface instabilities was made by Biot [155]. An elastomeric half-space would deform in a sinusoidal pattern, which we identify now as wrinkles, provided that the in-plane strain exceeds a threshold of 0.46 [155, 156]. Later, further theoretical and numerical [123, 128, 157] as well as experimental works [122, 127] showed that the creasing instability occurs at a critical strain threshold of $\epsilon_c \sim 0.30 - 0.35$. This latter threshold is lower than Biot's earlier prediction, meaning that creases appear before wrinkles as strain increases [125, 129, 158]. The creasing instability is triggered by imperfections, experimentally in the form of nanoscale roughness and numerically by introducing defects [129, 159–162]. The singular deformation of a crease requires the elastic energy to overcome the barrier of surface tension with the elasto-capillary length $l_{\text{ec}} \sim \gamma/G$ that characterizes a balance between surface tension and bulk elasticity. Let l be a relevant characteristic length of the considered system: for $l \leq l_{\text{ec}}$ the surface tension dominate over bulk elasticity, while for $l \geq l_{\text{ec}}$ the bulk elasticity dominates over surface tension. Creasing thus releases compression, and produces topographic variations that are reminiscent of the structural architecture of the brain [128, 157, 163]. Finally, creases are reversible in the case of compressed elastomers as compression is released. Yet, in the case of swelling gels, the irreversible character of a swelling-drying cycle renders the creasing irreversible too [30, 164].

If in a drying process, the ambient medium is air instead of solvent, and the initial and final states are precisely reversed compared to the swelling process, drying is only the time reversal of swelling if it occurs very slowly and elastic deformations are small [19]. Non-linearities that arise though large deformation can turn swelling and

deswelling into asymmetric processes [19, 20], and result in irreversible deformations, even in a single swelling-deswelling cycle [30]. Furthermore, evaporation reduces the volume fraction of solvent from the free surface, which may lead to an inhomogeneity of solvent concentration [22, 24, 28, 165, 166], and to an accumulation of solute at the surface. For instance, the so-called coffee-ring effect results from the latter mechanism [28, 165–167], as well as Marangoni flows [168–171]. In polymer films, the formation of a skin layer or "crust" may occur [24, 25, 27, 29, 172, 173], together with phase changes such as the glass transition in a region localized near the surface [23, 25, 27]. In sessile drops, the formation of pinned contact lines [23, 165, 168, 169, 174, 175] may lead to buckling instabilities [25, 172, 176, 177], as schematized in Fig. 1.7(c). More complex shapes such as rings [178–180], cracks [23, 28, 181], or wrinkles [131, 181] similar to the ones observed in the case of bilayered systems described here have been reported.

In the Chapter 2 of this thesis, we study the apparition of surface patterns at the surface of both swollen and dried polymer films. In particular, we report a complex pattern, resulting apparently from several types of instabilities, and we investigate in details the characteristic features of the deformed surfaces.

In the present subsection, we presented some surface instabilities that can occur when working with swelling and/or drying grafted polymer films. Such designed systems are notably used in the context of fundamental sciences, exploiting their soft-coating properties. In the next subsection, we focus on the influence of a soft boundary on a nearby mobile particle immersed in a viscous bath.

1.5.2 Soft lubrication

When a particle immersed in a viscous fluid is approached to a rigid boundary, the pressure field in the fluid in the confined region is strongly modified, and would diverge to infinity when contact would be reached. The lubrication layer of fluid located in between the wall and the particle theoretically prevents contact [32, 67]. Besides, the Stokes drag applied on the particle is modified by the confinement (see Sec. 1.1.3). If now the rigid wall is coated with a soft and elastic material, when the particle is approached towards the soft boundary, a hydrodynamic stress arises in the region of fluid that is confined between the particle and the soft boundary. The latter stress deforms the soft boundary, the elastic deformation modifies in turn the flow [182], and the latter finally influences the particle motion. The resulting coupling belongs to the field of elastohydrodynamics (EHD) [39, 56, 64, 183–186], and the particular situation of a rigid object moving near a soft wall within a lubrication layer defines the so-called soft-lubrication coupling [187–191].

Soft lubrication is relevant in many biomimetic contexts, and thus has been a field of research for the past 20 years. Indeed, several examples can be identified in the human body at different scales. The knees are made of cartilaginous menisci immersed in the synovial liquid, that make a lubricated and softer interface between stiff bones. Considering the weight that knees have to handle, the effective friction coefficient between bones is reduced by several orders of magnitude compared to a non-lubricated contact [192, 193], *i.e.* down to 10^{-6}, a value that is not yet reproduced in industry. Similarly, the eyes are constituted of eyelids sliding on eyeballs, the contact of which is lubricated by the tear fluid. Moreover, the presence of a gel-like layer of proteins at the surface of both the eyelid and the eyeball ensures a smooth transition between the solid parts and the liquid phase, and softens the contact [194, 195]. Finally, the circulation of red blood cells is carried out by the compliant blood vessels, presenting a protein-rich layer, called glycocalyx, on their surface. In a perspective of biomimetism, a work studied the flow

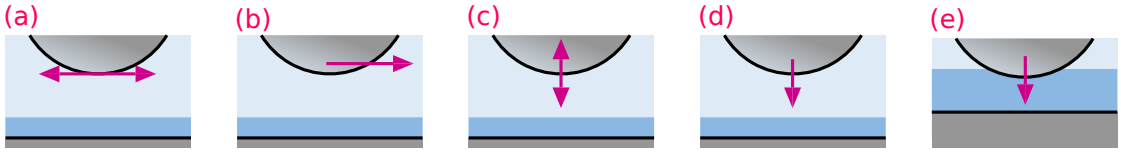

FIG. 1.8. **Different configurations for soft-lubrication investigation in the sphere-plane geometry.** *The sphere motion is (a): oscillatory and parallel to the soft-coating plane, (b): steady and parallel to the plane, (c): oscillatory and perpendicular to the plane, (d): steady and perpendicular to the plane, also called approach mode. (e): After the approach mode, the sphere is eventually in solid contact with the soft coating and indents it.*

of rigid particles in a millimetric channel coated with hyaluronan brushes that mimic glycocalyx [121], and showed that the particle trajectories are modified by the presence of the soft coating. More precisely, the particles are repelled from the walls. Thus these results provide important insights on the mechanism of blood circulation in the human body [196].

To rationalize physical phenomena associated to the soft-lubrication coupling, let us consider the sphere-plane geometry, in which several modes of motion can be identified as schematized in Fig. 1.8(a-d). For the purpose of this thesis, we focus only on translation motions, and not on rotation. Considering coatings made of a purely elastic material, these different configurations are largely documented in literature. First, the sphere motion can be parallel to the plane, either oscillatory (see Fig. 1.8(a)) or steady (see Fig. 1.8(b)). In both cases, previous works showed experimentally and theoretically that the motion of the sphere generates an asymmetric pressure field in the confined region of fluid. The latter results in a lift force, that repels the particle from the wall [121, 188, 190, 197–201]. Second, the sphere motion can be oscillatory, and perpendicular to the flat surface [202], as sketched on Fig. 1.8(c). In particular, the work of Leroy and Charlaix showed that both the storage and loss components of the resulting force applied on the sphere exhibit two regimes [203, 204], depending on the average sphere-plane distance. At large distances, the viscous dissipation occurring in the fluid phase, *e.g.* Stokes drag, is dominant, while at small distances, the elasticity of the soft coating is dominant in the force response. Third, the sphere motion can be steady, and towards the surface, which defines the approach mode, as sketched on Fig. 1.8(d). The inverse situation, where the sphere is coated with an elastic material and approaches a rigid wall, has also been studied [205–210]. A few other works predict that when the opposite motion is imposed, *e.g.* retraction, an elastohydrodynamic adhesion force is applied on the sphere, due to the presence of the soft coating [190, 211]. In the approach mode, the elastic coating can undergo small-to-large deformations. Linear EHD theories are well suited to describe small deformations [212], and non-linearities are rarely taken into account to describe large-deformation regimes [191]. Finally, the approach mode leads to a situation where the fluid layer thickness is smaller and smaller, up to physical contact. Then, the sphere indents the soft layer, as described in Fig. 1.8(e). The latter situations are respectively described by the framework of Hertz-like problems [213–215], and the so-called Hertz contact theory [216, 217].

However, if the soft-lubrication problem has largely been addressed in the case of purely elastic coatings, undergoing small deformation, more realistic descriptions in a biomimetic perspective are still to develop. Early works on purely porous substrates suggest an elastic-like description involving effective slippage at the interface, with either the slip length considered to be on the order of the pore size [90], or a full slip

boundary condition [218]. The effects of viscoelasticity have been recently investigated in detail [11–13, 219], yet, the effects of poroelasticity remain scarcely and partially addressed [15–17, 111]. Recent works developed a theoretical framework that describes in detail the swelling of poroelastic materials when immersed into a solvent, taking into account large deformations [220]. The purpose of this thesis is to develop a framework that describes the mechanical response of swollen hydrogels in a more realistic manner, taking into account both their elasticity and porosity.

Considering now swollen hydrogels as more complex systems, their mechanical response is determined by their interactions with the environment. If the gel is indented by a rigid object, as in the emblematic example of contact mechanics [112, 113, 214, 217, 221, 222], solvent molecules do not flow across the interface between the gel and the indenter, which is thus impermeable. The latter boundary condition is expressed as [111]:

$$\boldsymbol{J}(z=0)\cdot\boldsymbol{n}=0, \tag{1.48}$$

with $\boldsymbol{J}$ being the molecular flux of solvent inside the porous matrix of the gel, $\boldsymbol{n}$ a normal vector to the interface, and the interface being defined by $z=0$. In contrast, if the gel is immersed in its own solvent, then the solvent molecules can be transported across the gel-solvent interface, which is thus permeable. At the surface, the chemical potential μ is fixed to its bulk value μ_{bulk}, in the solvent reservoir. Thus, the permeable boundary condition is expressed as [10]:

$$\mu(z=0)=\mu_{\text{bulk}}. \tag{1.49}$$

In Chapter 3, we establish a model that describes the mechanical response of a permeable, poroelastic material, in both the semi-infinite and finite-thickness cases. In Chapter 4, we apply the latter model to the situation of a sphere oscillating perpendicularly to the coated surface, as sketched in Fig. 1.8(c), and use our theoretical framework to investigate the mechanical properties of a swollen hydrogel. Finally, Chapter 5 is dedicated to the investigation of a swollen hydrogel in approach mode up to contact, as sketched by Figs. 1.8(d) and (e).

Chapter 2

Transition in morphology at the surface of grafted hydrogel thin films

The present Chapter is dedicated to the study of surface instabilities that may occur at the surface of gels upon swelling and drying, as presented in the general introduction, Sec. 1.5.1. Here, we report on a morphological transition that occurs upon gel drying. We show surface patterns on nanometric-to-micrometric films in both the wet and dry states. We first describe the sample fabrication and the AFM-based measurement technique. We then investigate typical AFM images of dry and wet Poly-N-isopropylacrylamide (PNIPAM) films, showing a transition from a creased pattern to a more sinusoidal morphology with what we refer to as crease scars. We present a quantitative analysis of these results and discriminate different regimes associated with specific morphologies. Considering hydration-dependent elastic properties, we suggest mechanisms for the threshold of pattern formation. We finally discuss the role evaporation may play, in determining the final surface morphology.

2.1 Description of the experiment

2.1.1 Preparation of grafted hydrogel samples

In the present subsection, we describe the fabrication process of hydrogels. The protocol was originally developed by collaborators of the SIMM laboratory [1, 223], including Yvette Tran, and is summarized in Fig. 2.1. The first main steps consist in preparing the surface onto which polymer is grafted, then the polymer is deposited and cross-linked (or reticulated), and the final steps consist in washing the obtained sample.

2.1.1.1 Preparation of the surface

Cleaning: Either silicon wafers or glass substrates (coverslips in borosilicate glass) are chosen as the surfaces onto which the polymer gels are deposited. First, a "Piranha" solution is prepared, by mixing usually 200 mL of sulfuric acid (at $> 99\%$, *Sigma Aldrich*) with 400 mL of hydrogen peroxide (at 35%, *Sigma Aldrich*) in a large beaker (of at least 2 L). Teflon dishes are used. The resulting solution is left to rest at room temperature for at least 30 min, until it becomes a clear solution with no bubble, back to room temperature. The substrates are then immersed in the piranha solution for one hour. Water is then poured into the solution to decrease the concentration in acid and oxygen

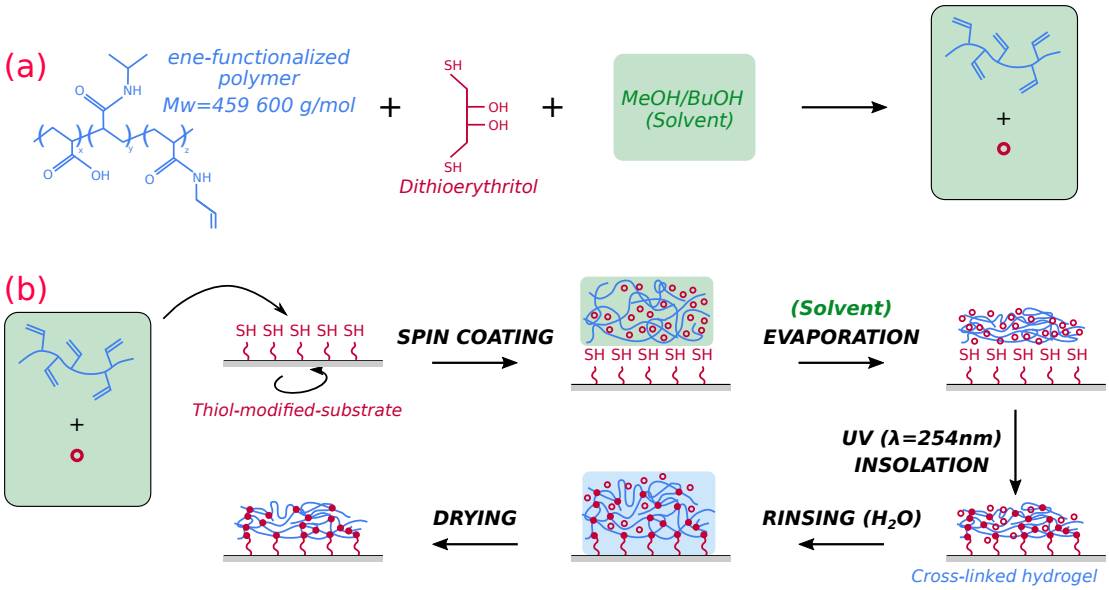

FIG. 2.1. **Fabrication of PNIPAM hydrogel films by click-chemistry.** *(a): A copolymer of P(NIPAM-co-AA) is mixed with DTT (a crosslinker agent), in a mixture of methanol and butanol (solvent). (b): The mixture is deposited onto a functionalized substrate and a uniform layer is obtained by spin-coating. After solvent evaporation, the mixture of melt P(NIPAM-co-AA) and DTT is cured by UV-insolation for 3 hours. The obtained reticulated gel is then rinsed by immersion in water, and dried under ambient air.*

peroxide, before removing the substrates from the beaker. Substrates are then rinsed with deionized water, dried with pressurized nitrogen flow, rinsed again with absolute ethanol (HPLC level, *Sigma Aldrich*), dried again. At this stage, if any dust remains visible at the surface of a substrate, the rinsing steps are done again.

Grafting sulfhydryl groups: A solution of silane is prepared by mixing 196 mL of absolute ethanol with 4 mL of 3-mercaptopropyltrimethoxysilane (95 % *Sigma Aldrich*). The solution is left at rest for one hour. The freshly cleaned substrates are then immersed for one hour in the silane solution. This step, called silanization, allows sulfhydryl groups (-SH) to attach on the extremely clean surfaces. Finally, the substrates are rinsed by immersion in a bath of absolute ethanol, and dried with pressurized nitrogen flow. We obtain chemically cleaned substrates, with thiol groups attached, that are referred to as functionalized surfaces.

2.1.1.2 Deposition of polymer

Preparation of the polymer solution: An in-house synthetized copolymer of Poly-N-isopropylacrylamide (PNIPAM) and acrylic acid (AA), functionalized with ene-reactive groups (weight-average molar mass $M = 459000\,\mathrm{g/mol}$, polydispersity index about 2) [1], was generously provided by colleagues from the SIMM laboratory under a desiccated form. A mixture of butanol and methanol (1/1 in volume) is used as a solvent. The desiccated polymer is dissolved in the solvent, at a chosen concentration c_{PNIPAM} (between 0.5% and 15% in mass). The solution can be left at rest overnight in the fridge, for the polymer to have time to dissolve. Just before being used, 1,4-dithioerythritol (DTT, *Sigma Aldrich*) is added to the solution, acting as a crosslinker agent. Typically

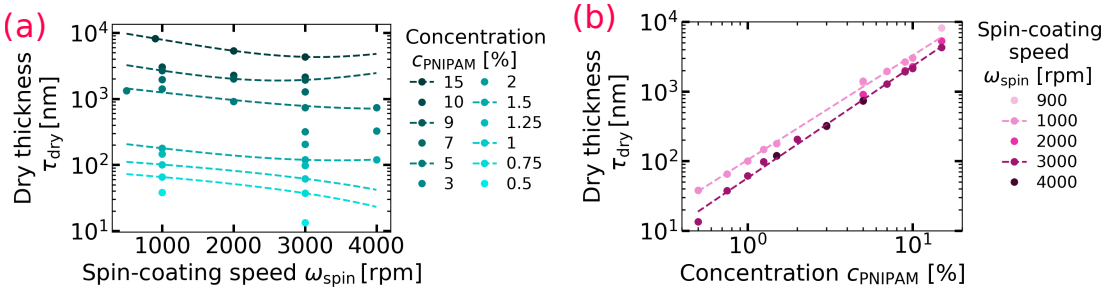

FIG. 2.2. **Hydrogel dry thickness as a function of the polymer concentration and the spin-coating speed.** *(a): Dry thickness τ_{dry} of the PNIPAM hydrogel sample as a function of the angular spin-coating velocity ω_{spin}, obtained from PNIPAM solutions of different concentrations c_{PNIPAM} (in mass), indicated in the legend. (b): Dry thickness τ_{dry} of the PNIPAM hydrogel sample as a function of the PNIPAM solution concentration c_{PNIPAM} (in mass), for different angular spin-coating velocities indicated in the legend.*

60% of DTT (in mass, compared to the P(NIPAM-co-AA)) is added.

Spin-coating: Uniform films of P(NIPAM-co-AA) copolymer are produced by spin-coating onto the prepared surfaces. The polymer solution is first transferred into a syringe for convenience. In the case of glass substrates, the solution is passed through a calibrated filter (0.2 μm), placed at the output of the syringe. A few drops are typically deposited onto the functionalized surface, and uniformly spread by spin-coating, with a spinning time of 30 s and at a chosen angular velocity ω_{spin} (in the range 1000 to 4000 rpm). To remove the excess of solvent, the obtained sample is placed onto a warming plate at 65°C for 1 min. At this stage, we obtain a uniform layer of polymer chains mixed with the cross-linker agent deposited on a functionalized substrate.

Reticulation of the gel: The hydrogel coating is cross-linked by performing a UV-irradiation (exposition carried out using a UV lamp, power 8 W, wavelength $\lambda = 254$ nm) for 3 hours. To remove uncured polymer and crosslinker excess, samples are immersed in deionized water for 4 h then in isopropanol (HPLC level, *Sigma aldrich*) for 15 min. Finally, the samples are dried under ambient conditions.

2.1.1.3 Benchmark of the obtained dry film thickness

Here, we present the calibrations of the obtained film thickness in dry conditions, as a function of the chosen polymer solution concentration and the chosen spin-coating angular velocity. These curves were established after several months of try-and-fails of sample fabrication. The purpose of this subsection is to help any future experimentalist to chose the appropriate experimental conditions to fabricate a PNIPAM gel of the desired thickness. Figure 2.2(a) shows the obtained thickness τ_{dry} as a function of the spin-coating velocity ω_{spin}, for different PNIPAM concentrations c_{PNIPAM} (in mass). Figure 2.2(b) shows the obtained thickness τ_{dry} as a function of the PNIPAM concentration c_{PNIPAM} (in mass), for different spin-coating velocities ω_{spin}.

2.1.2 Atomic Force Microscopy experiments

The hydrogels films are imaged by AFM (*Nanosurf CoreAFM*), both in dry and wet conditions, respectively in tapping and contact modes. We describe the imaging technique in both cases.

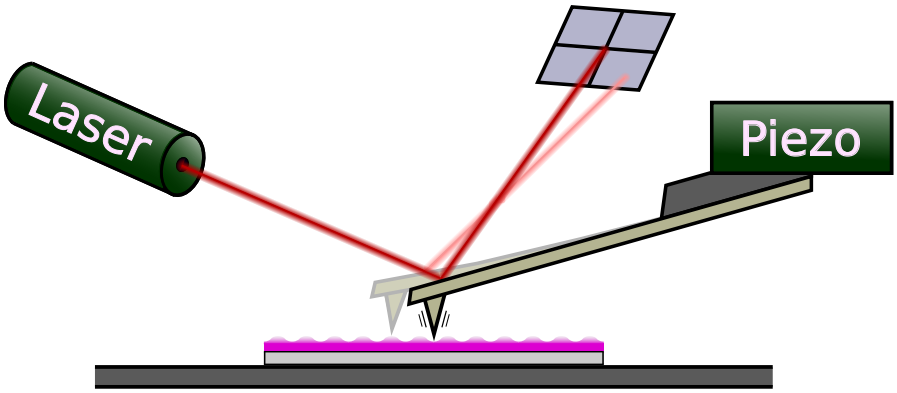

FIG. 2.3. **Schematic of an AFM.** *A sharp tip is held by a cantilever, which is supported by a chip. A piezo element moves vertically the chip, whose position is noted* z_{piezo}*. A laser beam is sent on the top face, at the edge of the cantilever. The reflection of the laser is monitored by a photodiode. From the shifted signal of the photodiode, the deflection of the cantilever* Z_{canti} *is extracted.*

2.1.2.1 Topography measurements

Principle of the AFM in tapping mode: The AFM is schematized in Fig. 2.3. A sharp tip is held by a cantilever [224–226]. The cantilever itself is held by a chip, mounted onto a holder, which is moved in the z direction by a piezo element, whose position is noted as z_{piezo}. A laser beam is sent on the edge of the cantilever, reflected by the latter, and this reflection is sent to a four-quadrant photodiode. The deflection Z_{canti} of the cantilever is measured by monitoring the signal of the photodiode. In tapping mode, the piezo element that holds the cantilever is made oscillating at a small amplitude, close to the resonance frequency of the cantilever.

The ensemble made of the holder, the laser and the photodiode constitutes the scan head of the AFM. When the scan head moves laterally, the tip may encounter a surface irregularity, which provokes a change in the oscillation amplitude of the edge of the cantilever. By applying a feedback loop on the amplitude of the cantilever deflection, the piezo element holding the chip is forced to move over a distance Δz_{piezo}, to correct the cantilever deflection amplitude. Thus the distance Δz_{piezo} provides a measurement of the height of the irregularity encountered.

A region whose topography has to be measured is defined. Then, the scan head browses that region following straight lines along a direction, going back and forth, and shifting in the other direction each time a new line is began.

Principle of the AFM in contact mode: The instrument is the same as in tapping mode. Yet, in contact mode, no oscillation of the cantilever is imposed, but the tip touches the sample, imposing a small deflection to the cantilever. When the scan head moves laterally and the tip encounters a surface irregularity, the cantilever deflection Z_{canti} is changed. A feedback loop is applied on the cantilever deflection, thus the piezo element holding the chip is forced to move over a distance Δz_{piezo} to maintain the cantilever deflection Z_{canti} at its prescribed value. Finally, the distance Δz_{piezo} provides a measurement of the height of the irregularity, as for the tapping mode. As for tapping mode, a region to measure is defined. Then, the scan head scans that region following lines, going back and forth.

2.1.2.2 Force spectroscopy measurements in AFM

A spectroscopy measurement in AFM consists in an indentation experiment performed with an AFM tip [227]. The tip is initially retracted, and no oscillation is imposed on the piezo element holding the cantilever. Then, a downwards velocity of approach is imposed to the piezo. The probe gets closer to the sample until reaching contact. The approach is continued until reaching a threshold in force (or in traveled distance). Then, the cantilever is retracted by imposing an upwards velocity to the piezo element. The cantilever deflection as a function of the position of the piezo, $Z_{\text{canti}}(z_{\text{piezo}})$, constitutes the approach curve. The latter is then analyzed, to extract various physical properties of the investigated material, such as the elasticity, or the adhesion energy.

In the following, we describe briefly some calibration steps that are necessary to convert electric signals, what are measured in the AFM, into forces and distances. The latter represent the physical quantities of interest for the mechanical description of a material.

2.1.2.3 Calibrations

In the standard force spectroscopy modes used for the present experiments, the calibration steps that are described in the following paragraphs are performed almost automatically, carried out by the software of the AFM. We show an example of calibration results performed on a standard contact-mode cantilever (*Nanosurf*, model *Stat0.2LAuD*), whose nominal resonance frequency and stiffness are $f_{0,\text{nom}} = 13\,\text{kHz}$ and $k_{\text{canti,nom}} = 0.2\,\text{N/m}$.

Calibration of the resonance frequency in dynamic mode: For experiments in tapping mode, a sweep in frequency (imposed by the piezo) is performed and the oscillation amplitude is recorded, as the response of the cantilever. The resulting motion of the edge of the cantilever is described by modeling the cantilever as a damped harmonic oscillator, to which a harmonic forcing is imposed. Then, by solving the equation of motion of the cantilever, one can derive the frequency-dependent complex cantilever deflection Z^*_{canti} [225]. The amplitude of the cantilever deflection reads:

$$\left|Z^*_{\text{canti}}\right|(\omega) = \frac{F_0/m_{\text{canti}}}{\sqrt{\left(\omega_0 - \omega\right)^2 + \left(\omega\omega_0/Q\right)^2}}, \tag{2.1}$$

with * indicating a complex variable, ω the angular frequency, ω_0 the resonance angular frequency, Q the quality factor, m_{canti} the effective mass of the cantilever and F_0 the amplitude of the external excitation. The measured amplitude of the cantilever deflection is fitted with Eq. (2.1). The resonance frequency $f_0 = \omega_0/(2\pi)$ and the quality factor Q are extracted as fitting parameters. In Figure. 2.4(a) we show an example of the amplitude of the cantilever deflection when submitted to an external harmonic forcing. On the present example, we measure a resonance frequency of $f_0 = 6.209\,\text{kHz}$ and a quality factor of $Q = 164$. The measured resonance frequency is lower than the expected nominal value, but still reasonable.

Calibration of the resonance frequency in static mode: For experiments performed in contact mode, the deflection of the cantilever due to its thermal noise is recorded and averaged over several measurements. The Brownian motion of the cantilever is described by modeling the cantilever as a damped harmonic oscillator to which

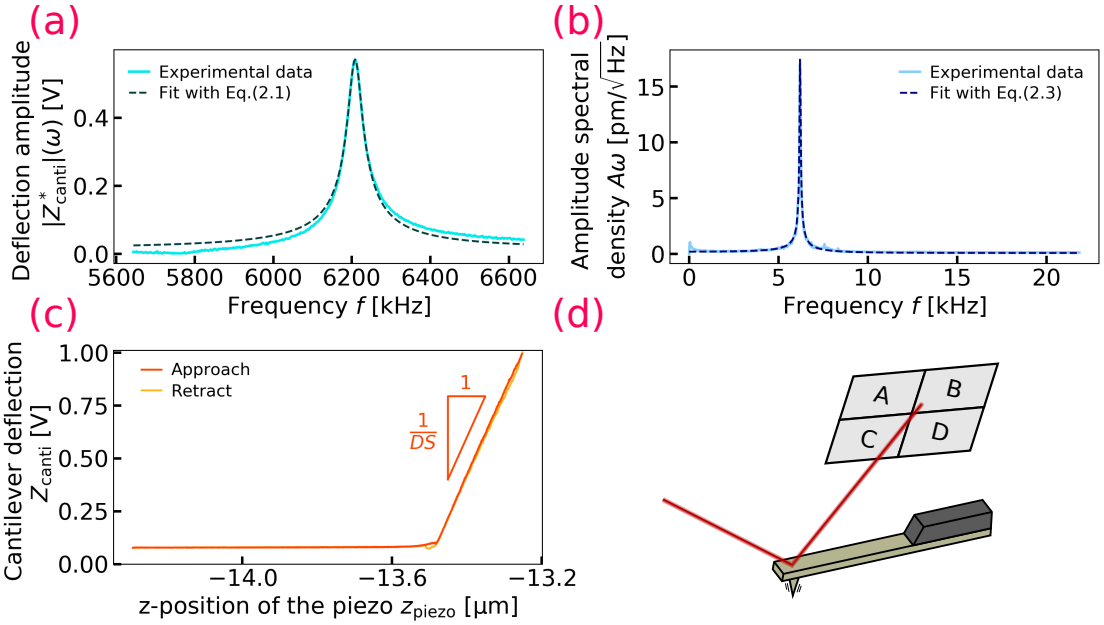

FIG. 2.4. **AFM calibrations.** *(a): Amplitude of the cantilever deflection* $|Z^*_{\text{canti}}|$ *when submitted to an external harmonic forcing, as a function of the temporal frequency* f*. The experimental data is fitted with Eq.* (2.1)*. (b): Amplitude spectral density* A_ω *of the cantilever as a function of the temporal frequency* f*, in the absence of any external forcing, resulting only from thermal noise. The experimental data is fitted with Eq.* (2.3)*. (c): Deflection sensitivity DS measurement. The signal received by the photodiode, which corresponds to the cantilever deflection* Z_{canti} *in V, is plotted as a function of the position of the driving piezo* z_{piezo}*. The final part of the curve corresponds to the range where the contilever is in contact with the hard surface. The deflection sensitivity DS is computed as the inverse of the slope. (d): Schematic of the four-quadrant photodiode that follows the direction of the reflected beam.*

a Langevin force is applied. Then, by solving the Langevin equation for a damped harmonic oscillator, one can derive the power spectral density of the cantilever deflection Z^*_{canti} [225], as:

$$\left|\frac{\mathrm{d}Z^*_{\text{canti}}}{\mathrm{d}\omega}\right| = \frac{k_{\text{B}}T}{\pi m^2_{\text{canti}}} \frac{\omega_0 Q}{Q^2(\omega_0^2-\omega^2)^2+\omega_0^2\omega^2}, \tag{2.2}$$

with k_{B} the Boltzmann constant and T the room temperature [1]. The amplitude spectral density A_ω is then defined by taking the square root of Eq. (2.2):

$$A_\omega(\omega) = \sqrt{\left|\frac{\mathrm{d}Z^*_{\text{canti}}}{\mathrm{d}\omega}\right|}. \tag{2.3}$$

The measured amplitude spectral density of the cantilever is fitted with Eq. 2.3. The resonance frequency $f_0 = \omega_0/(2\pi)$ and quality factor Q are extracted as fitting parameters. In Figure. 2.4(b) we show a typical example of the spectrum of the Brownian motion amplitude of the cantilever. Here, we measure a resonance frequency $f_0 = 6.211\,\text{kHz}$ and a quality factor $Q = 107$. The measured resonance frequency is again lower than the expected nominal value, but still in a good range. Moreover it is consistent with the measurement performed in dynamic mode, detailed in the previous paragraph.

[1] The present calibration step is detailed again in Sec. 4.2.2.1.

Calculation of the cantilever stiffness: Then, the Sader method is used to compute the stiffness [228–232], based on the geometrical properties of the cantilever and its resonance frequency. In summary, for rectangular cantilevers, the spring constant is computed as:

$$k = M_{\text{eff}} \rho b h L \omega_{\text{vac}}, \tag{2.4}$$

with h, b and L the thickness, width and length of the cantilever, M_{eff} a normalized effective mass ($M_{\text{eff}} = 0.2427$ for $L/b > 5$), ρ the density of the cantilever material and ω_{vac} the angular resonance frequency in vacuum [228, 230]. The latter is computed by taking into account a correction to the angular resonance frequency in air ω_0 [229]. The Sader method is also extended for V-shaped cantilevers [231]. The AFM we used has a function to perform the calculation, based on the geometry and the material of the cantilever (Silicon nitride most of the time). For the example presented here, we find a stiffness $k = 0.127\,\text{N/m}$.

Deflection sensitivity: In AFM, the measurement of the deflection sensitivity value DS is used to convert the electric signal received from the photodiode (in V) into the deflection of the cantilever Z_{canti} (in nm) [2]. The deflection sensitivity is measured by approaching the cantilever close to a hard surface, touching the surface, and the approach continues until reaching a prescribed limiting deflection. The cantilever is then fully retracted. The measurement is typically repeated ten times. The vertical signal of the photodiode (*i.e.* the cantilever deflection Z_{canti} up to a factor, but in V) is monitored as a function of the position of the piezo z_{piezo}. A linear relation between the signal of the photodiode and the piezo position is typically obtained when the cantilever is in contact with the hard surface, and the coefficient between both corresponds to the deflection sensitivity DS in nm/V. Figure 2.4(c) shows a typical measurement of the signal of the photodiode Z_{canti} as a function of the vertical position of the piezo z_{piezo}. In this example, the calculated deflection sensitivity is 254 nm/V based on a good quality fit ($\chi^2 = 0.009$). In practice, the measurement of the deflection sensitivity is automated by the AFM software, repetitions and averaging included. The product of the deflection sensitivity by the cantilever stiffness $DS\,k_{\text{canti}}$ enables to convert the voltage signal of the photodiode into a force.

Cross-talk compensation: In AFM, the deflection of the cantilever Z_{canti} is monitored by following the reflected ray of the laser pointed at its edge. In Fig. 2.4(d), we show a basic schematic of the four-quadrant photodiode that records the direction of the reflected beam. The photodiode is constituted by four detection cells, noted A, B, C, and D. The vertical deflection of the cantilever is deduced from $(A+B)-(C+D)$, while the lateral deflection, or torsion, is deduced from $(A+C)-(B+D)$. Imperfections of the system can perturb the independency of the different channels - a phenomenon named "cross talk". The latter can result from several sources. First, a mechanical origin is considered when the surface has significant variations in its topography, and the whole range of the piezo holding the chip is used. Second, electronic origins are often cited. Third, a geometric origin is considered when the alignment of the different optical elements involved in the laser detection is imperfect [233, 234]. For instance, on Fig. 2.4(c), cross-talk would be observed if the approach and retract curves were not superimposed on the linear final part of the curve $Z_{\text{canti}}(z_{\text{piezo}})$. Procedures have been developed to compensate the cross-talk, consisting in performing several spectroscopy measurements on a hard surface on the whole range of the piezo. The aim is to ensure that no cantilever

[2] This step is explained again in Sec. 4.2.2.2.

deflection is measured when moving only in air, and a linear deflection of the cantilever, as a function of the piezo position $Z_{\text{canti}}(z_{\text{piezo}})$, is measured when forcing onto a hard surface. On the *Nanosurf* AFM we use, the cross-talk compensation constitutes a step of the automatized calibration of the apparatus. This calibration should be done especially when working with patterned samples with a high variation amplitude of the topography.

2.1.2.4 Measuring surface topography of wet and dry samples

The surface of dry and wet PNIPAM films are visualized by AFM, respectively using a sharp and standard tip (*Nanosurf*, model *Dyn190Al*, $f_{0,\text{nom}} = 190\,\text{kHz}$ and $k_{\text{canti,nom}} = 48\,\text{N/m}$) in tapping mode, and using a thin cone-shaped tip (*Nanosensors*, model *qp-BioAC-Cl*, $f_{0,\text{nom}} = 30\,\text{kHz}$ and $k_{\text{canti,nom}} = 0.06\,\text{N/m}$) in contact mode.

The advantage of tapping mode is the non-invasive aspect. Indeed, the probe only touches the surface intermittently, which reduces the risk of damaging a fragile sample. This technique is used to image the dried PNIPAM films. To approach the probe to the sample, and thus define the feedback, the amplitude of the cantilever vibration is prescribed far from the sample (0.5 V in the experiments presented in this Chapter), and referred to as free vibration amplitude. When approaching close to the sample, the vibration amplitude of the cantilever is decreased by the interaction with the close boundary. We consider that the tip has approached the sample when the resulting vibration amplitude of the cantilever is 50% of the free vibration amplitude. The feedback loop will maintain the cantilever oscillation amplitude at that given threshold. A region to measure is delimited, then the scan head moves in lines to browse all the region. In tapping mode, the speed of motion of the scan head can be less than 1 s per line, thus an image is typically recorded in 10-15 minutes.

The advantage of the contact mode is that the tip follows the surface of the sample, with less risk of losing track of the surface. This technique is used to image the swollen PNIPAM hydrogels, that are particularly fragile and difficult to measure. The precise protocol was developed in collaboration with Henrik Peisker from *Nanosurf instruments*, in Langen (Germany) [3]. The approach of the probe close to the sample is defined by a setpoint in force, first at 10 nN. The experiment is started. Then the setpoint is slowly reduced step by step to minimize the indentation of the swollen hydrogel. The electronic tuning of the feedback is adapted at the same time. When reaching $2 - 3\,\text{nN}$ in force setpoint, the image is started again with the fine-tuned parameters. In contact mode in water, the experiment has to run slowly, thus an image is typically recorded in 1-2 hours. Yet, when starting the record, the user should always verify that enough water is present on the sample, not to run out of water before ten end of the measurement.

2.2 Results

2.2.1 Topography of dry polymer films

A major part of the AFM images obtained on dry PNIPAM films that are shown in this Chapter were recorded by Clemence Gaunand, intern in the team for a few months. The project presented here started with the observation of a pattern at the surface of a grafted PNIPAM film, in a context where flat and thin gels were needed. For the Surface Force Apparatus experiments presented in Chapter 5, the flatness of samples was systematically checked and the dry thickness was measured by AFM, for a given set

[3] The present collaboration benefited from EUSMI TA support, which allowed to travel to site.

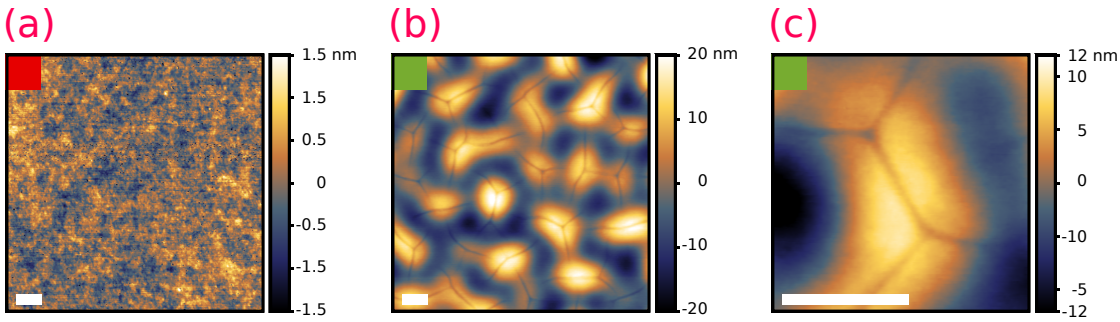

FIG. 2.5. **First observation of a dry, patterned PNIPAM film.** *(a): AFM image of a flat PNIPAM film, for reference. The measured thickness is* $\tau_{\text{dry}} = 54 \pm 3\,\text{nm}$. *The sample was fabricated using a spin-coating velocity of* $\omega_{\text{spin}} = 3000\,\text{rpm}$ *and a polymer solution concentration of* $c_{\text{PNIPAM}} = 1\,\%$. *The little red square indicates a color code referring to flat samples. (b): AFM image of the destabilized surface of a PNIPAM films, exhibiting a complex pattern. The measured thickness is* $\tau_{\text{dry}} = 324 \pm 20\,\text{nm}$. *The sample was fabricated using a spin-coating velocity of* $\omega_{\text{spin}} = 4000\,\text{rpm}$ *and a polymer solution concentration of* $c_{\text{PNIPAM}} = 3\,\%$. *The little green square indicates a color code referring to samples with such a morphology. (c): Zoom on a fault observed at the surface of the same sample as in (b). In (a), (b) and (c), the white bar represents* $1\,\mu\text{m}$.

of fabrication conditions. Within this context, a pattern with an unusual morphology was observed at the surface of a PNIPAM film grafted onto a glass substrate. In this following subsection, we show the first patterned surface we observed. Then we show different patterns characterized by different morphologies in the dry state. Finally we compare the results to the morphology observed in the wet state.

2.2.1.1 First pattern

In this subsection, we exhibit an image of the patterned PNIPAM film that started the project presented in this Chapter. Such an AFM image is obtained from raw imaging data after a few treatment steps, that are detailed in Appendix A.1. In Fig. 2.5(a) we show an AFM image of a flat sample, as a reference of what is desired, while in Fig. 2.5(b) we show an image of the destabilized surface of a dry PNIPAM film. The first dry film was fabricated using a PNIPAM solution at $c_{\text{PNIPAM}} = 1\,\%$ and a spin-coating speed of $\omega_{\text{spin}} = 3000\,\text{rpm}$. The thickness of the dry film is measured by AFM at $\tau_{\text{dry}} = 54 \pm 3\,\text{nm}$ (see Appendix A.2 for the details of the thickness measurement technique and the estimation of the error). The second, patterned film was fabricated using a PNIPAM solution at $c_{\text{PNIPAM}} = 3\,\%$ and a spin-coating speed of $\omega_{\text{spin}} = 4000\,\text{rpm}$ and the obtained thickness is measured at $\tau_{\text{dry}} = 324 \pm 20\,\text{nm}$. In the case of the first film, we observe a nanometric surface roughness, without defined morphology. In the case of the second film, that is thicker, we observe a regular pattern with a defined shape, characterized by smooth hollows and bumps, with small and sharp faults on the top of the bumps. In Fig. 2.5(c) we show a zoomed image of such a fault, with three branches.

In summary, we observe here that the thinner sample exhibits no pattern, while the thicker one does. In the following, thin samples exhibiting only a nanometric surface roughness without defined morphology are qualified as *flat* by opposition to samples exhibiting patterns with defined shapes. To understand where the pattern comes from, in the next subsection we investigate the surface topography of two samples of different thicknesses, at different steps of the fabrication process.

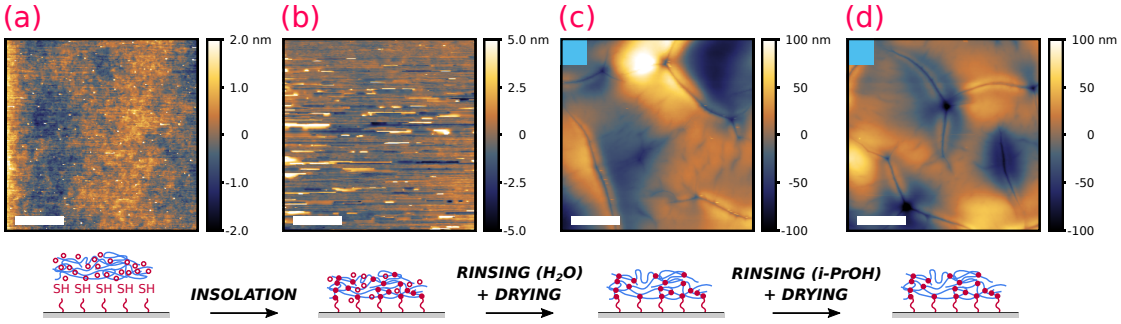

FIG. 2.6. **Topography of a PNIPAM film during the fabrication process** *(a): After spin-coating and soft-baking steps, a uniform layer of the mixture of melt polymer and cross-linker agent is observed ($\tau_{\text{melt}} = 2.8\,\mu\text{m}$). (b): After deep-UV curing, the sample is cross-linked and has a flat surface ($\tau_{\text{cured}} = 2.6\,\mu\text{m}$). (c): After the first rinsing-and-drying step, with water, we observe a pattern at the surface of the PNIPAM film ($\tau_{\text{dry},1} = 1.8\,\mu\text{m}$). The little blue square indicates a color code, referring to samples with such a morphology. (d): After the second step of rinsing-and-drying, with isopropanol, we make the same observations as in (c) ($\tau_{\text{dry},2} = 1.55\,\mu\text{m}$). The sample was fabricated using a spin-coating speed of $\omega_{\text{spin}} = 3000\,\text{rpm}$ and a polymer solution concentrated at $c_{\text{PNIPAM}} = 9\,\%$. The white bar represents $5\,\mu\text{m}$.*

2.2.1.2 Emergence of a pattern during the fabrication process

To understand which step of the fabrication process produces a patterned surface, a new sample is prepared and imaged at several stages. In Fig. 2.6, we show AFM images of a PNIPAM film of resulting dry thickness $\tau_{\text{dry}} = 1.6\,\mu\text{m}$, at different stages of the preparation protocol. The PNIPAM film which is used in the present subsection was prepared from a polymer solution at $c_{\text{PNIPAM}} = 9\,\%$ and using a spin-coating velocity of $\omega_{\text{spin}} = 3000\,\text{rpm}$. The thickness of the film is also measured at each stage.

A first AFM image, that is presented in Fig. 2.6(a), shows the surface topography of the PNIPAM film just after spin-coating and evaporation of the solvent. A nanometric surface roughness is observed, without any defined shape. In this case, we observe only a flat and uniform film of a mixture of melt polymer and cross-linker agent. The measured thickness of the film is $\tau_{\text{melt}} = 2.8\,\mu\text{m}$. A second image is recorded just after UV-insolation for 3 hours, and is shown in Fig. 2.6(b). Surface roughness is also observed, albeit the fact that the sample was sticky, which made the image difficult to obtain. The thickness is slightly smaller, with $\tau_{\text{cured}} = 2.6\,\mu\text{m}$, which indicates that the chemical reaction occurring thanks to the UV-insolation makes the material denser. A third AFM image, that is presented in Fig. 2.6(c), is recorded after a first rinsing with water and subsequent drying. At this step, we observe a defined pattern, whose morphology will be described in detail in a next subsection. Furthermore, the measured thickness is significantly smaller than before rinsing, with $\tau_{\text{dry},1} = 1.8\,\mu\text{m}$. A smaller thickness indicates that the rinsing-and-drying process has removed matter, such as the excess of cross-linker agent, or free polymer chains. Finally, a fourth image is shown in Fig. 2.6(d), after a rinsing-and-drying cycle, using isopropanol instead of water as the rinsing solvent. We make the same observation as at the previous step: a precise pattern is observed, and is similar to the one observed on the previous image. The measured thickness is slightly smaller, with $\tau_{\text{dry},2} = 1.55\,\mu\text{m}$. As for the previous step, some excess of material has been rinsed out.

In summary, we observe that the pattern appears after the first exposition to a solvent, which can be either water or isopropanol, and subsequent drying. To go deeper

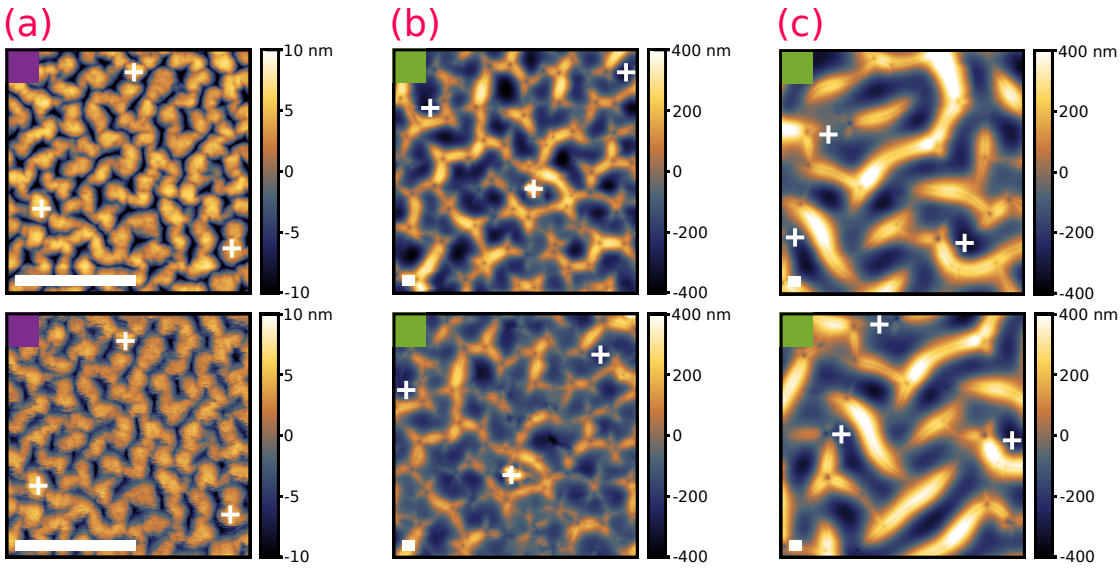

FIG. 2.7. **Comparison of patterns before and after immersion in a solvent and drying.** *AFM images of samples before (top row) and after (bottom row) immersion into a solvent and drying. (a): The PNIPAM film was immersed in water. The measured thickness is* $\tau_{\text{dry}} = 232\,\text{nm}$*, obtained using a spin-coating speed of* $\omega_{\text{spin}} = 3000\,\text{rpm}$ *and a polymer concentration of* $c_{\text{PNIPAM}} = 2\,\%$*. (b): In water. The measured thickness is* $\tau_{\text{dry}} = 1.8\,\mu\text{m}$*, obtained using a spin-coating speed of* $\omega_{\text{spin}} = 3000\,\text{rpm}$ *and a polymer concentration of* $c_{\text{PNIPAM}} = 10\,\%$*. (c): In acetone. The measured thickness is* $\tau_{\text{dry}} = 2.95\,\mu\text{m}$*, obtained using a spin-coating speed of* $\omega_{\text{spin}} = 1000\,\text{rpm}$ *and a polymer concentration of* $c_{\text{PNIPAM}} = 10\,\%$*. (a-c): The white bar represents* $5\,\mu\text{m}$*. The three white crosses are placed on remarkable spots to guide the eye in the comparison between the top and the bottom rows.*

in details on the influence of swelling into a solvent, in the next subsection we compare the obtained pattern before and after a given swelling-drying cycle.

2.2.1.3 Reproducibility of the pattern with swelling-drying cycles

The first swelling-and-drying step is responsible for the apparition of patterns at the surface of grafted PNIPAM films. In the present section, we investigate the influence of an extra swelling-and-drying step on the drawing of the pattern. We thus use samples that already exhibit a defined pattern, and make a first AFM image on a given region of each sample. The samples are exposed to a given solvent, then let to dry, and their surface topography is measured again, on the same region as much as possible.

On the top row of Fig. 2.7, we show AFM images of three samples, of respective dry thicknesses $\tau_{\text{dry}} = 232\,\text{nm}$, $1.9\,\mu\text{m}$ and $2.95\,\mu\text{m}$, that exhibit patterns at the end of the fabrication process. The two first samples are then immersed into water and the third one into acetone. After complete drying, the topography of each sample is measured again at the same spot, as shown on the bottom row of Fig. 2.7. For the three samples presented here, the region of measurement was found again, within a shift of $20\,\mu\text{m}$. We observe exactly the same pattern. Albeit a slight decrease in amplitude for the pattern of the second sample (see Fig. 2.7(b)) and the lower quality of the after-immersion image of the first sample (see Fig. 2.7(a)), each pair of images could be superimposed for the three samples. In summary, once formed after the first exposition to a solvent, the detail of surface patterns is fixed and irreversible to subsequent swelling-drying events. This

observation is consistent with observations on swollen gels reported in the literature [164], and contrasts with compressed elastomers which exhibit reversible creases.

Since the beginning of Sec. 2.2.1, samples exhibiting different patterns have been studied. In the next subsection we explore the variety of patterns observed at the surface of PNIPAM films, as a function of the thickness.

2.2.1.4 Distinct morphologies on dry samples

Following the preliminary observations presented in the previous subsection, different grafted PNIPAM films with different thicknesses are prepared. In Fig. 2.8 we show AFM images of six different samples, with increasing thickness. The flat sample already shown in Fig. 2.5(a) is reproduced here, in Fig. 2.8(a), as the thinnest sample of the series. Increasing the thickness, in Figs. 2.8(b) and (c) we observe at the surface of the PNIPAM films a defined pattern, reminiscent of the brain or intestine structure. Such shapes resemble the singular patterns typical of a creasing instability, observed on the surface of elastomers subject to in-plane mechanical compression or swollen gels [30, 122, 124, 129, 135, 136, 143, 144, 235–238]. This comprises smooth upper peaks separated by sharp plunging creases. In the following, we refer to this morphology as *brain-like pattern*. Still with increasing thickness, in Figs. 2.8(e), (g), (h) and (i) we observe a completely different type of pattern, with a defined morphology. The present shape is similar to the one of the first observed sample, of which an AFM image is shown in Fig. 2.5(b). We observe a regular pattern, exhibiting smooth hollows and bumps, with small and sharp faults on the edges of the bumps. The small and sharper peaks are reminiscent of the creases observed on previous samples. In the following, we refer to this morphology as *volcano pattern*. The distinction between pattern types is moreover rationalized by quantitative criteria based on the height distributions, detailed in Appendix. A.3. Finally, Figs 2.8(d) and (f) show the surface image of an intermediate-thickness sample. We observe a transition regime in morphology, exhibiting features of both the brain-like pattern and the volcano pattern.

From the observations of pattern types with varying thickness, of which a few examples are shown in Fig. 2.8, conditions on the dry thickness arise for observing patterns. First, we observe no defined pattern for samples thinner than a threshold thickness $\tau_{\mathrm{dry}} \leq 70\,\mathrm{nm}$. Second, we observe that samples with an intermediate range in thickness, $70\,\mathrm{nm} \leq \tau_{\mathrm{dry}} \leq 1.5\,\mu\mathrm{m}$, exhibit a brain-like pattern. Finally, we observe that thicker samples, $\tau_{\mathrm{dry}} \geq 2\,\mu\mathrm{m}$, exhibit a volcano pattern.

2.2.1.5 Elements of discussion

In previous subsections, we observed that the swelling-and-rinsing step triggers the apparition of patterns. The swelling ratio is defined as the ratio between the wet thickness and the dry thickness, as:

$$S_{\mathrm{R}} = \frac{\tau_{\mathrm{wet}}}{\tau_{\mathrm{dry}}}. \tag{2.5}$$

For the PNIPAM films presented in this Chapter, the wet thickness of the samples was also measured. The swelling ratio is estimated to be $S_{\mathrm{R}} = 3.5$, for samples thicker than $\tau_{\mathrm{dry}} \geq 150\,\mathrm{nm}$, which is consistent with results from *Li et al.* [1]. The swelling ratio is related to the mechanical strain ϵ in the vertical direction, as:

$$\epsilon = \nu(S_{\mathrm{R}} - 1). \tag{2.6}$$

Thus, for swollen samples with dry thickness thicker than $\tau_{\mathrm{dry}} \geq 150\,\mathrm{nm}$, a mechanical strain of $\epsilon \approx 0.62$ is estimated in the wet state, taking a Poisson ratio of $\nu = 0.25$ [239,

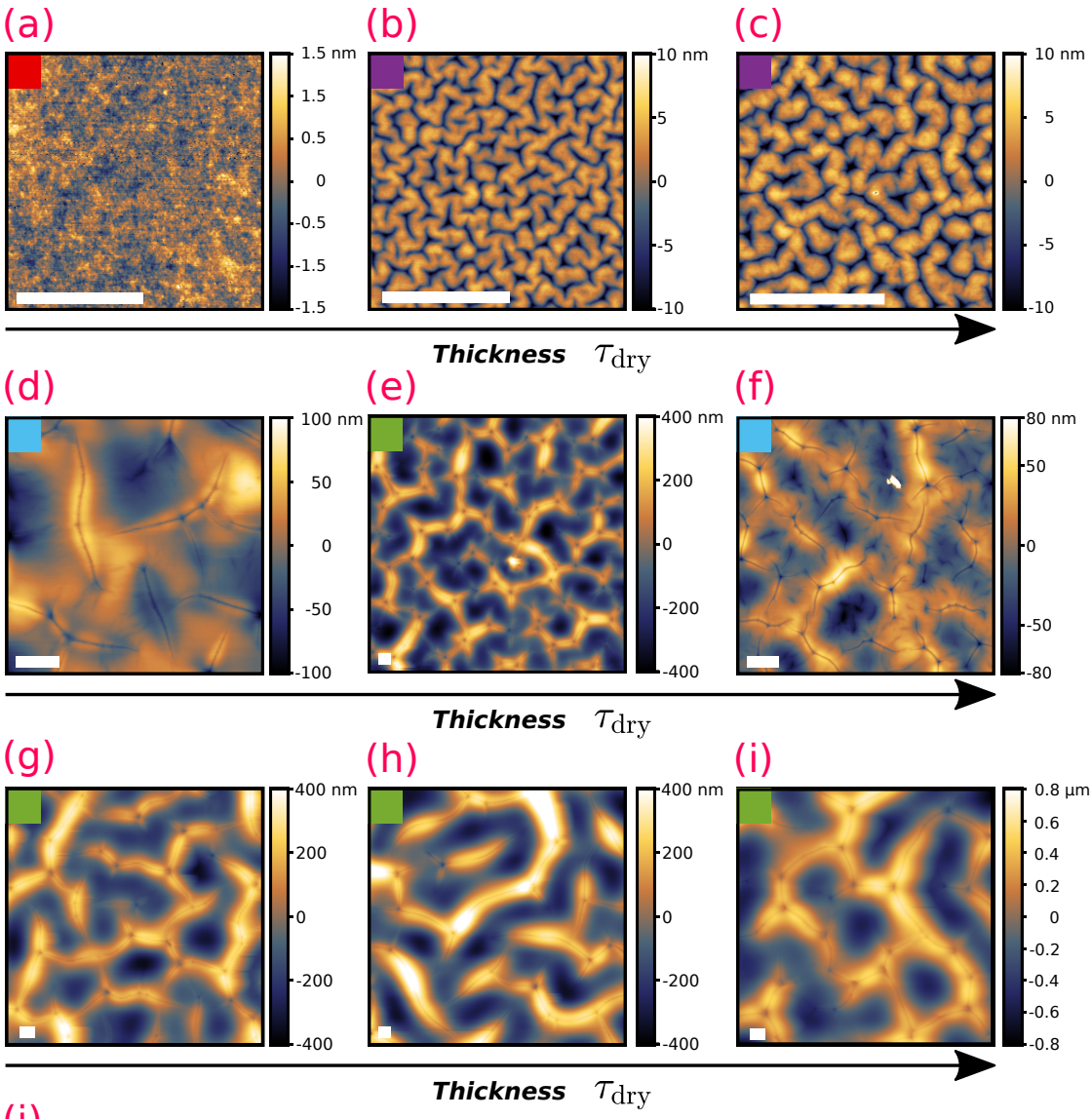

(j)

Image	(a)	(b)	(c)	(d)	(e)	(f)	(g)	(h)	(i)
ω_{spin} [rpm]	3000	3000	3000	3000	3000	2500	1000	1000	1000
c_{PNIPAM} [%]	1	2	2	9	10	5	9	10	5
τ_{dry} [nm]	54	152	232	1550	1800	1950	2695	2950	4550

FIG. 2.8. **Different morphologies of patterns at the surface of dry PNIPAM films.** *(a-i): Surface topography of PNIPAM films with increasing thickness, measured by AFM. The spin-coating speed* ω_{spin}*, PNIPAM solution concentration* c_{PNIPAM} *and resulting thickness* τ_{dry} *are indicated in the table below for each sample. On each image, the white bar represents* $5\,\mu m$*, and the colored square indicates the pattern type, following a color code. (a): The sample is flat (red square). (b) and (c): We observe brain-like patterns (purple square). (d) and (f): Transition regime (light blue square). (e) and (g-i): Volcano pattern (green square). (j): Table giving the spin-coating velocity* ω_{spin} *and the concentration of the polymer solution* c_{PNIPAM} *used to fabricate each sample, as well as the measured thicknesses* τ_{dry}*.*

240]. The latter strain is greater than the critical threshold strain of $\epsilon_c = 0.35$, which

corresponds to a swelling ratio of $S_R \approx 2.4$, above which creases can be observed [122, 123, 127, 128, 157].

Yet, we observe that the swelling ratio decreases monotonically on decreasing the sample thickness below $\tau_{dry} \leq 150\,nm$, which is still confirmed by results from *Li et al.* [1]. Indeed, swelling is strongly affected by the surface attachment for ultrathin PNIPAM films. Moreover, for samples with $\tau_{dry} \leq 70\,nm$, we observe no pattern. This suggests that osmotic stresses produce a mechanical strain at the critical threshold $\epsilon_c = 0.35$ for swollen samples of dry thickness $\tau_{dry} \approx 70\,nm$. Below that thickness threshold, the osmotic stresses generate a swelling and a mechanical strain that are insufficient to destabilize the surface in the wet state. On the contrary, above that thickness threshold, the osmotic stresses generate a swelling and a mechanical strain that are sufficient to destabilize the surface of wet samples, and result in creases.

In summary, for samples such that $\tau_{dry} \geq 70\,nm$, the mechanical strain due to swelling is enough to trigger a surface instability in the wet state. However, in the previous sections we showed observations that were made only on dry films. Thus, in the following section we investigate patterns observed at the surface of swollen PNIPAM gels.

2.2.2 Topography of swollen polymer gels

To understand the morphologies of patterns observed at the surface of dried PNIPAM films, we investigate the surface aspect on swollen films. Wet hydrogels are ultra-soft materials, composed of about 80 % of water, which makes them particularly challenging to probe by AFM. In Fig. 2.9 we show AFM images of six swollen PNIPAM hydrogels on the top rows, and compare with AFM images recorded on the same samples, but in the dry state, shown on the bottom rows. In the next paragraph, we describe the observed surfaces in the wet state and compare them with those obtained in the dry state, with increasing thicknesses measured on dried films.

In Fig. 2.9(a), we exhibit in both the wet and the dry states, the surface topography of an ultra-thin sample ($\tau_{dry} = 24\,nm$), that is flat in the dry state. We observe on the resulting topography in the wet state a nanometric surface roughness, without defined morphology, thus still a "flat" surface. In Figs. 2.9(b-d), the surface topography of samples exhibiting a brain-like pattern in the dry state is shown, in both the dry and the wet states. We observe surface patterns on the swollen gels, reminiscent of brain-like patterns observed on the same samples in the dry state. For the sample shown in Fig. 2.9(b), the pattern observed presents feature of creases, but the latter is not easy to classify only looking at the AFM image. Yet, creases are clearly observed on the samples shown in Figs. 2.9(c) and (d). The little pink square indicates a color code and refers to the creased pattern observed at the surface of swollen gels. Finally, in Figs. 2.9(e) and (f), the surface topography of two samples exhibiting respectively a transitional pattern and a volcano pattern in the dry state are shown, in both the dry and the wet states. We again observe a creased pattern in the wet state, similar to the brain-like pattern observed on thinner samples in the dry state.

In summary, the pattern observed at the surface of swollen PNIPAM films is typical of a creasing instability, similarly to the brain-like pattern observed on dried samples of intermediary thickness ($70 \leq \tau_{dry} \leq 1500\,nm$). Such patterns have been already observed on soft and swollen gels [30, 122, 135, 136, 143, 144, 235, 237]. However, patterns on dried films are rarely reported [124], as well as the link between both. Finally, the volcano pattern is not reported in the literature to our knowledge, except in one figure of *Ortiz et al.* [124], without further description. We reproduce the latter image in Fig. 2.10, for comparison.

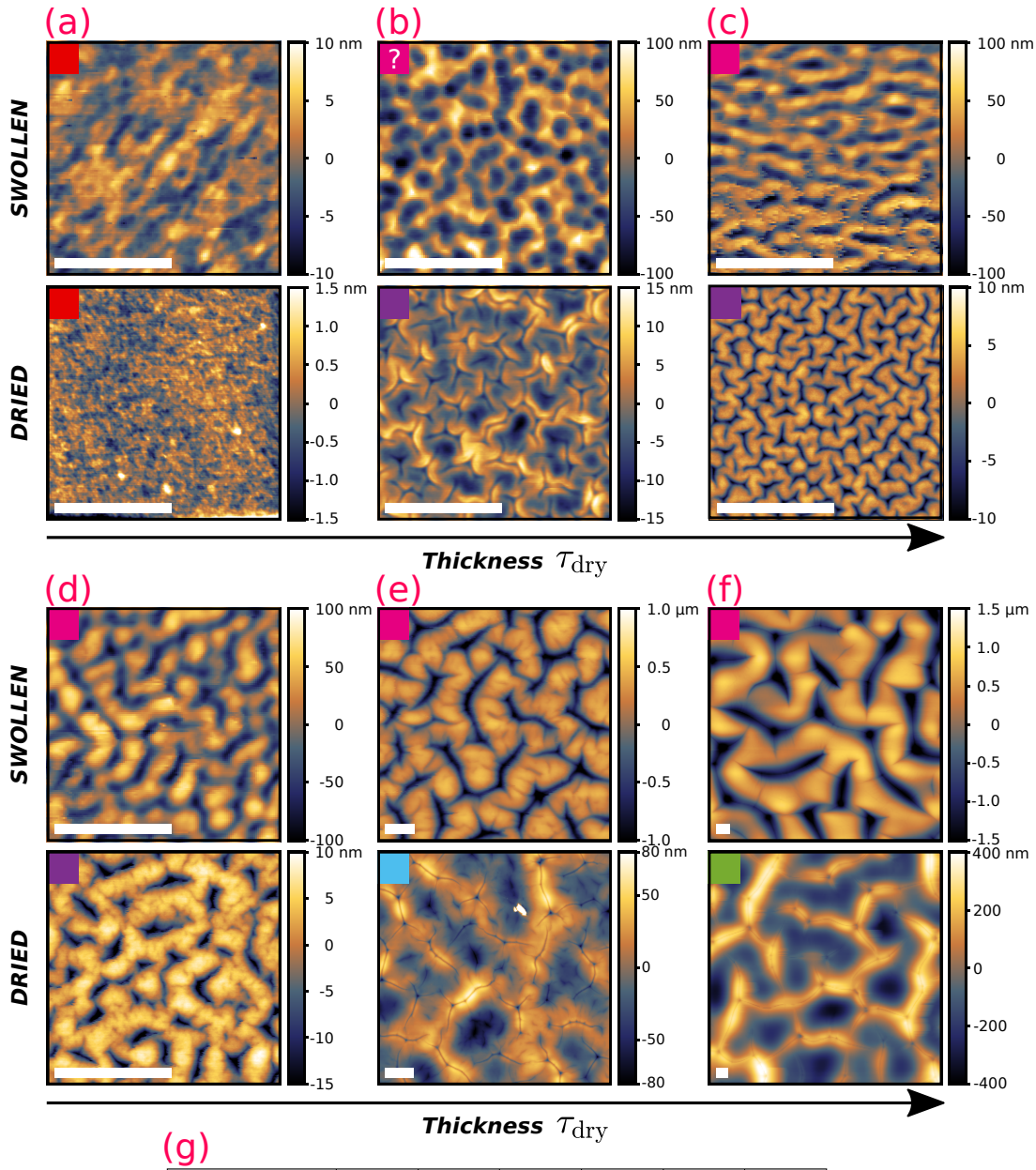

(g)

Image	(a)	(b)	(c)	(d)	(e)	(f)
ω_{spin} [rpm]	2000	3000	3000	3000	2500	1000
c_{PNIPAM} [%]	0.75	2	2	3	5	9
τ_{dry} [nm]	24.3	133	152	316	950	2690

FIG. 2.9. **Morphology of patterns at the surface of wet PNIPAM films.** *(a-f): Surface topography of samples of increasing thickness, in the wet state (top rows) and in the dry state (low rows), measured by AFM. The spin-coating speeds ω_{spin}, PNIPAM solution concentration c_{PNIPAM} and thickness measured on dried films τ_{dry} are indicated in the table below for each sample. On each image, the white bar represents 5 µm, and the colored square indicates the pattern type, following a color code. (g): Table giving the spin-coating velocity ω_{spin} and the concentration of the polymer solution c_{PNIPAM} used to fabricate each sample, as well as the measured thicknesses τ_{dry}. The images in the wet state were obtained from a collaboration with Henrik Peisker from Nanosurf Instrument, benefiting from EUSMI TA support.*

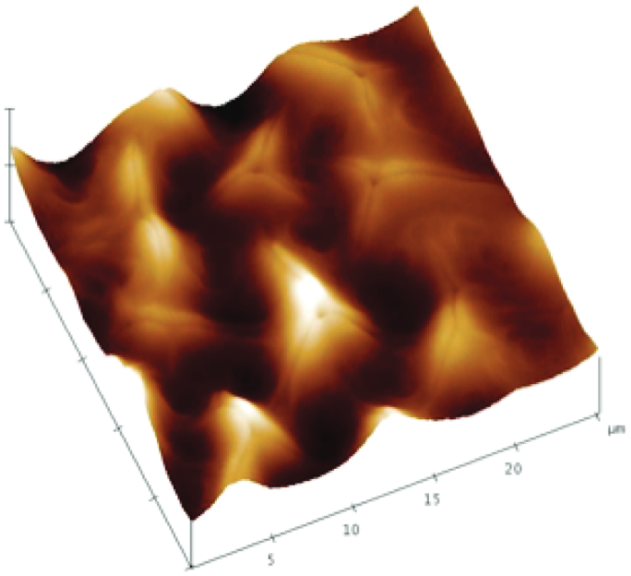

FIG. 2.10. **Volcano pattern reported in the literature.** *Figure 6 from Ortiz et al. [124], showing an AFM image of a* 800 nm*-thick dried film of a copolymer of PNIPAM and methacroyloxybenzophenone (MaBP). The observed pattern is similar to the volcano pattern observed and presented in this Chapter.*

2.2.3 Elasticity of dry and wet PNIPAM films

Following topography measurements, force spectroscopy measurements were performed. On dry PNIPAM films, measurements were performed using a *Bruker* probe, model *RTESPA-300*, of nominal stiffness $k_{\text{nom}} = 40\,\text{N/m}$ and nominal resonance frequency $f_{0,\text{nom}} = 300\,\text{kHz}$. The analysis protocol of the raw spectroscopy data is detailed in Appendix A.3. The processing of the force-distance curves is done using the *AtomicJ* software [241]. The measured Young's modulus is $E_{\text{dry}} \approx 700 \pm 100\,\text{MPa}$ (the technique is explained in Sec. 2.1.2.2), and the measurement is almost uniform over a given pattern. Details are shown in Appendix A.4. The measured value of the Young's modulus is higher but in the same order of magnitude as that of a glassy polymer [242]. We note that a higher measured value may be due to the use of an indentation-based technique [243, 244].

On wet samples, the experiment was performed in collaboration with Henrik Peisker, on a *Nanosurf FlexAFM*, whose particularity is to use an infrared laser to monitor the cantilever deflection. We used a *BudgetSensors* cantilever, model *Tap150GD-G*, of nominal stiffness $k_{\text{nom}} = 5\,\text{N/m}$ and resonance frequency $f_{0,\text{nom}} = 150\,\text{kHz}$, in silicon, and adapted for probing fragile and soft materials. In Fig. 2.11, we show results of spectroscopy performed on a swollen PNIPAM hydrogel, of dry thickness $\tau_{\text{dry}} = 950\,\text{nm}$, fabricated using a spin-coating speed of $\omega_{\text{spin}} = 2500\,\text{rpm}$ and a PNIPAM solution concentration of $c_{\text{PNIPAM}} = 5\,\%$. In Fig. 2.11(a), we show an AFM image close to the investigated region (a shift of $< 50\,\mu\text{m}$ is due to a change of cantilever between the topography and the spectroscopy measurements), for reference. Then, a measurement grid of 40×40 points was defined on a $30 \times 30\,\mu\text{m}$ window. In Fig. 2.11(b), we show the measured Young's modulus as a function of the x, y-position of the measurement. Interestingly, the pattern shown on the AFM image can be guessed on the Young's modulus map. The Young's modulus varies with the topography: the swollen gel is softer on the top of the bumps than in the depth of the dips. The latter observation may be due to an inhomogeneity of solvent fraction at the surface, with the topography variations, as

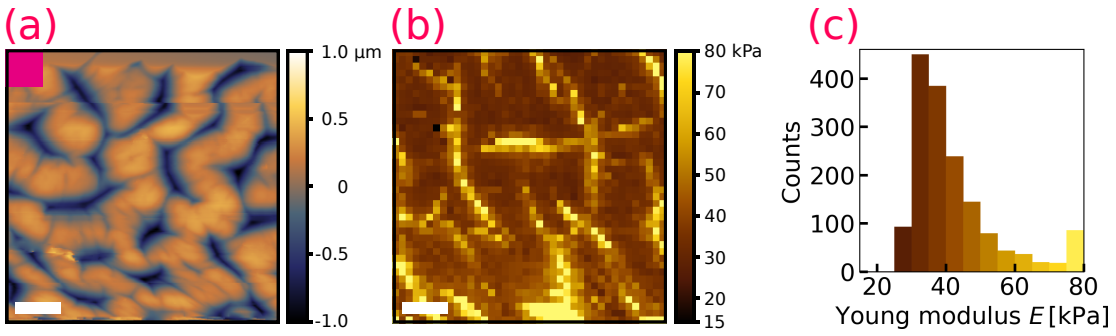

FIG. 2.11. **Measurement of the Young's modulus of swollen PNIPAM hydrogels.** *(a): AFM image of the investigated region. The PNIPAM film shown here was fabricated using a spin-coating speed of* $\omega_{\text{spin}} = 2500\,\text{rpm}$ *and a polymer solution concentration of* $c_{\text{PNIPAM}} = 5\,\%$*. The resulting dry thickness is measured to be* $\tau_{\text{dry}} = 950\,\text{nm}$*. The white bar represents* $5\,\mu\text{m}$ *(b): Measured Young's modulus* E *as a function of the* x, y*-position of the measurement. (c): Histogram of the measured values of the Young's modulus* E*. We retain the value* $E = 35 \pm 5\,\text{kPa}$*.*

the elastic bulk modulus is known to vary with the solvent volume fraction [18, 86, 101]. In the upper regions at the top of bumps, the polymer network may be more stretched, and thus the gel may contain more water. On the contrary, in the deeper regions, the polymer matrix may be more compressed by the singular shape of creases, and thus the volume fraction of water may be lower. As a result, regions containing more water would be softer.

From the map of the measured Young's modulus, statistics were computed. An histogram of measured values is shown in Fig. 2.11(c). We retain a Young's modulus value of $E_{\text{wet}} \approx 35 \pm 5\,\text{kPa}$, which corresponds to the average Young's modulus measured towards the top of bumps, where no singularity changes drastically the surface shape. Again, the measured value is higher but in the same order of magnitude than values from the literature for swollen PNIPAM ($E = 8\,\text{kPa}$), which can be due to the use of an indentation-based technique with sharp probes [243, 244].

The measurements of Young's modulus in both wet and dry conditions reveal drastically different stiffnesses. Indeed, the Young's modulus of PNIPAM is known to sharply increase by several orders of magnitude at the glass transition [245]. In both cases, we measure higher values than expected, but in a correct range. In the next subsections, we present the techniques we used to characterize quantitatively the different patterns observed at the surfaces of both swollen and dried samples.

2.2.4 Quantitative analysis of AFM images

2.2.4.1 Height profiles extracted from surface topography

Two examples AFM images of patterned PNIPAM hydrogels are shown in Fig. 2.12. Figures 2.12(a) and (b) show typical brain and volcano patterns, respectively. To extract a wavelength and an amplitude from a given image, the height profile of the destabilized surface is plotted along a line, as shown below each image. The wavelength λ_{p} of the pattern is deduced by counting the spatial periods over the extracted height profile, and averaging. The average amplitude A_{p} of the pattern is also deduced from the height profile. The process is repeated between 10 and 20 times for a given image, and the results are averaged. For the example of brain pattern shown in Fig. 2.12(b), the extracted wavelength and amplitude are $\lambda_{\text{p}} = 0.6 \pm 0.3\,\mu\text{m}$ and $A_{\text{p}} = 20 \pm 3\,\text{nm}$,

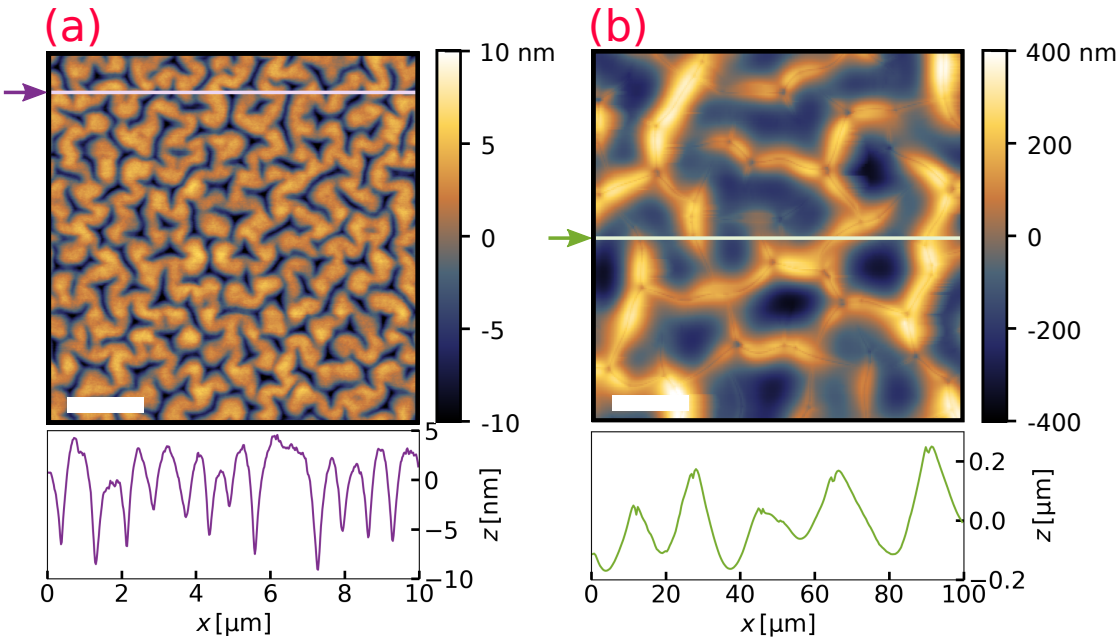

FIG. 2.12. **Extraction of the wavelength and amplitude from AFM images.** *(a): Topography of a dry PNIPAM hydrogel sample, exhibiting a typical brain pattern, of dry thickness* $\tau_{\mathrm{dry}} = 152\,\mathrm{nm}$*, obtained from a polymer solution at* $c_{\mathrm{PNIPAM}} = 2\,\%$ *and a spin-coating velocity of* $\omega_{\mathrm{spin}} = 3000\,\mathrm{rpm}$*. The height profile shown in the panel below is extracted from the mauve line indicated on the AFM image. (b): Topography of a dry PNIPAM hydrogel sample, exhibiting a typical volcano pattern, of dry thickness* $\tau_{\mathrm{dry}} = 2695\,\mathrm{nm}$*, obtained from a polymer solution at* $c_{\mathrm{PNIPAM}} = 9\,\%$*, and a spin-coating velocity of* $\omega_{\mathrm{spin}} = 1000\,\mathrm{rpm}$*. The height profile shown in the panel below is extracted from the light green line indicated on the AFM image.*

respectively. For the example of volcano pattern shown in Fig. 2.12(a), the extracted wavelength and amplitude are $\lambda_{\mathrm{p}} = 19.5 \pm 1.1\,\mu\mathrm{m}$ and $A_{\mathrm{p}} = 660 \pm 41\,\mathrm{nm}$, respectively.

The method to extract the wavelength λ_{p} and the amplitude A_{p} from an AFM image, that is detailed in the previous paragraph, has been used to analyze all the AFM images of the project presented in this Chapter. A 2D-Fourier analysis was also tested. However the results given by the hand-based method are better. Indeed, an image typically shows between 5 and 20 spatial periods, which is not enough to precisely compute the Fourier transform in all cases. In the next subsections, we study the measured wavelengths and amplitudes, for the different morphologies, as a function of the thickness in the dry state.

2.2.4.2 Wavelength and amplitude of the different patterns

From surface topography measured by AFM, patterns are characterized quantitatively by measuring the wavelength and amplitude, in both wet and dry conditions. The dry thickness τ_{dry} is systematically measured on each investigated sample. In Figs. 2.13(a) and (b), the wavelength λ_{p} and amplitude A_{p} are respectively shown as a function of the PNIPAM film thickness in the dry state τ_{dry}. In the following, we first detail the observations about the wavelength, before turning to the amplitude.

Wavelength: The wavelength of the instability $\lambda_{\mathrm{p}}^{\mathrm{wet}}$ observed at the surface of swollen gels seems to increase monotonically with the initial, dry thickness τ_{dry}, on the full range of achieved thicknesses. In the previous section, qualitative observations of patterns at

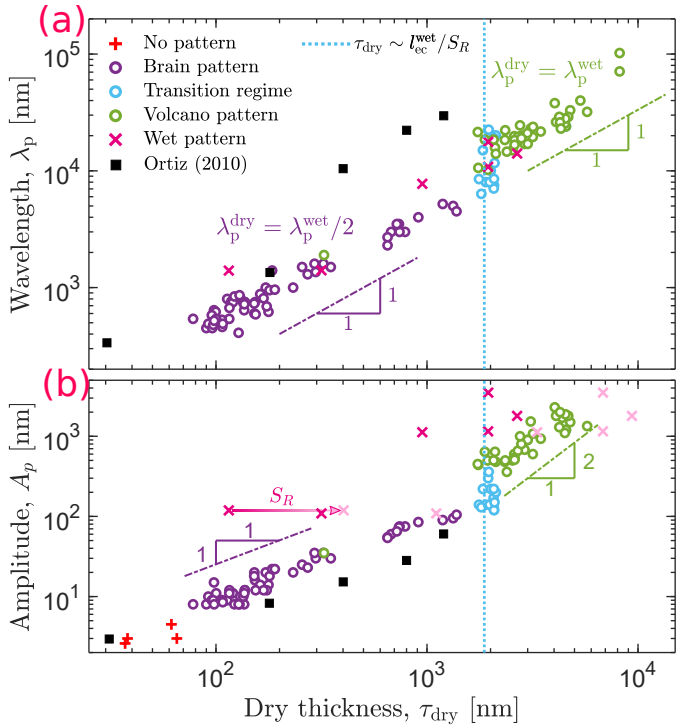

FIG. 2.13. **Wavelength and amplitude of surface patterns.** *(a): Wavelength* λ_p *as a function of the dry thickness* τ_{dry}*. The different morphologies are indicated by the color code and the legend. The data of Ortiz et al. on block-co-polymer (PNIPAM-co-MaBP) films are reproduced [124], and correspond to the black squares. A transition takes place at a critical wet thickness comparable to the wet elasto-capillary lengthscale* $\tau_{wet} \approx S_R \tau_{dry} \sim l_c^{wet}$ *(light blue dashed line). (b): Amplitude* A_p *as a function of the dry thickness* τ_{dry}*. Light pink crosses stand for the amplitude of wet patterns* A_p^{wet} *as a function of wet thickness* $\tau_{wet} = S_R \tau_{dry}$*.*

the surface of swollen gels showed that one type of pattern is clearly recognized. The latter is typical of a creasing instability. However, for dried films, we observe two regimes depending on the thickness in the dry state τ_{dry}. In both the thin and the thick-film regimes, the wavelength λ_p^{dry} increases monotonically with the dry thickness τ_{dry}, yet with a different prefactor. Additionally, in the thick-film regime, the prefactor is twice the one in the thin-film regime. Thus, we observe a *period-doubling* at the transition. Moreover, the two regimes correspond to the two types of morphologies we observed in the previous section. In the thin-film regime, brain-like patterns are identified at the surface of dried films, and in the thick-film one, volcano patterns are identified. A transition happens at the crossover between these two regimes in thickness, at a critical dry thickness of about $\tau_{dry,c} \approx 1.86\,\mu$m, that we will discuss in a following section. Additionally, the transition in thickness corresponds to the transition in morphology previously observed. Finally, in the thick-film regime we observe that the wavelengths of swollen and dried gels are comparable among the investigated samples. In the thin-film regime, we observe that the wavelength of swollen gels is twice the one of dried films. By generalizing the latter statements, we estimate the wet wavelength of each sample, as:

$$\begin{cases} \lambda_p^{wet} = 2\lambda_p^{dry}, & \text{for} \quad \tau_{dry} \leq \tau_{dry,c} \\ \lambda_p^{wet} = \lambda_p^{dry}, & \text{for} \quad \tau_{dry} \geq \tau_{dry,c}, \end{cases} \tag{2.7}$$

with $\tau_{dry,c} = 1.86\,\mu$m.

For a matter of comparison, the results of *Ortiz et al.* [124], obtained with dried films of PNIPAM copolymerized with methacroyloxybenzophenone (MaBP), are also included in Figs. 2.13(a), for reference. Even if their focus is on submicron thick gels, their work mentions also a greater wavelength for samples thicker than a critical thickness, which is about 400 nm in their case, and also exhibits a doubling of the thickness dependency. Some of the AFM images presented in their work show creased patterns for samples thinner than 400 nm, and one image of what we recognize as a volcano pattern for a sample of dry thickness 800 nm (see Fig. 2.10). However the classification of their images in pattern types remains difficult as they focus more on the study of rinsing solvents, not on pattern shapes.

Amplitude: The amplitude of the instability A_p is shown as a function of the dry thickness τ_dry in Fig. 2.13(b). First, a standard nanometric surface roughness is measurable on dried films thinner than 70 nm, which exhibit no pattern. Then, for dried films thick enough to show a pattern ($\tau_\mathrm{dry} \geq 70\,\mathrm{nm}$), we observe two regimes depending on the dry thickness τ_dry, as for the wavelength. In the thin-film regime, the amplitude $A_\mathrm{p}^\mathrm{dry}$ increases linearly with the dry thickness τ_dry. Yet, in the thick-film regime, the amplitude $A_\mathrm{p}^\mathrm{dry}$ increases with the dry thickness τ_dry as a power law, with an exponent 2. Moreover, as for the wavelength, the two regimes in thickness correspond to the two pattern types described in previous sections, which are brain-like and volcano patterns. The crossover between the two regimes appears at the same critical dry thickness as for the wavelength, $\tau_\mathrm{dry,c} = 1.86\,\mu\mathrm{m}$. At the pattern transition thickness, we observe a sharp increase in amplitude. Additionally, the amplitude of the pattern observed at the surface of swollen gels seems to scale linearly with the initial, dry thickness of the films τ_dry, with some dispersion of the data. Such a linear dependency of the amplitude as a function of the thickness is also observed for dry brain-like patterns, that are similar to the creased pattern observed on swollen gels. However, the prefactor is greater in the case of swollen gels. Now, by taking into account the increase of the thickness with swelling, by a factor which is the swelling ratio S_R, we consider the amplitude as a function of the wet thickness τ_wet instead. This comes down to apply a factor S_R (represented by the pink arrow on Fig. 2.13(b)). Then, the wet amplitude $A_\mathrm{p}^\mathrm{wet}$ scales linearly with the wet thickness τ_wet, and with a similar prefactor as the dry amplitude $A_\mathrm{p}^\mathrm{dry}$ as a function of the dry thickness τ_dry in the thin-film regime.

For a matter of comparison, the results of *Ortiz et al.* [124], obtained with dried films of PNIPAM-co-MaBP, are also included in Fig. 2.13(b). Their data would show a convex tendency, on five data points, which is not enough to conclude about a transition from a linear to a power-law regimes in the thickness dependency of the pattern amplitude.

2.3 Discussion: dry patterns resulting from wet patterns at the surface of polymer films

In Sec. 2.2.1.2 we observed that patterns appear at the surface of dried PNIPAM films after the first exposition to a solvent. Then, observations made on AFM images in Sec. 2.2.2 showed that the swollen and the dried cases are distinct by morphology. Additionally, the more quantitative observations made on both the wavelength and the amplitude as a function of the initial, dry thickness τ_dry, detailed in the two previous subsections, show that the distinction is also quantitative, in terms of scalings and prefactors. In the following subsection, we aim to understand the links between the different observed patterns and their features.

2.3.1 Apparition of two regimes upon drying

When swollen, PNIPAM films exhibit one regime in morphology, characterized by creases, while when dried, they exhibit two regimes characterized by distinct morphologies, that we call the brain-like and the volcano patterns. Thus, when drying, the mechanics of (in)stability of the surface becomes different depending on the thickness of the gel. We define the wet elastocapillary length $l_{\mathrm{ec}}^{\mathrm{wet}}$ based on wet mechanical properties, as the result of a balance between surface tension and volume elasticity, as:

$$l_{\mathrm{ec}}^{\mathrm{wet}} = \frac{\gamma}{G}, \tag{2.8}$$

with γ the interfacial tension between swollen PNIPAM hydrogel and air, and G the shear modulus of swollen PNIPAM. We recall the link between the shear modulus G and the Young's modulus E:

$$G = \frac{E}{2(1+\nu)}, \tag{2.9}$$

with ν the Poisson ratio. Thus, for swollen PNIPAM, we compute first a shear modulus of 14 kPa, based on our measured value of the Young's modulus, which is $E = 8\,\mathrm{kPa}$ (see sec. 2.2.3), and taking a Poisson ratio of 0.25 from the literature [239, 240]. Then, we compute a wet elastocapillary length of $l_{\mathrm{ec}}^{\mathrm{wet}} = 3\,\mu\mathrm{m}$, taking from the literature the surface tension between swollen PNIPAM and air, $\gamma = 41.8\,\mathrm{N/m}$ [246]. Keeping in mind that our value of the Young's modulus may be overestimated, the same calculation can be done using the value from the literature $E = 8\,\mathrm{kPa}$ [243], and leads to a wet elastocapillary length of $l_{\mathrm{ec}}^{\mathrm{wet}} = 13.1\,\mu\mathrm{m}$.

In Section 2.2.4.2, we observed that the transition in morphology happens at a critical dry thickness of $\tau_{\mathrm{dry,c}} = 1.86\,\mu\mathrm{m}$, which corresponds to a critical wet thickness of $\tau_{\mathrm{wet,c}} = S_{\mathrm{R}}\tau_{\mathrm{dry,c}} = 6.5\,\mu\mathrm{m}$. Indeed, as the transition in morphology appears upon drying, and as the drying process starts from the wet state, we treat the problem in the wet state. Finally, the critical wet thickness at which the transition on morphology happens is comparable to the wet elastocapillary length $\tau_{\mathrm{wet,c}} \sim l_{\mathrm{ec}}^{\mathrm{wet}}$. More precisely, the obtained critical wet thickness $\tau_{\mathrm{wet,c}}$ is comprised between the wet elastocapillary length computed from our measurement of the Young's modulus and the one computed from a Young's modulus value given by the literature.

In summary, the wet thickness τ_{wet} of PNIPAM hydrogels determines the final morphology of the surface instability in the dry state, after a complete drying. For samples thicker than the wet elastocapillary length in the wet state, *i.e.* $\tau_{\mathrm{wet}} \gtrsim l_{\mathrm{ec}}^{\mathrm{wet}}$, bulk elasticity dominates over surface tension. As a result of drying, we observe a strongly destabilized surface, whose amplitude increases with thickness as a power law. The shape changes upon drying. For samples thinner than the wet elastocapillary length in the wet state, *i.e.* $\tau_{\mathrm{wet}} \lesssim l_{\mathrm{ec}}^{\mathrm{wet}}$, surface tension dominates over bulk elasticity. As a result of drying, we observe a surface instability that keeps the same shape, yet the spatial frequency of pattern is multiplied by two. To conclude, a track to explain the observed features on dry PNIPAM films is thus to understand the transition from the wet to the dry states, which implies to understand the features observed on wet PNIPAM films. In the following, we propose a quantitative scaling for the observed wavelength, based on the one observed on swollen gels.

2.3.2 Rescaling on swollen-gel data

To understand the observed patterns on dried films, one must first understand the ones on swollen gels, following the chronology of the rinsing-drying step that reveals patterns.

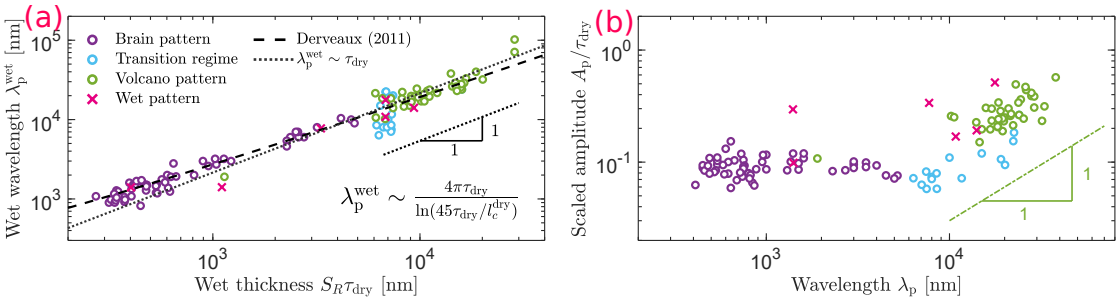

FIG. 2.14. **Rescaled wavelength and amplitude of surface patterns.** *(a): Expected wavelength λ_{wet} on a swollen sample as a function of expected wet thickness $\tau_{wet} = S_R\tau_{dry}$. The wet wavelength λ_{wet} scales linearly with the dry thickness τ_{dry}, albeit a logarithmic correction indicated on the panel, given in Eq.* (2.10)*. (b): Amplitude scaled by film thickness A_p^{dry}/τ_{dry} when dried, as a function of the wavelength λ_p^{dry} (open circles). Wet amplitude scaled by the wet thickness, $A_p/(S_R\tau_{dry})$, as a function of the wet wavelength λ_p^{wet} (magenta crosses).*

Thus, in Fig. 2.14(a), we show the estimated wet wavelength λ_p^{wet} as defined by Eqs. (2.7), as a function of the estimated wet thickness, $\tau_{wet} = S_R\tau_{dry}$. We observe that all the data for brain-like patterns, volcano patterns and creases observed on wet films follow the same apparently-linear trend, with the same prefactor. Indeed, in the wet state, all the observed patterns are identified as coming from a creasing instability, thus finding a common scaling is consistent.

Furthermore, finer scalings were derived for the wavelength at the surface of a creased surface, as a function of the initial thickness, in both the cases of an expanding elastomer [144] and a swelling gel [143]. The swelling gel is modeled as an elastic material, fixed at a bottom interface and expanding in the free direction, perpendicularly to that interface. Surface tension intervenes to balance bulk elasticity. In this framework, developed by M. Ben Amar, J. Dervaux and P. Ciarletta, the wavelength of the creasing instability scales with the initial dry thickness, as:

$$\lambda_p^{wet} = \frac{4\pi\tau_{dry}}{\log\left(\frac{44.953\tau_{dry}}{d}\right)}, \tag{2.10}$$

with d a regularization length that we interpret as l_{ec}^{dry}, the dry elastocapillary length, based on initial, dry mechanical properties, resulting from a balance between the elastic shear modulus G_{dry} and the surface tension γ:

$$l_{ec}^{dry} = \frac{\gamma}{G_{dry}}. \tag{2.11}$$

Thus, the wet wavelength λ_p^{dry} scales linearly with the thickness τ_{dry}, albeit a logarithmic correction, involving the dry elastocapillary length l_{ec}^{dry}. The latter acts as a regularization length, that tunes the importance of the logarithmic correction, brought to the *zeroth-order* linear scaling. The dry elastocapillary length defines a threshold for the apparition of creases: for an initial, dry thickness small compared to the elastocapillary length, *i.e.* $\tau_{dry} \lesssim l_{ec}^{dry}$, surface tension dominates over volume elasticity. Thus, the surface is not destabilized, resulting in a flat surface in the wet state. On the contrary, for sample having an initial, dry thickness comparable or greater than the elastocapillary length, *i.e.* $\tau_{dry} \gtrsim l_{ec}^{dry}$, bulk elasticity is sufficient to overcome surface tension. As a result, the surface is destabilized, taking a singular shape characterized by the presence of cusps, named creases.

The experimental data shown in Fig. 2.13(a) can be compared to the theoretical wavelength λ_p^{wet} as a function of the dry thickness τ_{dry}, given in Eq. (2.10). We performed a non-linear fit of our data on the model, letting a prefactor and the elastocapillary length l_{ec}^{dry} as two fitting parameters. In other words, we used the following equation to fit our data:

$$\lambda_p^{wet} = \alpha_1 \frac{4\pi\tau_{dry}}{\log\left[\frac{44.953\tau_{dry}}{\alpha_2}\right]}, \tag{2.12}$$

with α_1 and α_2 being free parameters. We exploit also the observation of the period doubling, defined in Eq. (2.7). With this expectation of wavelength λ_p^{wet} in the wet state, our data for dried samples show an excellent agreement with the theoretical prediction of Derveaux and Ben Amar [143], as shown by the best fit line represented on Fig. 2.14(a). In this model, the agreement can be interpreted as surface tension smoothing out defects that act as nucleation sites for crease formation and imposing an energy barrier between the flat state and the creased state [158].

As a result of the fit, we obtain an estimation of the dry elastocapillary length, $l_{ec}^{dry} = \alpha_2 = 152.7\,\text{nm}$, and a prefactor $\alpha_1 = 3.46$. Using the surface tension value from the literature $\gamma = 41.8\,\text{mN/m}$ [246], we estimate first the shear modulus $G = 274\,\text{kPa}$. The link between the shear modulus G and the Young's modulus E is recalled in Eq. (2.9). By taking from the literature a Poisson ratio $\nu = 0.25$ [239, 240], we finally obtain a Young's modulus $E = 684\,\text{kPa}$. This estimation of the Young's modulus corresponds to the effective value the material would show in the dry state, if it was a rubber-like polymeric material. Yet, PNIPAM exhibits a glass transition upon dehydration [107, 245], which explains that our measurement of the Young's modulus in the wet state is greater by three orders of magnitude. Moreover, the calculation of the latter Young's modulus is based on the surface tension value $\gamma = 41.8\,\text{mN/m}$ found in the literature [246], which is measured for a swollen gel in contact with ambient air. To be more consistent, the surface tension between dry PNIPAM and ambient air should be considered. The latter can be expected to be higher, and thus lead to an even greater value of the Young's modulus.

The fit presented in this section is based on the strong hypothesis of period-doubling, summarized in Eqs. (2.7), which claims that in the thin-film regimes, the wavelength in the wet state is exactly twice the one in the dried state. The validity of the latter hypothesis is tested by performing the same fit on the same model, but with setting the factor between the wavelengths in both the dry and wet states as a third fitting parameter α_3. In that case, we obtain a dry elastocapillary length $l_{ec}^{dry} = \alpha_2 = 157.4\,\text{nm}$, a prefactor $\alpha_1 = 3.52$ and a multiplying factor between the dry and wet wavelengths $\alpha_3 = 2.04$. The results are detailed in Appendix A.5. In conclusion, our results support strongly the hypothesis of the period doubling formulated in Eq. (2.7).

2.3.3 The challenge of fabricating thicker samples

To measure the relative importance of the instability, in Fig. 2.14(b) we show the amplitude in both dry and wet conditions, scaled by the initial, dry thickness τ_{dry}, as a function of the wavelength. We observe that the relative amplitude for dried films in the thin-film regime is constant with the wavelength, which is a signature of a form of self-similarity of the creasing instability. The same observation can be made about data from swollen gels, but the data is more disperse, and the prefactor is greater than in the case of dried films. Finally, for dried films in the thick-film regime exhibiting a volcano pattern, the relative amplitude scales linearly with the wavelength. We interpret the latter feature as a signature of a highly unstable surface in the thick-film regime, as with

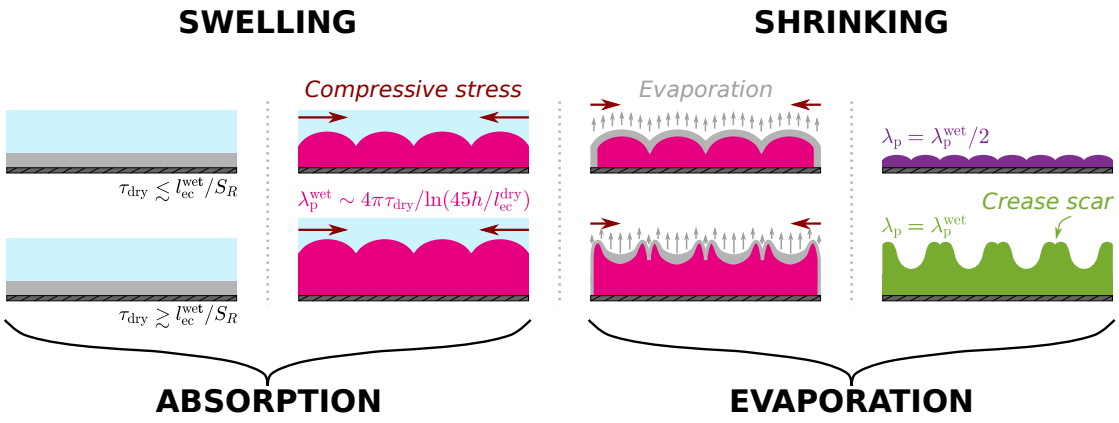

FIG. 2.15. **Proposition of a mechanism to explain the apparition of patterns on PNIPAM films.** *PNIPAM films are grafted onto rigid substrates (first column). When exposed to a solvent, the PNIPAM films swell, resulting in creases at the free surfaces (second column). When exposed to ambient air, PNIPAM swollen hydrogels dry (third column). Depending on the thickness, the final morphology observed on dried PNIPAM film corresponds either to a brain-like pattern (first row, thin-film regime), or a volcano pattern (second row, thick-film regime).*

increasing thickness the instability in the z-direction grows faster than in the in-plane direction.

In the present project, one challenge was to fabricate the thickest samples. Indeed, thicker samples were achieved by using a highly concentrated polymer solution ($c_{\mathrm{PNIPAM}} = 15\,\%$ at the maximum), which is difficult to realize. Such a concentration must be close to saturation, as the polymer takes hours to dissolve. Moreover, the obtained solution is highly viscous, which limits diffusion and homogeneity. Finally, at such a concentration, spin-coating does not ensure a uniform layer of deposited solution, as we observe important ridges on sides.

Yet, an interesting feature of the amplitude measurement is that for the volcano patterns, it scales as a power law of the thickness, thus having access to data from thicker samples would be of a certain interest. Indeed, following the observed scaling of the relative amplitude A_p/τ_{dry} with the wavelength λ_p^{dry} (or equivalently with the dry thickness τ_{dry}), in principle, the relative amplitude could reach one, which is physically unrealistic. Thus, with increasing thickness, a third, distinct regime could probably be highlighted. In the work of *Ortiz et al.* [124], as well as in other published works [131, 152, 154, 163, 247–249], folding of a top layer is observed for thicker samples. With such a change of geometry and instability direction, amplitudes greater than thicknesses could be achieved.

2.3.4 Proposition of a mechanism

In the present subsection, we attempt to explain the observed patterns at the surface of dried PNIPAM films, from observations made on swollen gels. The proposed mechanism is schematized in Fig. 2.15. The formation of patterns at the surface of wet films, as a result of swelling, is already well understood and described in the literature [122–131]. When a hydrophilic, polymeric material is brought in contact with water, the polymer swells into the water and a gel is formed. Additionally, when the polymer is grafted onto a glass substrate, surface-attachment constrains the gel to swell in only one direction, perpendicular to the plane of the substrate (see Fig. 2.15, first and second columns).

Such an anisotropic swelling results in an in-plane, compressive stress in the polymer matrix. When the swelling is sufficient, *i.e.* when the mechanical strain exceed a critical strain above which the free surface is destabilized, creases form, which result in the formation of the typical patterns observed at the surface of swollen PNIPAM hydrogels.

The drying process is initiated on a gel whose surface is already strongly destabilized. Depending on the wet thickness, at the beginning of the drying phase, we observe two regimes, that we rationalize with two possible scenarios. In the thin-film regime (when the wet thickness is smaller than the wet elastocapillary length, $\tau_{\text{wet}} \lesssim l_{\text{cap}}^{\text{wet}}$), the gel shrinks upon drying (see Fig. 2.15, third and fourth columns, first row). More creases appear, as their wavelength (respectively their spatial frequency) scales with the thickness (respectively the inverse of the thickness). Yet, as the surface is already destabilized when drying starts, the pre-existing creases stay in place and the new creases have to distribute symmetrically between the ancient ones. As a result, the multiplying factor between the wavelengths in the wet and dry states is necessarily an integer number. We indeed observe that this integer number is two, exploiting the period-doubling hypothesis.

In the thick-film regime (when the wet thickness is greater than the wet elastocapillary length, $\tau_{\text{wet}} \gtrsim l_{\text{cap}}^{\text{wet}}$), the solvent evaporates from the free surface upon drying (see Fig. 2.15, third and fourth columns, second row). Previous works show that a crust forms at the surface of a drying polymeric material [25, 27, 29, 166, 172, 173, 176], characterized by a drastically lower solvent concentration than in the underlying layer of hydrated polymer. In the case of PNIPAM films, a glass-transition may be observed [107], triggered by dehydration, since PNIPAM is glassy at room temperature. As a result, the crust that is formed by drying at the surface of a PNIPAM gel may be stiffer than the still-hydrated gel underneath, by four orders of magnitude (see Sec. 2.2.3). Moreover, as drying generates a loss of solvent, the stiff layer of the crust shrinks, and pulls the surface of the still-hydrated swollen gel underneath. In such a situation, which is schematized by considering a stretched, stiff and thin layer on a thick and soft material, numerous published works showed that a wrinkling instability can appear [125, 131, 132, 145, 148–152, 163, 250]. The surface is destabilized, taking a regular, sinusoidal shape. In our case, a wrinkling instability appears on an already-destabilized surface. As a result, the wavelength of wrinkles and their spatial distribution are pre-selected. By opposition to the depth of creases, the bumped regions are less constrained and thus deform further, creating an inversion of the topography. The resulting surface morphology is characterized by a globally-sinusoidal profile, with scars of creases present at the upper regions.

2.4 Conclusion

In the present Chapter, we have shown AFM images of grafted PNIPAM films that exhibit surface instabilities, both in the wet and dry states, as a result of swelling and drying processes. Irreversible and reproducible surface deformations were characterized by their morphology: swelling leads to a creased pattern for films thicker than 70 nm, while drying leads to two types of instability depending on their thickness. Dried films respectively thinner and thicker than 1 μm show a brain-like and a volcano patterns. We have shown that the wavelength and amplitude are prescribed by the thickness, and in the case of dried films, by the pre-existing instability at the surface of wet gels. Finally, we have exposed a mechanism based on observations and published works to rationalize the apparition of different morphologies.

To enforce our hypothetical mechanism that would explain the formation of the volcano pattern, an estimation of the thickness of the evaporation-formed crust is desired. Very recent published works could be applied to our system, to provide such a crucial information [173]. Indeed, together with our measurements of elastic moduli, the ratio of the different layer thicknesses upon drying would provide a quantitative theoretical prediction for the wavelength of the instability [148–150, 250]. A comparison with our experimental data on dried and thick PNIPAM films could finally allow to critically assess our proposition of mechanism.

In the following Chapters, we will be interested in the mechanical response of poroelastic materials to a pressure field generated by a nearby sphere, when immersed in a solvent. We will use PNIPAM films as a model system for experiments. From a theoretical point of view, we will describe our experiments in lubrication conditions, using a sphere-plane geometry, thus we will assume that the sample surface is flat. In practice, the study of instabilities presented in this Chapter allows to predict exactly whether an investigated sample of PNIPAM hydrogel is flat or destabilized, and how, depending on its thickness. Thus, we will consider that the hypothesis of flatness hold when the wavelength of the instability is short compared to a relevant length scale of the contactless rheology to be defined later, if the sample is thick enough to show an instability.

The following Chapter sets the theoretical framework to describe the mechanical response of a permeable, poroelastic substrate to any axisymmetric pressure field, in terms of deformations. Both the cases of an infinitely-thick and a finite-thickness substrate will be studied.

Chapter 3

Mechanical response of a permeable poroelastic gel to an external pressure field

This chapter is inspired from published work on the mechanical response of a permeable, poroelastic and infinitely-thick medium [251], included in Appendix E. The content of the publication is intersperse between the present chapter and the next one, which focuses on colloidal-probe rheology of soft and porous gels.

The present Chapter aims to mathematically describe poroelasticity, inspired from the context of soft-lubrication problems as presented in the general introduction, in Sec. 1.5.2. Here, we derive a model to characterize the mechanical response of poroelastic gels, in both cases of infinitely-thick and thin layers. Since we are interested in describing gels in contact with a reservoir of solvent, a full-permeability boundary condition at the gel-solvent interface is considered. Our focus contrasts with a previous study in the impermeable case [110, 111], that is more relevant to methods involving direct solid contact. In the first part, we expose the framework of linear poroelastic theory. In the second part, we adapt this framework in the case of a permeable layer to the fundamental situation of a punctual pressure field suddenly applied. In the third part, we derive a mathematical solution to express the deformation profile of the gel in this fundamental situation. We use the formalism of Green's functions in axisymmetric conditions, as it was done for purely elastic media in the context of soft lubrication [184, 189, 202, 208, 209, 212], or for a poroelastic but impermeable soft substrate [110]. In a last part, we generalize the fundamental solution of the third part to any axisymmetrical arbitrary pressure field.

3.1 Linear poroelastic theory

3.1.1 Equations of poroelasticity

The considered system is shown in Fig. 3.1. It consists of a gel that occupies the half-space defined by $z \leq 0$ or a layer of space defined between $-\tau \leq z \leq 0$, respectively represented by Fig. 3.1(a) and Fig. 3.1(b) [1]. We suppose that the mechanics of the gel is described by the linear poroelastic theory. As mentioned in the introduction, this model

[1] The semi-infinite case described in Fig. 3.1(a) is published [251], article being included in Appendix E. The finite-size case described in Fig. 3.1(b) is not but comes from the same development.

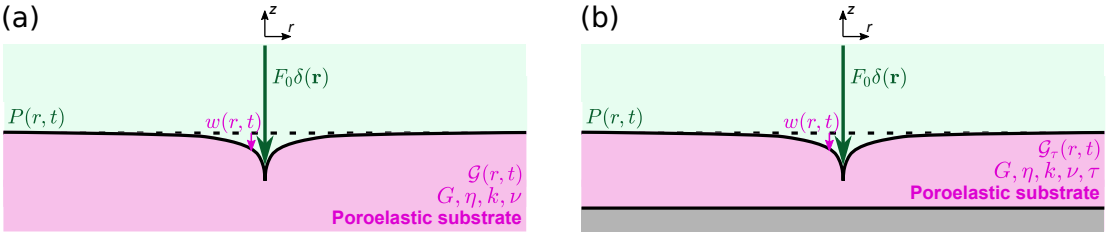

FIG. 3.1. **Semi-infinite and finite-thickness permeable poroelastic media deformed by a punctual external pressure field.** *A point-force pressure field* $P(r,t) = F_0\delta(\mathbf{r})$ *is suddenly applied at* $t = 0$ *on the poroelastic substrate, and generates a surface deformation* $w(r,t)$*. The latter is directly related to the Green's function* $\mathcal{G}(r,t)$ *by Eq.* (3.50)*. We denote* G*,* ν*, and* k*, the shear elastic modulus, Poisson ratio, and porosity of the substrate, respectively, as well as* η *the shear viscosity of the solvent flowing in the porous material. (a): Semi-infinite medium. (b): Finite-thickness medium, where we denote* τ *the thickness of the substrate.*

was first established by Biot [10], and was adapted to model the migration of solvent in elastomeric gels [110, 111, 214]. We take as a reference state a swollen gel, with a homogeneous solvent concentration c_0, and where the chemical potential of the solvent inside the gel is μ_0. The elastic deformation of the gel is characterized by the strain tensor $\boldsymbol{\epsilon}$. The latter is defined as the symmetric part of the displacement field gradient tensor, as:

$$\boldsymbol{\epsilon} = \frac{1}{2}\left[\boldsymbol{\nabla}\mathbf{u} + (\boldsymbol{\nabla}\mathbf{u})^T\right], \tag{3.1}$$

where $\mathbf{u}$ denotes the displacement field with respect to the reference state. The solvent mass being conserved, the concentration c satisfies the continuity equation:

$$\frac{\partial c}{\partial t} + \boldsymbol{\nabla}\cdot\mathbf{J} = 0, \tag{3.2}$$

where the flux of solvent inside the gel is denoted $\mathbf{J}$. The linear poroelastic theory assumes that the solvent flow is driven by the gradient of solvent chemical potential μ, through the Darcy law:

$$\mathbf{J} = -\Big(\frac{k}{\eta\Omega^2}\Big)\boldsymbol{\nabla}\mu. \tag{3.3}$$

Here, η and Ω are the viscosity and molecular volume of the solvent, respectively, and k is the permeability that is on the order of the pore surface area of the swollen polymeric network. The solvent and the polymer network are both assumed to be incompressible. As a consequence, the local variations of volume of the polymer network are due to the local changes in solvent concentration, which sets the incompressibility condition:

$$\mathrm{Tr}(\boldsymbol{\epsilon}) = \boldsymbol{\nabla}\cdot\mathbf{u} = (c - c_0)\Omega, \tag{3.4}$$

where Tr is the trace. As discussed in Ref. [221], we expect that the free energy density $\mathcal{U}$ of the gel is a function of the strain tensor and the concentration field. The work done on a gel element is given by $\delta\mathcal{U} = \sigma_{ij}\delta\epsilon_{ij} + (\mu - \mu_0)\delta c$, where σ is the mechanical stress tensor. Nevertheless, due to the incompressibility condition in Eq. (3.4), the solvent concentration is no longer an independent variable, and the free energy density only depends on strain. The latter is supposed to follow the standard linear-elastic energy density, *i.e.* $\mathcal{U} = G\left[\boldsymbol{\epsilon}:\boldsymbol{\epsilon} + \frac{\nu}{1-2\nu}\mathrm{Tr}^2(\boldsymbol{\epsilon})\right]$, where G and ν are the effective shear elastic

modulus and Poisson ratio, respectively. The stress tensor is then given by [221]:

$$\boldsymbol{\sigma} = 2G\Big[\boldsymbol{\epsilon} + \frac{\nu}{1-2\nu}\mathrm{Tr}(\boldsymbol{\epsilon})\mathbf{I}\Big] - \frac{\mu-\mu_0}{\Omega}\mathbf{I}, \tag{3.5}$$

where $\mathbf{I}$ is the identity tensor. The difference in chemical potentials per molecular volume appears as a hydrostatic pressure, often called *pore pressure*, and is obtained by enforcing the incompressibility condition with a Lagrange multiplier. In the absence of body force, the mechanical equilibrium is expressed by Navier's closure equation:

$$\boldsymbol{\nabla}\cdot\boldsymbol{\sigma} = \mathbf{0}. \tag{3.6}$$

3.1.2 Coupling between diffusion and hydrostatic pressure

Combining the Eqs. (3.5) and (3.6) leads to:

$$G\Omega\left(\boldsymbol{\nabla}^2\mathbf{u} + \frac{\Omega}{1-2\nu}\boldsymbol{\nabla}(c-c_0)\right) = \boldsymbol{\nabla}(\mu-\mu_0). \tag{3.7}$$

Invoking Eq. (3.3), Eqs. (3.2),(3.4), and (3.7) form a closed system of five equations for the five fields μ, c, and the three components of $\mathbf{u}$. Combining the latter equations reduces the problem to a set of two coupled equations on the concentration field c and chemical potential μ, as:

$$\boldsymbol{\nabla}^2\left[(\mu-\mu_0) - 2G\Omega^2\frac{1-\nu}{1-2\nu}(c-c_0)\right] = 0, \tag{3.8a}$$

$$\mathcal{D}_{\mathrm{pe}}\boldsymbol{\nabla}^2 c - \frac{\partial c}{\partial t} = 0, \tag{3.8b}$$

where we have introduced an effective, poroelastic diffusion coefficient

$$\mathcal{D}_{\mathrm{pe}} = \frac{2(1-\nu)}{1-2\nu}\frac{Gk}{\eta}. \tag{3.9}$$

Equation (3.8a) couples the chemical potential with the concentration, as the flow of solvent is driven by gradients of chemical potential (or equivalently, gradients of pore pressure). Equation (3.8b) describes the diffusion of solvent through the porous matrix, with $\mathcal{D}_{\mathrm{pe}}$ of Eq. (3.9) constructed using macroscopic material parameters. Physically, a mechanical stress would generate (i) a mechanical strain (by elasticity) and (ii) a gradient of chemical potential (or pore pressure). The latter would generate a fluid flow, thus an inhomogeneity of solvent and polymer concentrations.

We note lastly, however, that even while $\mathcal{D}_{\mathrm{pe}}$ is constructed from these macroscopic parameters, one can recover a molecular-scale diffusion coefficient. To make the correspondence, we use the Stokes-Einstein relation for molecular diffusion, $\mathcal{D}_{\mu} \sim k_{\mathrm{B}}T/(\eta a)$, with $k_{\mathrm{B}}T$ and $a \approx \Omega^{1/3}$ the thermal energy and monomer size, respectively. Estimating furthermore the typical polymeric modulus $G \sim k_{\mathrm{B}}T/(Na^3)$, and the permeability $k \sim Na^2$, where N is a typical number of monomers between crosslinks in the network, we find $\mathcal{D}_{\mathrm{pe}} \sim \mathcal{D}_{\mu}$ upon substitution into Eq. (3.9).

3.2 Point-force driving of the gel deformation

In this section, we derive the response of a gel to a point force. We first describe the boundary condition at the top interface, which applies for both thick and thin gels. Secondly we distinguish an infinitely thick gel and a finite-size gel regarding the boundary condition at the bottom interface. Then, we expose a path to resolve the calculation which applies to both thick and thin gels, and use it in both cases. Finally, we illustrate the theoretical results on the surface deformation of both thick and thin gels.

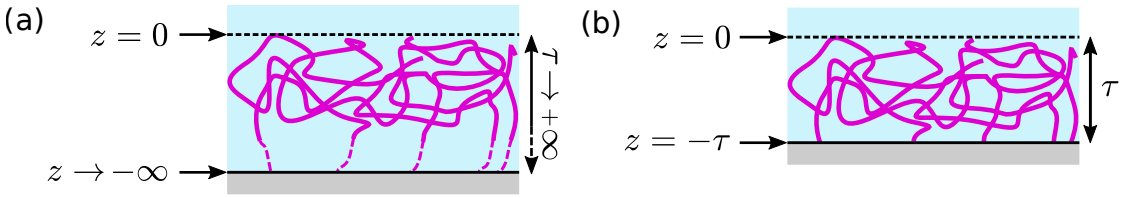

FIG. 3.2. **Boundary condition** *The interface between the poroelastic substrate and the reservoir of solvent at $z = 0$ is considered permeable and allows fluid exchange between the reservoir and the substrate. The permeability condition is translated by the chemical potential being fixed to its equilibrium value at $z = 0$. (a): The substrate is infinitely thick, thus in the limit $z \to -\infty$ the stress and strain fields vanish and the concentration field reaches its equilibrium value. (b): The substrate has a finite thickness τ and is bounded to a rigid boundary at the bottom. Thus the displacement field vanishes at $z = -\tau$ and the gel is considered impermeable at the interface with the rigid boundary.*

3.2.1 Description of the solvent-gel interface

3.2.1.1 Sudden application of an external pressure field

We now derive the response of the gel to a spatially delta-distributed force density applied to the surface of the gel. Prior to the application of such a force, *i.e.* for times $t \leq 0$, we suppose that the gel is in the (swollen) reference state with strain- and stress-free conditions. For $t \geq 0$, a point-force pressure source of magnitude F_0 is suddenly applied on the surface as represented in Fig. 3.1. This forcing drives a deformation of the gel surface, and solvent flow within the polymer matrix. At the interface (*i.e.* $z = 0$ in the reference state), the stress boundary condition is therefore given by:

$$\boldsymbol{\sigma} \cdot \mathbf{e}_z = -F_0 \delta(\mathbf{r}) H(t) \mathbf{e}_z, \tag{3.10}$$

where $H(t)$ denotes the Heaviside step function and $\delta(\mathbf{r})$ the Dirac distribution.

At infinitesimally small times after the point force has been applied, the solvent does not have time to flow, so that the solvent concentration is the same as the one at $t < 0$ as illustrated in Fig. 3.10(a), *i.e.*:

$$c(r, z, t = 0) = c_0. \tag{3.11}$$

3.2.1.2 Permeable solvent-gel interface

We suppose that the gel is in contact with a reservoir of solvent molecules as described in Fig. 3.2, which sets the surface chemical potential to the reference equilibrium value μ_0. Such a permeability condition allows for solvent exchange between the gel and the outer reservoir, and is relevant to situations where the gel is immersed in a liquid phase (*e.g.* its own solvent) with some affinity between the two. Thus, the permeable boundary condition on the chemical potential at the interface reads:

$$\mu(r, z = 0, t) = \mu_0. \tag{3.12}$$

In a perspective of comparison, the same reasoning can be used to describe the mechanical response of an impermeable gel. In that case, solvent exchange between the gel and an outer reservoir is forbidden, thus the normal gradient of chemical potential at the interface $z = 0$ vanishes. The impermeability condition is relevant to situations where a solid object is in contact with the gel surface, thus where there is no reservoir, or to situations where the gel is immersed in another liquid which is not miscible with

the solvent of the gel. The impermeable boundary condition on the chemical potential at the interface reads [110]:

$$\frac{\partial \mu}{\partial z}(r, z = 0, t) = 0. \tag{3.13}$$

In this chapter, we focus on the permeable boundary condition given in Eq.(3.12). We aim to describe situations where the gel is immersed in its own solvent, and eventually interacts with a solid object through a hydrodynamic coupling. The analogous calculation for an impermeable gel is presented in Appendix D.2.

3.2.2 Thick and thin limit cases

3.2.2.1 Infinitely thick gel

In the limit $z \to -\infty$, the stress and strain fields vanish as represented in Fig. 3.2a. The solvent concentration and chemical potential fields reach their reference equilibrium values c_0 and μ_0, respectively.

3.2.2.2 Finite-thickness gel

At the interface with the substrate, located at $z = -\tau$, the gel is bounded to the rigid boundary as described in Fig. 3.2b. Thus, the displacement field is set at zero, as:

$$\mathbf{u}(z = -\tau) = \mathbf{0}. \tag{3.14}$$

Yet, the stress field does not necessarily vanish at $z = -\tau$. The rigid boundary is impermeable, thus no exchange of solvent is allowed at the interface between the gel and the rigid substrate. The impermeable boundary condition at the bottom of the gel reads:

$$\frac{\partial \mu}{\partial z}(z = -\tau) = 0. \tag{3.15}$$

3.3 Resolution

3.3.1 Expression in terms of potential functions

To determine the surface deformation $w(r, t)$ associated with the pressure source of Eq. (3.10) (see Fig. 3.1(a)), we follow the method introduced by McNamme & Gibson [117, 252–254]. The key ingredient of that method is the introduction of two displacement potentials $A(r, z, t)$ and $B(r, z, t)$, defined by:

$$u_r = z\frac{\partial A}{\partial r} + \frac{\partial B}{\partial r}, \tag{3.16a}$$

$$u_z = z\frac{\partial A}{\partial z} - A + \frac{\partial B}{\partial z}, \tag{3.16b}$$

and that satisfy the following equations:

$$\boldsymbol{\nabla}^2 A = 0, \tag{3.17a}$$

$$\nabla^2 B = \Omega(c - c_0), \tag{3.17b}$$

$$2G\Omega\frac{\partial A}{\partial z} = (\mu - \mu_0) - 2G\Omega^2\frac{1-\nu}{1-2\nu}(c - c_0), \tag{3.17c}$$

$$\mathcal{D}_{\mathrm{pe}}\boldsymbol{\nabla}^4 B = \frac{\partial \boldsymbol{\nabla}^2 B}{\partial t}. \tag{3.17d}$$

Using Eq. (3.17), the solvent concentration and chemical potential fields can be expressed as:

$$c - c_0 = \frac{1}{\Omega}\Delta B, \tag{3.18a}$$

$$\mu - \mu_0 = 2G\Omega\left[\frac{\partial A}{\partial z} + \frac{1-\nu}{1-2\nu}\Delta B\right]. \tag{3.18b}$$

Using Eq. (3.5), (3.16) and (3.17), the components of the stress tensor can be expressed as:

$$\sigma_{rr} = 2G\left(z\frac{\partial^2 A}{\partial r^2} - \frac{\partial A}{\partial z} + \frac{\partial^2 B}{\partial r^2} - \Delta B\right), \tag{3.19a}$$

$$\sigma_{zz} = 2G\left(z\frac{\partial^2 A}{\partial z^2} - \frac{\partial A}{\partial z} + \frac{\partial^2 B}{\partial z^2} - \Delta B\right), \tag{3.19b}$$

$$\sigma_{rz} = 2G\left(\frac{\partial^2 B}{\partial r \partial z} + z\frac{\partial^2 A}{\partial z \partial r}\right). \tag{3.19c}$$

We note that azimuthal stresses and displacements have not been considered here, we indeed neglect hoop stresses in this axisymmetric problem.

To solve Eqs. (3.17), we reconsider the problem in the spectral domain. Specifically, we use the Hankel transform of j-th order in space and the Laplace transform in time, with $j \in \{0, 1\}$. In such a framework, a given field $X(r,t)$ is transformed into:

$$\hat{X}(s,q) = \int_0^\infty \mathrm{d}t\, e^{-qt} \int_0^\infty \mathrm{d}r\ X(r,t) r J_j(sr), \tag{3.20}$$

where J_j is the Bessel function of the first kind and j-th order. The inversion formula reads:

$$X(r,t) = \frac{1}{2\pi i}\int_{\gamma-i\infty}^{\gamma+i\infty} \mathrm{d}q\, e^{qt} \int_0^\infty \mathrm{d}s\, \hat{X}(s,q) s J_j(sr), \tag{3.21}$$

where the inverse Laplace transform is written using the Bromwich integral. Then, expressing Eqs. (3.17) in the spectral domain and invoking the initial condition $\nabla^2 B(r,z,0) = 0$, we get the following ordinary differential equations on the transformed potentials $\hat{A}(s,z,q)$ and $\hat{B}(s,z,q)$:

$$\left(\frac{\partial^2}{\partial z^2} - s^2\right)\hat{A} = 0, \tag{3.22}$$

and

$$\left(\frac{\partial^2}{\partial z^2} - s^2 - \frac{q}{\mathcal{D}_{\mathrm{pe}}}\right)\left(\frac{\partial^2}{\partial z^2} - s^2\right)\hat{B} = 0. \tag{3.23}$$

We note that $\hat{A}$ and $\hat{B}$ are calculated using the Hankel transforms of order 0 of A and B, respectively. The solutions to Eqs. (3.22) and (3.23) depend on the boundary conditions set at the bottom of the gel, thus a distinction is made between infinitely thick and finite-size gels.

3.3.1.1 Infinitely-thick gel

The solutions to Eqs. (3.22) and (3.23) that vanish at $z \to -\infty$ read:

$$\hat{A} = a_1 e^{sz}, \tag{3.24a}$$

$$\hat{B} = b_1 e^{sz} + b_2 e^{z\sqrt{s^2 + q/\mathcal{D}_{\mathrm{pe}}}}, \tag{3.24b}$$

where a_1, b_1, b_2 are integration constants, that depend on the spectral variables s and q. Expressing the stress and chemical-potential boundary conditions of Eqs. (3.10) and (3.12) in reciprocal space in terms of the potentials, we obtain:

$$\hat{\sigma}_{sz}(s, z=0, q) = \quad 0 \quad = -2Gs\left[b_1 s + b_2\sqrt{s^2 + \frac{q}{\mathcal{D}_{\mathrm{pe}}}}\right], \tag{3.25a}$$

$$\hat{\sigma}_{zz}(s, z=0, q) = -\frac{F_0}{2\pi q} = 2G\left[-a_1 s + (b_1 + b_2)s^2\right], \tag{3.25b}$$

$$\hat{\mu}(s, z=0, q) - \hat{\mu}_0 = \quad 0 \quad = 2G\Omega\left[\frac{1-\nu}{1-2\nu} b_2 \frac{q}{\mathcal{D}_{\mathrm{pe}}} + a_1 s\right]. \tag{3.25c}$$

We note that $\hat{\sigma}_{sz}$ and $\hat{u}_s$ are computed using the Hankel transforms of order 1 of σ_{rz} and u_r, respectively, using $\frac{\mathrm{d}}{\mathrm{d}r}(rJ_1(sr)) = srJ_0(sr)$ and doing an integration by parts; while $\hat{\sigma}_{zz}$, $\hat{\sigma}_{ss}$, $\hat{u}_z$, $\hat{c}$ and $\hat{\mu}$ are computed using the Hankel transforms of order 0 of σ_{zz}, σ_{ss}, u_z, c and μ, respectively. We introduce intermediate auxiliary functions that depend on s and q to lighten the notation:

$$\chi = \frac{\mathcal{D}_{\mathrm{pe}} s^2}{q}, \tag{3.26a}$$

$$\beta = \sqrt{1 + \frac{q}{\mathcal{D}_{\mathrm{pe}} s^2}} = \sqrt{1 + \frac{1}{\chi}}. \tag{3.26b}$$

In the following, the dimensionless quantities defined in Eqs. (3.26) are used in the intermediate calculation steps. We denote the compressibility factor Λ where the Poisson ratio ν appears, as:

$$\Lambda = \frac{1-2\nu}{1-\nu}. \tag{3.27}$$

Eqs. (3.25) can be written under the form of a matrix equation with division by the factors $-2Gs^2$, $2Gs^2$ and $2G\Omega s^2$ on each line, respectively, as:

$$\begin{pmatrix} 0 \\ -\frac{F_0}{4\pi G s^2 q} \\ 0 \end{pmatrix} = \begin{pmatrix} 0 & 1 & \beta \\ -\frac{1}{s} & 1 & 1 \\ \frac{1}{s} & 0 & \frac{1}{\Lambda\chi} \end{pmatrix} \cdot \begin{pmatrix} a_1 \\ b_1 \\ b_2 \end{pmatrix}. \tag{3.28}$$

Solving Eq. (3.28) by inverting the 3x3 matrix, we obtain a_1, b_1 and b_2, as:

$$\begin{pmatrix} a_1 \\ b_1 \\ b_2 \end{pmatrix} = \frac{F_0}{4\pi G s^2 q} \begin{pmatrix} \dfrac{s}{1 + \Lambda\chi(1-\beta)} \\ \dfrac{\Lambda\beta}{\chi + \Lambda(1-\beta)} \\ \dfrac{\Lambda}{\chi + \Lambda(1-\beta)} \end{pmatrix}. \tag{3.29}$$

Using Eqs. (3.16b), (3.24) and (3.29), we express finally the vertical displacement field, as:

$$\hat{u}_z(s, z) = -\frac{F_0}{4\pi G s q} \frac{\left[1 - sz - \Lambda\chi\beta\right] e^{sz} + \Lambda\beta\chi e^{sz\beta(s,q)}}{1 + \Lambda\chi(1-\beta)}, \tag{3.30}$$

using the dimensionless quantities defined in Eqs. (3.26) and (3.27). In the expression of the vertical displacement field in reciprocal space, we observe a superposition of two exponential decays in depth. The variables χ and β make a transition between the two terms, thus the two penetration depths. The form of χ and thus β shows that the smooth switching in time from one penetration depth to the other follows a diffusive-like dynamics.

3.3.1.2 Finite-thickness gel

The solutions to Eqs. (3.22) and (3.23) in the finite-thickness case are:

$$\hat{A} = a_1 e^{sz} + a_2 e^{-sz}, \tag{3.31a}$$

$$\hat{B} = b_1 e^{sz} + b_2 e^{sz\beta} + b_3 e^{-sz} + b_4 e^{-sz\beta}, \tag{3.31b}$$

where $a_1, a_2, b_1, b_2, b_3, b_4$ are integration constants, that depend on the spectral variables s and q. We use the two auxiliary functions introduced in the previous section 3.3.1.1 through Eqs. (3.26), given in Eqs. (3.32a) and (3.32b). We add a third one, Eq. (3.32c) that rescales the spatial frequency with the inverse of the thickness τ, adapted to describe a finite-sized layer of gel. These functions are:

$$\chi = \frac{\mathcal{D}_{\mathrm{pe}} s^2}{q}, \tag{3.32a}$$

$$\beta = \sqrt{1 + \frac{q}{\mathcal{D}_{\mathrm{pe}} s^2}} = \sqrt{1 + \frac{1}{\chi}}, \tag{3.32b}$$

$$\zeta = s\tau. \tag{3.32c}$$

The definition of the compressibility factor Λ is still given by Eq. (3.27). Expressing the stress, displacement and chemical-potential boundary conditions of Eqs. (3.10), (3.12), (3.14) and (3.15) in terms of the potentials, we obtain:

$$\hat{\sigma}_{sz}(s, z=0, q) = 0 = -2Gs^2 \left[b_1 - b_3 + (b_2 - b_4)\beta\right], \tag{3.33a}$$

$$\hat{\sigma}_{zz}(s, z=0, q) = -\frac{F_0}{2\pi q} = 2Gs^2 \left[-\frac{a_1}{s} + \frac{a_2}{s} + (b_1 + b_2 + b_3 + b_4)\right], \tag{3.33b}$$

$$\hat{\mu}(s, z=0, q) - \hat{\mu}_0 = 0 = 2G\Omega s^2 \left[\frac{a_1}{s} - \frac{a_2}{s} + \frac{1}{\Lambda\chi}(b_2 + b_4)\right], \tag{3.33c}$$

$$\hat{u}_s(s, z=-\tau, q) = 0 = -s\left[-\tau\left(a_1 e^{-\zeta} + a_2 e^{\zeta}\right) + b_1 e^{-\zeta} + b_2 e^{-\zeta\beta} + b_3 e^{\zeta} + b_4 e^{\zeta\beta}\right], \tag{3.33d}$$

$$\hat{u}_z(s, z=-\tau, q) = 0 = -s\left[\frac{1+\zeta}{s} a_1 e^{-\zeta} + \frac{1-\zeta}{s} a_2 e^{\zeta} - e^{-\zeta} b_1 + \beta b_2 e^{-\zeta\beta} + e^{\zeta} b_3 + \beta b_4 e^{\zeta\beta}\right], \tag{3.33e}$$

$$\frac{\partial \mu}{\partial z}(s, z=-\tau, q) = 0 = 2G\Omega s^3 \left[\frac{a_1}{s} e^{-\zeta} + \frac{a_2}{s} e^{\zeta} + \frac{\beta}{\Lambda\chi} b_2 e^{-\zeta\beta} - \frac{\beta}{\Lambda\chi} b_4 e^{\zeta\beta}\right]. \tag{3.33f}$$

Eqs. 3.33 can be written under the form of a matrix equation, with division by the factors $-2Gs^2$, $2Gs^2$,$2G\Omega s^2$, $-s$, $-s$, $2G\Omega s^3$ on each line, respectively, as:

$$\begin{pmatrix} 0 \\ -\frac{F_0}{4\pi G s^2 q} \\ 0 \\ 0 \\ 0 \\ 0 \end{pmatrix} = \begin{pmatrix} 0 & 0 & 1 & \beta & -1 & -\beta \\ -\frac{1}{s} & \frac{1}{s} & 1 & 1 & 1 & 1 \\ \frac{1}{s} & -\frac{1}{s} & 0 & \frac{1}{\Lambda\chi} & 0 & \frac{1}{\Lambda\chi} \\ -\tau e^{-\zeta} & -\tau e^{\zeta} & e^{-\zeta} & e^{-\zeta\beta} & e^{\zeta} & e^{\zeta\beta} \\ \frac{1+\zeta}{s} e^{-\zeta} & \frac{1-\zeta}{s} e^{\zeta} & -e^{-\zeta} & \beta e^{-\zeta\beta} & e^{\zeta} & \beta e^{\zeta\beta} \\ \frac{1}{s} e^{-\zeta} & \frac{1}{s} e^{\zeta} & 0 & \frac{\beta}{\Lambda\chi} e^{-\zeta\beta} & 0 & -\frac{\beta}{\Lambda\chi} e^{\zeta\beta} \end{pmatrix} \cdot \begin{pmatrix} a_1 \\ a_2 \\ b_1 \\ b_2 \\ b_3 \\ b_4 \end{pmatrix}. \tag{3.34}$$

As for the semi-infinite case, the resulting product of the inverse 6x6 matrix by the right-hand-side vector and the expression of $\hat{u}_z(s, z, q)$ are computed using the formal calculation software *Mathematica*. The code is reproduced in Appendix C.4.

3.3.2 Results and discussion

3.3.2.1 Infinitely-thick gel

Having solved the poroelastic problem of Eqs. 3.8-3.13 for the potentials A, B defined in the previous section, we find the surface normal deformation of the gel $\hat{w}(s,q) = -\hat{u}_z(s, z=0, q)$ in reciprocal space (see Eq. (3.20)) by invoking Eq. (3.16b) and Eq. 3.30, as:

$$\hat{w}(s,q) = \frac{F_0}{4\pi G s q} \frac{1}{1 + \Lambda \frac{\mathcal{D}_{\rm pe} s^2}{q}\left(1 - \sqrt{1 + \frac{q}{\mathcal{D}_{\rm pe} s^2}}\right)} , \tag{3.35}$$

where the Poisson ratio appears in the compressibility factor defined in Eq. (3.27).

We first note that if the gel is nearly incompressible, *i.e.* as $\nu \to 1/2$, then $\Lambda \to 0$ and the poroelasticity does not affect the surface deformation, as revealed in Eq. (3.35). In such a case, the poroelastic medium responds as a purely elastic and incompressible one, at all times. Similarly, if the permeability is small, *i.e.* as $k \to 0$, the diffusion constant $\mathcal{D}_{\rm pe}$ of the solvent vanishes, and the medium again behaves as an incompressible elastic material. In the opposite limit of large permeability, the solvent can diffuse almost instantaneously, and the stress is immediately relaxed, so that the response is the one of a compressible elastic material at all times.

In Fig. 3.3(a) is shown the dimensionless surface deformation in reciprocal space $\hat{w}(s,q)$ plotted as a function of the spatial frequency s for a given temporal frequency q, both on linear (main) and logarithmic scales (inset). We choose a value $\nu = 0.1$, which is a typical value for swollen gels and giving finite Λ. The vertical normalisation is chosen such that dimensionless values of s and q were used, length is normalised by $\sqrt{F_0/G}$, and time by $F_0/(\mathcal{D}_{\rm pe} G)$. We choose $qF_0/(\mathcal{D}_{\rm pe} G) = 1$. Fig. 3.3(b) shows the surface deformation in reciprocal space $\hat{w}(s,q)$ plotted as a function of s for various q. The results show parallel power-law decays in the small- and large-s limits, with a larger prefactor for large s (small distance). Furthermore, the two prefactors for the small- and large-s limits respectively depend on the value chosen for q. To explain this observation, we explore the temporal asymptotics of the governing Eq. 3.35. We find:

$$\hat{w}(s,q) \underset{q\to\infty}{\sim} \frac{F_0}{4\pi G s q}, \tag{3.36a}$$

$$\hat{w}(s,q) \underset{q\to 0}{\sim} \frac{F_0(1-\nu)}{2\pi G s q}. \tag{3.36b}$$

The initial- and final-value theorems can be used in the short-time and long-time limits of the surface deformation. By invoking the inverse Laplace transform we get, in reciprocal-space (*e.g.* Hankel) and real-time domains:

$$\hat{w}(s, t=0^+) = \lim_{q\to\infty} q\hat{w}(s,q) = \frac{F_0}{4\pi G s}, \tag{3.37a}$$

$$\hat{w}(s, t\to\infty) = \lim_{q\to 0^+} q\hat{w}(s,q) = \frac{F_0(1-\nu)}{2\pi G s}, \tag{3.37b}$$

leading to the deformation in real space, by invoking the inverse Laplace and Hankel transforms given in Eq. (3.21):

$$w(r, t=0^+) = \frac{F_0}{4\pi G r} = w^{\rm incomp}(r), \tag{3.38a}$$

$$w(r, t\to\infty) = \frac{F_0(1-\nu)}{2\pi G r} = w^{\rm comp}(r). \tag{3.38b}$$

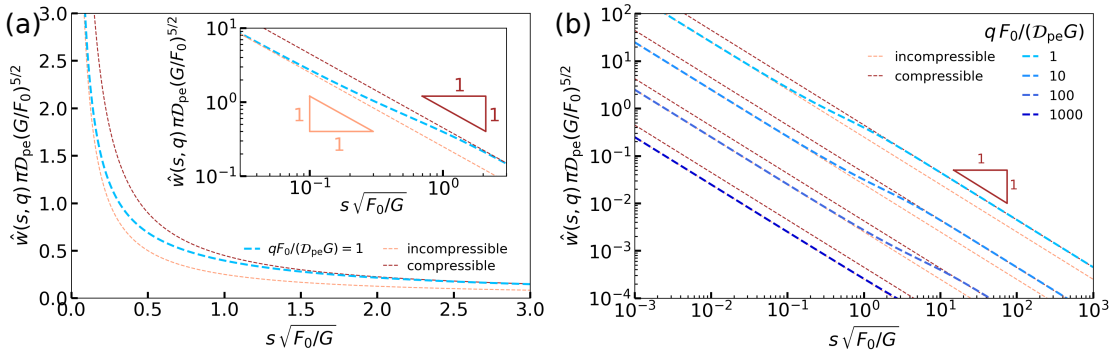

FIG. 3.3. **Surface deformation of a poroelastic half space induced by a point-force pressure source in Hankel-Laplace space.** *(a): Dimensionless, reciprocal-space surface deformation* $\hat{w}(s,q)$ *as computed from Eq.* (3.35) *using* $\nu = 0.1$*, as a function of the spatial frequency* s*, normalized by* $\sqrt{G/F_0}$*, for a given temporal frequency* q*, normalized by* $\mathcal{D}_{\rm pe}G/F_0$*. The orange and red dashed lines correspond to Eqs.* (3.36a) *and* (3.36b)*, respectively. Main : linear scale. Inset : logarithmic scale. (b): Dimensionless, reciprocal-space surface deformation* $\hat{w}(s,q)$ *as computed from Eq.* (3.35) *using* $\nu = 0.1$*, as a function of the scaled spatial frequency,* s*, for various scaled temporal frequencies,* q*. The orange and red dashed lines are the same as in (a).*

Thus, for both short and long times, we find in Eqs. (3.37) that the surface deformation in reciprocal space follows a power-law decay, in both short- and long-time limits. The former expression is the point-force solution of a purely elastic, incompressible, and semi-infinite medium of shear modulus G, denoted $w^{\rm incomp}(r)$. At long times, we have the point-force solution of a purely elastic and semi-infinite medium of shear modulus G and Poisson ratio ν, denoted $w^{\rm comp}(r)$. Eqs. (3.36) are plotted using dashed lines in Fig. 3.3(a) and 3.3(b). These expressions thus form a link between poroelastic and elastic materials [188, 196]: at large distances (small s), the solvent has no time to flow inside the porous matrix and the response is elastic-like, with an incompressibility condition due to the liquid fraction. At small distances (large s), the solvent does not flow anymore and the response recovers a steady elastic deformation, with compression (*i.e.* a concentration change, as illustrated in Fig. 3.10(b)) as compared to the initial state. In between the two asymptotic regimes, the surface deformation smoothly changes from the short-time (incompressible) to the long-time (compressible) elastic-like behaviors, as shown in Fig. 3.3(b) using a finite q.

To investigate the effect of inverse time, we remark that Eq. (3.35) is under the form of a prefactor built with physical parameters multiplied by a dimensionless function. The prefactor scales in $1/q$, as a natural result of performing a Laplace transform. Thus, in Fig. 3.4(a) is shown $q\hat{w}(s,q)$ plotted as a function of s for various q, both on linear (main) and logarithmic scales (inset). With this scaling the parallel power-law decays observed in the small- and large-s limits are independent on the chosen temporal frequency q as predicted by Eqs. (3.36). The evolution of the response $\hat{w}(s,q)$ multiplied by q, with decreasing q, from the large-q to the small-q asymptotes, given respectively by Eq. (3.36a)(a) and (3.36b)(b), is clearly seen.

To connect the asymptotic inverse space and time responses, we note that at fixed Λ, Eq. (3.35) depends on the auxiliary function noted $\chi = \mathcal{D}_{\rm pe}s^2/q$ in section 3.3.1.1, that physically represents a dimensionless, diffusive variable. This is expected since the solvent concentration follows a diffusive-like law with a diffusion constant $\mathcal{D}_{\rm pe}$. In

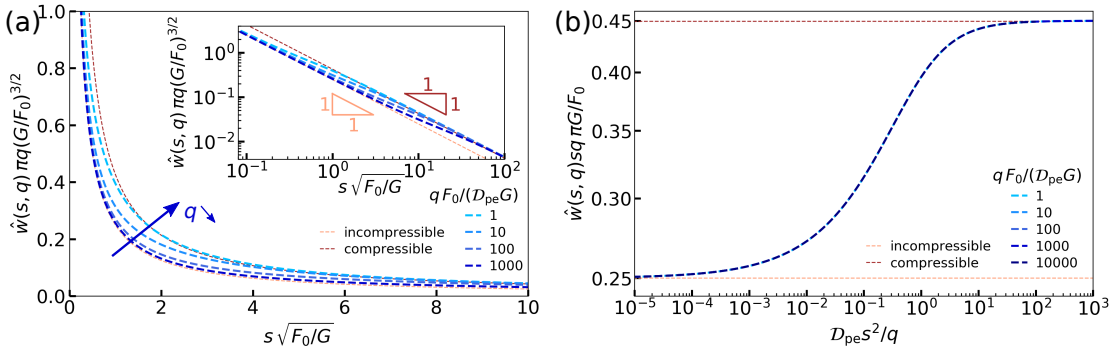

FIG. 3.4. **Rescaled surface deformation of a poroelastic half-space induced by a point-force pressure source in Hankel-Laplace space.** *(a): Normalized surface deformation in reciprocal space $\hat{w}(s,q)$, multiplied by the scaled temporal frequency q, normalized by $\mathcal{D}_{\mathrm{pe}}G/F_0$, as a function of the scaled spatial frequency s, normalized by $\sqrt{G/F_0}$, for various scaled temporal frequencies q, and for $\nu = 0.1$, as computed from Eq.* (3.35)*. The orange and red dashed lines correspond to Eqs.* (3.36a) *and* (3.36b)*, respectively, multiplied by q. Main : linear scale. Inset : logarithmic scale. (b): Normalized surface deformation in reciprocal space $\hat{w}(s,q)$ multiplied by the space frequency s and the temporal frequency q, as a function of the scaled spatial frequency s, for $\nu = 0.1$, as computed from Eq.* (3.35)*. The orange and red dashed lines are the same as in (a).*

Fig. 3.4(b), we thus plot the normalized surface deformation in reciprocal space, as a function of the normalized diffusive variable, having fixed the Poisson ratio. Given the normalization and the form of Eq. 3.35, we find that a single curve describes the response in reciprocal space. Interpreting the response physically, we note that when the gel starts to be indented, it first exhibits an incompressible elastic-like response, as discussed above. Later, at a given time t, the solvent and stress have typically diffused over a radial distance $r_{\mathrm{c}} \sim \sqrt{\mathcal{D}_{\mathrm{pe}}t}$, giving a self-similar curve in reciprocal space.

To have a direct view on the spatial and temporal relaxations described above in reciprocal space, the inverse Laplace transform of Eq. 3.35 was numerically computed using the Talbot algorithm [255]. The inverse Hankel transform was computed with Riemann summation over a finite spectral domain. Residual numerical oscillations were smoothed using a Savitzky-Golay filter of order 3 on a window of 9 points over the total 200 000 points used in the linear discretisation of the r, and s axes. Numerical tools are detailed in Appendix C. The results are presented in Fig. 3.5(a), where the deformation in real space is plotted as a function of the radial coordinate for various times. For $r < r_{\mathrm{c}}$ noted in the previous paragraph, the gel state has essentially relaxed and the response is compressible (red dashed line), while for $r > r_{\mathrm{c}}$ the state and response are not modified with respect to the initial, incompressible elastic ones (orange dashed line). The transition between compressible and incompressible deformations are also elucidated in the logarithmic representation of the data shown in the inset, where the short- and long-time asymptotic relaxations are shown.

In Fig. 3.5(b), we quantitatively show the gel's relaxation to its final state, plotting the difference of the data in (a) with that of the asymptotic late-time limit in Eq. (3.38b) as a function of the radial coordinate. A continuous decay towards the late-time value is observed for all radii. Taking a few examples, we show in the inset of Fig. 3.5(b) the temporal decay towards the final state for the three radii noted by vertical dashed lines in the main part of the figure. For early times, we note a plateau at a value $F_0(1-2\nu)/(4\pi G)$, corresponding to the difference between the two asymptotic limits in

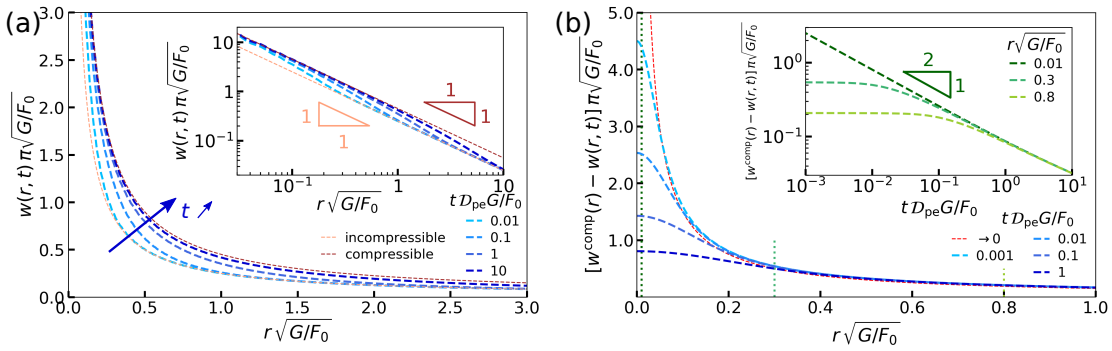

FIG. 3.5. **Surface deformation induced by a point-force pressure source.** *(a): Surface deformation $w(r,t)$ normalized by $\sqrt{F_0/G}$, as a function of the radial coordinate r normalized by $\sqrt{F_0/G}$, for the times t noted in the legend and normalized by $F_0/(\mathcal{D}_{\rm pe}G)$, as computed from the inverse transform of Eq.* (3.35) *and using $\nu = 0.1$. The orange and red dashed lines correspond to the asymptotic limits in Eqs.* (3.38)*. The inset shows the same data on logarithmic scales. (b): Difference $w^{comp}(r) - w(r,t)$ (normalized) between the surface deformation of a purely elastic compressible material (see Eq.* (3.38b)*) and the one of the poroelastic material, as a function of normalized radial coordinate r, for the dimensionless times t noted in the legend. The inset shows the same data, but as a function of time and for various radial positions r (corresponding to the vertical dashed green lines in the main panel), using logarithmic scales.*

Eq. (3.38). Remarkably, a temporal power law with exponent $-1/2$, characteristic of a diffusive process, is reached for all the radii at long times. To explain this observation, we perform an expansion of Eq. 3.35 at small temporal frequency q (or similarly at large time t), as done in Eq. (3.36b) to a higher order in q. This leads to:

$$\begin{aligned}\hat{w}(s,q) &\underset{q\to 0}{\sim} \frac{F_0}{4\pi G s q}\frac{1}{1+\frac{1-2\nu}{1-\nu}\frac{\mathcal{D}_{\rm pe}s^2}{q}\left(1-\left[1+\frac{1}{2}\frac{q}{s^2\mathcal{D}_{\rm pe}}-\frac{1}{8}\left(\frac{q}{s^2\mathcal{D}_{\rm pe}}\right)^2\right]\right)} \\ &= \frac{F_0(1-\nu)}{2\pi G s q}\frac{1}{1+\frac{(1-2\nu)}{4}\frac{q}{\mathcal{D}_{\rm pe}s^2}}.\end{aligned} \tag{3.39}$$

We recover the result given in Eq. (3.36b), by taking Eq. (3.39) at order 1 in q at the denominator. Taking the inverse Laplace transform of Eq. (3.39), we get:

$$\hat{w}(s,t) \underset{t\to\infty}{\sim} \frac{F_0(1-\nu)}{2\pi G s}\left[1-\exp\left(-\frac{4}{1-2\nu}\mathcal{D}_{\rm pe}s^2 t\right)\right]. \tag{3.40}$$

Finally, taking the inverse Hankel transform, we get in real space:

$$\begin{aligned}w(r,t) &\underset{t\to\infty}{\sim} \frac{F_0(1-\nu)}{2\pi G r}\left[1-\sqrt{\pi(1-2\nu)}\frac{r}{\sqrt{\mathcal{D}_{\rm pe}t}}I_0\left(-\frac{(1-2\nu)}{32}\frac{r^2}{\mathcal{D}_{\rm pe}t}\right)\exp\left(-\frac{(1-2\nu)}{32}\frac{r^2}{\mathcal{D}_{\rm pe}t}\right)\right] \\ &\simeq \frac{F_0(1-\nu)}{2\pi G r} - \frac{F_0(1-\nu)\sqrt{(1-2\nu)\pi}}{2\pi G\sqrt{16\mathcal{D}_{\rm pe}t}},\end{aligned} \tag{3.41}$$

where I_0 is a modified Bessel function of the first kind, of order 0, and the last expansion is obtained by taking the long-time limit. The first term of the right-hand side gives the purely elastic and compressible response of the material at long time. The second term

corresponds to the long-term correction to the latter, as plotted in Fig. 3.5(b). The decay does not depend on r and scales as $\sim 1/\sqrt{\mathcal{D}_{\rm pe}t}$, as recovered through the asymptotic $-1/2$ exponent in the inset of Fig. 3.5(b). The intercept between the asymptotic decay law and the initial plateau value indicates its typical duration time, that scales with the diffusion time $r^2/\mathcal{D}_{\rm pe}$.

Lastly, we note that in Appendix D.2, we compare the results of the present permeable description to the case of an impermeable surface. For the impermeable case, the solvent flux vanishes at the interface. This alternative boundary condition is relevant when the gel is not in contact with its own liquid solvent. Such a situation arises when a gel is indented by a rigid object [112, 113, 214, 217, 221, 222], as well as in some configurations of soft wetting [110, 219]. The surface deformations are found to adopt qualitatively similar shapes in the permeable and impermeable cases. However, the respective behaviours quantitatively differ, and the stress relaxation is faster in particular in the permeable case, due to the allowed exchange of solvent with the outer reservoir.

3.3.2.2 Finite-thickness gel

As for the semi-infinite case described in the previous section, we find the surface normal deformation of the gel $\hat{w}_\tau(s,q) = -\hat{u}_z(s,z=0,q)$ in the finite-thickness case, solving for Eqs. (3.8)-(3.15) in reciprocal space (see Eq. (3.20)) by invoking Eq. (3.16b) and solving Eq. (3.34), as:

$$\hat{w}_\tau(s,q) = \frac{F_0}{4\pi G s q}\,\frac{N_1+N_2+N_3}{D_1+D_2+D_3}, \tag{3.42}$$

with the six terms $N_1, N_2, N_3, D_1, D_2, D_3$ expressed as:

$$\begin{cases} N_1 = -4\Lambda\beta\chi\sinh(\zeta) \\ N_2 = \left[(\Lambda\chi+1)\sinh(2\zeta) - 2\zeta\right]\beta\cosh(\beta\zeta) \\ N_3 = \Lambda(3\chi+2-\chi\cosh(2\zeta))\sinh(\beta\zeta) \\ D_1 = 4\Lambda\beta\chi\left[\zeta\cosh(\zeta) - (1+\Lambda\chi)\cosh(\zeta)\right] \\ D_2 = \beta\left[2\zeta^2 + \Big(1+2\Lambda\chi(\Lambda\chi+1)\Big)\Big(1+\cosh(2\zeta)\Big)\right]\cosh(\beta\zeta) \\ D_3 = -\Lambda(2\chi+1)\left[2\zeta + (\Lambda\chi+1)\sinh(2\zeta)\right]\sinh(\beta\zeta), \end{cases} \tag{3.43}$$

where the dimensionless quantities χ, β, ζ are defined in Eqs.(3.32). The Poisson ratio appears in the compressibility factor Λ defined in Eq. (3.27).

As for the semi-infinite case exposed in the previous section, we first note that if the gel is nearly incompressible, *i.e.* as $\nu \to 1/2$, and thus $\Lambda \to 0$, the terms N_1, N_3, D_1, D_3 are zero and the surface deformation of the gel reads:

$$\hat{w}_\tau(s,q) \underset{\nu\to 1/2}{=} \frac{F_0}{4\pi G s q}\,\frac{\sinh(2\zeta)-2\zeta}{1+2\zeta^2+\cosh(2\zeta)} = \frac{1}{q}\hat{w}_\tau^{\rm incomp}(s), \tag{3.44}$$

with $\zeta = s\tau$, hence we recover the Laplace transform of the result known for a purely elastic layer of thickness τ denoted $\hat{w}_\tau^{\rm incomp}(s)$, taking the particular incompressible value for the Poisson ratio $\nu = 0.5$ [203, 212]. Similarly, if the permeability is small, *i.e.* as $k \to 0$, the diffusion constant $\mathcal{D}_{\rm pe}$ of the solvent vanishes, $\chi \to 0$ and $\beta \sim \chi^{-1/2}$, and we recover the same limit. The medium again behaves as an incompressible elastic finite-sized layer. In the opposite limit of large permeability, *i.e.* large $\mathcal{D}_{\rm pe}$, $\chi \to +\infty$ and $\beta \to 1$, the surface deformation of the gel is finite and reads:

$$\hat{w}_\tau(s,q) \underset{k\to\infty}{=} \frac{F_0(1-\nu)}{2\pi G s q}\,\frac{2\zeta - (4\nu-3)\sinh(2\zeta)}{5+4\nu(2\nu-3)+2\zeta^2-(4\nu-3)\cosh(2\zeta)} = \frac{1}{q}\hat{w}_\tau^{\rm comp}(s), \tag{3.45}$$

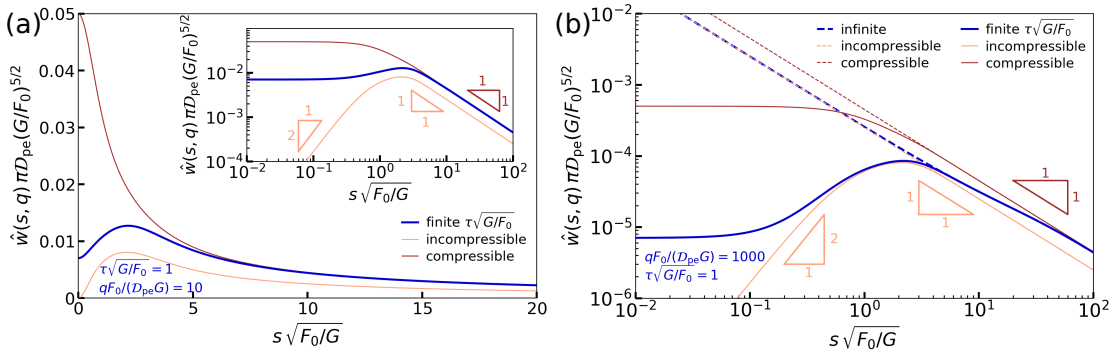

FIG. 3.6. **Surface deformation of a poroelastic finite-thickness layer induced by a point-force pressure source in Hankel-Laplace space.** *(a): Normalized, reciprocal-space surface deformation* $\hat{w}_\tau(s,q)$ *as computed from Eqs.* (3.42) *and* (3.43)*, as a function of the normalized spatial frequency* s*, for a given normalized temporal frequency* q*, using* $\nu = 0.1$ *and* $\tau\sqrt{G/F_0} = 1$*. The orange and red full lines correspond to Eqs.* (3.46a) *and* (3.46b)*, respectively. Main : in linear scales. Inset : in logarithmic scales. (b): Normalized surface deformation* $\hat{w}_\tau(s,q)$ *of a poroelastic half-space (dashed lines) as computed from Eq.* (3.35) *and of a finite-thickness poroelastic layer (full lines) as computed from Eqs.* (3.42) *and* (3.43)*, respectively, as functions of the spatial frequency* s *for a given normalized temporal frequency* q*, using* $\nu = 0.1$ *and* $\tau\sqrt{G/F_0} = 1$*. The orange and red full lines are described in (a). The orange and red dashed lines correspond to Eqs.* (3.36a) *and* (3.36b)*, respectively.*

where we recover the Laplace transform of the known result for a compressible purely elastic layer of thickness τ denoted $= \hat{w}_\tau^{\text{comp}}(s,q)$, for any Poisson ratio ν [203, 212], in contrast to Eq. (3.44) that recovers the incompressible solution ($\nu = 0.5$). In Appendix D.4, the known Green's function for a purely elastic material is recovered using the same calculation path as in the present chapter. Exactly as for the semi-infinite case, the solvent diffuses almost instantaneously and the stress is immediately relaxed, such that the response is the one of a compressible finite-sized layer.

In Fig. 3.6(a), the dimensionless surface deformation in reciprocal space $\hat{w}_\tau(s,q)$ is plotted as a function of the spatial frequency s for a given temporal frequency q, both on linear (main) and logarithmic scales (inset). We choose the same value $\nu = 0.1$ than in the semi-infinite case. The normalization of radial length, time and vertical deformation are kept the same than in the semi-infinite case. We choose a value of $qF_0/(\mathcal{D}_{\text{pe}}G) = 10$. In Fig. 3.6(b) is shown $\hat{w}_\tau(s,q)$ and $\hat{w}(s,q)$ plotted as a function of s for a given q. We choose $qF_0/(\mathcal{D}_{\text{pe}}G) = 1000$, a value that highlights the asymptotical behaviors. To demonstrate the generality of the observations concerning Fig. 3.6, in Fig. 3.7(a) is shown $\hat{w}_\tau(s,q)$ plotted as a function of s for various q. The results show the same parallel power-law decays in the large-s limit for both infinite and finite thicknesses. The two prefactors for small and large s limits respectively depend on the value chosen for q. Yet in the small-s limit the finite-thickness response appears as constant, and at the transition between large- and small- s limits it grows with a different power law. To explain the observed power-law behaviors, we explore the temporal asymptotics of the governing Eqs. (3.42) and (3.43). We find:

$$\hat{w}_\tau(s,q) \underset{q\to\infty}{\sim} \frac{F_0}{4\pi G s q}\,\frac{\sinh(2\zeta)-2\zeta}{1+2\zeta^2+\cosh(2\zeta)} = \frac{1}{q}\hat{w}_\tau^{\text{incomp}}(s), \tag{3.46a}$$

$$\hat{w}_\tau(s,q) \underset{q\to 0}{\sim} \frac{F_0(1-\nu)}{2\pi G s q}\,\frac{2\zeta-(4\nu-3)\sinh(2\zeta)}{5+4\nu(2\nu-3)+2\zeta^2-(4\nu-3)\cosh(2\zeta)} = \frac{1}{q}\hat{w}_\tau^{\text{comp}}(s), \tag{3.46b}$$

with $\zeta = s\tau$. Equations (3.46) are plotted in Fig. 3.6(a) and Fig. 3.6(b). We note that we recover the same results computed in the small and large permeability limits respectively, which are the known responses of a purely elastic, finite-thickness layer, respectively incompressible and compressible [203, 212]. By invoking the initial and final-value theorems in the short-time and long-time limits of the surface deformation, we get:

$$\hat{w}_\tau(s, t = 0^+) = \lim_{q\to\infty} q\hat{w}_\tau(s, q) = \hat{w}_\tau^{\text{incomp}}(s), \tag{3.47a}$$

$$\hat{w}_\tau(s, t \to \infty) = \lim_{q\to 0^+} q\hat{w}_\tau(s, q) = \hat{w}_\tau^{\text{comp}}(s). \tag{3.47b}$$

Thus, at initial times we recover the response to a point force of a purely elastic incompressible layer, of shear modulus G and thickness τ. At long times, we have the response to a point force of a purely elastic compressible layer, of shear modulus G, thickness τ and Poisson ratio ν. We then compute the asymptotics of Eqs. (3.46) in the small- and large-s limits, as:

$$\hat{w}_\tau^{\text{incomp}}(s) \underset{s\to 0}{\sim} \frac{F_0\tau^3}{6\pi G}s^2, \tag{3.48a}$$

$$\hat{w}_\tau^{\text{incomp}}(s) \underset{s\to\infty}{\sim} \frac{F_0}{4\pi G s}, \tag{3.48b}$$

$$\hat{w}_\tau^{\text{comp}}(s) \underset{s\to 0}{\sim} \frac{F_0\tau}{\pi G}\frac{2(1-\nu)^2}{1+4\nu(\nu-2)}, \tag{3.48c}$$

$$\hat{w}_\tau^{\text{comp}}(s) \underset{s\to\infty}{\sim} \frac{F_0(1-\nu)}{2\pi G s}. \tag{3.48d}$$

Using the inverse Laplace and Hankel transforms as defined in Eq. (3.21) on the asymptotics written in Eqs. (3.48), we get an estimate of the purely-elastic response behaviour in real space, as:

$$w_\tau(r, t = 0^+) = w_\tau^{\text{incomp}}(r) \underset{r\to\infty}{\sim} 0, \tag{3.49a}$$

$$w_\tau(r, t = 0^+) = w_\tau^{\text{incomp}}(r) \underset{r\to 0}{\sim} \frac{F_0}{4\pi G r}, \tag{3.49b}$$

$$w_\tau(r, t \to \infty) = w_\tau^{\text{comp}}(r) \underset{r\to\infty}{\sim} \frac{F_0\tau}{\pi G q}\frac{2(1-\nu)^2}{1+4\nu(\nu-2)}\frac{\delta(r)}{r} \underset{r\to\infty}{\sim} 0, \tag{3.49c}$$

$$w_\tau(r, t \to \infty) = w_\tau^{\text{comp}}(r) \underset{r\to 0}{\sim} \frac{F_0(1-\nu)}{2\pi G r}, \tag{3.49d}$$

recalling that the inverse Hankel transforms of a constant is $\delta(r)/r$ and the one of the square function s^2 is identically 0.

We analyze now the different asymptotic behaviors exhibited in each of the four lines of Eqs. (3.48) and (3.49).

Incompressible response - small r: We find with Eq. (3.48b) that the incompressible response of a purely elastic material follows in reciprocal space a power-law decay in s^{-1} in the limit of large-s. Additionally, in the limit of large s, which corresponds to the small-r limit in real space, we recover the asymptotic behavior of a semi-infinite, elastic incompressible medium computed in Eq. (3.36a). At large spatial frequencies s (*e.g.* at small radii r), the point-force response of a poroelastic finite-thickness layer is the same as the one of a semi-infinite medium as shown by Eq. (3.49b), at initial times. This means the finite-sized aspect of the material is not probed in the small-r limit.

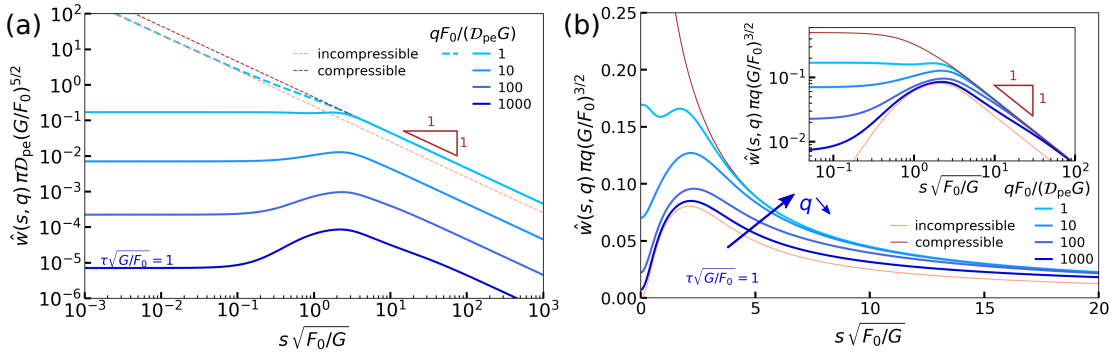

FIG. 3.7. **Rescaled surface deformation of a poroelastic finite-thickness layer induced by a point-force pressure source in Hankel-Laplace space.** *(a): Dimensionless, reciprocal-space surface deformation $\hat{w}(s,q)$ of a half space (dashed lines) and $\hat{w}\tau(s,q)$ of a finite-thickness layer (full lines), as computed from Eq.* (3.35)*and Eq.* (3.42) *respectively, as a function of the spatial frequency s, normalized by $\sqrt{G/F_0}$, for various temporal frequencies q, normalized by $\mathcal{D}_{\rm pe}G/F_0$, using $\nu=0.1$ and $\tau\sqrt{G/F_0}=1$. The orange and red dashed lines correspond to Eqs.* (3.36a) *and* (3.36b)*, respectively, for $qF_0/(\mathcal{D}_{pe}G)=1$. (b): Normalized surface deformation in reciprocal space $\hat{w}_\tau(s,q)$ multiplied by the temporal frequency q, as a function of the scaled spatial frequency s, for $\nu=0.1$ and $\tau\sqrt{G/F_0}=1$, as computed from Eq.* (3.42)*. The orange and red full lines correspond to Eqs.* (3.46a) *and* (3.46b)*, respectively. Main : linear scales. Inset : logarithmic scales.*

Incompressible response - large r: We find with Eq. (3.48a) that the incompressible response of a purely elastic material follows in reciprocal space a power-law growth in s^2 in the limit of small-s. While at small spatial frequencies s (*e.g.* at large radii r), the point-force response of a poroelastic finite-thickness layer differs from the one of a semi-infinite medium, increasing with a power law in reciprocal spaces, at initial times. This means that in comparison to the semi-infinite case, the finite-sized aspect of the material is seen in the large-r limit, exhibiting no deformation, as shown by Eq (3.49a).

Compressible response - small r: We find that the compressible response of a purely elastic material follows a power-lay decay in s^{-1} in the limit of large-s as shown by Eq. (3.48d). As for the incompressible case just described, in the limit of large-s, which corresponds to the small-r limit in real space, we recover the asymptotic behavior of a semi-infinite, elastic compressible medium computed in Eq. (3.36b). At large spatial frequencies s (*e.g.* at small radii r), the point-force response of a poroelastic finite-thickness layer is the same as the one of a semi-infinite medium as shown by Eq. (3.49d), at long times, which means again that the finite-sized aspect of the material is not probed in the small-r limit.

Compressible response - large r: We find that the compressible response of a purely elastic material is a constant in the limit of small s as shown by Eq. (3.48c). At small spatial frequencies s (*e.g.* at large radii r), the point-force response of a poroelastic finite-thickness layer differs from the one of a semi-infinite medium and reaches a constant value, at long times. This means that in comparison to the semi-infinite case, the finite-sized aspect of the material is seen in the large-r limit, still exhibiting no deformation as shown by Eq. (3.49c).

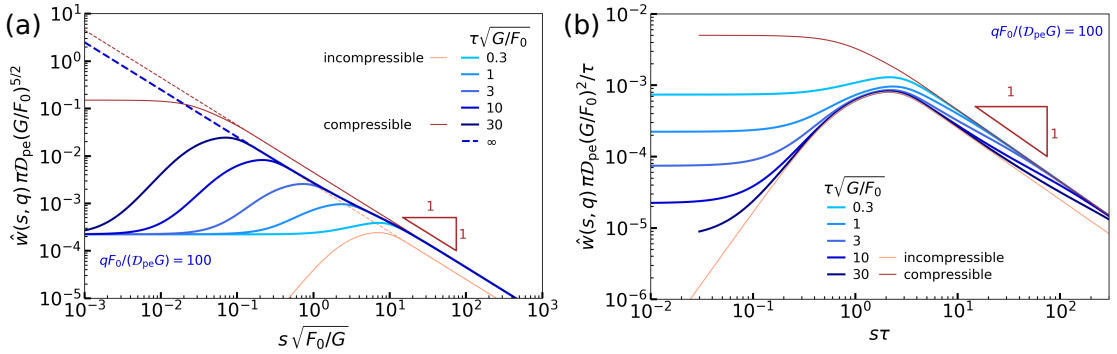

FIG. 3.8. **Surface deformation induced by a point-force pressure source in Hankel-Laplace space, for various thicknesses of the material.** *(a): Dimensionless, reciprocal-space surface deformation of a finite-thickness layer w_τ (full line) and of a semi-infinite medium w (dashed line), as a function of the spatial frequency s, normalized by $\sqrt{G/F_0}$, for various normalized thicknesses τ, as computed from the inverse transforms of Eqs.* (3.42) *and* (3.35) *respectively, using $\nu = 0.1$ and $q\mathcal{D}_{pe}G/F_0 = 100$. The orange and red dashed and full lines correspond to Eqs.* (3.36a), (3.36b), (3.46a) *and* (3.46b), *respectively. (b): Normalized surface deformation in reciprocal space $\hat{w}_\tau(s,q)$ divided by the thickness τ, as a function of the dimensionless variable $s\tau$, for various thicknesses, with $\nu = 0.1$ and $q\mathcal{D}_{pe}G/F_0 = 100$, as computed from Eq.* (3.42). *The orange and red full lines are the same as in (a)*

In the asymptotic limit of small r, for both the incompressible and compressible responses, the finite-size aspect of the material is not highlighted, surprisingly, meaning that the presence of the rigid boundary underneath the soft and porous gel does not affect the mechanical behavior of its top free surface. The poroelastic model used in this chapter is based on a linear stress-strain relationship, which supposes a relatively small strain rate (typically $\boldsymbol{\epsilon} \lesssim 30\%$ [108]). To preserve this assumption, the force exerted at $r = 0$ should not be too large then. Otherwise, a correction taking into account gradients of the strain tensor $\boldsymbol{\nabla\epsilon}$ should be taken into account in the stress-strain relationship, switching from a linear to a non-linear elasticity model.

To investigate the effect of inverse time as for the semi-infinite case, we remark that the prefactor in Eq. (3.42) scales in $1/q$, as a natural result of performing a Laplace transform. Thus in Fig. 3.7(b) is shown $q\hat{w}_\tau(s,q)$ plotted as a function of s for various q. With this scaling the power-law growth and decay observed in the large-s limits are independent on the chosen temporal frequency q as predicted by Eqs. (3.46). The scaled response $q\hat{w}_\tau(s,q)$ with decreasing q clearly evolves from the incompressible to the compressible asymptotes, given respectively by Eq. (3.46a)(a) and (3.46a)(b). Yet, in comparison with the semi-infinite case, the universality of the response in reciprocal space when scaled by the diffusive variable $\chi = \mathcal{D}_{pe}s^2/q$ is lost. This is expected given the complex form of Eq. (3.42) where two natural and dimensionless variables, x and $\zeta = s\tau$ appear.

For both the incompressible and compressible responses, the smooth transition between the asymptotic behaviors at small-s and large-s seems to happen at spatial frequencies of about $s\sqrt{F_0/G} \sim 1$ with the choice $\tau\sqrt{G/F_0} = 1$. To investigate the dependency of the transition between the small-s and large-s regimes on the thickness τ, we show in Fig. 3.8 $q\hat{w}_\tau(s,q)$ plotted as a function of rescaled s for various τ, for a poroelastic finite-size layer. The deformation of a purely elastic, impressible and compressible,

finite-size layer and semi-infinite medium, corresponding to Eqs. (3.46a), (3.46b), (3.36a) and (3.36b) are also represented for comparison. Indeed, the transition between the asymptotic behaviors at small-s and large-s happens at a spatial frequency $s \sim 1/\tau$. With increasing thickness, the transition region is wider in s and the deformation in reciprocal space reaches a higher value, following more closely the semi-infinite asymptote. In Fig. 3.8(b) is thus plotted $q\hat{w}_\tau(s,q)$ divided by the thickness τ as a function of rescaled variable $s\tau$, for various τ. The latter representation shows, following the present theoretical prediction, that the finite-size aspect of the material is probed by observing a zero response in the peripheral region $r \geq \tau$, while the response observed in the central region $r \leq \tau$ is the one of an incompressible elastic semi-infinite medium at initial times and the one of a compressible elastic semi-infinite medium at final times. As for the semi-infinite case, the link between poroelastic and purely elastic materials is observed in the asymptotical behaviors. At large distances (small s), the point-force response vanishes. The finite-thickness aspect induces a local, finite-range deformation. At small distances (large s), the solvent has flowed and does not flow any more: the response recovers an elastic deformation with compression (*i.e.* change in volume), as in the semi-infinite case. At intermediary distances ($s \sim 1/\tau$), with increasing s, the response smoothly changes from no deformation to a regime where the solvent has no time to flow inside the porous matrix. In this intermediary regime, the response is the one of an elastic layer, incompressible due to the solvent fraction, for a small range in s. Still with increasing s, the surface deformation then smoothly changes from the intermediate, short-time (incompressible) to the long-time (compressible) elastic-like behaviors, as shown in Fig. 3.6.

As for the semi-infinite case, to have a direct view on the spatial and temporal relaxations described above in reciprocal space, the deformation in reciprocal space given by Eq.(3.42) was first computed with the technique described in Appendix C.2.5. Then the inverse Laplace and Hankel transforms of Eq.(3.42) were numerically computed using the Talbot Algorithm and Riemann summation. A Savitsky-Golay filter was finally applied to smoothen residual oscillations. The process is detailed in Appendix C. A few traces of numerical errors remain, for instance on Fig. 3.7(b), where the curve corresponding to $qF_0/(\mathcal{D}_{\rm pe}G) = 1$ shows a minute residual oscillation at small s.

In Fig. 3.9(a) is shown the deformation of a finite-thickness layer and a semi-infinite medium, respectively, as a function of the radial coordinate r for a given time t. We choose the same values of $\nu = 0.1$ and $\tau\sqrt{G/F_0} = 1$ as before. We choose a value of $t\mathcal{D}_{\rm pe}G/F_0 = 0.1$ representing an intermediate value. The responses of a incompressible and compressible material are plotted in orange and red respectively. The full line and dashed line represent the finite-thickness and semi-infinite cases respectively, corresponding to Eqs. 3.38 and the inverse transform of Eqs. 3.46 respectively. The results show a match between the point-force response of a finite-thickness layer and a semi-infinite medium at small r, as predicted by asymptotics in Eqs. (3.49). Yet, at large r, the deformation of a finite-thickness layer vanishes faster than the one of a semi-infinite medium, again as predicted by asymptotics in Eqs. (3.49). In Fig. 3.9(b) is shown the deformation of a finite-thickness layer as a function of the radial coordinate r, for various times t. As for the semi-infinite case described in the previous section, the poroelastic response exhibits a crossover from a purely elastic incompressible regime to a purely elastic compressible regime with increasing time. In a central area defined by $r \leq \tau$, a significant deformation is predicted and is similar to the one of an infinite-thickness layer. In a transition zone defined by $r \sim \tau$ the deformation shows an inflection due to the finite thickness, while in the peripheral region defined by $r \geq \tau$ the response is killed by the finite-thickness effect. Thus for a more detailed description of the relaxation in the

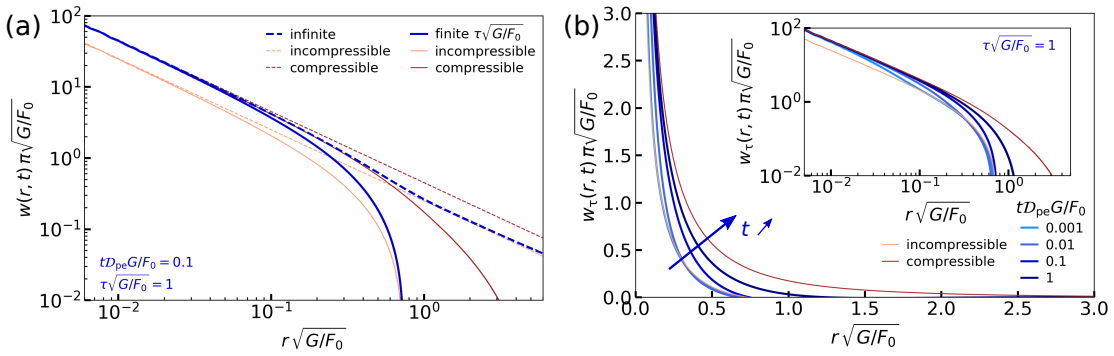

FIG. 3.9. **Surface deformation induced by a point-force pressure source.** *(a): Normalized surface deformation of a finite-thickness layer w_τ (full line) and of a semi-infinite medium w (dashed line), as a function of the radial coordinate r, normalized by $\sqrt{F_0/G}$, for a given time t, normalized by $\mathcal{D}_{\rm pe}G/F_0$, as computed from the inverse transform of Eq.* (3.42)*, using $\nu = 0.1$ and $\tau\sqrt{G/F_0} = 1$. The orange and red dashed and full lines correspond to Eq. 3.38 and the inverse transform of Eq. 3.46, respectively. (b): Normalized surface deformation of a finite-thickness layer w_τ as a function of the radial coordinate r, for the times noted in the legend, as computed from the inverse transform of Eq.* (3.42)*, using $\nu = 0.1$ and $\tau\sqrt{G/F_0} = 1$. The orange and red dashed and full lines are describes in (a). The inset shows the same data on logarithmic scales.*

central area, one can refer to the semi-infinite case. The deformation relaxes following a diffusive dynamics in the central area, as described by Fig. 3.5(b).

3.4 Solution for an arbitrary pressure field

In real systems, gels are indented with probes that have finite sizes [112, 113, 221, 222]. In these cases, the external load is not a point force, and the outer pressure field has a finite spatial extent. Additionally, the outer pressure field may exhibit temporal variations. Since the above model only involves linear operators, we can apply the superposition principle. Henceforth, the surface deformation generated by an arbitrary time-dependent and space-dependent pressure field $p(\mathbf{r}, t)$, is given by the convolution:

$$w(\mathbf{r},t) = \int_{-\infty}^{t} \mathrm{d}t' \int_{\mathbb{R}^2} \mathrm{d}^2\mathbf{r}'\, \mathcal{G}(|\mathbf{r}-\mathbf{r}'|, t-t')\, p(\mathbf{r}', t'), \tag{3.50}$$

where $\mathcal{G}$ is the Green's function of the problem, which is the surface deformation induced by a point force $\delta(\mathbf{r})\delta(t)$. If on a one hand the gel is semi-infinite, the latter is directly related to Eq. (3.35), through:

$$\hat{\mathcal{G}}(s,q) = \frac{1}{4\pi G s} \frac{1}{1 + \Lambda \frac{\mathcal{D}_{\rm pe} s^2}{q}\left(1 - \sqrt{1 + \frac{q}{s^2 \mathcal{D}_{\rm pe}}}\right)}\,. \tag{3.51}$$

If on the other hand the gel has a finite thickness, the Green's function is related to Eq. (3.42), through:

$$\hat{\mathcal{G}}_\tau(s,q) = \frac{1}{4\pi G s q} \frac{N_1 + N_2 + N_3}{D_1 + D_2 + D_3}, \tag{3.52}$$

with the six terms $N_1, N_2, N_3, D_1, D_2, D_3$ given in Eq. (3.43). The inverse transform reads:

$$\mathcal{G}(r,t) = \frac{1}{2i\pi} \int_{\gamma - i\infty}^{\gamma + i\infty} \mathrm{d}q\, e^{qt} \int_0^\infty \mathrm{d}s\; \hat{\mathcal{G}}(s,q) s J_0(sr). \tag{3.53}$$

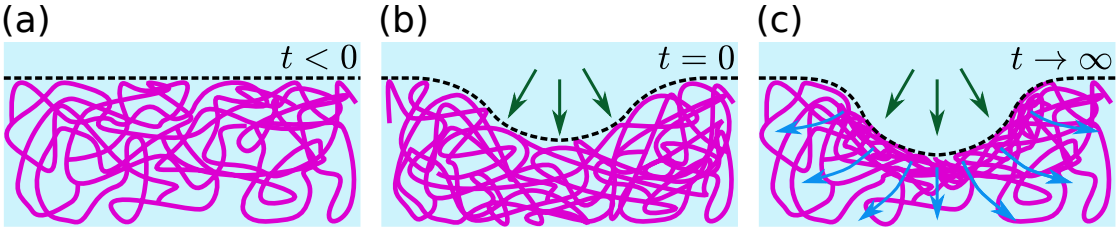

FIG. 3.10. **Reticulated polymer matrix filled with a solvent.** *(a): An undeformed reticulated gel is swollen in a solvent and forms an ideal poroelastic system. For negative times, the concentration field of solvent is considered homogeneous and fixed at c_0, and the chemical potential field is homogeneous at equilibrium and fixed at μ_0. (b): When a sudden pressure field is applied at $t = 0$, the concentration field c of solvent is still isotropic due to the incompressibility of the liquid, but non-zero gradients of chemical potential μ arise. The material responds as an elastic incompressible solid. (c): In the long-time limit, solvent had time to flow, due to the gradients of chemical potential. The concentration field of solvent c is inhomogeneous but the chemical potential has reached again its equilibrium value μ_0. The material responds as an elastic compressible solid.*

Yet, the Green's function in real space has no explicit form, for both the semi-infinite and finite-thickness cases. To perform efficient calculations, an adequate path is thus to work in reciprocal spaces. The pressure field is first expressed in Hankel and Laplace spaces and denoted $\hat{p}(s,q)$. Using properties on transformation of convolution products, we thus write:

$$w(r,t) = \frac{1}{2i\pi}\int_{\gamma-i\infty}^{\gamma+i\infty} \mathrm{d}q\, e^{qt} \int_0^\infty \mathrm{d}s\ \hat{w}(s,q) s J_0(sr) \tag{3.54a}$$

$$= \frac{1}{2i\pi}\int_{\gamma-i\infty}^{\gamma+i\infty} \mathrm{d}q\, e^{qt} \int_0^\infty \mathrm{d}s\ \hat{\mathcal{G}}(s,q)\hat{p}(s,q) s J_0(sr). \tag{3.54b}$$

In Eq. (3.54) the expression of the Green's function $\hat{\mathcal{G}}(s,q)$ is explicit while the pressure field $p(s,q)$ may be an unknown field to compute numerically. In the following chapters of this thesis, the substitution of a convolution product by a standard product in reciprocal space will be largely used to solve equations on pressure fields.

3.5 Conclusion and perspectives

Fig. 3.10 summarizes qualitatively a major result from this chapter. Poroelastic behaviors are characterized by a time-dependent transition from the limit of an incompressible elastic response towards the one of a compressible elastic response. Fig. 3.10(a) illustrates the initial state of the gel, which is undeformed and swollen in its solvent. The solvent concentration and chemical potential are fixed at their equilibrium values, respectively c_0 and μ_0. At $t = 0$ a pressure field is turned on as illustrated by Fig. 3.10(b). Then, the gel reacts as a purely elastic solid with an incompressibility condition, due to the solvent fraction. The solvent concentration is still fixed at its equilibrium value c_0 but gradients of chemical potential arise and testify of the out-of-equilibrium state of the gel. With increasing times, driven by chemical-potential gradients, fluid flows happen in the porous matrix. The gel relaxes towards its equilibrium state with a diffusive-like dynamics. Such a transitional state exhibits features of both incompressible-like and compressible-like solids. In the limit of long times $t \to \infty$, the fluid has flowed and the gel reacts as a purely elastic solid with a compressibility condition, due to the loss

in volume of solvent. The solvent concentration c is inhomogeneous and the chemical potential has reached again its equilibrium value μ_0, which testifies of the equilibrium state of the gel.

In the present Chapter, we theoretically addressed the mechanical response of semi-infinite and finite-thickness, permeable, linear poroelastic substrates to an external axisymmetric pressure field. The point-force response was first computed. By convolution of the latter to any outer axisymmetric pressure field, the surface deformation profile can be computed. Additional numerical work enables to compute the deformation profile generated in time. In summary, we showed that the mechanical response of both a semi-infinite and a finite-size media to a point force is characterized by a transition in time from a purely elastic and incompressible behavior to a purely elastic and compressible one. Furthermore, for semi-infinite medium, the transition between these two limits is observed on the deformation profile, at a coordinate that depends on time as $r_c = \sqrt{\mathcal{D}_{pe} t}$. Thus, the purely elastic and compressible response diffuses over the incompressible one. For a finite-thickness medium, in a peripheral region defined by $r_c \geq \tau$, the poroelastic response to a point force vanishes, while in a central area defined by $r \leq \tau$, the deformation profile is similar to the one observed in the semi-infinite case and follows the same diffusive dynamics.

The poroelastic model used in this chapter is based on a linear stress-strain relationship, which supposes that the strain rate is kept small. When the force applied on the free surface is important enough to generate a larger strain rate, gradients of strain tensor are no longer negligible and a non-linear stress-strain relationship should be chosen instead to describe the behavior of the gel. In a next chapter the needed transition from a linear elasticity law to a non-linear correction to that elasticity law to describe the observed mechanical behavior of the soft gel will be shown.

In the perspective of investigating the mechanics of soft hydrogels, the theoretical description presented in this chapter can describe the deformation field of the porous matrix as a function of time, when submitted to any axisymmetric load. An experimental validation could be provided by any technique able to produce images of the vertical deformation field: for instance, after preparing a gel with trapped fluorescent particles inside, one could develop a technique based on confocal microscopy. A relevant choice of the frame rate with respect to the relaxation dynamics of the gel should be thought about, in order to track in time the motion of each fluorescent particle. Or, the same idea could be applied in Total Internal Reflection Fluorescent Microscopy (TIRFM) [48, 49, 256–258], which consists in imaging fluorescent trackers close to a rigid boundary ($\leq 1\mu$m) by an evanescent wave.

A direct application of the general tools derived in this Chapter to describe poroelasticity would be to address the problem of the poroelastic adhesive force. Indeed, considering a hard sphere immersed in a solvent and moving normally towards a purely elastic boundary, it has been theoretically shown by Vincent Bertin, a former PhD student and a close collaborator, that an adhesive term arises in the expression of the resulting force at first order in compliance, which is defined by the length ratio between the deformation of the wall and the distance to the sphere [211]. This phenomenon arises from a elastohydrodynamic coupling between the confined layer of surrounding fluid and

the elastic boundary. Considering instead a poroelastic boundary, the adhesion term is expected to be influenced by the timescale of the sphere motion, ranging from an incompressible to compressible response of the boundary. The theoretical derivation of this suction term in the context of a poroelasticity would be of a great interest. Additionally, an experimental study based on colloidal-probe AFM for instance, would nicely complement and (in)validate the theoretical predictions.

Another perspective of the work presented in this Chapter would be to compute a poroelastic response to a point-force in a different geometry, with a planar symmetry, using the same type of calculation path. Then, a direct application would be to address the poroelastic lift force. Indeed, when a hard sphere immersed in a solvent moves tangentially to a purely elastic boundary, the softness of the close wall results in a lift force applied on the sphere [188, 198]. Thus, the latter is repealed from the boundary. The elastohydrodynamic lift force arises from the asymmetry of the pressure field in the confined region of fluid, which is due to a coupling between the fluid viscosity and the elasticity of the nearby boundary. As for the adhesive force, we could study the poroelastic lift force, that we expect to be influenced by time scales, both theoretically and experimentally. In a biomimetic context, such a situation is relevant to describe several organs in the human body: a classical example is about the blood cells flowing in the blood vessels [121].

The theoretical results presented in this chapter stand as a basis to describe more realistic situations. Motivated by the recent development of contactless colloidal-probe rheological experiments on soft and complex materials, our general results will be applied in the next chapter to the specific case of a sphere oscillating vertically near a gel, within an outer fluid identical to the solvent present in the polymeric matrix.

Chapter 4

Contactless colloidal-probe rheology of soft hydrogels

In this Chapter, we apply the general results of the previous one to a specific outer pressure field that is relevant to contactless colloidal-probe rheological methods. Here specifically, we focus on the elastohydrodynamic coupling between a rigid sphere of radius R and a semi-infinite permeable poroelastic medium (see Fig. 1.8(c)). For this purpose, we invoke the linear-response theory introduced by Leroy & Charlaix [203], and widely used in contactless measurements of the mechanical properties of soft surfaces [197, 204, 259–263]. In a first part, we establish the theoretical framework of a lubricated sphere oscillating close to a permeable, poroelastic half space. We derive the theoretical loss and storage components of the force applied on the sphere, with complementing numerics. In a second part, we present preliminary AFM-based experiments performed on a thick, swollen PNIPAM hydrogel, that fits to the theoretical situation detailed in the first part. The experimental results are confronted to the theoretical predictions.

4.1 Theoretical model

4.1.1 Soft-lubrication approximation

The situation we consider is that one of a sphere of radius R, placed at a distance H from the undeformed surface of a gel, and that oscillates vertically with angular frequency ω and amplitude h_0, as schematized in Fig 4.1. The gel is assimilated to a semi-infinite poroelastic medium, of shear modulus G, Poisson ratio ν and porosity k. The ensemble is fully immersed in a Newtonian fluid (identical to the solvent in the gel here) of dynamic shear viscosity η and density ρ. We suppose that the sphere-plane distance H is small with respect to the sphere radius R, and can thus invoke the lubrication approximation [32]. We suppose furthermore that the fluid-gap thickness H is small compared to the hydrodynamic radius $\sqrt{2RH}$. Thus, the sphere profile can be approximated by a parabola in the lubricated contact region, and the liquid-film thickness profile is thus given by:

$$h(r,t) \simeq H + h_0 \cos(\omega t) + w(r,t) + \frac{r^2}{2R}. \tag{4.1}$$

The Reynolds number $\rho H^2 \omega/\eta$ is assumed to be small compared to unity, so that the flow is laminar. Furthermore, we suppose that the typical viscous penetration depth is large compared to the liquid-gap thickness: $\sqrt{\eta/(\rho\omega)} \gg h$. Therefore, the flow can be

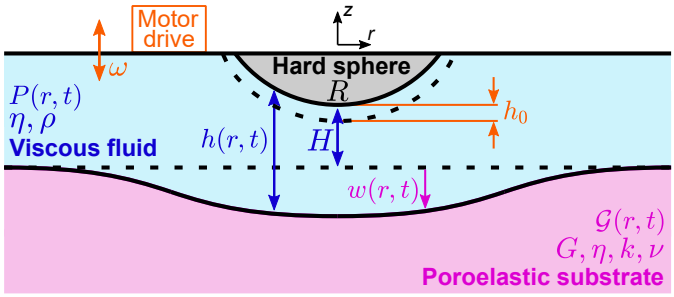

FIG. 4.1. **Semi-infinite permeable poroelastic medium deformed by the pressure field generated with an oscillating lubricated sphere.** *In contactless colloidal-probe rheological methods, a micrometric sphere is oscillating at angular frequency ω and amplitude h_0 normally to the substrate in a liquid of dynamic shear viscosity η and density ρ. The substrate is a semi-infinite permeable poroelastic medium. We denote G, ν, and k, its effective shear elastic modulus, effective Poisson ratio, and porosity. The surrounding liquid is identical to the solvent flowing in the porous material. The hydrodynamic lubrication pressure field $P(r,t)$ generated by the associated flow deforms the gel surface, leading to a deformed liquid gap profile. We note $w(r,t)$ the deformation profile and $h(r,t)$ the fluid gap profile.*

described by the steady Stokes equation at leading order [64], which reads:

$$0 = -\frac{\partial p}{\partial r} + \eta \frac{\partial^2 v_r}{\partial z^2}. \tag{4.2}$$

We assume no-slip boundary conditions at both the sphere and gel surfaces. This latter condition is assumed since the typical slip length at poroelastic surfaces is comparable to the pore size $\sim \sqrt{k}$ [90, 94], which is nanometric. We neglect the normal flow to the interface between the gel and the fluid, as exchanges of solvent between the both are modeled by the permeability boundary condition expressed by Eq. (3.12). The solution to Stokes equation is a Poiseuille flow characterized by a parabolic velocity profile. The volumetric flux in the vertical direction is derived by integrating over the surface of the sphere, and the one in the radial direction is derived by integrating on azimuths and the z variable, which defines a cylinder at a given radial position r. By invoking the flux conservation, the liquid-film thickness profile follows the axisymmetric thin-film equation [64], as:

$$\frac{\partial h}{\partial t} = \frac{1}{12\eta r}\frac{\partial}{\partial r}\left[r h^3 \frac{\partial p}{\partial r}\right], \tag{4.3}$$

where p is the excess pressure field in the liquid with respect to the atmospheric pressure. In the lubrication approximation, the ratio between the shear stress and the normal stress σ_{rz}/σ_{zz} is of order $\sqrt{H/2R}$, thus the viscous shear stresses are negligible compared to the pressure in the fluid. Therefore, at the gel interface the force balance takes the same form as in Chapter 3:

$$\sigma_{zz} = -p. \tag{4.4}$$

Recalling the results obtained in Chapter 3, the surface deformation profile can be computed in the general case from Eq. (3.50), and thus reads:

$$w(\mathbf{r},t) = \int_{-\infty}^{t} \mathrm{d}t' \int_{\mathbb{R}^2} \mathrm{d}^2\mathbf{r}'\, \mathcal{G}(|\mathbf{r}-\mathbf{r}'|, t-t')\, p(\mathbf{r}', t'), \tag{4.5}$$

where $\mathcal{G}$ is the Green's function of the problem. The latter is the surface deformation induced by a point force $F_0\delta(\mathbf{r})$. In the case of a permeable, semi-infinite poroelastic

layer, the Green's function was derived in Chapter 3 in Hankel and Laplace space, and is given by Eq. (3.51), as:

$$\hat{\mathcal{G}}(s,q) = \frac{1}{4\pi G s} \frac{1}{1+\Lambda\frac{\mathcal{D}_{\rm pe}s^2}{q}\Big(1-\sqrt{1+\frac{q}{s^2\mathcal{D}_{\rm pe}}}\Big)}\,, \tag{4.6}$$

where the compressibility factor is defined from the Poisson ratio ν by Eq. (3.27), that we recall:

$$\Lambda = \frac{1-2\nu}{1-\nu}, \tag{4.7}$$

and the effective poroelastic diffusion coefficient is given by Eq. (3.9), that we recall:

$$\mathcal{D}_{\rm pe} = \frac{2(1-\nu)}{1-2\nu}\frac{Gk}{\eta}. \tag{4.8}$$

The inverse transform is given by Eq. (3.21), as:

$$\mathcal{G}(r,t) = \frac{1}{2\pi i}\int_{\gamma-i\infty}^{\gamma+i\infty} \mathrm{d}q\, e^{qt}\int_0^\infty \mathrm{d}s\, \hat{\mathcal{G}}(s,q) s J_0(sr). \tag{4.9}$$

4.1.2 Linear-response theory

Following Ref. [203], we suppose that the oscillation amplitude is much smaller than the liquid-gap thickness: $h_0 \ll h$. Additionally, the response function $\mathcal{G}$ of the gel to a point force is derived from a linear stress-strain relation, allowed by the hypothesis of small deformations. Thus, we assume that the deformation profile is small compared to the liquid-gap thickness: $w(r,t) \ll h(r,t)$. At orders zero and one in h_0/h, Eq. (4.1) reduces then to:

$$h^{(0)}(r,t) \simeq H + \frac{r^2}{2R}\,, \tag{4.10a}$$

$$h^{(1)}(r,t) \simeq h_0\cos(\omega t) + w(r,t)\,. \tag{4.10b}$$

Recalling that p is the extra pressure in the fluid with respect to the atmospheric pressure, p is considered of order one in h_0/h. Hence, we invoke the linear-response theory, and write the fields, as:

$$w(r,t) = \mathrm{Re}[w^*(r)e^{i\omega t}], \quad p(r,t) = \mathrm{Re}[p^*(r)e^{i\omega t}]\,, \tag{4.11}$$

where * indicates complex variables, $i^2=-1$, and Re is the real part. Equation (4.3) is then linearized, giving at order one in h_0/h:

$$i\omega\Big(h_0 + w^*\Big) = \frac{1}{12\eta r}\frac{\mathrm{d}}{\mathrm{d}r}\left[r\Big(H+\frac{r^2}{2R}\Big)^3\frac{\mathrm{d}p^*}{\mathrm{d}r}\right]. \tag{4.12}$$

To adapt to the steady-state description of the linear-response theory imposed by Eq. (4.11), we write the response function $\mathcal{G}$ of the gel to an external axisymmetrical pressure field under a complex form, in reciprocal space. To do so, we first write the forward and backward Hankel transforms of a complex field X^*, as:

$$\hat{X}^*(s) = \int_0^\infty \mathrm{d}r\, X^*(r) r J_0(sr), \quad X^*(r) = \int_0^\infty \mathrm{d}s\, \hat{X}^*(s) s J_0(sr), \tag{4.13}$$

and the Green's function reads:

$$\hat{\mathcal{G}}^*(s) = \frac{1}{2Gs}\frac{1}{1-i\Lambda\frac{\mathcal{D}_{\rm pe}s^2}{\omega}\Big(1-\sqrt{1+\frac{i\omega}{\mathcal{D}_{\rm pe}s^2}}\Big)}. \tag{4.14}$$

The particular case of the calculation of $\mathcal{G}$ in the steady-state regime is detailed in Appendix D.3. Using Eq. (4.5) in reciprocal space, the deformation is finally obtained with:

$$\hat{w}^*(s) = \hat{p}^*(s)\hat{\mathcal{G}}^*(s) = \frac{\hat{p}^*(s)}{2Gs}\,\frac{1}{1 - i\Lambda\frac{\mathcal{D}_{\mathrm{pe}}s^2}{\omega}\Big(1 - \sqrt{1 + \frac{i\omega}{\mathcal{D}_{\mathrm{pe}}s^2}}\Big)}\,. \tag{4.15}$$

The thin-film equation Eq. (4.12) that is written in complex variables, is associated to the deformation-pressure relation given by Eq. (4.15). Solving for the pressure field p^* and the deformation profile w^*, we describe the steady-state regime of an oscillating sphere near a semi-infinite poroelastic medium.

4.1.3 Non-dimensionalization

From Eq. (4.1), the lubricated-contact length $\sqrt{2RH}$ - *i.e.* the so-called hydrodynamic radius - sets a typical horizontal length scale. Besides, h_0 sets a typical vertical length scale. Thus, we introduce the following dimensionless variables:

$$\tilde{r} = \frac{r}{\sqrt{2RH}}, \quad \tilde{s} = s\sqrt{2RH}, \quad \tilde{w}^*(\tilde{r}) = \frac{w^*(r)}{h_0}. \tag{4.16}$$

From the horizontal projection of the Stokes equation, and the incompressibility condition, we find that the typical lubrication pressure scale is $2\eta R\omega h_0/H^2$. Thus, we introduce the following dimensionless pressure field:

$$\tilde{p}^*(\tilde{r}) = \frac{H^2 p^*(r)}{2\omega R\eta h_0}. \tag{4.17}$$

Injecting these new variables in Eq. (4.3), the dimensionless thin-film equation becomes:

$$i\big(1 + \tilde{w}^*(\tilde{r})\big) = \frac{1}{12\tilde{r}}\frac{\mathrm{d}}{\mathrm{d}\tilde{r}}\left[\tilde{r}\Big(1 + \tilde{r}^2\Big)^3\frac{\mathrm{d}\tilde{p}^*}{\mathrm{d}\tilde{r}}\right]. \tag{4.18}$$

Then, we introduce two characteristic parameters. First, we define the critical distance at which the surface deformation and sphere oscillation amplitude are of the same order [203]:

$$H_{\mathrm{c}} = 8R\Big(\frac{\eta\omega}{2G}\Big)^{2/3}. \tag{4.19}$$

Second, we define the critical poroelastic angular frequency at which the solvent typically diffuses over the contact length at the critical distance during one oscillation:

$$\omega_{\mathrm{c}} = \frac{\mathcal{D}_{\mathrm{pe}}}{2RH_{\mathrm{c}}} = \frac{\mathcal{D}_{\mathrm{pe}}}{16R^2}\Big(\frac{2G}{\eta\omega}\Big)^{2/3}. \tag{4.20}$$

Using the dimensionless variables and critical parameters above, we can write the Green's function given in Eq. (4.14) in dimensionless form, as:

$$\hat{\tilde{\mathcal{G}}}^*(s) = \frac{1}{\tilde{s}}\left[1 - i\Lambda\frac{\omega_{\mathrm{c}}H_{\mathrm{c}}\tilde{s}^2}{\omega H}\Big(1 - \sqrt{1 + i\frac{\omega H}{\omega_{\mathrm{c}}H_{\mathrm{c}}\tilde{s}^2}}\Big)\right]^{-1}, \tag{4.21}$$

and the dimensionless deformation profile is calculated in reciprocal space with the dimensionless form of Eq (4.15), as:

$$\hat{\tilde{w}}^*(s) = \frac{\hat{\tilde{p}}^*(\tilde{s})}{8}\left(\frac{H_{\mathrm{c}}}{H}\right)^{3/2}\hat{\tilde{\mathcal{G}}}^*(s) \tag{4.22a}$$

$$= \frac{\hat{\tilde{p}}^*(\tilde{s})}{8\tilde{s}}\left(\frac{H_{\mathrm{c}}}{H}\right)^{3/2}\left[1 - i\Lambda\frac{\omega_{\mathrm{c}}H_{\mathrm{c}}\tilde{s}^2}{\omega H}\Big(1 - \sqrt{1 + i\frac{\omega H}{\omega_{\mathrm{c}}H_{\mathrm{c}}\tilde{s}^2}}\Big)\right]^{-1}. \tag{4.22b}$$

Finally, the complex pressure field $\hat{\tilde{p}}^*(s)$ in reciprocal space is derived by applying the dimensionless form of the forward Hankel transform. Similarly, the complex deformation profile $\tilde{w}^*(r)$ in real space is derived by applying the dimensionless form of the inverse Hankel transform. Transforms are given in Eq. (4.13) and can be rewritten as:

$$\hat{\tilde{p}}^*(\tilde{s}) = \int_0^\infty \mathrm{d}\tilde{r}\, \tilde{p}^*(\tilde{r})\tilde{r}J_0(\tilde{s}\tilde{r}), \tag{4.23a}$$

$$\tilde{w}^*(\tilde{r}) = \int_0^\infty \mathrm{d}\tilde{s}\, \hat{\tilde{w}}^*(\tilde{s})\tilde{s}J_0(\tilde{s}\tilde{r}). \tag{4.23b}$$

4.1.4 Comparison to the purely elastic case

To compare to the response of a purely elastic material, we use the known response of elastic, incompressible and compressible, semi-infinite media that we recalled in Chapter 3, Sec. 3.3.2.1. Using the linear response theory, the Green's functions for purely elastic, incompressible and compressible materials, read in reciprocal space:

$$\hat{\mathcal{G}}_{\mathrm{incomp}}(s) = \frac{1}{2Gs} \tag{4.24a}$$

$$\hat{\mathcal{G}}_{\mathrm{comp}}(s) = \frac{1-\nu}{Gs}, \tag{4.24b}$$

and the complex deformation profiles read:

$$\hat{w}^*_{\mathrm{incom}}(s) = \frac{\hat{p}^*(s)}{2Gs} \tag{4.25a}$$

$$\hat{w}^*_{\mathrm{incom}}(s) = \frac{(1-\nu)\hat{p}^*(s)}{Gs}. \tag{4.25b}$$

Switching to dimensionless variables, the latter equations are transformed into:

$$\hat{\tilde{w}}^*_{\mathrm{incom}}(\tilde{s}) = \hat{\tilde{w}}^*(s) = \frac{\hat{\tilde{p}}^*(\tilde{s})}{8\tilde{s}} \left(\frac{H_\mathrm{c}}{H}\right)^{3/2} \tag{4.26a}$$

$$\hat{\tilde{w}}^*_{\mathrm{incom}}(\tilde{s}) = \hat{\tilde{w}}^*(s) = \frac{(1-\nu)\hat{\tilde{p}}^*(\tilde{s})}{4\tilde{s}} \left(\frac{H_\mathrm{c}}{H}\right)^{3/2}. \tag{4.26b}$$

4.1.5 Resolution

In this paragraph, following Ref. [203], we detail how Eqs. (4.18), (4.22b) together with Eq (4.23) are gathered into one integro-differential equation that can be solved numerically. We first inject Eq. (4.22a) in Eq. (4.23b), then inject the result in Eq. (4.18) and multiply each side by $12\tilde{r}$, to get:

$$12i\tilde{r}\left[1 + \int_0^\infty \mathrm{d}\tilde{s}\, \frac{\hat{\tilde{p}}^*(\tilde{s})}{8} \left(\frac{H_\mathrm{c}}{H}\right)^{3/2} \hat{\tilde{\mathcal{G}}}^*(s)\tilde{s}J_0(\tilde{s}\tilde{r})\right] = \frac{\mathrm{d}}{\mathrm{d}\tilde{r}}\left[\tilde{r}\left(1+\tilde{r}^2\right)^3 \frac{\mathrm{d}\tilde{p}^*}{\mathrm{d}\tilde{r}}\right]. \tag{4.27}$$

As such, we obtained an equation only on the complex pressure field in real and reciprocal space, respectively $\tilde{p}^*$ and $\hat{\tilde{p}}^*$. By integrating Eq. (4.27) on $\tilde{r}$ between 0 and $\tilde{r}$, and multiplying each side by $\tilde{r}(1+\tilde{r}^2)^3$ we get:

$$\frac{\mathrm{d}\tilde{p}^*}{\mathrm{d}\tilde{r}} = \frac{6i\tilde{r}}{\left(1+\tilde{r}^2\right)^3} + \frac{3i}{2\left(1+\tilde{r}^2\right)^3} \left(\frac{H_\mathrm{c}}{H}\right)^{3/2} \int_0^\infty \mathrm{d}\tilde{s}\, J_1(\tilde{s}\tilde{r})\hat{\tilde{\mathcal{G}}}^*(s)\hat{\tilde{p}}^*(\tilde{s}). \tag{4.28}$$

Finally, by performing a first-order Hankel transform of Eq. (4.28) and multiplying each side by $-1/\tilde{k}$, we obtain an integro-differential equation on $\hat{\tilde{p}}^*$, which is called the Fredholm equation of the second kind:

$$\hat{\tilde{p}}^*(\tilde{k}) = -\frac{3i\tilde{k}}{4}K_1(\tilde{k}) - \frac{3i}{2\tilde{k}}\left(\frac{H_c}{H}\right)^{3/2}\int_0^\infty \mathrm{d}\tilde{s}\,\hat{\tilde{\mathcal{G}}}^*(s)\hat{\tilde{p}}^*(\tilde{s})\int_0^\infty \mathrm{d}\tilde{r}\;\frac{\tilde{r}J_1(\tilde{s}\tilde{r})J_1(\tilde{k}\tilde{r})}{\left(1+\tilde{r}^2\right)^3}, \quad (4.29)$$

where K_n is the modified Bessel function of the second kind of order n. The kernel of the Fredholm equation has an analytical solution [261], given by:

$$\begin{aligned}\int_0^\infty \mathrm{d}\tilde{r}\,\frac{\tilde{r}J_1(\tilde{k}\tilde{r})J_1(\tilde{s}\tilde{r})}{(1+\tilde{r}^2)^3} &= \frac{\tilde{k}^2+\tilde{s}^2}{8}I_1(\tilde{s})K_1\left(\tilde{k}\right) - \tilde{s}\tilde{k}\frac{I_2(\tilde{s})K_2\left(\tilde{k}\right)}{4} \quad \text{for } \tilde{s}<\tilde{k},\\ &= \frac{\tilde{k}^2+\tilde{s}^2}{8}I_1(\tilde{k})K_1\left(\tilde{s}\right) - \tilde{s}\tilde{k}\frac{I_2(\tilde{k})K_2\left(\tilde{s}\right)}{4} \quad \text{for } \tilde{k}<\tilde{s},\end{aligned} \quad (4.30)$$

where I_n is the modified Bessel function of the first kind of order n. Integrals are numerically evaluated with the Gauss-Legendre-quadrature method, described in Appendix C.2.2. The numerical resolution of Eq. (4.29) is based on linear algebra and is detailed in Appendix C.3.

Finally, having solved Eq. (4.29) for the complex pressure field in reciprocal space $\hat{\tilde{p}}(\tilde{k})$, the deformation profile is computed in real space by performing a dimensionless backward Hankel transform, using Eq. (4.22a):

$$\tilde{w}^*(\tilde{r}) = \int_0^\infty \mathrm{d}\tilde{k}\,\hat{\tilde{w}}^*(\tilde{k})\tilde{k}J_0(\tilde{k}\tilde{r}) \quad (4.31a)$$

$$= \int_0^\infty \mathrm{d}\tilde{k}\,\frac{\hat{\tilde{p}}^*(\tilde{k})}{8}\left(\frac{H_c}{H}\right)^{3/2}\hat{\tilde{\mathcal{G}}}^*(s)\tilde{k}J_0(\tilde{k}\tilde{r}). \quad (4.31b)$$

The same calculation path can be used to compute the complex pressure field in reciprocal space:

$$\tilde{p}^*(\tilde{r}) = \int_0^\infty \mathrm{d}\tilde{k}\,\hat{\tilde{p}}^*(\tilde{k})\tilde{k}J_0(\tilde{k}\tilde{r}), \quad (4.32)$$

and the complex deformation profile $\tilde{w}^*(\tilde{r})$ for a purely elastic material, in both the incompressible and compressible cases.

4.1.6 Normal force

In real colloidal-probe experiments, the rheological investigation of gels is made at a controlled angular frequency ω and the spherical probe is placed at a given distance H of the gel. Thus, in an experiment, the dimensionless parameters ω/ω_c and H/H_c are computed, based on the physical parameters of the gel and the solvent (*e.g.* porosity, viscosity...), and the experimental choices of angular frequency ω and distance H. Moreover, the measured experimental quantity is often the total force applied on the probe. Theoretically, the amplitude F^* of the vertical elastohydrodynamic force exerted on the sphere is obtained by integrating the amplitude of the lubrication pressure field over the surface of the sphere, as:

$$F^* = 2\pi\int_0^\infty \mathrm{d}r\,r\,p^*(r). \quad (4.33)$$

From Eq. (4.33) and the typical lubrication pressure scale (see Eq. (4.17)), a typical elastohydrodynamic force scale is $8\pi\eta\omega h_0 R^2/H$. Thus we introduce the following dimensionless force:

$$\tilde{F}^* = \frac{H_c}{8\pi\eta\omega h_0 R^2}F^*, \quad (4.34)$$

which depends on the dimensionless parameters, D/D_c, ω/ω_c, and Λ. Then, the dimensionless force is computed, as:

$$\tilde{F}^* = \frac{H_c}{H}\int_0^\infty \mathrm{d}\tilde{r}\,\tilde{r}\,\tilde{p}^*(\tilde{r}), \tag{4.35}$$

to keep the dependency on the dimensionless parameter H/H_c inside the expression of the dimensionless force as a function of the lubrication pressure field. Recalling the expression of the dimensionless complex pressure in reciprocal space, and using $J_0(0) = 1$, we have:

$$\hat{\tilde{p}}^*(\tilde{s}=0) = \int_0^\infty \mathrm{d}\tilde{r}\,\tilde{p}^*(\tilde{r})\tilde{r}J_0(0\times\tilde{r}) = \int_0^\infty \mathrm{d}\tilde{r}\,\tilde{r}\,\tilde{p}^*(\tilde{r}). \tag{4.36}$$

Finally the complex force is computed without performing an inverse Hankel transform, as:

$$\tilde{F}^* = \frac{H_c}{H}\hat{\tilde{p}}^*(\tilde{s}=0). \tag{4.37}$$

The complex force can be calculated in both the cases of purely incompressible and compressible elastic materials using the same method.

4.1.7 Results and discussion

Examples of the obtained surface deformation and pressure fields are plotted in Fig. 4.2(a) and (b) respectively, for various sphere-substrate distances. In a contactless colloidal-probe rheological experiment, however, it is not the deformation amplitude that is typically measured. Rather, the sampled surface slowly approaches the oscillating spherical probe using a piezo stage, with the typical experimental outputs being the measured force amplitude and phase as functions of the sphere-substrate distance. Thus in Fig. 4.2(c) and (d) are plotted the theoretically obtained force amplitude and phase shift, respectively, for various oscillation frequencies. The other parameters are kept constant. From the amplitude and phase, the real and imaginary components of the complex force can be evaluated, the amplitude and phase being the modulus and the argument, respectively, of the complex force. These force components and the amplitude of the pressure field can be evaluated numerically, using Eq. (4.37). Therefore, in Fig. 4.2(e), we plot the dimensionless, real and imaginary parts of the force, as a function of the dimensionless distance, for various oscillation angular frequencies.

Two regimes can be observed, based on the probe-gel distance. At large distance, *i.e.* $H/H_c \gg 1$, the surface deformation is small with respect to the oscillation amplitude (see Fig. 4.2(a)). As a result, the elastohydrodynamic coupling is weak, and the force is dominated by the viscous dissipation in the liquid film. In the far-field asymptotic regime, we observe that the modulus of the complex force (*i.e.* the amplitude) decays as a power law with a -1 exponent in H/H_c. Additionally, we observe that the imaginary part of the complex force, which corresponds to the dissipative force, decays as a power law with a -1 exponent in H/H_c too. To explain the observed power-law decay, we can multiply each side of Eq. (4.12) by $12\eta r$ and integrate between 0 and r in the absence of substrate deformation ($w^* = 0$). Multiplying by $r\left(H + \frac{r^2}{2R}\right)^3$ on each side, we obtain:

$$6i\eta\omega h_0 \frac{r}{H^3\left(1+\frac{r^2}{2RH}\right)^3} = \frac{\mathrm{d}p^*_{\mathrm{rigid}}}{\mathrm{d}r}. \tag{4.38}$$

By integrating Eq. (4.38) between r and ∞ we then obtain the complex pressure field

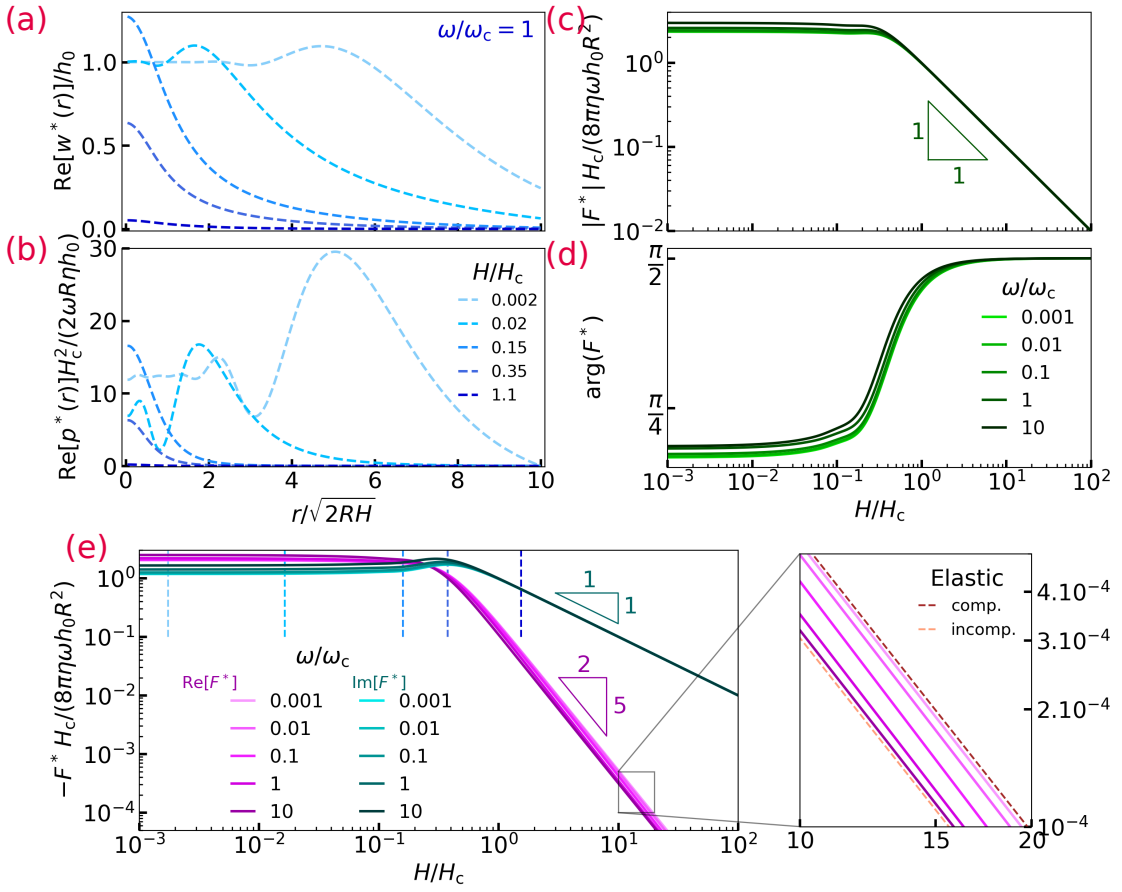

FIG. 4.2. **Mechanical response of a poroelastic gel in the contactless colloidal-probe configuration.** *(a): Normalized amplitude w^*/h_0 of the surface deformation profile as a function of the rescaled radial coordinate $r/\sqrt{2RH}$, for various normalized sphere-substrate distances, as computed from Eq. (4.31b) with $\omega/\omega_c = 1$ and $\nu = 0.1$. (b): Normalized pressure $p^*H_c^2/(2\omega R\eta h_0)$ applied on the surface deformation profile as a function of the rescaled radial coordinate $r/\sqrt{2RH}$, for the same various normalized sphere-substrate distances as in (a), as computed from Eq. (4.32) with $\omega/\omega_c = 1$ and $\nu = 0.1$. (c): Amplitude of the normalized force $F^*H_c/(8\pi\eta\omega h_0 R^2)$ exerted on the spherical probe as a function of the normalized sphere-substrate distance, for various reduced angular frequencies ω/ω_c. (d): Phase of the normalized force exerted on the spherical probe as a function of the normalized sphere-substrate distance, for the same various reduced angular frequencies. (e): Real (pink) and imaginary (blue-green) parts of the normalized force $F^*H_c/(8\pi\eta\omega h_0 R^2)$ exerted on the spherical probe as functions of normalized sphere-substrate distance, for the same various reduced angular frequencies, as computed from Eq. (4.37) with $\nu = 0.1$. The vertical dashed blue lines correspond to the distances at which the surface deformation profiles are plotted in (a). The zoomed inset shows the purely elastic incompressible case (orange) and the purely elastic compressible case (red).*

generated by a sphere oscillating at a distance H of a rigid boundary:

$$p^*_{\mathrm{rigid}}(r) = -\frac{3i\eta\omega h_0 R}{H^2\left(1+\frac{r^2}{2RH}\right)^2}. \tag{4.39}$$

Finally by integrating Eq. (4.39) between 0 and ∞, we recover the classical confined

Stokes drag:

$$F^*_{\text{Stokes,confined}} = -\frac{6i\pi\eta h_0 \omega R^2}{H_c}\frac{H_c}{H}, \tag{4.40}$$

which decays as the observed power law [67]. Thus, when probing a poroelastic sample, in the far-field regime the force is dominated by its imaginary part, which is the classical Stokes drag. The real part of the force amplitude in the far field is much smaller than the imaginary part and decays as a power law with a $-5/2$ exponent in H/H_c. To explain this observation, we refer to the case of a purely elastic and incompressible medium probed by an oscillating sphere. The dimensionless Green's function of the problem is $\hat{\mathcal{G}}^*_{\text{incomp}}(\tilde{s}) = 1/\tilde{s}$. We then compute the limit of the dimensionless complex pressure field, given by Eq. (4.29), when $\tilde{k} \to 0$, and get:

$$\hat{\tilde{p}}^*_{\text{incomp}}(0) = -\frac{3i}{4} - \frac{3i}{32}\left(\frac{H_c}{H}\right)^{3/2}\int_0^\infty \mathrm{d}\tilde{s}\,\hat{\tilde{p}}^*(\tilde{s})\tilde{s}K_1(\tilde{s}), \tag{4.41}$$

such that the complex force reads with Eq.(4.37):

$$\tilde{F}^*_{\text{incomp}}(0) = -\frac{3i}{4}\left(\frac{H_c}{H}\right) - \frac{3i}{32}\left(\frac{H_c}{H}\right)^{5/2}\int_0^\infty \mathrm{d}\tilde{s}\,\hat{\tilde{p}}^*(\tilde{s})\tilde{s}K_1(\tilde{s}). \tag{4.42}$$

We recover in the first term the Stokes drag while the prefactor of the second term shows explicitly $(H/H_c)^{-5/2}$. With the choices of scaling detailed in Sec. 4.1.3, the integral over the complex pressure field does not scale as a power of H/H_c. Additionally, thin-film equation associated to the linear response theory given in Eq. (4.12) ensures that the complex pressure field is dominated by its imaginary part. Thus, the real part of the complex force, which corresponds to the conservative force, displays a signature of the elasticity of the substrate through an asymptotic decay with the distance as $\sim (H/H_c)^{-5/2}$. The exact prefactor of this scaling law can be obtained by expanding the solution in (H_c/H) [203, 263].

At small distance, *i.e.* $H/H_c \ll 1$, the substrate deformation saturates and scales with the oscillation amplitude (see Fig. 4.2(a)). As a consequence, the real and imaginary parts of the force amplitude saturate as well to values that do not depend on the distance. The inset of Fig. 4.2(e) represents a zoom on the dimensionless, real part of the force, and we additionally plot the force obtained in the purely elastic incompressible and compressible cases. At small frequency, the elastohydrodynamic coupling is similar to the one of a purely elastic compressible layer; conversely, at large frequency, the elastohydrodynamic coupling is similar to the one of a purely elastic incompressible layer.

Finally, in these scaled variables, we observe a small influence of the solvent diffusion in the gel on the elastohydrodynamic coupling, despite the diffusion constant being varied over 4 orders of magnitude (via the critical frequency). Therefore, from our model, it appears that contactless colloidal-probe rheological methods in the linear-response regime are not appropriate to robustly measure the effects of the solvent diffusion through the gel network. In contrast, such methods appear to be well suited for measuring the effective shear elastic moduli and Poisson ratios of gels. In the next section, we present preliminary results of contactless colloidal-probe experiments on soft and swollen hydrogels.

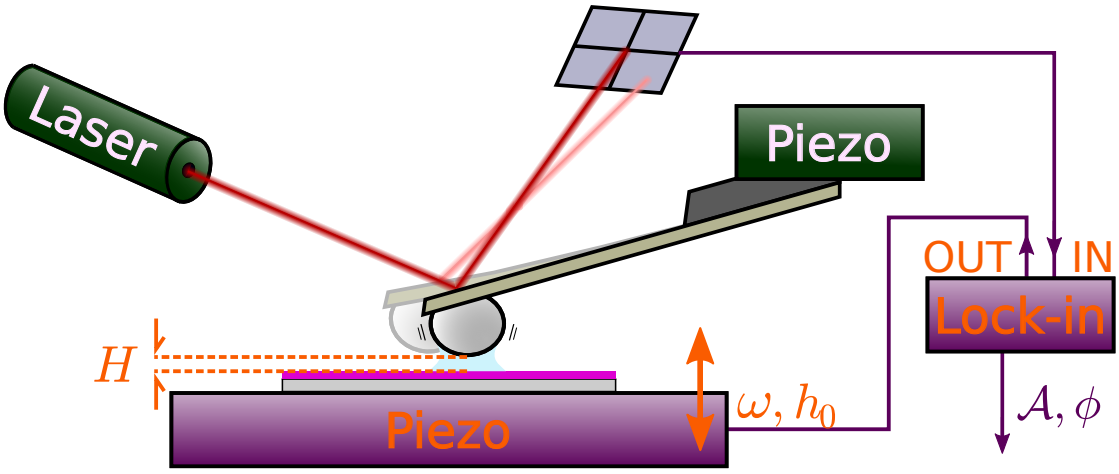

FIG. 4.3. **Colloidal-probe AFM based setup to probe swollen hydrogels in contactless mode.** *A swollen hydrogel sample is deposited on a stage in contact with a piezo element. A colloidal probe held by an AFM cantilever is brought at a distance H to the free surface of the hydrogel. A laser beam pointed on the cantilever extremity is reflected by the latter, and the reflected beam is sent to a four-quadrant photodiode. The motion of the probe is measured by monitoring the signal of the photodiode. A lock-in amplifier sends a harmonic signal (OUT) and thus generates the vertical, oscillatory motion of the piezo under the stage, at an angular frequency ω and with an amplitude h_0. Simultaneously, the lock-in amplifier receives the signal from the photodiode (IN) and thus measures the vertical, oscillatory motion of the colloidal probe. A simultaneous comparison is made between the in and out signals, and with the lock-in amplifier giving an amplitude $\mathcal{A}$ (see Eq. (4.50)) of the modulated signal and a phase shift ϕ (see Eq. (4.51)), that are recorded with time.*

4.2 Preliminary experiments

In this section we describe preliminary experimental results on soft hydrogels obtained with a colloidal-probe AFM based setup [1]. This setup was developed based on the theoretical ideas of the oscillatory colloidal-probe experiments described in the first part of the present Chapter. A custom stage was build to meet the special requirements of the oscillatory rheology on an AFM. The fabrication protocol of thick PNIPAM hydrogels described in Chapter 2 was used to make a thick hydrogel, as a test sample.

4.2.1 Experimental setup

A schematic of the experiment is presented in Fig. 4.3. An already existing Atomic Force Microscope (*Nanosurf CoreAFM*) was adapted to enable an oscillatory experimental mode. The standard AFM used to realize topographic measurements was described in Chapter 2. In contrast, here we first describe the colloidal-probe AFM used to perform force measurements, then we present the adaptation work done on the apparatus.

Colloidal-probe AFM: The standard AFM is described in Chapter 2. In the experiment described here, home-made colloidal probes are used instead of cantilevers with

[1] The theoretical development described in the first part 4.1 of the present Chapter is published [251], with the article included in Appendix E. The experimental work described in the present section is not published yet, but constitutes the experimental situation fitting the theoretical development of the previous section.

sharp tips. A silica sphere of $R \approx 45\,\mu$m is glued with epoxy resin on the edge of a tip-less, triangular-shaped cantilever. The obtained colloidal probes are then placed on the cantilever holder as standard probes.

Oscillatory mode: The AFM is then adapted. On the one hand, a piezo element (named "*the cube*" due to its cubic shape, of about 2 cm each side) able to move in the three directions of space is used as a stage on which the sample is held. A sinusoidal electric signal is sent (OUT) to this piezo element through an amplifier (not represented here) to generate its motion. On the other hand, the sinusoidal signal received (IN) from the 4-quadrant photodiode of the AFM is monitored through the AFM controller (not represented here). A lock-in amplifier compares simultaneously the IN and OUT signals. A product of amplitudes $\mathcal{A}$ and a phase shift ϕ between the two signals are extracted, as measured quantities.

4.2.2 Calibrations

To convert the amplitude of electric signals into forces and distances, several calibration steps are performed.

4.2.2.1 Cantilever stiffness

The probes used in the experiment presented in this Chapter are commercialized by *Bruker*, model *NP-O10*, four V-shaped tip-less cantilevers, in silicon nitride with a reflective gold coating. We use the cantilever noted D on the chip (see a picture in Fig 4.4(c)), whose nominal resonance frequency in air and stiffness are $f_{0,\mathrm{nom}} = 18 \pm 6\,$kHz and $k_{\mathrm{canti,nom}} = 0.06 \in [0.3; 0.12]$ N/m.

For the experiment described here, and when using home-made colloidal probes, the cantilever stiffness is measured experimentally with the method of the added mass [264], that we describe in the following. Before gluing the silica sphere (see a picture of colloids in Fig. 4.4(d)) on the edge of the tip-less cantilever, the deflection of the latter due to its thermal noise is recorded and averaged over several measurements. The Brownian motion of the cantilever is described by modeling the cantilever as a damped harmonic oscillator to which a Langevin force is applied. Then, by solving the Langevin equation for a damped harmonic oscillator, one can derive the power spectral density of the cantilever deflection Z^*_{canti} in the steady-state regime [225], as:

$$\left|\frac{\mathrm{d}Z^*_{\mathrm{canti}}}{\mathrm{d}\omega}\right| = \frac{k_{\mathrm{B}}T}{\pi m^2_{\mathrm{canti}}} \frac{\omega_0 Q_0}{Q_0^2(\omega_0^2-\omega^2)^2 + \omega_0^2\omega^2}, \tag{4.43}$$

with * indicating a complex variable, ω the angular frequency, ω_0 the resonance angular frequency, Q_0 the quality factor, m_{canti} the effective mass of the cantilever, k_{B} the Boltzmann constant and T the room temperature [2]. The amplitude spectral density A_ω is then defined from Eq. (4.43) by taking the square root :

$$A_\omega(\omega) = \sqrt{\left|\frac{\mathrm{d}Z^*_{\mathrm{canti}}}{\mathrm{d}\omega}\right|}. \tag{4.44}$$

The measured amplitude spectral density of the cantilever is fitted with Eq. (4.44). The resonance frequency $f_0 = \omega_0/(2\pi)$ and quality factor Q_0 are extracted as fitting parameters. Then, a micrometric silica sphere is glued at the edge of the cantilever and the thermal noise of the cantilever is recorded again. The resonance frequency f_1 and

[2] The present calibration step is also detailed in Sec. 2.1.2.3

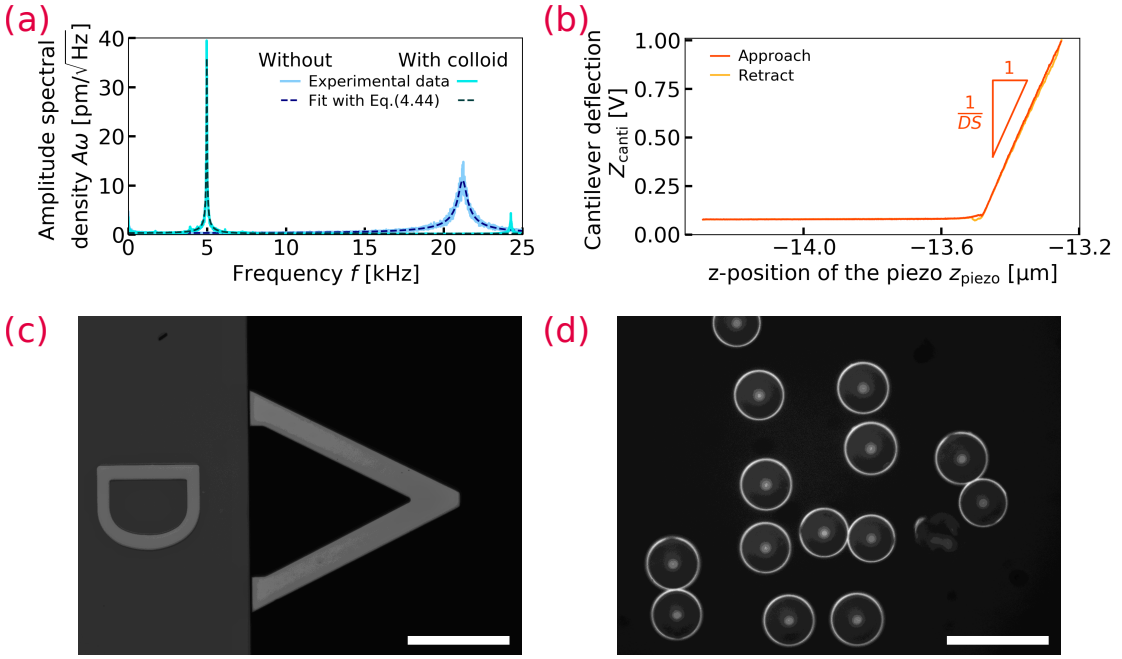

FIG. 4.4. **Calibration of the AFM**. *(a): Amplitude spectral density A_ω of the cantilever as a function of the temporal frequency f, before (light blue) and after (light blue-green) gluing a silica sphere at its edge. Dark blue and dark blue-green lines correspond to fits of the experimental data based on Eq.* (4.44)*, before and after gluing the colloid respectively. (b): Deflection Sensitivity DS measurement. The signal received by the photodiode, which corresponds to the cantilever deflection Z_{canti} in V, is plotted as a function of the position of the driving piezo z_{piezo}. The final part of the curve corresponds to the range where the cantilever is in contact with the hard surface. The deflection sensitivity DS is computed as the inverse of the slope. (c): Picture of a cantilever, of the same model as the one used in the present experiment. (d): Picture of a few colloids spread on a glass slide, from the same batch as the one used in the present experiment. (c) and (d) were made with an inverted microscope (×20). The scale bar represents* 100 µm *in both panels.*

quality factor Q_1 of the cantilever holding a colloid are extracted too. In Fig. 4.4(a) is shown the spectrum of the Brownian motion amplitude of the cantilever, with and without the attached sphere.

The cantilever being modeled as an harmonic oscillator, the resonance frequencies before and after gluing the silica sphere are given respectively by [264]:

$$f_0 = \frac{1}{2\pi}\sqrt{\frac{k_{\text{canti}}}{m_{\text{canti}}}} \quad \text{and} \quad f_1 = \frac{1}{2\pi}\sqrt{\frac{k_{\text{canti}}}{m_{\text{canti}} + m_{\text{sphere}}}}, \tag{4.45}$$

with k_{canti} the stiffness of the cantilever and m_{sphere} the mass of the sphere. The cantilever stiffness is then calculated by:

$$k_{\text{canti}} = (2\pi)^2 \frac{m_{\text{sphere}}}{\frac{1}{(f_1)^2} - \frac{1}{(f_0)^2}}. \tag{4.46}$$

The quality factors provide estimates of the errors on the resonance frequencies:

$$\Delta f_0 = \frac{f_0}{2Q_0} \quad \text{and} \quad \Delta f_1 = \frac{f_1}{2Q_1}. \tag{4.47}$$

The errors Δf_0 and Δf_1 extracted from the width of the distributions defined by the amplitude spectral densities A_ω are usually slightly overestimated, as the width of the distributions is harder to fit than the maxima f_0 and f_1 to locate. Then, the errors on the resulting stiffnesses can be calculated too. Knowing the radius of the sphere ($R = 45 \pm 3\,\mu$m, see Fig. 4.4(d)) and the silica density ($\rho_{\text{Si}} = 2.950\,\text{g/cm}^3$), the sphere mass is evaluated to be 140 ± 23 ng. We neglect the mass of the glue, estimated at 0.1 ng at the maximum. With the added-mass method [264] described in the present section, we measure a stiffness of $k_{\text{canti}} = 0.14 \pm 0.02\,\text{N/m}$, which is slightly above the maximal nominal value but still meaningful. The obtained cantilever stiffness k_{canti} is used to convert the deflection of the cantilever (in nm) into the force exerted of the spherical probe (in nN). The deflection measurement is thus described in the following subsection.

4.2.2.2 Deflection sensitivity

In AFM, the deflection sensitivity DS is used to convert the signal received from the photodiode (in V) into the deflection of the cantilever Z_{canti} (in nm) [3]. The deflection sensitivity is measured by approaching the cantilever close to a hard surface, touching the surface, and then continuing the approach until a prescribed limit deflection is reached. The cantilever is then fully retracted. The measurement is typically repeated ten times. The vertical signal of the photodiode (*i.e.* the cantilever deflection Z_{canti} up to a factor, but in V) is monitored as a function of the position of the piezo z_{piezo}. A linear relation between the signal of the photodiode and the piezo position is typically obtained when the cantilever is in contact with the hard surface, and the coefficient between both corresponds to the deflection sensitivity DS in nm/V. Figure 4.4(b) shows a typical measurement of the signal of the photodiode Z_{canti} (*i.e.* the cantilever deflection but in V) as a function of the vertical position of the piezo z_{piezo}. In this example, the calculated deflection sensitivity is 254 nm/V based on a good quality fit ($\chi^2 = 0.009$). In practice, the measurement of the deflection sensitivity is automated by the AFM software, repetitions and averaging included. The product of the deflection sensitivity by the cantilever stiffness $DS\,k_{\text{canti}}$ enables to convert the voltage signal of the photodiode into a force.

4.2.2.3 Extraction of Amplitude and phase shift with the lock-in amplifier

As depicted in Fig. 4.3, we generate a sinusoidal signal U_{OUT} from the lock-in amplifier that is sent to the piezo cube. The sinusoidal signal U_{IN} is received from the photodiode. The two signals read:

$$U_{\text{OUT}} = a_{\text{out}} \cos(\omega t) + u_{\text{out}} \tag{4.48a}$$

$$U_{\text{IN}} = a_{\text{in}} \cos(\omega t + \phi) + u_{\text{in}}, \tag{4.48b}$$

with $\omega = 2\pi f$ the angular frequency, a_{out} and a_{in} the amplitudes (in V) of the OUT and IN signals respectively, ϕ the phase shift. The lock-in amplifier (*Zurich Instruments, MFLI 500 kHz*) is used to compare simultaneously both the signals sent to the piezo U_{OUT} and the signal received from the photo diode U_{IN}. To compare both the IN and OUT signals, the lock-in amplifier computes the modulated signal U_{MOD} as:

$$U_{\text{MOD}} = a_{\text{out}} a_{\text{in}} \cos(\omega t)\cos(\omega t + \phi) = \frac{a_{\text{out}} a_{\text{in}}}{2}\left[\cos(2\omega + \phi) + \cos(\phi)\right]. \tag{4.49}$$

In Fig. 4.5(a) we show an example of the OUT, IN and modulated signals, respectively U_{OUT}, U_{IN} and U_{MOD}, on a few periods. The mean values of the OUT and IN signals,

[3] This step was already detailed as is in Sec. 2.1.2.3

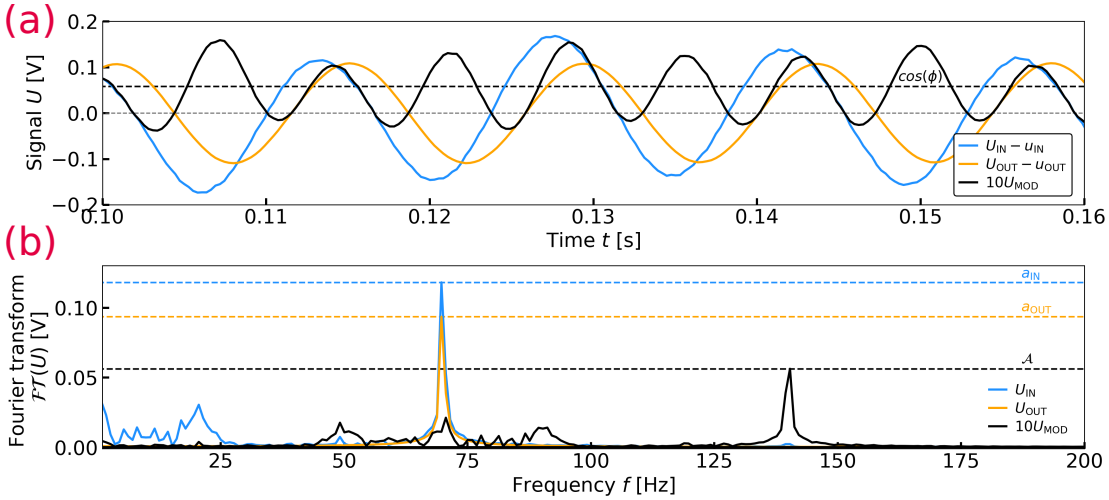

FIG. 4.5. **Raw sinusoidal signals compared by the lock-in amplifier**. *(a): Oscillating part of the OUT and IN sinusoidal signals, respectively* U_{OUT} *and* U_{INT}*, respectively sent to cube and received from the photodiode, as a function of time* t*. The modulated signal* U_{MOD} *is computed from the IN and OUT signals, and represented with a factor 10 for more readability. The phase shift is extracted from the mean value of the modulated signal, through Eq.* (4.51)*. (b): Fourier transforms of the signals shown in (a). The amplitudes of the respective peaks of the* U_{IN}*,* U_{OUT} *and* U_{MOD} *signals are linked by Eq.* (4.50)*.*

respectively u_{OUT} and u_{IN}, are subtracted for a better readability. Then, the amplitude $\mathcal{A}$ is obtained by computing the Fourier transform of the modulated signal and taking the intensity of the peak at the angular frequency 2ω:

$$\mathcal{A} = \frac{a_{\mathrm{out}} a_{\mathrm{in}}}{2} \tag{4.50}$$

and the cosine of the phase shift ϕ is obtained, by taking the average value of the modulated signal, as:

$$\cos(\phi) = \frac{< U_{\mathrm{MOD}} >}{\mathcal{A}}. \tag{4.51}$$

In Fig. 4.5(b), we show the Fourier transforms of the examples of OUT, IN and modulated signals. In practice, the amplitude a_{out}, mean value u_{out} and angular frequency ω of the OUT signal are prescribed by the low-frequency generator function of the apparatus. The amplitude of the IN signal a_{in} is directly monitored by using the scope function of the apparatus. The phase shift ϕ is finally computed by the apparatus.

4.2.2.4 Cube calibration

The calibration of the piezo element (*Piezosystem Jena, microTRITOR*) which plays the role of the sample stage consists in establishing the relation between the command electric signal U_{OUT} sent to the latter and its induced displacement. This measurement is performed with a standard cantilever with a sharp tip (*Nanosurf*, model *Dyn190Al*, $f_{0,\mathrm{nom}} = 190\,\mathrm{kHz}$ and $k_{\mathrm{canti,nom}} = 48\,\mathrm{N/m}$). The deflection sensitivity DS with the chosen cantilever is measured first of all. Then the cantilever is approached in contact mode close to the surface of the piezo cube, up to contact, with a set point in force at $10 - 50\,\mathrm{nN}$, forcing a deflection of the cantilever to maintain contact at any time. When

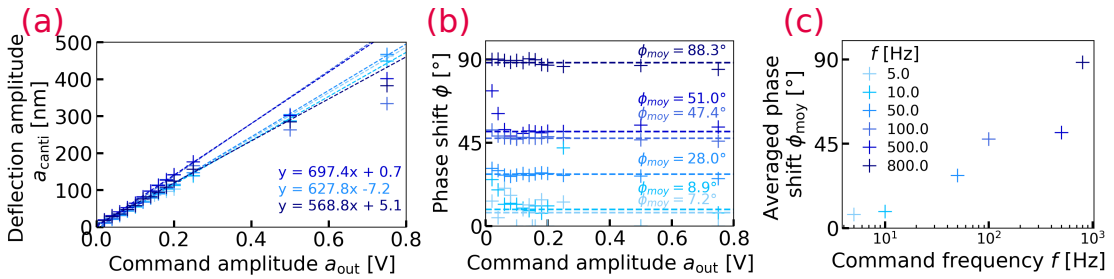

FIG. 4.6. **Calibration of the piezo cube**. *(a): Amplitude of the oscillating cantilever deflection Z_{canti} as a function of the driving amplitude a_{out} of the electric signal OUT sent to the piezo cube, for different driving frequencies f. Depending on the driving frequency f, we obtain a factor of $0.56 - 0.7\,\mu$m/V between the command tension amplitude a_{out} and the driving oscillation amplitude h_0. (b): Phase shift ϕ as a function of the command tension amplitude a_{out}. Depending on the driving frequency f, we measure a phase shift ϕ between the command signal U_{OUT} and the oscillation of the cube $h_0 \cos(\omega t)$. (c): Averaged phase shift ϕ_{moy} as a function of the driving frequency f.*

contact is established, the AFM feedback is turned off, so that the cantilever response is only due to the oscillation of the piezo cube.

The cantilever deflection is given by $Z_{\text{canti}} = DS\,U_{\text{IN}}$ in nm, with U_{IN} the electric signal received from the photodiode. The cantilever deflection follows the motion of the piezo cube. Considering only the oscillating term, we have:

$$Z_{\text{canti}} - < Z_{\text{canti}} >= a_{\text{canti}} \cos(\omega t + \phi) = h_0 \cos(\omega t + \phi), \tag{4.52}$$

with $h_0 = DS\,a_{\text{in}}$ the oscillation amplitude of the cube (in nm), ϕ the phase shift, and $< Z_{\text{canti}} >= DSu_{\text{in}}$ the mean value of the cantilever position. Figure. 4.6(a) shows the oscillation amplitude of the cantilever deflection a_{canti}, which is equal to h_0 as long as both the cantilever and the cube are in contact, as a function of the amplitude of the command signal a_{out}, for different driving frequencies f. We obtain a linear relation, with a slope that slightly varies depending on the driving frequency f. This measurement gives the conversion between the amplitude a_{out} of the command signal in V sent to the cube and the resulting motion amplitude of the cantilever a_{canti} in nm. We obtain a factor between the amplitude of the command signal a_{out} and the cantilever motion amplitude h_0 of $0.56 - 0.7\,\mu$m/V, depending on the driving frequency f.

The comparison between the IN and OUT signals by using the lock-in amplifier reveals a phase shift ϕ that depends on the frequency f. On Fig. 4.6(b) is plotted the phase shift ϕ as a function of the amplitude of the command signal a_{out} for different frequencies f. We observe that the phase shift does not depend on the amplitude a_{out} but only on the frequency f. Thus on Fig. 4.6(c) is plotted the averaged phase shift ϕ_{moy} as a function of the driving frequency f.

The precise origin of the phase shift is not known and should be investigated rigorously in the future of this project. The piezo cube has a resonance frequency around 1 kHz, which means that the oscillation amplitude should depend on the frequency. Furthermore, the signal U_{OUT} is first sent to an amplifier (not represented on Fig. 4.1), then the amplified signal is sent to the piezo cube. Both the amplifier and the piezo itself may introduce phase shifts depending on the frequency. Finally, the sample is attached onto the piezo cube with double-face tape. The glue of the tape itself may also introduce a phase shift depending on the frequency.

4.2.3 Experimental protocol

In this section, we describe the protocol to run an experiment to probe the mechanical response of a soft and hydrated poroelastic hydrogel, for a given oscillation amplitude h_0 at a given frequency f.

Calibration: The preparation of the spherical probe and the measurement of the cantilever stiffness k_{canti} constitute the first steps of calibration, followed by a deflection sensitivity DS measurement (on a hard surface, no sample) of the AFM scan head. At the chosen frequency f is associated the calibration curve of the piezo cube, which gives the coefficient between the electric signal amplitude a_{out} that is sent and the motion amplitude h_0 that results. The intrinsic phase shift ϕ_{moy} associated to the cube at the frequency f is also noted. Both the IN and OUT signals and the phase shift are monitored.

Initialization: In order to use the semi-infinite poroelastic half space model presented in the previous Chapter, a thick (the swollen thickness should be large compared to the hydrodynamic radius) hydrated gel is placed on the piezo cube. A high offset u_{out} ($= 5 - 8\,\text{V}$), with a zero amplitude a_{out} are set to begin the experiment. Using the standard functions of the AFM, at a low set point in force ($\approx 5\,\text{nN}$) and in static mode, the probe is brought in contact with the gel. Then the offset of the command signal U_{OUT} is turned down to typically $\approx -5\,\text{V}$ to drive away the cube, and the amplitude a_{out} is set to obtain the chosen value h_0 of its motion amplitude. At this stage of the experiment the IN signal should be almost zero, since the coupling between the probe and the gel is weak when both are far away from each other.

Approach: The experiment is run varying the offset of the OUT signal u_{OUT}. For a given a_{OUT}, samplings of both the IN and OUT signals are recorded, for a given value of offset u_{OUT}. The amplitude $\mathcal{A}$ and phase shift ϕ of the modulated signal are extracted. The signals are recorded with special care to choose an adapted sampling rate (at least 20 measurement points by period) and a sufficient duration time (at least 50 periods) to collect enough information, without excess. The measurement is repeated for a range of offsets u_{OUT}, typically from the initial -5 V value to $5 - 8$ V. The range in offsets corresponds to a range in distances, from large distances (almost no interaction sphere-cube) to small distances (contact), compared to the typical height at which the probe and the gel interact. Thus, varying the offsets realizes an approach of the cube holding the sample towards the spherical probe.

Extracting the raw data: The oscillation amplitude of the cantilever a_{canti} is computed from the signal of the photodiode by $DS\,a_{\text{in}}$. The phase shift ϕ is directly monitored through the lock-in amplifier software. The absolute height of the piezo cube is deduced from the calibration described in Sec. 4.2.2.4. The initialization and approach steps are finally repeated for each desired frequency f.

4.2.4 Preliminary results

4.2.4.1 Raw data

In Fig. 4.7 we show preliminary results of contactless, colloidal-probe experiments in oscillatory mode on a hydrated PNIPAM hydrogel film (dry thickness $\tau = 300\,\text{nm}$, swollen thickness $\tau_{\text{swollen}} = 4\tau = 1.2\,\mu\text{m}$, Appendix. A.2 for the thickness measurement),

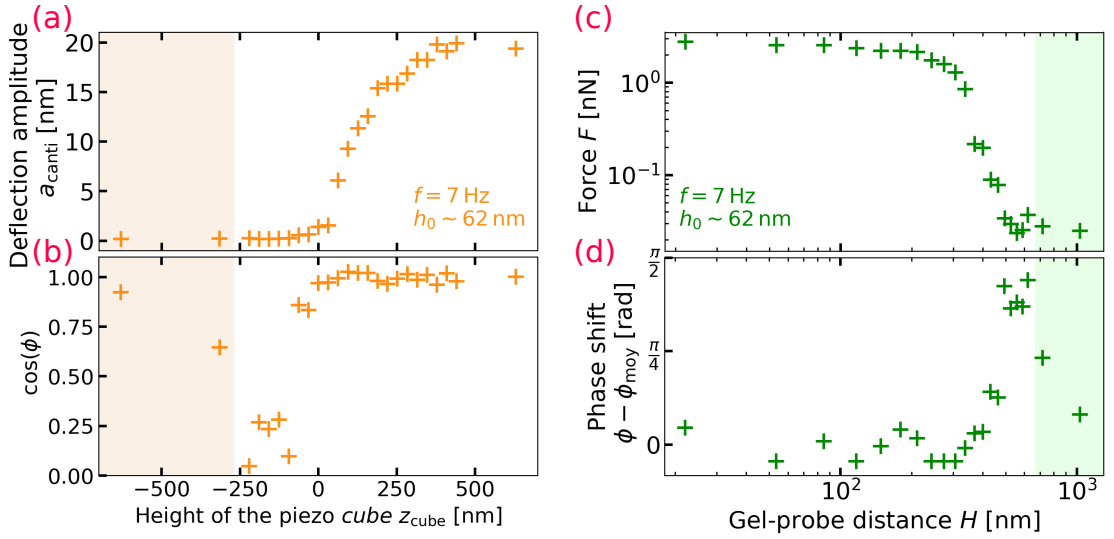

FIG. 4.7. **Raw data of contactless rheology obtained in oscillatory contactless mode on a soft and thick hydrogel.** *(a): Amplitude of AFM cantilever deflection* a_{canti} *as a function of the piezo cube height* z_{cube}*, choosing an oscillation frequency of* $f = 7\,\text{Hz}$ *and an oscillation amplitude of* $h_0 \approx 62\,\text{nm}$*. The colored region indicates the noise floor. (b): Cosine of the phase shift* $\cos(\phi)$ *between the IN and OUT signals, sent to the piezo cube and received from the AFM photodiode respectively, as a function of the piezo cube height* z_{piezo}*. The colored region indicates the noise floor. (c): Amplitude of the force* F *exerted on the spherical probe as a function of the distance between the probe and the gel surface* H*. The colored region indicates the noise floor. (d): Phase shift* ϕ *between the IN and OUT signals, corrected by the average phase shift* $\phi_{\text{moy}} = 8°$ *measured during the piezo cube calibration, as a function of the gel-probe distance.The colored region indicates the noise floor.*

for a driving frequency $f = 7\,\text{Hz}$ and a driving amplitude $a_{\text{out}} = 100\,\text{mV}$ (*i.e.* an oscillation amplitude $h_0 \gtrsim 62\,\text{nm}$). Figure. 4.7(a) and (b) show the oscillation amplitude of the cantilever a_{canti} and the cosine of the frequency shift ϕ between the IN and OUT signals, respectively, as a function of the cube height z_{cube}. The raw data exhibit a transition between two regimes depending on the piezo cube height. At small height, the probe is far from the sample and the elastohydrodynamic coupling between both is weak. As a result the cantilever deflection amplitude (at the driving angular frequency ω) is close to zero. The measured cantilever motion is dominated by white noise and thus the cosine of the phase shift $\cos(\phi)$ takes random values. At larger height the opposite is observed: the cantilever deflection amplitude increases sharply at the transition until reaching a plateau value at $a_{\text{canti}} \approx 20\,\text{nm}$ for $z_{\text{cube}} \gtrsim 400\,\text{nm}$. A similar behavior is observed on the cosine of the phase shift: after a sharp transition with increasing the cube height, a plateau is reached at $\cos(\phi) \lesssim 1$.

Such saturating behaviors are interpreted as the physical contact being established between the surface of the gel and the probe. In the limit of large heights, the amplitude of the cantilever deflection matches the one of the gel surface. Both the probe and the cube oscillate in phase, which means that in the gel elasticity dominates over viscous dissipation. The amplitude of the cantilever deflection is still lower than the one of the piezo cube, when the probe touches the gel surface. This is due to the gel elasticity that “absorbs" the harmonic forcing of the probe on its surface. Indeed, by considering one oscillation of the cube, at the lowest point the forcing on the cantilever is weaker. Thus,

the resulting force applied on the gel is lower than at the highest point. As a result, the gel exhibits a smaller strain at the lowest point of the cube than at the highest, due to its elasticity. This explains why the amplitude of the cantilever deflection (*e.g.* the amplitude of the surface deformation) is still lower than the one of the piezo cube (*e.g.* the imposed amplitude of motion at the bottom of the gel).

4.2.4.2 Contact point estimate

The observed saturation allows to estimate the contact height at $z_{\text{cube}} \approx 400\,\text{nm}$. The mean gel-probe distance can then be deduced as $H = 400 - z_{\text{cube}}$. Using the cantilever stiffness k_{canti}, the amplitude of the force F applied on the probe is deduced from the cantilever deflection amplitude a_{canti}. Thus in Fig. 4.7(c) and (d) the force amplitude F and the phase shift $\phi - \phi_{\text{moy}}$ between the oscillation of the cube and the one of the probe, respectively, are represented as functions of the gel-probe distance H. The correction of $\phi_{\text{moy}} = 8°$ on the phase shift comes from the non-zero phase shift between the IN signal sent to the piezo cube and its oscillatory motion, measured as a function of the frequency (see Fig. 4.6(c)). At small distances H_{c}, the force amplitude reaches a plateau value at $F \approx 3\,\text{nN}$ and the phase ϕ is small. The elastohydrodynamic coupling between the probe and the gel is strong, and the low values of the phase shift indicate a regime where elasticity dominates, as predicted by theory in Sec. 4.1.7. At large distances, the measured force is on the order of the typical resolution of the instrument ($F = 0.1 - 1\text{pN}$) and the phase shift takes random values: the coupling is weak and the force is lower than what the instrument is able to measure. The crossover between the short- and large-distance regimes is exhibited by a sharp transition on both the force and the phase shift. In the transition window ($H_{\text{c}} = 300 - 700\,\text{nm}$), the phase shift rapidly saturates at $\phi \lesssim \pi/2$ with increasing H_{c}, indicating that viscous dissipation dominates as predicted by theory in Sec. 4.1.7. The force decreases rapidly until reaching the limit of the AFM resolution.

In summary, the dissipative, large-distance regime is observed for $H_{\text{c}} \gtrsim 500\,\text{nm}$. However, in this regime, the measurement of the elastohydrodynamic coupling is limited by the resolution in force of the instrument, thus, the measured values of both the force and the phase shift are irrelevant for $H_{\text{c}} \gtrsim 700\,\text{nm}$. The limitations of the AFM being taken into account, the representations of both the force amplitude F and the phase shift ϕ shown in Figs. 4.7(c) and (d) are then reminiscent of the theoretical predictions shown in Figs. 4.2(c) and (d). In the next section we will investigate how the experimentally imposed frequency changes the force response, and will additionally investigate the conversion of the amplitude and phase shift into storage and loss components of the mechanical response, also in comparison to the theory of Sec. 4.1.

4.2.4.3 Different responses as functions of the frequency

The experimental protocol described in Sec. 4.2.3 was repeated for different driving frequencies. From the obtained raw data, we estimate the contact point, applying the process described in the previous subsection. In Fig. 4.8(a) and (c) we show the measured deflection amplitude of the cantilever a_{canti} as a function of the gel-probe distance H for different frequencies f. In Fig. 4.8(b) and (d) we show the phase shift between the oscillatory motions of the piezo cube and of the cantilever $\phi - \phi_{\text{moy}}$ as a function of the gel-probe distance H for different frequencies f. In linear scale in Figs. 4.8(a) and (b), by definition of H the contact point is estimated as $H = 0$. Then, the negative distances correspond to the regime where the probe is always in contact with the gel. This regime does not appear in logarithmic scale in Figs. 4.8(c) and (d).

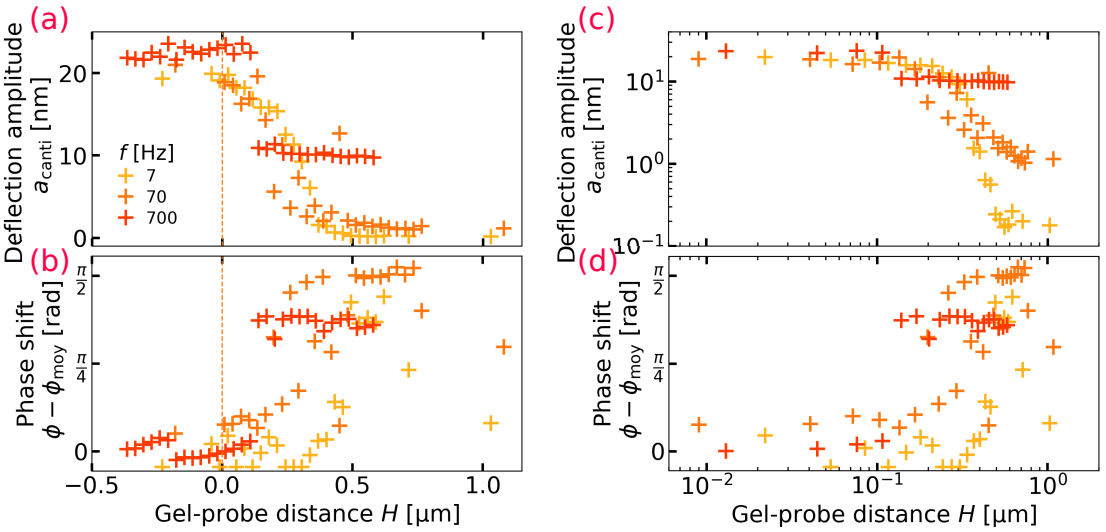

FIG. 4.8. **Frequency-dependent, mechanical response of a hydrogel in oscillatory contactless mode** *(a): Cantilever deflection amplitude* a_{canti} *as a function of the gel-probe distance* H*, for three frequencies of oscillation* f *indicated in legend, in linear scale. The vertical orange dashed line at* $H = 0$ *represents the estimated contact point: for negative distances* H *the gel and the probe are in contact at any time. (b): Phase shift* $\phi - \phi_{\text{moy}}$ *between the oscillatory motion of the piezo cube and the oscillatory motion of the cantilever, for three frequencies of oscillation* f*, in linear scale. The correction* ϕ_{moy} *takes into account an intrinsic phase shift of the piezo cube and is described in Sec. 4.2.2.4. The vertical orange dashed line is described in (a). (c): Same as in (a), on logarithmic scale. (d): Same as in (b), on semi-logarithmic scale.*

For the three frequencies investigated in this experiment, $f = \{7, 70, 700\}$ Hz, we observe the same general features described in the previous section for a unique frequency $f = 7$ Hz. At small distances we observe a plateau both for the deflection amplitude of the cantilever and the phase shift in logarithmic scale. Then, we observe a sharp decrease of the deflection amplitude of the cantilever a_{canti} with increasing distance H, associated to a sharp increase of the phase shift $\phi - \phi_{\text{moy}}$ (linear and logarithmic scales). At large distances we observe a saturation of the deflection amplitude of the cantilever, associated to random values of the phase shift, which corresponds to the limit of the AFM resolution (linear and logarithmic scales). Yet, with increasing frequency f, the transition between the short- and large-distance regimes is sharper, and even happens on a too short range in distance to be visible for $f = 700$ Hz. The small-distance plateau values in amplitude and phase are similar for the three investigated frequencies, and the large-distance ones are similar for two out of three frequencies. Indeed, at large distance for $f = 700$ Hz, the saturation of the oscillation amplitude of the cantilever is higher, and the saturation in phase shift is lower, than for $f = \{7, 70\}$ Hz. The large-distance value of the oscillation amplitude of the cantilever is above the AFM resolution ($= 0.1 - 1$ nm). The observed features of the $f = 700$ Hz data we just described constitute a piece of evidence to assess the quality of this measurement. A possible explanation would be that the driving frequency of $f = 700$ Hz is close to the resonance frequency of the piezo cube.

To properly compare the results obtained with the three driving frequencies, we need to rescale the data. We use the theoretical framework developed in the first part of this Chapter (Sec. 4.1), assuming the hydrogel is thick enough to be described as a

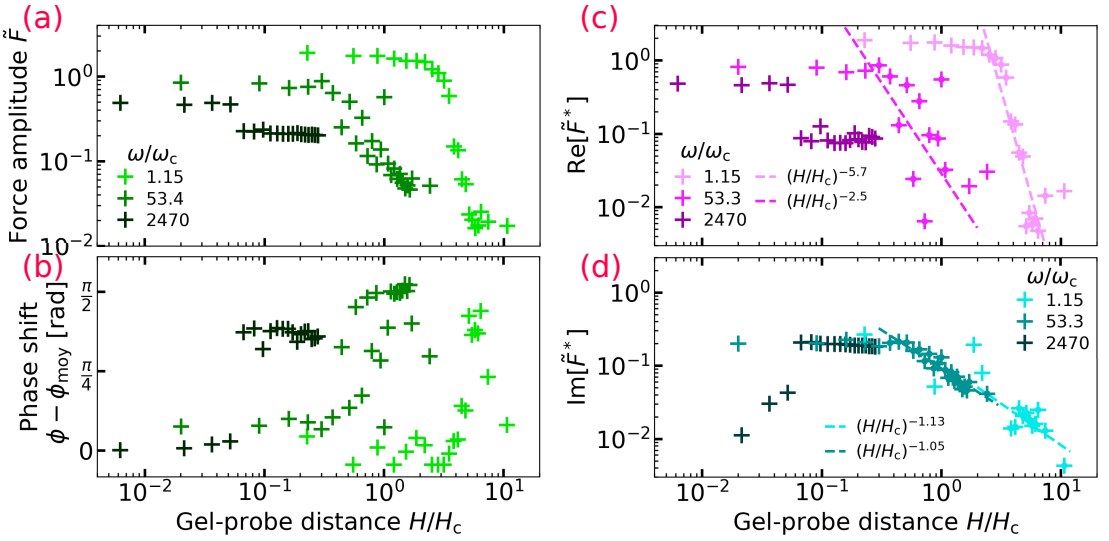

FIG. 4.9. **Rescaled force exerted by a hydrogel in oscillatory contactless mode** *(a): Dimensionless force amplitude $\tilde{F}$ (or modulus of the complex force) as a function of the normalized gel-probe distance H/H_c, for three normalized angular frequencies ω/ω_c. (b): Phase shift $\phi - \phi_{moy}$ (or argument of the complex force) as a function of the normalized gel-probe distance H/H_c, for three normalized angular frequencies ω/ω_c. The correction ϕ_{moy} takes into account an intrinsic phase shift of the piezo cube and is described in Sec. 4.2.2.4. (c): Storage component of the dimensionless force (or real part of the complex force) as a function of the normalized gel-probe distance H/H_c, for three normalized angular frequencies ω/ω_c. The dashed lines represent power laws fitted on the "+" data points marked by a thick dot, with resulting exponents indicated in the legend. (d): Loss component of the dimensionless force (or imaginary part of the complex force) as a function of the normalized gel-probe distance H/H_c, for three normalized angular frequencies ω/ω_c. The dashed lines represent power laws, with resulting exponents indicated in the legend. The color shades used to plot each quantity on each panel are identical to the ones used in Fig. 4.2, to guide the comparison.*

semi-infinite poroelastic medium. In comparison to the gel-probe distance H, the latter statement is true as the swollen thickness of the gel is about $\tau_{swollen} \approx 1.2\,\mu$m. Compared to the hydrodynamic radius $\sqrt{2RH}$, considering the gel as a semi-infinite layer is more questionable.

4.2.4.4 Rescaled data

Using the cantilever stiffness, the cantilever oscillation amplitude is converted into force amplitude. The gel-probe distance H and the angular frequency $\omega = 2\pi f$ are normalized by the critical distance H_c and the critical angular frequency ω_c respectively, given by Eqs. (4.19) and (4.20) respectively, as:

$$\frac{H}{H_c} = \frac{H}{8R}\left(\frac{2G}{\eta\omega}\right)^{2/3} \quad \text{and} \quad \frac{\omega}{\omega_c} = \frac{2R\omega H_c}{\mathcal{D}_{pe}} = \frac{16(1-2\nu)}{(1-\nu)}\frac{R^2}{k}\left(\frac{\eta\omega}{2G}\right)^{5/3}. \tag{4.53}$$

We use the following values: the probe radius $R = 45\,\mu$m, the water viscosity $\eta = 10^{-3}\,$Pa.s, the shear modulus $G \approx 5\,$kPa (see the next Chapter), the Poisson ratio of PNIPAM $\nu = 0.2$ [239, 240] and the permeability $k \sim l_p^2$ based on the pore size $l_p \approx 5\,$nm [1]. The effective poroelastic diffusion coefficient can be also estimated with

Eq. (4.8), as $\mathcal{D}_{\rm pe} \approx 333\,\mu{\rm m}^2/{\rm s}$, which is about 7 times smaller than the self-diffusion coefficient of water. The three driving frequencies $f = \{7, 70, 700\}$ Hz correspond respectively to the reduced angular frequencies $\omega/\omega_{\rm c} = \{1.15, 53.4, 2470\}$. The force amplitude is normalized using Eq. (4.34), as:

$$\tilde{F} = \frac{F H_{\rm c}}{8\pi\eta\omega h_0 R^2} = \frac{F}{\pi R h_0 \left(\eta\omega\right)^{1/3} \left(2G\right)^{2/3}}, \tag{4.54}$$

with $h_0 = 62\,{\rm nm}$ being the oscillation amplitude of the piezo cube. In Fig 4.9(a) and (b) we show the dimensionless force amplitude $\tilde{F}$ and phase shift $\phi - \phi_{\rm moy}$, respectively, as functions of the dimensionless gel-probe distance $H/H_{\rm c}$. The two latter graphs correspond to the theoretical predictions of Figs. 4.2(c) and (d) respectively, and are represented with the same color shades.

As predicted by the theory, and as for the raw data, we observe for $f = \{7, 70\}$ Hz the small- and large-distance regimes on both the force amplitude $\tilde{F}$ and the phase shift $\phi - \phi_{\rm moy}$, that we detail in the following. First, we describe small distances, $H/H_{\rm c}$. In this regime, the normalized force amplitude as a function of the normalized distance exhibits a plateau which reaches the values $\tilde{F} \approx \{1.8, 0.8, 0.5\}$, respectively for the reduced angular frequencies $\omega/\omega_{\rm c} = \{1.15, 53.4, 2470\}$. These measured values can be compared to the predicted values based on the linear poroelasticity theory developed in Sec. 4.1. In particular, the numerical resolution of the force is used as in Fig. 4.2(c) to predict the theoretical dimensionless force values, as $\tilde{F} = 2.3 - 3$, the value increasing with increasing frequency. The phase shift also exhibits a plateau, the value of which is about $0°$ for the reduced angular frequencies $\omega/\omega_{\rm c} = \{1.15, 2470\}$ and about $15°$ for $\omega/\omega_{\rm c} = 53.4$. As for the force, these measured phase shifts can be compared to the predicted values, which are $\phi = 30 - 33°$. The qualitative features of the experimental data match the theory at small distances, which suggests that the elastic response of the gel dominates. However, the quantitative measurements exhibit deviations from the theory that we will discuss below. Before such discussion, we next describe large distances.

For $H/H_{\rm c} \gtrsim \{3, 0.3\}$ the normalized force amplitudes decay as power laws for the reduced angular frequencies $\omega/\omega_{\rm c} = \{1.15, 53.4\}$ respectively. For $\omega/\omega_{\rm c} = 2470$, we do not observe a decay, but a second plateau for $H/H_{\rm c} \gtrsim 0.06$. This observation is in contrast with the theory, predicting a power-law decay for $H/H_{\rm c} \gtrsim 0.3$. At the same threshold values in $H/H_{\rm c}$, we observe a sharp increase of the phase shift, reaching $\phi - \phi_{\rm moy} \approx \{80, 94, 70\}°$ respectively for the reduced angular frequencies $\omega/\omega_{\rm c} = \{1.15, 53.4, 2470\}$ (theoretical predicted value $\phi = 90°$). At large distances, the qualitative features of the experimental data match the theory for the angular frequencies $\omega/\omega_{\rm c} = \{1.15, 53.4\}$, which means that the viscous, dissipative response of the fluid dominates. The quantitative measurement of the threshold in $H/H_{\rm c}$ and the phase shift are close to the theoretical prediction for $\omega/\omega_{\rm c} = 53.4$.

From the normalized force amplitude and the phase shift, we can compute the normalized complex force $\tilde{F}^*$, as:

$$\tilde{F}^* = \tilde{F} e^{i(\phi - \phi_{\rm moy})} = {\rm Re}\left[\tilde{F}^*\right] + i{\rm Im}\left[\tilde{F}^*\right], \tag{4.55}$$

the amplitude $\tilde{F}$ being the modulus and the phase shift $\phi - \phi_{\rm moy}$ being the argument of the complex force. The real and imaginary parts of the complex force are shown in Figs. 4.9(c) and (d) respectively. The two latter graphs corresponds to the theoretical prediction of Fig. 4.2(e), and are represented with the same color shades.

As predicted by the theory, as for the raw data and the amplitude-phase representation, we observe for $f = \{7, 70\}$ Hz the small- and large-distance regimes on both the real

and imaginary parts of the normalized complex force Re $\left[\tilde{F}^*\right]$ and Im $\left[\tilde{F}^*\right]$ respectively, that we detail in the following. On the one hand, at small distances H/H_c, the real part of the normalized force as a function of the normalized distance exhibits a plateau which reaches the values Re $\left[\tilde{F}^*\right] \approx \{1.8, 0.8, 0.5\}$, respectively for the reduced angular frequencies $\omega/\omega_c = \{1.15, 53.4, 2470\}$, that correspond respectively to the three driving frequencies $f = \{7, 70, 700\}$ Hz (theoretical predicted value Re $\left[\tilde{F}^*\right] = 2 - 2.5$). The imaginary part exhibits a plateau too, which reaches the values Im $\left[\tilde{F}^*\right] \approx 0.2$ for the reduced angular frequency $\omega/\omega_c = 53.4$ (theoretical predicted value Im $\left[\tilde{F}^*\right] = 1.3 - 1.6$). A unique point at Im $\left[\tilde{F}^*\right] \approx 0.2$ is observed for $\omega/\omega_c = 1.15$ at a similar value in force, and no plateau is observed at small distances for $\omega/\omega_c = 2470$. The qualitative features at small distances match the theory for $\omega/\omega_c = 1.15$ and partly for $\omega/\omega_c = 53.3$, which means that the elastic response of the gel dominates. Yet, the quantitative measurements exhibit deviations from the predicted values. On the other hand, for $H/H_c \gtrsim \{3, 0.3\}$ the real part of the normalized force decays approximately as a power law for the reduced angular frequencies $\omega/\omega_c = \{1.15, 53.4\}$ respectively, with -5.7 ± 0.1 and -2.5 ± 0.6 fitted exponents respectively. For $\omega/\omega_c = 2470$, we do not observe a decay, but we observe only a second plateau for $H/H_c \gtrsim 0.06$. The theory predicts a decay for $H/H_c \gtrsim 0.3$ with a -2.5 exponent. At the same threshold values in H/H_c, the imaginary part of the normalized force decays in a power law $\omega/\omega_c = \{1.15, 53.4\}$, with -1.13 ± 0.02 and -1.05 ± 0.01 fitted exponents respectively (theoretical predicted exponent -1). For $\omega/\omega_c = 2470$ we observe a plateau instead for $H/H_c \gtrsim 0.06$. At large distances, the qualitative features of the experimental data match the theory for the angular frequencies $\omega/\omega_c = \{1.15, 53.4\}$, which means that the viscous, dissipative response of the fluid dominates. The quantitative measurement of the threshold in H/H_c and the decay exponents both for the real and imaginary parts are close to the theoretical prediction for $\omega/\omega_c = 53.4$.

In summary, three data sets are presented here. First, the experimental data set at $f = 700$ Hz ($\omega/\omega_c = 2470$) does not match the qualitative features of the theory. Second, the experimental data set at $f = 7$ Hz ($\omega/\omega_c = 1.15$) exhibit the qualitative but not the quantitative features of the theory. Third, the experimental data set at $f = 70$ Hz ($\omega/\omega_c = 53.4$) matches the theoretical prediction qualitatively and quantitatively at short and large distance, albeit the slightly low value of the force at small distances. In the next section we discuss these agreements and disagreements in more detail.

4.2.5 Discussion

4.2.5.1 Validity of the hypotheses

We observe a qualitative agreement of the experimental data with the theory for $\omega/\omega_c = \{1.15, 53.4\}$ and furthermore a quantitative one for $\omega/\omega_c = 53.4$. The theoretical framework of the contactless, colloidal-probe rheology experiment presented here is developed based on several hypotheses. First the lubrication approximation should be valid, which stipulates that the fluid gap is small compared to the hydrodynamic radius: $H \ll \sqrt{2RH}$. The largest gel-probe (*i.e.* fluid gap) distance H taken into account here is $1\,\mu$m. The sphere radius being $45\,\mu$m, then $\sqrt{2RH} = 9.5\,\mu$m and thus limit of validity of the lubrication approximation is reached. Second, the viscous penetration depth should be large compared to the fluid gap: $\sqrt{\eta/(\rho\omega)} \gg H$. For the highest frequency $f = 700$ Hz,

the viscous penetration depth can be estimated at $15\,\mu$m, which is one order of magnitude more than the largest distance H. Again, the limit of validity of this hypothesis is reached. Third, the oscillation amplitude should be small compared to the fluid gap: $h_0 \ll H$. In the experiment presented here, the oscillation amplitude is $h_0 = 62\,$nm. The experiment is conducted varying the cube height on a sufficiently large range so that the contact between the sample and the probe is achieved. The contact point is deduced from the raw data to extract the gel-probe distance. Thus, for a few data points at the smallest distances H, this hypothesis breaks necessarily down. Here, arguing that at least an order of magnitude should be kept between h_0 and H to verify the hypothesis, the range in distances for which the latter is verified starts at $\approx 600\,\mu$m which falls in the observed large-distance regime. Thus, for all the data points at smaller distances than $600\,\mu$m, which covers both the small-distance regime and the crossover with the large-distance regime, the hypothesis is not verified, and a large-deformation modeling would be probably relevant. Yet, interestingly, the qualitative expected features of the force-distance data are observed, and even quantitatively for one over three driving frequencies, even though the last hypothesis is not satisfied. To conclude, in order to preserve the three hypotheses listed above, the experiment should first of all be run at a smaller oscillation amplitude (*i.e.* $h_0 \lesssim 10\,$nm). Then, a bigger probe could be tested, to preserve safely the lubrication approximation. Finally, to ensure a large viscous penetration depth, one can fix an upper bound for the frequency range to explore at 500 Hz.

4.2.5.2 Asymptotic compressible-like behavior

In the theoretical framework presented in this Chapter, the response in force of a poroelastic gel exhibits a transition from an incompressible-like response to a compressible-like response with increasing reduced angular frequency. The incompressible asymptote is almost reached for $\omega/\omega_c = 0.001$ and the compressible one for $\omega/\omega_c = 10$. Thus, in the goal of showing an evidence of the porous signature of the poroelastic gel, the range of angular frequencies to explore should match these two bounds. In the experiment presented in this Chapter, the reduced frequencies are in the high-frequency limit ($\omega/\omega_c = \{1.15, 53.4, 2470\}$). Thus, the asymptotic compressible-like behavior is mainly probed. Reducing the normalized angular frequency down to 0.001 would probe the asymptotic incompressible-like behavior and the range of frequencies in between these two boundaries would probe the crossover behavior between the two limit incompressible and compressible cases. In practice, as the reduced angular frequency scales with $\omega^{5/3}$ (see Eq. 4.53), to achieve a range of four orders of magnitude in ω/ω_c, the frequency f (in Hz) has to vary only of a factor $10^{12/5} \approx 250$, the other experimental parameters being kept fixed. Alternatively, we can consider that the sample is kept identical, thus the experiment has to be adapted. To reduce the normalized angular frequencies, a probe of smaller radius could be chosen (but not so small either, as to risk losing the validity of the lubrication approximation).

Otherwise, fine tuning the mechanical properties of the hydrogel to highlight its porous signature by the experiment presented here could be a track: the hydrogel should then be stiffer and/or having a larger pore size (thus a larger porosity k). Finally, the variation between the two limit incompressible-like and the compressible-like behaviors, due to the porosity, is small as predicted by the theory. The experiment presented here may show an evidence of the porosity of a sample, but this signature would be a discrete feature in any case. To ensure the validity of such a delicate measurement, the experiment should be repeated to ensure good enough statistics.

4.2.5.3 Quality of the experiment

The preliminary results presented in Sec. 4.2.4 were collected during a single crash-test experiment, which first aimed only at testing the recently-built setup and the home-made code running all the experiment. Because of a lack of time, the experimental data were deeply analyzed far later and the experiment was not repeated. For these reasons, the prescribed experimental parameters such as the oscillation amplitude h_0 and the frequency f could not be fine-tuned. The hydrogel sample may also be too thin to be considered as a semi-infinite poroelastic media. Finally, such a delicate experiment needs some practice, and there was only one try.

Despite these considerations, the collected data show promising results: on two out of three driving frequencies f we observe qualitatively the predicted response of the hydrogel, for one we find moreover a quantitative agreement with the theory. The force response is characterized by two regimes depending on the gel-probe distance. At small distances, the elasticity of the gel dominates in the response in force, which translates by a saturation of the force amplitude and a low value of the phase shift. At large distances, the viscous dissipation happening in the fluid phase dominates in the response in force, which translates by exponential decays of the storage and loss components of the force with characteristic exponents. Thus, the results presented here constitute a proof-of-concept that the built experiment can probe the mechanical response of a soft and porous thick gel, as predicted by the theory developed in Sec. 4.1.

4.3 Conclusion

In the first part of the present Chapter, we derived theoretically the mechanical response of a gel to a vertically oscillating spherical probe in lubrication conditions within a fluid. The gel is modeled as a poroelastic, compressible, permeable, semi-infinite medium and the surrounding fluid is identical to the solvent present in the polymeric matrix. The complex amplitude of the force exerted on the spherical probe was numerically computed and studied. As a result, contactless colloidal-probe methods in the linear response regime appear as good candidates to robustly measure the effective elastic properties of soft and fragile gels, without risk of wear and adhesion. However, such experimental techniques are not suitable to probe permeability. In the second part of the present Chapter, we presented a contactless, colloidal-probe, AFM-based experiment on a thick PNIPAM hydrogel film immersed in water. We showed preliminary results demonstrating the efficiency of the method to probe elastic mechanical properties of a soft hydrogel. With fine-tuning, the method could also highlight the porous signature of the soft hydrogel.

The data collected with the contactless experiment on a swollen PNIPAM gel presented in this Chapter constitute in a sense dynamic rheology data, since they present a study of the mechanical response of the material as a function of the excitation frequency. Then, a natural comparison would be to confront these data to pure rheology data collected on PNIPAM microgels and grafted PNIPAM gels. The measured response in the limit of small gel-probe distances could be compared to rheology data. Yet, some adaptation work would be needed. A pure rheology experiment is realized with a probe in contact with the material to investigate, thus presents a risk of damaging the sample, which in turn could modify the measured mechanical response of it. Here, the strength of the method lies in the contactless aspect, thus the latter prevents the risk of damaging

the sample.

Exploiting the experimental method associated with the theoretical framework developed in this Chapter, more complex systems such as bending membranes or biological samples could be investigated without damage. Extending the theory to other complex materials, such as viscoelastic matter, or even samples exhibiting a plastic behavior, the experiment could be adapted to probe such non-trivial materials, still in a non-invasive, contactless mode to prevent damages.

In the next Chapter we present experimental results on the mechanical response of PNIPAM thin films, based on a contact-mode method, to contrast with the present Chapter. We investigate the properties of the hydrogel by approaching a lubricated spherical probe until touching the gel, then the probe continues to indent the gel, provoking large deformations and the dehydration of the gel.

Chapter 5

Mechanical response of a hydrogel: from small deformations to the dehydration-induced glass transition

In the present Chapter, we investigate the mechanical response of PNIPAM hydrogel thin films using an approach method (see Fig. 1.8(d)). When the contact is established between the probe and the hydrogel, the experiment continues, such that the gel is probed by indentation (see Fig. 1.8(e)). The method described in this Chapter allows to probe several regimes of mechanical response, from a small-deformation and lubricated regime, to a large-deformation, in-contact one. Here, we perform Surface Forces Apparatus (SFA) experiments, in sphere-plane geometry, on initially fully swollen PNIPAM hydrogels. In a first part, we describe the experimental setup, in which the approach of the probe gradually compresses the hydrogel, until reaching full compression. In a second part, we present the theoretical modeling of the observed experimental data. Several regimes characterizing different physical behaviors are observed during an approach. Efforts are made to identify and characterize each regime: complementary numerical simulations are developed to describe early lubricated regimes while a non-linear fitting method is implemented to describe the late contact problem and resolve the transition between these two main regimes. We show that the hydrogel undergoes a glass transition, triggered by dehydration, itself due to the large indentation. We finally find the point that marks the onset of the dehydration-induced glass transition of the PNIPAM hydrogel.

5.1 Experimental setup

The experimental setup consists in a miniature Surface Forces Apparatus (μ-SFA) in sphere-on-flat geometry, observed through the objective of an inverted microscope [265]. Fig. 5.1(a) shows a schematic of the SFA and Fig. 5.1(b) a picture of the lens from a top view. The SFA is used to investigate the mechanical properties of swollen PNIPAM hydrogels thin films.

5.1.1 μ-SFA

A sample to investigate is first deposited on a circular glass coverslip, which is glued to the stainless steel support of the SFA, using a UV-curable glue (*Nordland Optical Adhesive, NOA81*). The body of the μ-SFA contains a glass spherical lens of radius $R \approx 2.1\,\text{cm}$, which is held by a stainless steel support, connected to two metal blades acting as a spring of stiffness $K \approx 1000\,\text{N/m}$. The lens is initially placed up, with the help of a coarse screw acting on the back of the metal blades. The support on which the sample is glued is then mounted onto the μ-SFA body. We then aim to place the glass lens at about 0.5 cm of the sample, with the help of the coarse screw. A distillated water drop is deposited in between the lens and the sample, using a syringe, and forms a capillary bridge between the lens and the sample. Finally, an electric motor acts on the extremities of the metal blades and drives the lens upwards and downwards. A continuous electrical voltage is applied to the motor (typically $U = 5 - 11\,\text{V}$, direct current(DC)), so that the back of the metal blades is driven at a constant velocity V.

In this Chapter we show typical experiments on thin, grafted PNIPAM hydrogel. The samples are prepared on circular coverslips (diameter 22 mm, *VWR, Micro Cover Glasses, round, no.2*), following the protocol given in Chapter 2, Sec. 2.1.1. The sample is mounted onto the SFA body with a concern for extreme cleanliness. Several approach

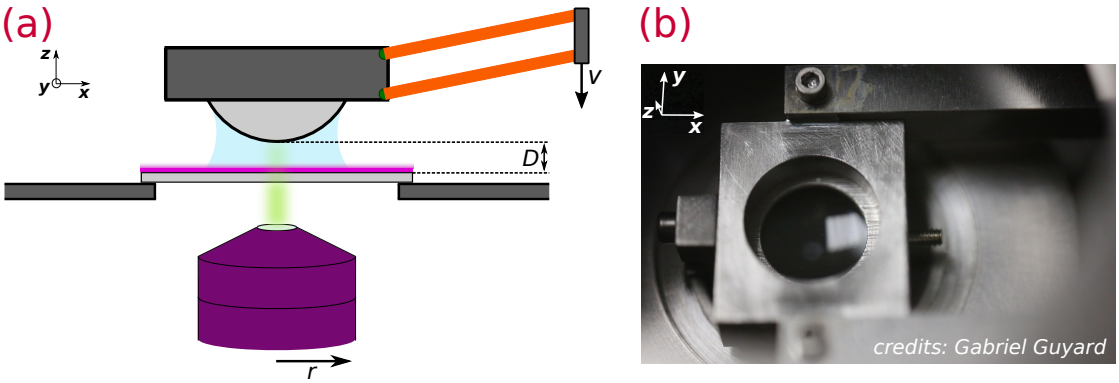

FIG. 5.1. **Surface Forces Apparatus.** *(a): Schematic of the SFA. A glass lens is held by two metal blades (in orange) acting as a spring. By driving downwards the back of the metal blades at a velocity V, the lens is approached close to an investigated sample (in magenta), immersed in water. The sample is held by a planar glass coverslip, which is transparent. The apparatus is placed above the objective of an inverted microscope: a light ray sent through the coverslip is reflected on the lens. The interference between the incident and reflected rays is observed in the microscope. The distance D between the two glass surfaces is measured by interferometry (see Fig. 5.2). (b): Top-view picture of the glass lens, housed in its metallic support. The two metal blades holding the lens support are visible on the top and bottom of the picture. The square support is about* 1.5 cm.

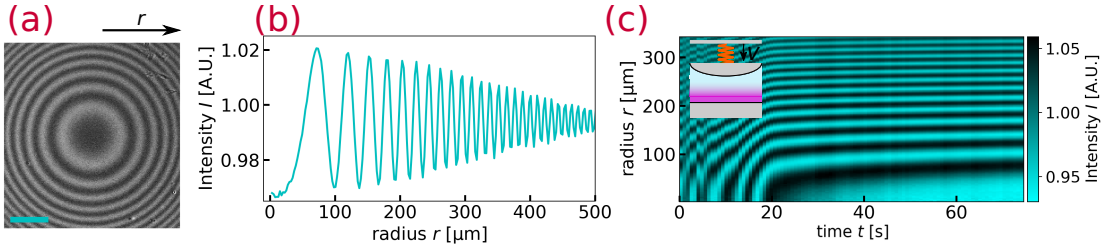

FIG. 5.2. **Analysis of the interference pattern.** *(a): Typical interference pattern, called Newton's rings, recorded at the inverted microscope and divided by the background image, for a distance D smaller than the coherence length of the incident light (wavelength centered at $\lambda \approx 595\,\mathrm{nm}$). The blue bar represent $100\,\mu\mathrm{m}$. (b): Normalized light intensity from the image (a), averaged over the azimuths, as a function of the radial coordinate r. (c): Reconstructed interferogram. The averaged radial intensity is plotted in colored scale as a function of the radial coordinate (vertical axis) and as a function of time (horizontal axis).*

velocities are tested. A given approach is ended by switching the motor off, when the probe is compressing the gel at a point where we do not observe any further evolution of the interference pattern. Several more images are recorded. Then, the probe is retracted by inverting the polarity voltage on the motor. The retraction experiments are not shown here.

5.1.2 Images of Newton's rings

The apparatus is placed on the top of the objective of an inverted microscope. We use a multicolored LED light source (*CooLED pe-4000*, 16 colors). In particular, we use the yellow color (whose wavelength is centered around $\lambda \approx 595$ nm). The light beam is sent through the objective and passes successively through the glass coverslip, the hydrogel film and the water drop. The ray reflects at each interface, and in particular on the surface of the spherical lens. Then, the reflected ray passes successively through the same media, and interferes with the incident ray. The reflected ray is reflected again on the glass surface of the coverslip, and again on the one of the sphere, *etc.* The multiple reflections between the two glass surfaces build an interference pattern, that we refer to as Newton's rings. The minimal distance between the two glass surfaces is noted D. If the optical path difference $2D$ is smaller that the coherence length of the incident light, we can observe in the microscope the interference pattern at the surface of the coverslip. A CCD camera (*Hamamatsu ORCA-ER II*) is mounted onto the inverted microscope and records the interference pattern.

A background image is recorded when the distance D is long enough so that the Newton's rings disappear. In Fig. 5.2(a) is shown a typical interference image which consists in a raw image taken at a close distance D, divided by the background image. A first Matlab code written by one of my supervisors finds the center of the rings, and computes the radial intensity profile averaged on azimuths, as shown on Fig. 5.2(b) (see Appendix A.6 for the details of the algorithm). During an approach of the spherical probe towards the soft sample, the interference pattern is recorded with time, and the averaged intensity profiles are extracted for each image at each time step. In Fig. 5.2(c) we show a reconstructed interferogram of the averaged intensity as a function of the radial coordinate r and the time t. We observe that with the decrease of the distance D as the spherical lens approaches the sample, more rings are visible on the image, and the contrast is enhanced.

5.1.3 Modeling the interference pattern

5.1.3.1 Multiple reflections between two glass interfaces

The interference pattern observed at the interface between the coverslip and the gel is generated by multiple reflections of an incident light ray onto the coverslip and the glass interface of the lens. This phenomenon is modeled with geometrical optics, by considering a three-layer system. The coverslip and the lens are made of glass, and have an optical index noted n_g. In between, water and the swollen gel are present. The latter is composed of $\approx 80\%$ of water, thus we assimilate it to water and consider its optical index to be the same than the one of water, noted n_w. The Fresnel coefficients at the coverslip and lens interfaces respectively [266] read:

$$r_\mathrm{gw} = \frac{n_\mathrm{w} - n_\mathrm{G}}{n_\mathrm{w} + n_\mathrm{g}}, \tag{5.1a}$$

$$r_\mathrm{wg} = \frac{n_\mathrm{g} - n_\mathrm{w}}{n_\mathrm{w} + n_\mathrm{g}}. \tag{5.1b}$$

The optical indices n depend slightly on the light wavelength λ. Tables of the optical index of a given material (*e.g.* water or glass) as a function of the wavelength can be found at `https://refractiveindex.info/about`. In Fig. 5.3(a) we show the tabulated optical indices of water and glass, n_w and n_g respectively, as functions of the wavelength λ that we use in the present analysis. Then, the numerical aperture of the microscope is small, so that we consider a normal incidence. The sphere radius R being large compared to the thickness D of the water-and-hydrogel layer, we consider the two interfaces to be flat, and that the reflected ray stays normal to the interfaces. In such conditions, the reflectance of the system can be derived [266], as:

$$\mathcal{R}(\Phi) = \frac{r_\mathrm{gw}^2 + 2r_\mathrm{gw}r_\mathrm{wg}\cos(2\Phi) + r_\mathrm{wg}^2}{1 + 2r_\mathrm{gw}r_\mathrm{wg}\cos(2\Phi) + r_\mathrm{gw}^2 r_\mathrm{wg}^2}, \tag{5.2}$$

with Φ the phase shift introduced by a reflection, which reads:

$$\Phi(D) = \frac{2\pi}{\lambda} n_\mathrm{g} D. \tag{5.3}$$

The reflectance $\mathcal{R}$ is shown as a function of the distance D for different light wavelengths λ in Fig. 5.3(b). Combining Eqs. (5.2) and (5.3), and normalizing, we get the light intensity as a function of the distance D between the two glass interfaces, for a given wavelength.

5.1.3.2 Spectrum bandwidth of the light source

In practice, we use a LED light source, that emits a yellow light whose wavelength is centered around $\lambda \approx 595\,\mathrm{nm}$. The spectrum of the light source has a finite bandwidth. A precise measurement of the spectrum was provided by the manufacturer, and is shown in Fig. 5.3(c). After smoothening and applying corrections to the measured spectrum, based on measured data, a calibrated filter is established, whose transmission function is noted $\mathcal{T}(\lambda)$. The intensity as a function of the distance is then obtained with a summation of the reflectance $\mathcal{R}$ over the wavelengths λ, weighted by the transmission function of the filter $\mathcal{T}$, such that:

$$I(D) = \int_0^\infty \mathrm{d}\lambda\, \mathcal{R}(D,\lambda)\mathcal{T}(\lambda). \tag{5.4}$$

The resulting intensity is shown in Fig. 5.3(b).

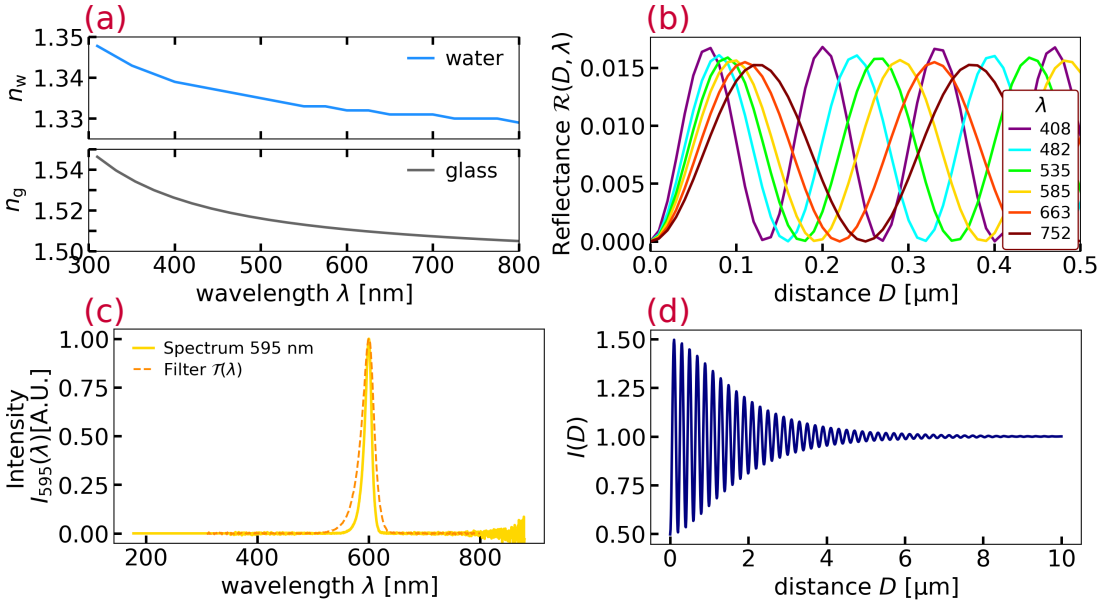

FIG. 5.3. **Modeled light intensity as a function of the distance between the two glass surfaces.** *(a): Optical indices of glass and water, n_g and n_w respectively, as functions of the light wavelength λ. (b): Reflectance $\mathcal{R}$ as a function of the distance between the two glass interfaces D, for different wavelengths λ. (c): Normalized intensity of the 595 nm channel of the LED light source, measured as a function of the wavelength λ (yellow). Corrections based on measured data are applied to this measurement, which establish a calibrated filter (orange). (d): Theoretical light intensity I as a function of the distance D, as computed with Eq.* (5.4).

5.1.3.3 Fitting of the intensity profiles to extract the distance to the probe

The spherical lens profile is modeled as a parabola, making the assumption that the radius of the sphere R is large compared to the distance between the two glass surfaces $D(r = 0)$. Thus, the sphere profile can be written as:

$$D(r) = D(0) + \frac{r^2}{2R}. \tag{5.5}$$

As a result, from a given experimental intensity profile, we can compute the light intensity as a function of the distance to the sphere surface. A second code written by one of my supervisors performs a fit of the intensity as a function of the distance $D(r)$, based on the model described in the previous section (see Fig. 5.3(d)), with the distance at the center $D(0)$ being a fit parameter. As such, the distance $D(0)$ is extracted as a function of time for a given approach of the spherical probe.

5.1.4 Experimental results

5.1.4.1 SFA data in approach mode towards a ultra-thin PNIPAM hydrogel

The series of images, an example of which is shown in Fig. 5.2, was made during an approach towards an ultra-thin grafted PNIPAM hydrogel, of dry thickness $\tau_{dry} = 66\,nm$, immersed in water (thus, of swollen thickness $\tau \approx 4\tau_{dry}$). To preserve the cleanliness, the dry thickness is measured by AFM after performing the SFA experiment, and is presented in Appendix A.2. Similarly, the flatness of the sample can be checked *a posteriori* by AFM. In Chap. 2, we showed that a threshold in thickness at about $\tau \approx 70\,nm$ determines

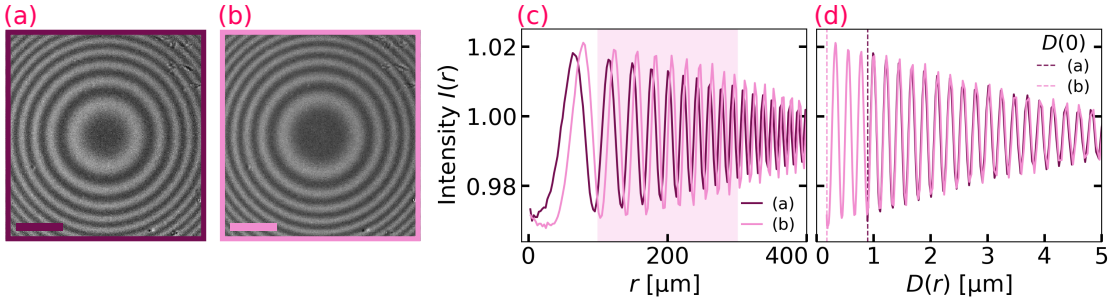

FIG. 5.4. **Fits of two intensity profiles extracted from Newton's rings images.** *(a) and (b): Two Newton's rings images obtained after division by the background image, at two different times of an approach indicated in Fig. 5.5. The pink bar represents* $100\,\mu$m*. (c): Intensity profiles* $I(r)$ *extracted from (a) and (b). The colored zone represents the range used for fitting. (d): Intensity* I *as a function of* $D(r)$*, using Eq.* (5.5)*, and the respective fitted values of* $D(0)$ *as indicated in the legend.*

the onset of creasing instability. Thus, thinner samples are expected to be flat. On the contrary, to enhance the effect of the hydrogel presence on the SFA results, we aim at fabricating a hydrogel as thick as possible. Then, a hydrogel whose thickness is a little below the threshold of $\tau \approx 70\,$nm may show some elastic signature and is expected to be flat, which is indeed the case in the experiment presented in this section.

From each image of a series constituting one approach, the intensity profile is extracted. In Figs. 5.4(a) and (b), we show two images of Newton's rings, at two different times, and their respective intensity profiles (see Fig. 5.4(c)). The distance $D(0)$ is fitted on each profile represented as a function of $D(r)$ using Eq. (5.5) (see Fig. 5.4(d)), typically on a range $r \in [100; 300]$ μm along the radial axis. Thus, in Fig. 5.5(a) we show the fitted distance D as a function of time t. The two experimental points corresponding to the images shown in Fig. 5.4 are marked on Fig. 5.5(a), using the same color code. Three regimes can be observed, with increasing time. First, we observe a linear regime, in which the hydrodynamic probe-gel interaction is weak. The constant Stokes drag, applied on the spherical probe as it moves at a constant velocity V in a viscous liquid, constitutes the dominant force. The linear regime can be fitted, and the slope provides a measurement of the velocity of approach. In the data shown in Fig. 5.5(a), we measure a velocity of $V = 50.8\,$nm/s. Second, an intermediate regime starts where the experimental curve shows a deviation from the linear fit, at about $t \approx 20\,$s. In this regime the hydrodynamic probe-gel coupling is strong. The glass substrate on which the sample is grafted constitutes a rigid boundary. The presence of both the sample and the substrate influence the hydrodynamic motion of the spherical probe in the liquid. At a certain point during the approach, the contact between the probe and the gel is reached, and the probe indents the gel. Thus, the elastic response of the gel to indentation becomes dominant, and influences the motion of the sphere. Third, in a final regime, starting at about $t \approx 100\,$s, the distance between the two glass surfaces D reaches a plateau value, at $D_{\text{final}} = 0.156\,\mu$m. In this regime the gel is fully compressed and the spherical probe does not indent the gel any further. The motor is turned off at $t_{\text{stop}} = 142.5\,$s when the final regime is observed.

The two metal blades holding the spherical lens act as a spring, of equivalent stiffness K. Thus, the compression of the equivalent spring corresponds to the resulting force, up to the stiffness, and constitutes a relevant information to extract. From the distance

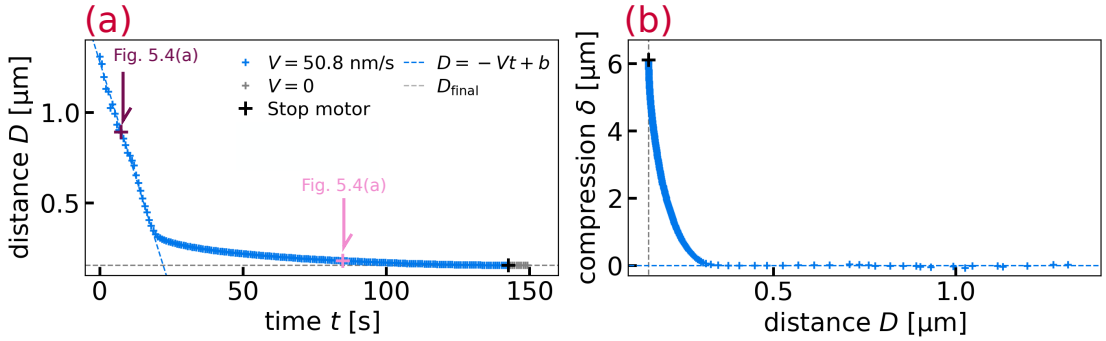

FIG. 5.5. **Raw SFA data on a swollen PNIPAM hydrogel.** *(a): Distance between the two glass surfaces D as a function of time t (blue cross symbols). A linear fit of the initial regime provides a measurement of the approach velocity: $V = 50.8\,\mathrm{nm/s}$. When no change is visible on the interference pattern, the motor is turned off (black cross symbol). A few more images are recorded (gray cross symbols).(b): Spring compression δ, as computed in Eq. 5.6 from the data of (a), as a function of the distance between the two glass surfaces D. The black cross symbol is explained in (a).*

D as a function of time t, the spring compression δ can be computed, as:

$$\delta(t) = D(t) - (-Vt + b) \quad \text{for} \quad t \leq t_{\mathrm{stop}}, \tag{5.6a}$$

$$\delta(t) = D(t) - (-Vt_{\mathrm{stop}} + b) \quad \text{for} \quad t \geq t_{\mathrm{stop}}, \tag{5.6b}$$

with V the velocity of approach, and b the y-intercept of the linear fit. In Eq. (5.6), the difference between the distance D and the initial linear regime $(-Vt+b)$ defines the compression. This definition does not take into account an initial offset in compression. As the sphere is moving in a viscous liquid, the Stokes drag is initially present and results in an offset of spring compression. We can compute an order of magnitude of the initial spring compression, as:

$$\delta(0) \sim \frac{6\pi\eta RV}{K} \sim 10^{-5}\,\mathrm{nm}, \tag{5.7}$$

with the water viscosity $\eta = 10^{-3}\,\mathrm{Pa.s}$, the radius of the sphere $R = 20.3\,\mathrm{mm}$, the spring stiffness $K = 1000\,\mathrm{N/m}$, and the velocity $V = 20 - 50\,\mathrm{nm/s}$. As a result, the initial spring compression is negligible compared to the sensitivity of the instrument (about 1 nm). Similarly, an order of magnitude of the Stokes drag can be computed, as:

$$F_{\mathrm{Stokes}} = 6\pi\eta RV \sim 10^{-2}\,\mathrm{nN}. \tag{5.8}$$

In summary, in the definition of δ given in Eq. (5.6), the Stokes drag is subtracted, and is negligible compared to the sensitivity of the instrument and the others forces. A previous work on confined ionic liquids studied in SFA comes to the same conclusions [267].

From the distance D as a function of time t, the spring compression δ is computed as a function of time t. Combining $\delta(t)$ with the data of the distance D as a function of time, we can get the spring compression as a function of the distance $\delta(D)$, which corresponds to a force-distance curve (up to the stiffness). In Fig. 5.5(b) is shown the spring compression δ, as computed in Eq. (5.6), as a function the distance between the two glass surfaces D. The same three regimes as in Fig. 5.5(a) are observed. First, at large distance D, the measured compression δ is zero, which corresponds to the initial regime. In this regime, the hydrodynamic probe-gel coupling is weak. Thus, the spherical probe moves at a constant velocity V in the viscous solvent, and the Stokes drag applied on the spherical probe constitutes the dominant force. Second, at small

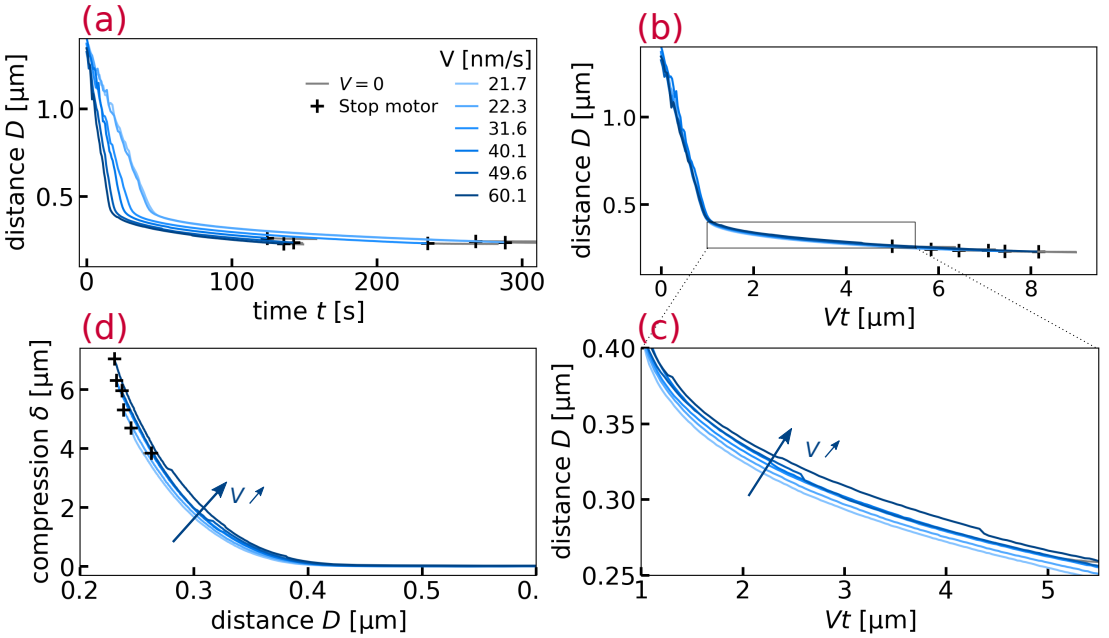

FIG. 5.6. **Influence of the dynamics on SFA data on a swollen PNIPAM hydrogel** *(a): Distance between the two glass surfaces D as a function of time t, for different command velocities V indicated in legend (blue curves). The black cross symbols marks the moment when the motor is turned off. The measurement is stopped a few tens of seconds later (gray curves). (b): Distance between the two glass surfaces D as a function of the traveled distance imposed at the back of the spring Vt, for different command velocities V. The black cross symbols are explained in (a). The black rectangle indicates a zoomed region. (c): Zoom of (b), as indicated by the gray rectangle on (b). (d): Spring compression δ, as computed in Eq.* (5.6) *from the data of (a), as a function of the distance between the two glass surfaces D, for different command velocities V. The black cross symbols are explained in (a).*

distances D, the spring compression δ increases strongly with decreasing distances. In this regime, the hydrodynamic probe-gel coupling is strong. The vicinity of the boundary slows down the sphere velocity, as a result of an additional force applied on the latter. Then, the spherical probe touches the gel and starts to indent it. Thus a transition between a lubricated regime and a contact regime happens. Third, at the final distance $D_{\text{final}} \approx 0.156\,\mu\text{m}$, the spring compression diverges until the motor is turned off, at about $\delta(t_{\text{stop}}) \approx 6\,\mu\text{m}$. In this regime, the maximum compression of the gel is reached. After the motor is turned off at t_{stop}, the velocity of the back of the spring is 0. Thus, the spring compression δ does not increase anymore and keeps its final value $\delta(t_{\text{stop}})$.

5.1.4.2 Influence of the dynamics

The experiment described above is repeated on a given sample for a range of command voltages sent to the motor, which is typically in the range of $U = 5 - 11\,\text{V}$ (DC). The resulting approach velocities range typically from 20 to 60 nm/s. In this section we present SFA results performed on a similar ultra-thin PNIPAM hydrogel (dry thickness $\tau_{\text{dry}} = 65\,\text{nm}$) than in the previous section, fabricated in the exact same experimental conditions, investigated with six different command velocities. In Fig. 5.6(a) is shown the distance D between the two glass surfaces as a function of time, for each command velocity V. For an easier reading, offsets in time were introduced such that all curves

start from the same point $D(0) \approx 1.35\,\mu$m. The experimental data points are connected with full lines to avoid confusion. As expected, the six experimental curves exhibit different velocities, in the initial, linear regime. The final distances D_{final} are similar among the six curves, with four over six in the interval $D_{\text{final}} \in [0.230; 0.238]$ μm, the last two being $D_{\text{final}} = 0.245\,\mu$m and $D_{\text{final}} = 0.263\,\mu$m. To make the initial regimes merge among the six experimental curves, we plot instead in Fig. 5.6(b) the distance D between the two glass surfaces as a function of the time multiplied by each velocity Vt, which corresponds to the distance traveled by the back of the spring. We observe at first sight that the six curves collapse in such a representation. However, the travel distance imposed to the back of the spring Vt_{stop} at the time t_{stop}, at which the motor is stopped because no further evolution of the Newton's fringes is seen, seems to increase with the velocity. Furthermore, by taking a zoom as shown in Fig. 5.6(c), we observe a slight dependence of the distance D as a function of the travel distance Vt imposed to the back of the spring on the command velocity V. Finally, in Fig. 5.6(d) we show the spring compression δ, as computed from Eq. (5.6), as a function of the distance D between the two glass surfaces. Here, the dependency on the command velocity V is clearly observed.

5.1.4.3 Discussion

A purely elastic, conservative system would show always the same response in terms of force-distance curves. In the results presented here, a velocity-dependent response testifies of dissipative effects in the system. Several possible causes of dissipation can be identified.

Stokes drag: First, as the spherical probe of radius R moves in a viscous liquid of dynamic viscosity η, at a constant velocity V, viscous dissipation happens at the interface between the sphere and the fluid. In the initial, linear-in-time regime, the resulting Stokes drag $\boldsymbol{F}_{\text{Stokes}} = -6\pi\eta R\boldsymbol{V}$ is constant and is not taken into account in the force measurement presented in Fig. 5.6, up to the stiffness factor. However, in the intermediate regime, one should consider a correction to the classical Stokes drag, taking into account the vicinity of a boundary [67, 211]. In the case of a rigid boundary, the corrected form of the Stokes drag is expressed as follows:

$$F_{\text{Stokes,confined}} = -6\pi\eta\frac{R^2}{D}\frac{\mathrm{d}D}{\mathrm{d}t}. \tag{5.9}$$

In the present experiment, several confinement effects on viscous dissipation could be relevant: (i) when the spherical probe enters in the zone of the immediate vicinity of the gel surface, (ii) as long as the velocity of the sphere in the liquid is large, (iii) while there is a lubrication fluid layer in between the sphere and the gel surface, which is true until the spherical probe touches the gel surface.

Hydrogel porosity: Second, the porous matrix of the PNIPAM gel typically swells four times in thickness when immersed in water. As a result, the swollen hydrogel is composed of about 75 % of water in volume. The pore size is estimated at $l_{\text{p}} \approx 10\,\text{nm}$ [243], and we make the hypothesis that the permeability scales with the pore size to the square: $k \sim l_{\text{p}}^2$. When a viscous fluid of dynamic viscosity η is forced to flow inside a porous network, dissipation occurs at the interfaces between the fluid and the polymer chains. The latter effect is modeled from a coarse view by Darcy's law, which

links the applied pressure field P to the resulting fluid velocity $\boldsymbol{v}$, as:

$$\boldsymbol{v} = -\frac{k}{\eta}\boldsymbol{\nabla} P. \tag{5.10}$$

Thus, based on Darcy's law, a higher pressure difference is applied inside the pores by imposing a higher fluid velocity on a same length scale. Dissipation occurs inside the porous matrix. Finally, dissipation in the hydrogel would occur either with a lubrication fluid layer in between its surface and the spherical probe, either with the spherical probe being in contact with the hydrogel surface.

At this point, a better understanding of the SFA data is desired. A first hint would be to identify the contact point, and thus make the difference between the lubricated regime and the contact regime. Then, the discussion around possible sources of dissipation can be adapted depending on the boundary condition at the gel surface. In the next part of this Chapter we present modeling efforts, whose results provide a more precise estimation of the contact point. Different regimes are highlighted, and the experimental results are described separately before and after the contact point.

5.2 Theoretical modeling

In this section we present different models that are used to describe the experimental SFA data. Numerical simulations and non-linear fitting methods are used in complement to rationalize the data. The first question to answer, at least by making an estimation, is the resolution of the contact point, that marks the transition between two different physical situations. Before the spherical probe touches the surface of the gel, we consider a lubrication problem, coupled with the (poro)elasticity of the gel. After the contact is made, we consider a contact-mechanics problem. We start with the contact-mechanics problem, that enables to estimate the contact point. Then, we continue with the lubrication problem.

5.2.1 Contact regime: Hertz theory

5.2.1.1 Theory

A schematic of the situation is presented in Fig. 5.7. We consider that a sphere of radius R indents over a depth b_{ind}, a semi-infinite elastic medium, of Young's modulus E and Poisson ratio ν. The resulting force F exerted by the sphere on the semi-infinite elastic medium is derived from the Hertz contact theory [216], and reads:

$$F = \frac{4}{3}E^*\sqrt{R}b_{\text{ind}}^{3/2} \quad \text{with} \quad E^* = \frac{E}{1-\nu^2}. \tag{5.11}$$

In the case of the SFA experiments presented here, the spring deflection is considered instead of the force. Both are linked by a factor, which is the stiffness K. The spring deflection reads:

$$\delta = \frac{F}{K} = \frac{4}{3}\frac{E}{K(1-\nu^2)}\sqrt{R}b_{\text{ind}}^{3/2}. \tag{5.12}$$

Hertz theory intervenes when the sphere touches and indents the gel. Thus, in the Hertz regime, the distance D between the two glass surfaces is smaller than the undeformed thickness τ. The indentation b_{ind} is then defined by computing the difference between the thickness and the distance to the glass substrate, as:

$$b_{\text{ind}}(t) = \tau - D(t) \quad \text{for} \quad D \leq \tau. \tag{5.13}$$

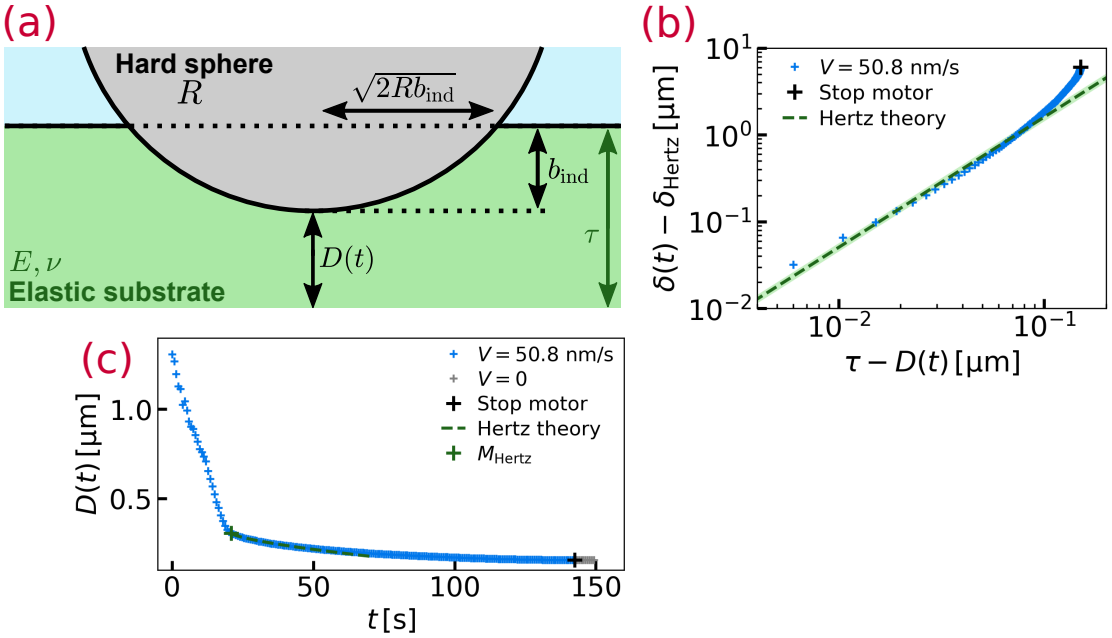

FIG. 5.7. **Hertz contact model for a sphere indenting an elastic material.** *(a): An infinitely rigid sphere of radius R indents over a depth b_{ind} an elastic and compressible material, of Young's modulus E and Poisson ratio ν. The typical area of contact is given by $2Rb_{ind}$. (b): Spring compression δ as a function of indentation $b_{ind} = \tau - D$, and fit with Hertz theory (dashed line). The thickness is estimated at $\tau \approx 306$ nm. The fit is obtained within an error given by $\chi^2 = 0.15$, which is represented by the green zone. (c): Distance D as a function of time t. The point M_{Hertz} is defined by the coordinates (t_{Hertz}, τ) and marks the transition between the lubrication and the contact regimes.*

5.2.1.2 Non-linear fitting method

We perform a fit of the experimental spring compression δ with the Hertz model, based on the logarithm of Eq. (5.12), as:

$$\log\left[\delta(t) - \delta_{Hertz}\right] = \log\left[\frac{4}{3}\frac{E}{K(1-\nu^2)}\sqrt{R}\right] + \frac{3}{2}\log\left[\tau - D(t)\right]. \tag{5.14}$$

with the thickness τ and the prefactor containing the reduced Young's modulus E^* being fit parameters (the thickness is taken in a given range of physically-possible values, $\tau \in [200, 350]$ nm). The thickness τ defines a time t_{Hertz}, and an offset in compression, as:

$$D(t_{Hertz}) = \tau, \tag{5.15a}$$

$$\delta_{Hertz} = \delta(t_{Hertz}). \tag{5.15b}$$

In Eqs. (5.15), t_{Hertz} corresponds to the time at which contact would be made if the gel was an infinitely rigid solid. δ_{Hertz} corresponds to the actual compression at that precise time, and gathers other lubrication forces from previous regimes. The couple (t_{Hertz}, τ) defines the point M_{Hertz}. The fit is performed using a least-square method on Eq. (5.14), with the slope 3/2 being fixed.

5.2.1.3 Numerical computation of the distance as a function of time

The fit of the experimental data to the Hertz model is performed on the compression-distance representation. The fit results in an offset which is the thickness τ, and a

prefactor including the Young's modulus E. One can switch back to the distance-time representation using Eq. (5.6), as:

$$D(t) = \delta(t) + (-Vt + b) \tag{5.16a}$$

$$= \left[\frac{4}{3}\frac{E}{K(1-\nu^2)}\sqrt{R}\right] \times [\tau - D(t)]^{3/2} + \delta_{\text{Hertz}} + (-Vt + b)\,, \tag{5.16b}$$

using Eq. (5.14). Equation (5.16) thus represents an equation on D, that is solved numerically, for a range of time $t \geq t_{\text{Hertz}}$.

5.2.1.4 Results

Physical parameters: In Fig. 5.7(b) is shown a fit with Hertz theory on typical experimental approach data in SFA. The swollen thickness is estimated at $\tau \approx 0.306\,\mu$m, which is slightly greater than expected but still reasonable. We also obtain a time $t_{\text{Hertz}} = 21\,$s and an offset in compression $\delta_{\text{Hertz}} \approx 0.091\,\mu$m. Finally, assuming a spring stiffness of $K = 1000\,$N/m and taking for the sphere radius the value that was adjusted when fitting the intensity profiles (see Sec. 5.1.3.3), $R = 20.27\,$mm, we obtain a prefactor giving a reduced Young's modulus of $E^* \approx 267 \pm 23\,$MPa, which is characteristic for a glassy polymer but surprising for a hydrated hydrogel. This somewhat surprising result will be discussed further, in Sec. 5.3.4.

In Fig. 5.7(c) we show the same data, on the distance-time representation. The theoretical curve corresponding to the Hertz model is computed numerically, solving Eq. (5.16). A characteristic point M_{Hertz} is defined by its coordinates $(t_{\text{Hertz}}; D(t_{\text{Hertz}}))$. This point is placed near the main inflection point of the experimental curve, and marks where the Hertz theory starts to match the experimental data. Then, we observe that both the intermediate and final regimes we identified in Sec. 5.1.4.1 correspond to the contact regime. In the following, we will refer to early- and late-time regimes, using the point M_{Hertz} as the delimiter.

Late-time regime and finite-size effects: The present result shows that a significant part of the late-time regime is well-described by the Hertz contact theory, even while a deviation at final time is observed. Indeed, the spring compression as a function of the indentation, as represented in Fig. 5.7(b) grows in a power law with a 3/2 exponent, for indentations such that $b_{\text{ind}} \leq 0.1\,\mu$m, which corresponds to 20% of the thickness τ [268]. For deeper indentations, *i.e.* $b_{\text{ind}} \geq 0.1\,\mu$m , the spring compression grows in a power law with a higher exponent (up to 3), until the motor is stopped. This deviation from the Hertz theory attests of the finite-thickness aspect of the sample, and results in an apparent strain-hardening behavior. As a short-term perspective, a contact model taking into account the finite thickness of the sample could be developed, and especially the scaling of the spring compression as a function of the indentation would constitute the most relevant information.

Lubrication layer and estimation of the contact point: On the one hand, for very small indentations $b_{\text{ind}}(t)$, as the gel is immersed in water, a lubrication layer can still be present between the deformed surface of the gel and the spherical probe. Thus, even for positive indentation values, the contact point would not be reached yet. The first few data points on Fig. 5.7(b) represent this situation, where the Hertz scaling already catches the data while there is still a thin lubrication layer. This window represents the transition between the lubrication problem and the contact problem. In summary, the contact may be realized later than t_{Hertz}, but the, Hertz theory already catches

the data for a remaining, thin lubrication layer. On the other hand, the estimation of the thickness relies on the fit with the Hertz model. To be precise, the offset in distance D is interpreted as the swollen thickness. However, the latter statement might be exaggerated: for sure the offset in distance D is the distance from which the Hertz model catches the experimental data. The Hertz theory assumes that the probe and the gel are in contact, yet the presence of the fluid, that forms a lubrication layer, differs the moment where the contact is reached. The surface of the gel may be already strongly deformed at the time t_{Hertz}. Thus, the thickness τ would be underestimated.

In summary, the interpretation of the offset in distance D between the two glass surfaces, which would be at first glance the thickness τ, is uncertain. This is due to the transition between a lubrication problem and a contact problem. The validity of Hertz model may be differed by the presence of the lubricated layer. In the following, we investigate the early-time regime, in which a lubricated spherical probe approaches a soft hydrogel.

5.2.2 Lubrication regime at small deformations

5.2.2.1 Time scales of poroelasticity

The hydrogel can be modeled as a poroelastic layer of thickness τ. As described in Chapter 3, an important characteristics of poroelasticity is the time dependence. The poroelastic response shows a continuous transition from a purely elastic and incompressible behavior to a purely elastic and compressible one with time. The propensity of a poroelastic material to exhibit a more-or-less (in)compressible response is determined by the probed experimental time scale. For a hydrogel, of shear modulus G and permeability k, immersed in a solvent of viscosity η, we can first estimate the typical time the solvent takes to diffuse across the layer, as:

$$t_{\text{cross},\tau} = \frac{\tau^2}{\mathcal{D}_{\text{pe}}} = \frac{1-2\nu}{2(1-\nu)}\frac{\eta\tau^2}{Gk}, \tag{5.17}$$

with $\mathcal{D}_{\text{pe}}$ the effective diffusion coefficient as defined in Eq. (3.9) and ν the effective Poisson ratio of the hydrogel. For a PNIPAM hydrogel immersed in water, we use the same physical parameters than in Sec. 4.2.4.4: the water viscosity $\eta = 10^{-3}$ Pa.s, the shear modulus $G \approx 5$ kPa, the effective permeability $k \sim l_{\text{p}}^2$ based on the pore size $l_{\text{p}} \approx 10$ nm, the Poisson ratio $\nu = 0.2$. The effective diffusion coefficient is computed, as $\mathcal{D}_{\text{pe}} \approx 1300\,\mu\text{m}^2/\text{s}$, using Eq. (3.9). The thickness was estimated to be $\tau \approx 306$ nm in the previous section (see 5.2.1). We thus calculate a diffusion time $t_{\text{cross},\tau} \approx 0.07$ ms. This characteristic time can be compared to the typical time scale imposed by the SFA experiment. In the early-time, lubricated regime, the spherical probe is moving in the liquid at a velocity $V = 20-60$ nm/s. Thus, to travel a distance of the same order as the gel thickness, the probe takes a typical time $t_{\text{probe},\tau} = 5-15$ s. In the late-time regime, where the lubrication condition becomes unsatisfied, the spherical probe is moving at a velocity $\dot{D} \approx 1$ nm/s (see Appendix A.7), thus imposing a time scale even longer. To summarize, the intrinsic diffusive time scale of the hydrogel is smaller than the external one imposed by the experiment, by several orders of magnitude: $t_{\text{cross},\tau} \ll t_{\text{probe},\tau}$. Thus, the solvent has time to diffuse across the thickness of the hydrogel. We then consider the poroelastic response of the gel being in the late-time limit, which is equivalent to a purely elastic and compressible behavior.

The same reasoning can be applied on radial length instead of vertical length, at the limit of validity of the lubrication hypothesis, near the point M_{Hertz}. The typical time a

molecule of solvent needs to travel a distance equal to the hydrodynamic radius can be estimated as:

$$t_{\text{cross},\sqrt{2\text{Rh}}} = \frac{2Rh}{\mathcal{D}_{\text{pe}}}, \tag{5.18}$$

with h the fluid-gap thickness. Near M_{Hertz}, we can reasonably suppose the fluid thickness to be less or on the order of $h \lesssim 10\,\text{nm}$. Thus, taking the upper bound, we compute a time scale $t_{\text{cross},\sqrt{2\text{Rh}}} \approx 1.2\,\text{s}$. This characteristic time can be compared to the typical time scale imposed by the experiment, which close to M_{Hertz} reads:

$$t_{\text{probe},\sqrt{2\text{Rh}}} = \frac{\sqrt{2Rh}}{\dot{D}}. \tag{5.19}$$

The front velocity of the sphere is on the order of $\dot{D} \approx 1\,\text{nm/s}$. Thus, we compute a time scale $t_{\text{probe},\sqrt{2\text{Rh}}} \approx 2.10^4\,\text{s}$. In summary, again, the intrinsic diffusive time scale of the hydrogel is smaller than the external one imposed by the experiment: $t_{\text{cross},\sqrt{2\text{Rh}}} \ll t_{\text{probe},\sqrt{2\text{Rh}}}$. We then treat the hydrogel as a purely elastic and compressible material.

5.2.2.2 Modelisation of the SFA experiment

A schematic of the situation is presented in Fig. 5.8. The system is axisymmetric and a (r, z) frame is chosen. We consider that a hard sphere of radius R is held by a spring of stiffness K. The back of the spring is driven downwards at a constant velocity V, which generates a compression noted δ. Thus, the sphere is approached towards an elastic layer of thickness τ, which is supported by a hard boundary. The shear modulus and Poisson ratio of the elastic material are noted G and ν, respectively. The whole system is immersed in a viscous fluid of viscosity η. The sphere motion generates a non-homogeneous, time-dependent pressure field in the liquid, noted $P(r, t)$. The pressure is increased by confinement in the central region, which deforms the surface of the elastic coating. We note $w(r, t)$ the deformation profile of the elastic layer, and $h(r, t)$ the fluid height between the hard sphere and the deformed surface. Finally, we note $D(t)$ the distance between the hard wall and the center of the hard sphere, which corresponds to the distance between the two glass surfaces measured in SFA experiments.

Full model: Similarly to the situation described in Chapter 4, we suppose that the distance H between the sphere and the undeformed surface of the gel is small with respect to the sphere radius R. Thus, we can again invoke the lubrication approximation [32]. We still suppose that the fluid-gap thickness H is small compared to the hydrodynamic radius $\sqrt{2RH}$. Thus, the sphere profile is approximated by a parabola in the lubricated region, and the liquid-film thickness profile is given by:

$$h(r, t) \simeq H - Vt + w(r, t) + \delta(t) + \frac{r^2}{2R}. \tag{5.20}$$

The Reynolds number $\rho HV/\eta$ is assumed to be small compared to unity, so that the flow is laminar. Furthermore, we suppose that the typical viscous penetration depth is large compared to the liquid-gap thickness: $\sqrt{\eta/(\rho\omega)} \gg h$. We assume no-slip boundary conditions at both the sphere and gel surfaces. As detailed in Chapter 4, by invoking flux conservation, the liquid-film thickness profile follows the axisymmetric thin-film equation [64]:

$$\frac{\partial h}{\partial t} = \frac{1}{12\eta r}\frac{\partial}{\partial r}\left[rh^3\frac{\partial p}{\partial r}\right], \tag{5.21}$$

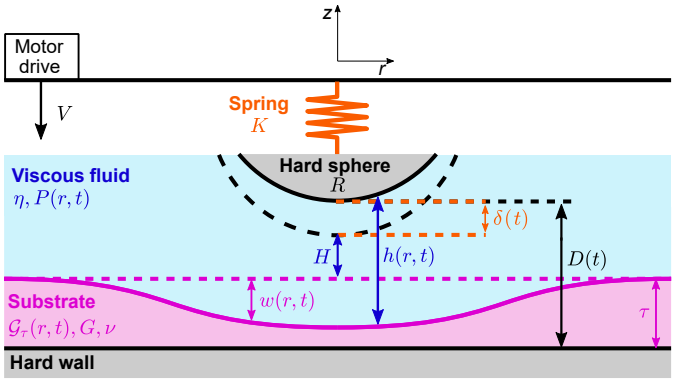

FIG. 5.8. **Modelisation of SFA in the lubrication regime.** *A hard sphere of radius R is held by a spring, which is driven downwards by a command velocity V applied at its back. From a reference distance H, the sphere is brought close to a purely elastic and compressible layer of thickness τ, shear modulus G and Poisson ratio ν. The system is immersed in a fluid of viscosity η. The sphere motion generates a pressure field $p(r,t)$ in the fluid phase, which in turn generates a surface deformation of the elastic layer $w(r,t)$ and a compression of the spring $\delta(t)$. The resulting fluid gap is noted $h(r,t)$. The distance $D(t)$ drawn in black indicates what experimental distance is measured in practice.*

where p is the excess pressure field in the liquid with respect to the atmospheric pressure. The force exerted by the fluid on the sphere is obtained by integrating the pressure field over the surface of the sphere, as:

$$F_p(t) = \int_0^\infty \mathrm{d}r \int_0^{2\pi} \mathrm{d}\theta \, rp(r,t) = 2\pi \int_0^\infty \mathrm{d}r \, rp(r,t). \tag{5.22}$$

The pressure force F_p is balanced by the elastic force exerted by the spring on the sphere, which is given by Hooke's law, as:

$$F_\delta = K\delta(t), \tag{5.23}$$

with δ being counted as positive in compression. Thus, the force balance of Eqs. (5.22) and (5.23) leads to:

$$\delta(t) = \frac{2\pi}{K} \int_0^\infty \mathrm{d}r \, rp(r,t). \tag{5.24}$$

Similarly to the contactless rheology situation developed in Chapter 4, in the lubrication approximation, the ratio between the shear stress and the normal stress σ_{rz}/σ_{zz} is of order $\sqrt{H/2R}$, thus the viscous shear stresses are negligible compared to the pressure in the fluid. Therefore, at the gel interface the force balance takes the same form as in Chapter 3:

$$\sigma_{zz} = -p. \tag{5.25}$$

The surface deformation profile can be computed in the general case, as:

$$w(\mathbf{r},t) = \int_{\mathbb{R}^2} \mathrm{d}^2\mathbf{r}' \, \mathcal{G}_\tau^{\mathrm{comp}}(|\mathbf{r}-\mathbf{r}'|) \, p(\mathbf{r}',t), \tag{5.26}$$

where $\mathcal{G}_\tau^{\mathrm{comp}}$ is the Green's function of the problem, which is the surface deformation induced by a point force $F_0\delta(\mathbf{r})$. Since the timescales imposed by the experiment are large compared to the appropriate diffusion times, as noted in the previous section, we

use the finite-thickness, purely elastic and compressible Green's function, that is derived in Appendix D.4 and in [212] in Hankel space. It is given by Eq. (D.48), as:

$$\hat{\mathcal{G}}_\tau^{\text{comp}}(s) = \frac{1-\nu}{Gs} \frac{2\zeta - (4\nu-3)\sinh(2\zeta)}{5 + 4\nu(2\nu-3) + 2\zeta^2 - (4\nu-3)\cosh(2\zeta)}, \tag{5.27}$$

where the auxiliary function ζ is given by Eq. (3.33f), *i.e.*:

$$\zeta = s\tau. \tag{5.28}$$

The inverse transform is defined by Eq. (3.21), as:

$$\mathcal{G}_\tau^{\text{comp}}(r) = \int_0^\infty \mathrm{d}s\, \hat{\mathcal{G}}_\tau^{\text{comp}}(s) s J_0(sr). \tag{5.29}$$

Using the properties of the convolution product, the surface deformation profile can be expressed in Hankel space, as:

$$\hat{w}(s,t) = \mathcal{G}_\tau^{\text{comp}}(s)\hat{p}(s,t) \tag{5.30a}$$

$$= \frac{\hat{p}(s,t)(1-\nu)}{Gs} \frac{2\zeta - (4\nu-3)\sinh(2\zeta)}{5 + 4\nu(2\nu-3) + 2\zeta^2 - (4\nu-3)\cosh(2\zeta)}, \tag{5.30b}$$

with the forward and backward Hankel transforms of the pressure field and deformation profile, respectively defined as:

$$\hat{p}(s,t) = \int_0^\infty \mathrm{d}r\, p(r,t) r J_0(sr) \quad \text{and} \quad w(r,t) = \int_0^\infty \mathrm{d}s\, \hat{w}(s,t) s J_0(sr). \tag{5.31}$$

The four Eqs. (5.20), (5.21), (5.24) and (5.30b), together with Eqs. (5.28) and (5.31), form a close system of coupled partial differential equations, with four unknowns being the pressure field p, the fluid gap h, the deformation profile w and the spring compression δ.

Boundary conditions: The problem is axisymmetric, so that the gradients of the different fields must vanish at the center:

$$\frac{\partial h}{\partial r}(r=0,t) = 0, \tag{5.32a}$$

$$\frac{\partial p}{\partial r}(r=0,t) = 0, \tag{5.32b}$$

$$\frac{\partial w}{\partial r}(r=0,t) = 0. \tag{5.32c}$$

In the $r \to \infty$ limit, the pressure field reaches the atmospheric pressure value. Thus the excess pressure p vanishes, and so does the deformation, *i.e.*:

$$\lim_{r\to\infty} p(r,t) = 0, \tag{5.33a}$$

$$\lim_{r\to\infty} w(r,t) = 0. \tag{5.33b}$$

Initial condition: Even if the problem is considered for positive times $t \geq 0$, we consider that the driving of the back of the spring at a velocity V has already started at $t = 0$. Thus, the initial condition reads:

$$h(r, t=0) = H + w(r,0) + \delta(0) + r^2. \tag{5.34}$$

Non-dimensionalization: From Eq. (5.21), the hydrodynamic radius $\sqrt{2RH}$ sets a typical horizontal length scale. Besides, H sets a typical vertical length scale. Additionally, a typical time scale is defined by H/V. Thus, we introduce the following dimensionless variables:

$$\tilde{r} = \frac{r}{\sqrt{2RH}}, \quad \tilde{h} = \frac{h}{H}, \quad \tilde{\delta} = \frac{\delta}{H}, \quad \tilde{w} = \frac{w}{H} \quad \text{and} \quad \tilde{t} = \frac{tV}{H}. \tag{5.35}$$

The geometrical Eq. (5.20) becomes:

$$\tilde{h}(\tilde{r}, \tilde{t}) \simeq 1 - \tilde{t} + \tilde{w}(\tilde{r}, \tilde{t}) + \tilde{\delta}(\tilde{t}) + \tilde{r}^2. \tag{5.36}$$

Besides, injecting these new variables in the thin-film Eq. (5.21), we find a natural pressure scale and define the dimensionless pressure, which reads:

$$\tilde{p} = \frac{H^2 p}{2\eta R V}, \tag{5.37}$$

and the thin-film Eq. (5.21) becomes:

$$\frac{\partial \tilde{h}}{\partial \tilde{t}} = \frac{1}{12\tilde{r}} \frac{\partial}{\partial \tilde{r}} \left[\tilde{r} \tilde{h}^3 \frac{\partial \tilde{p}}{\partial \tilde{r}} \right]. \tag{5.38}$$

The force balance Eq. (5.24) is written under a dimensionless form, as:

$$\tilde{\delta}(t) = \kappa_0 \int_0^\infty \mathrm{d}\tilde{r}\, \tilde{r} \tilde{p}(\tilde{r}, \tilde{t}), \tag{5.39}$$

with κ_0 a dimensionless parameter that represents the ratio between viscous stresses and spring elasticity, defined as:

$$\kappa_0 = 8\pi \frac{\eta R^2 V}{K H^2}. \tag{5.40}$$

Finally, the Hankel transform defined in Eq. (5.31) imposes the following dimensionless variables:

$$\tilde{s} = s\sqrt{2RH}, \quad \tilde{\hat{w}}(\tilde{s}) = \frac{\hat{w}(s)}{2RH^2}, \quad \tilde{\hat{p}}(\tilde{s}) = \frac{\hat{p}(s)H}{4\eta R^2 V}. \tag{5.41}$$

From Eq. (5.30b), the dimensionless deformation profile in Hankel space is given by:

$$\tilde{\hat{w}}(\tilde{s}, \tilde{t}) = \epsilon_0 \frac{\tilde{\hat{p}}(\tilde{s}, \tilde{t})(1-\nu)}{\tilde{s}} \frac{2\zeta - (4\nu - 3)\sinh(2\zeta)}{5 + 4\nu(2\nu - 3) + 2\zeta^2 - (4\nu - 3)\cosh(2\zeta)}, \tag{5.42}$$

with the auxiliary function ζ expressed as:

$$\zeta = s\tau = \tilde{s} \frac{\tau}{\sqrt{2RH}} = \tilde{s}\tau_0. \tag{5.43}$$

The dimensionless parameters τ_0 and ϵ_0 represent respectively the thickness normalized by the hydrodynamic radius, and the ratio between viscous stresses and the gel elasticity, defined as:

$$\tau_0 = \frac{\tau}{\sqrt{2RH}}, \tag{5.44a}$$

$$\epsilon_0 = \frac{\eta V}{GH} \left(\frac{2R}{H} \right)^{3/2}. \tag{5.44b}$$

The definition of the dimensionless parameter ϵ_0 must be compared to the one of the distance H_c in Chapter 4, Eq. (4.19). Both parameters compare the viscous stresses to

the gel elasticity, the link between both being made when taking the particular value $\epsilon_0 = 1/4$ and setting $H = H_c$. In the present Chapter, the value of ϵ_0 will be adjusted when running numerical simulations.

In the following paragraphs, to lighten the notation, we omit the tilde symbol ($\tilde{}$) on dimensionless quantities. We first present a resolution of the problem in simpler cases, before presenting the numerical results obtained by performing a numerical resolution of the full model.

5.2.2.3 Theoretical resolution for simpler cases

"Rigid-rigid" case: A way to tackle the complex model explained in the previous paragraph is to incorporate each element one by one in the considered problem. A first, trivial case may be considered in the absence of any spring and substrate. Thus, the problem reduces to a rigid sphere approaching a rigid wall, and only Eqs. (5.36) and (5.38) are considered, as:

$$h_{\text{rigid}}(r,t) = 1 - t + r^2, \tag{5.45a}$$

$$\frac{\partial h_{\text{rigid}}}{\partial t} = \frac{1}{12r}\frac{\partial}{\partial r}\left[r h_{\text{rigid}}^3 \frac{\partial p_{\text{rigid}}}{\partial r}\right]. \tag{5.45b}$$

Combining the two equations, we get a unique equation over the dimensionless pressure field p, which is:

$$-1 = \frac{1}{12r}\frac{\partial}{\partial r}\left[r\left(1 - t + r^2\right)^3 \frac{\partial p_{\text{rigid}}}{\partial r}\right]. \tag{5.46}$$

The latter equation is solved by integrating a first time over the radial coordinate r between 0 and r, then a second time over r between $+\infty$ and r. The pressure field reads:

$$p_{\text{rigid}}(r,t) = \frac{3}{2\left(1 - t + r^2\right)^2}. \tag{5.47}$$

The force resulting on the sphere is computed by integrating the pressure field over the surface of the sphere, and reads:

$$F_{\text{rigid}}(t) = \frac{3\pi}{2(1-t)}. \tag{5.48}$$

The theoretical force and pressure field in the rigid case are shown in Fig. 5.9. The force shows a divergence for $t = 1$, and the pressure field shows one for $r = 0$ and $t = 1$. This divergence is expected: in the rigid case, at $t = 1$, the lowest point of the sphere touches the rigid wall, chasing all the lubrication fluid in between.

"Spring only" case: In the present paragraph, we still neglect the presence of the substrate, but we consider the presence of the spring holding the rigid sphere. Thus, the problem is modeled from Eqs. (5.36), (5.38) and (5.39), as:

$$h_{\text{spring}}(r,t) = 1 - t + \delta(t) + r^2, \tag{5.49a}$$

$$\frac{\partial h_{\text{spring}}}{\partial t} = \frac{1}{12r}\frac{\partial}{\partial r}\left[r h_{\text{spring}}^3 \frac{\partial p_{\text{spring}}}{\partial r}\right], \tag{5.49b}$$

$$\delta(t) = \kappa_0 \int_0^\infty \mathrm{d}r\, r p_{\text{spring}}(r,t). \tag{5.49c}$$

We note that the spring compression $\delta(t)$ does not depend on the radial coordinate r. Thus, from Eqs. (5.49a) and (5.49b), the same calculation path as for the rigid-rigid case

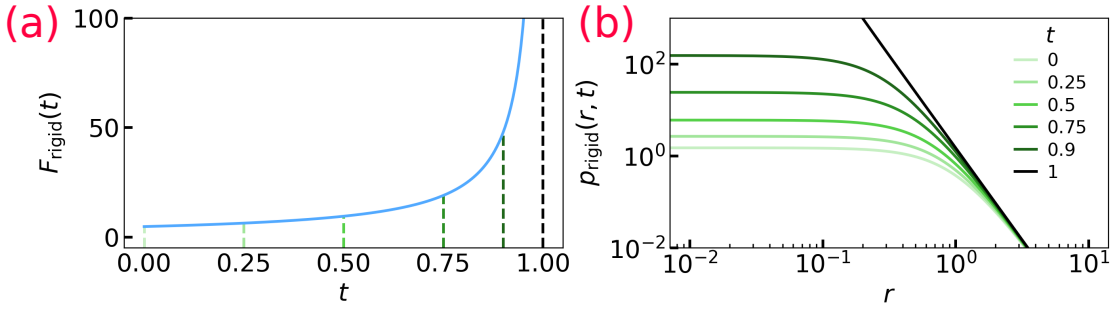

FIG. 5.9. **Theoretical force and pressure field in the rigid case.** *(a): Dimensionless theoretical force F_{rigid} as a function of dimensionless time t, computed from Eq.* (5.48)*. The green dashed lines indicate the times t at which the pressure is plotted in (b). (b): Dimensionless theoretical pressure field $p_{\text{rigid}}(r,t)$, computed from Eq.* (5.47)*, for different dimensionless times t, signaled in (a) by green dashed lines.*

is used to compute the pressure field, which reads:

$$p_{\text{spring}}(r,t) = \frac{3(1-\dot{\delta})}{2\left(1-t+r^2+\delta\right)^2}, \tag{5.50}$$

with $\dot{\delta}$ being the time derivative of the spring compression δ. By injecting the pressure field into Eq. (5.49c), we get the following non-linear differential equation over the spring compression δ:

$$\delta\left(1-t+\delta\right) = \frac{3\kappa_0}{4}\left(1-\dot{\delta}\right). \tag{5.51}$$

We note y the fluid height at the center, and y_{rigid} the fluid height without spring compression, as:

$$y = 1-t+\delta = h_{\text{spring}}(r=0,t) \quad \text{and} \quad y_{\text{rigid}} = 1-t. \tag{5.52}$$

By considering y as a function of y_{rigid}, denoting $y\prime$ its derivative with respect to y_{rigid}, we thus have $y\prime = -\dot{y}$, with $\dot{y}$ the derivative with respect to the time t. Eq. (5.51) becomes an equation over $y(y_{\text{rigid}})$, associated to the initial condition, as:

$$y \times \left[y - y_{\text{rigid}}\right] = \frac{3\kappa_0}{4} y\prime(y_{\text{rigid}}), \tag{5.53a}$$

$$y(y_{\text{rigid}} = 1) = 1 - \delta(0). \tag{5.53b}$$

Using a formal calculation software, like *Mathematica*, an explicit solution is found and reads:

$$y(y_{\text{rigid}}) = \frac{\left[1-\delta(0)\right] e^{-\frac{2y_{\text{rigid}}^2}{3\kappa_0}}}{e^{-\frac{2}{3\kappa_0}} + \sqrt{\frac{2\pi}{3\kappa_0}}\left[1-\delta(0)\right]\Delta\text{Erf}(t)}, \tag{5.54a}$$

$$\text{with} \quad \Delta\text{Erf}(y_{\text{rigid}}) = \left[\text{Erf}\left(\sqrt{\frac{2}{3\kappa_0}}\right) - \text{Erf}\left(\sqrt{\frac{2}{3\kappa_0}}y_{\text{rigid}}\right)\right], \tag{5.54b}$$

with Erf the Gauss error function. By performing the inverse change of variable, the fluid gap h_{spring} as a function of time is derived. Then the spring compression $\delta(t)$ reads:

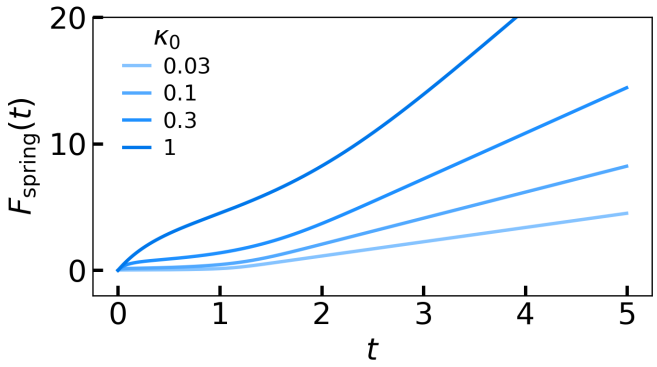

FIG. 5.10. **Theoretical force when only a spring is considered.** *Dimensionless theoretical force F_{spring} as a function of dimensionless time t, computed from Eq. (5.57), for different values of the ratio between viscous stresses and spring elasticity κ_0, as indicated in the legend, and for $\delta(0) = 0$.*

$$\delta(t) = \frac{[1-\delta(0)]\, e^{-\frac{2(1-t)^2}{3\kappa_0}}}{e^{-\frac{2}{3\kappa_0}} + \sqrt{\frac{2\pi}{3\kappa_0}}\,[1-\delta(0)]\,\Delta\mathrm{Erf}(t)} - 1 + t, \tag{5.55a}$$

$$\text{with} \quad \Delta\mathrm{Erf}(t) = \left[\mathrm{Erf}\left(\sqrt{\frac{2}{3\kappa_0}}\right) - \mathrm{Erf}\left(\sqrt{\frac{2}{3\kappa_0}}(1-t)\right)\right], \tag{5.55b}$$

and the pressure p_{spring} using Eq. (5.50), is found to be:

$$p_{\text{spring}}(r,t) = \frac{4\,[1-\delta(0)]\, e^{\frac{2}{3\kappa_0}}}{\kappa_0} \times \frac{(t-1)e^{\frac{2(t^2-2t)}{3\kappa_0}} + [1-\delta(0)] + (t-1)[1-\delta(0)]\sqrt{\frac{2}{3\kappa_0}}e^{\frac{2(t-1)^2}{3\kappa_0}}}{[1-\delta(0)] + r^2 e^{\frac{2(t^2-2t)}{3\kappa_0}}\left[1+\sqrt{\frac{2\pi}{3\kappa_0}}[1-\delta(0)]e^{\frac{2}{3\kappa_0}}\Delta\mathrm{Erf}(t)\right]}. \tag{5.56}$$

Finally, the force is computed as a function of time by integrating the pressure field over the surface of the sphere, with Eq. (5.22). The calculation is performed with *Mathematica*. Finally, the force reads:

$$F_{\text{spring}}(t) = \frac{2\pi}{\kappa_0}\frac{t - 1 + [1-\delta(0)]\, e^{\frac{2(2t-t^2)}{3\kappa_0}} + \sqrt{\frac{2\pi}{3\kappa_0}}\,[1-\delta(0)]\, e^{\frac{2}{3\kappa_0}}(t-1)\Delta\mathrm{Erf}(t)}{1 + \frac{2\pi}{3\kappa_0}\,[1-\delta(0)]\, e^{\frac{2}{3\kappa_0}}\Delta\mathrm{Erf}(t)}, \tag{5.57}$$

with the expression of $\Delta\mathrm{Erf}(t)$ being specified by Eq. (5.55b). The theoretical force F_{spring} is shown in Fig. 5.10, for different values of the parameter κ_0. We observe that the greater κ_0 is (*i.e.* the softer the spring is), the longer the force takes to reach the final, linear regime in time. This final regime corresponds to the case where the fluid gap is thin, and fluid hardly flows in the confined region. Thus, the displacement imposed at the back of the spring compresses the spring.

5.2.2.4 Numerical resolution of the full EHD model

In this section we consider the full model. To solve numerically the problem, a specific half-implicit half-explicit numerical scheme based on an integration kernel was developed in collaboration with Laurent Duchemin.

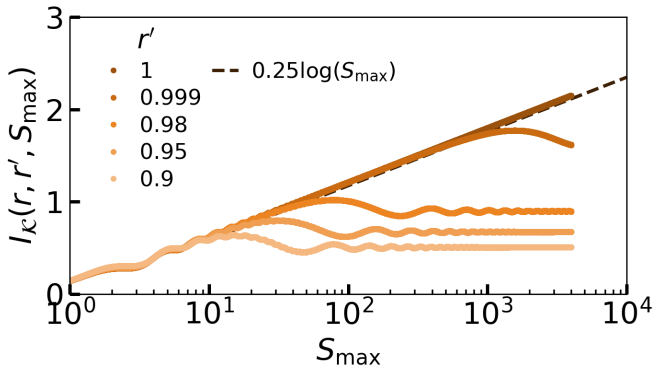

FIG. 5.11. **Convergence of the kernel integral in SFA simulations.** *Truncated integral $I_{\mathcal{K}}(r, r', S_{\max})$ of the product $s\mathcal{G}_\tau^{\text{comp}} J_0(sr)J_0(sr')$ as a function of $S_{\max}$, as defined in Eq. (5.60), for different r', for $r = 1$, $\nu = 0.2$ and $\tau_0 = 1$. For $r = r'$, the integral diverges following a logarithmic scaling.*

Definition of the kernel: We first define an integration kernel noted $\mathcal{K}_{\tau_0,\nu}(r, r')$ to express the deformation profile in a convenient way for numerics:

$$\mathcal{K}_{\tau_0,\nu}(r, r') = \int_0^\infty \mathrm{d}s\, \mathrm{d}s\, \mathcal{G}_\tau^{\text{comp}}(s) s J_0(sr) J_0(sr') \tag{5.58a}$$

$$= \int_0^\infty \mathrm{d}s\, J_0(sr) J_0(sr') \frac{(1-\nu)\left[2\zeta - (4\nu-3)\sinh(2\zeta)\right]}{5 + 4\nu(2\nu-3) + 2\zeta^2 - (4\nu-3)\cosh(2\zeta)}. \tag{5.58b}$$

The deformation profile is then computed from the pressure field, using the kernel $\mathcal{K}_{\tau_0,\nu}(r, r')$, as:

$$w(r,t) = \epsilon_0 \int_0^\infty \mathrm{d}r'\, r' p(r',t) \mathcal{K}_{\tau_0,\nu}(r, r'). \tag{5.59}$$

The geometrical equation (5.36), the thin-film equation (5.38) and the force-balance equation (5.39) are kept identical.

The convergence of the kernel integral defined in Eq. (5.58) may be questioned. We first define the truncated integral, as:

$$I_{\mathcal{K}}(r, r', S_{\max}) = \int_0^{S_{\max}} \mathrm{d}s\, \mathrm{d}s\, \mathcal{G}_\tau^{\text{comp}}(s) s J_0(sr) J_0(sr'). \tag{5.60}$$

The kernel $\mathcal{K}_{\tau_0,\nu}(r, r')$ is recovered by taking the limit $S_{\max} \to \infty$. In Fig. 5.11 we show the truncated integral $I_{\mathcal{K}}(r, r', S_{\max})$ defined in Eq. (5.60), as a function of $S_{\max}$, for different values of r' and a fixed $r = 1$, with $\nu = 0.2$ and $\tau_0 = 1$. We observe that the integral converges for $r \neq r'$, and does not converge for $r = r'$. As a consequence, the kernel $\mathcal{K}_{\tau_0,\nu}(r, r')$ given in Eq. (5.58) defines a distribution that exhibits a singularity for $r = r'$, and takes a finite (if not zero) value for $r \neq r'$. Similarly to a Dirac distribution, the kernel distribution is finite *almost everywhere*. Thus, the product of $r'p(r', t)\mathcal{K}_{\tau_0,\nu}(r, r')$ is integrable, and the deformation profile as written in Eq. (5.59) is still properly defined. Yet, numerical difficulties are encountered, and some fine tuning of various numerical parameters is necessary. In the following paragraphs, we first present a numerical study of the kernel integral as defined in Eq. (5.58). Then we present the full numerical scheme used to simulate a SFA approach.

Optimization of numerical parameters: The time axis t is discretized linearly on N_t points with a time step Δt. We denote the n-th point $t^n = n\Delta t$, and the upper

boundary is given by $T_{\max} = (N_t - 1)\Delta t$. The radial axis r is discretized linearly on N_r points with a space step Δr. We denote the i-th point by $r_i = i\Delta r$, and the upper boundary is given by $R_{\max} = (N_r - 1)\Delta r$. The Hankel axis s is discretized on N_s points being the zeros of the Legendre polynomial of degree N_s, up to the upper boundary noted $S_{\max}$. For each couple (r_i, r'_j), the kernel $\mathcal{K}_{\tau_0,\nu}(ri, r'_j)$ is computed using the Gauss-Legendre quadrature method (described in Appendix. C.2.2), and takes the form of a square matrix of size $N_r \times N_r$, that is denoted $\mathcal{K}_{\tau_0,\nu,ij}$. Equation (5.59) is discretized using a Riemann summation to compute numerically the deformation profile. The pressure field and the deformation profile, expressed at a radial point r_i and a time point t^n are denoted respectively p_i^n and w_i^n. The discretized deformation profile is expressed as:

$$w_i^n = \epsilon_0 \Delta r \sum_{j=0}^{N_r-1} r_j p_j^n \mathcal{K}_{\tau_0,\nu,ij}. \tag{5.61}$$

The method to optimize the problem is described as follows. We consider the set of four numerical parameters $R_{\max}$, N_r, $S_{\max}$, N_s. We use the explicit form of the pressure field in the rigid case given in Eq. (5.47) as a basis, to compute the deformation profile that would be generated by this pressure field. The numerical calculation of the deformation profile is performed on one side with *Python* (noted as w_{py}) using the set of four numerical parameters, and on the other side with *Mathematica* (noted as w_{math}), which is believed to be more precise [269–271]. Results of both methods are compared by computing a numerical error, defined as:

$$\text{Err}(t^n) = \frac{1}{N_r} \sum_{i=0}^{N_r-1} \left[w_{i,\text{py}}^n - w_{i,\text{math}}^n \right]^2. \tag{5.62}$$

The choice of the four parameters $R_{\max}$, N_r, $S_{\max}$, N_s then results from a trade-off between guaranteeing a low numerical error and maintaining a reasonable computation time. In Fig. 5.12(a), we show an example of the deformation profile calculated for a given set of numerical parameters with *Python* and *Mathematica*. We observe agreement between both, with the choice of parameters indicated on the figure. The associated numerical error as defined by Eq. (5.62) is shown in Fig. 5.12(b), for different $S_{\max}$, and $N_s = S_{\max}$. In this case, we find two minima, which define potentially interesting sets of numerical parameters. The study was ran systematically, varying the four parameters $R_{\max}$, N_r, $S_{\max}$, N_s. Two sets were identified: $R_{\max} = 5$, $N_r = 1000$, $S_{\max} = 200$, $N_s = 100$ and $R_{\max} = 10$, $N_r = 2000$, $S_{\max} = 200$, $N_s = 200$. The robustness of calculation with these two choices was tested by changing also the time t. Indeed, as time increases, the sphere gets closer to the rigid boundary and the resulting pressure field gets closer to its divergence point. In Fig. 5.12(c-e), the deformation profile and the associated error are shown for the two choices of numerical parameters, for three different times t. The error increases with the time t, but the calculation is robust as the match between *Mathematica* and *Python* results stays excellent.

In the following, simulations were performed using: $R_{\max} = 5$, $N_r = 1000$, $S_{\max} = 200$, $N_s = 100$, with a computation time of the kernel integral $t_{\text{comp}} \approx 0.1\,\text{s}$. The kernel matrix $\mathcal{K}_{\tau_0,\nu}$ is computed once for all at the beginning of a set of simulations.

One must note the paradoxical aspect of computing a deformation profile from the pressure field p_{rigid} that is specific to a rigid sphere approaching a rigid wall, thus neglecting the substrate deformation. Here, the pressure field p generated by a sphere approached close to a soft coating, with a EHD coupling given by the spring holding the sphere, is seen as a perturbation of the reference pressure field p_{rigid} in the rigid case. Thus, the scaling of the pressure field p, with an EHD coupling and a soft wall, with

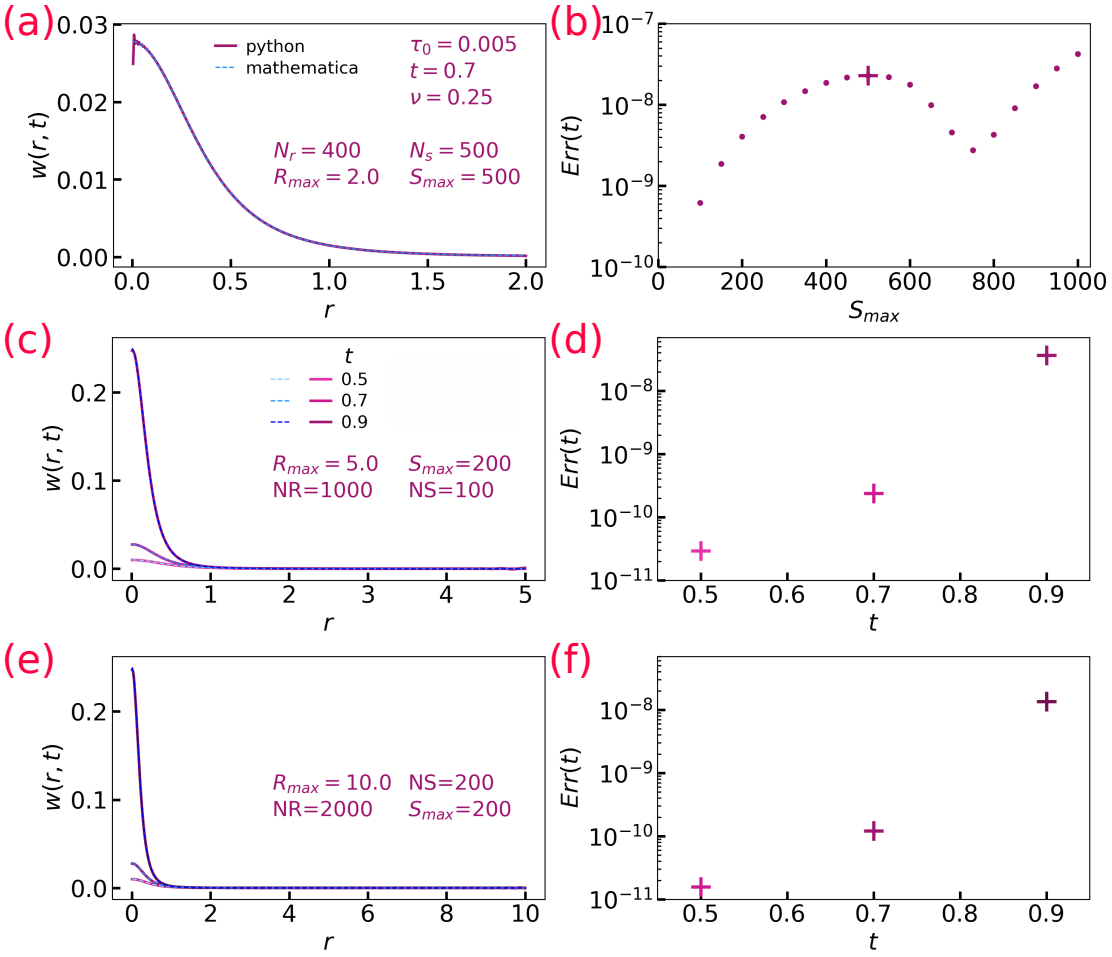

FIG. 5.12. **Optimization of numerical parameters.** *(a): Dimensionless deformation profile generated by the dimensionless pressure field in the rigid case* p_{rigid} *from Eq.* (5.59)*, computed with Mathematica (blue) and Python (pink), for a time* $t = 0.7$*, and using an example set of numerical parameters indicated on the legends, for a dimensionless thickness* $\tau_0 = 0.005$ *and a Poisson ratio* $\nu = 0.25$*. (b): Numerical error between Python and Mathematica results, as defined in Eq.* (5.62)*, as a function of the parameter* S_{max}*, for the three other parameters* N_r*,* N_{max} *and* N_s *indicated in (a). The cross indicates the precise case of (a). (c) and (e): Dimensionless deformation profiles computed with Mathematica (blue) and Python (pink), for three sets of numerical parameters indicated on the legends, a dimensionless thickness* $\tau_0 = 0.005$ *and a Poisson ratio* $\nu = 0.25$*, and three different dimensionless times* t*, computed with the two selected sets of numerical parameters. (d) and (f): Numerical errors as defined in Eq.* (5.62)*, as functions of dimensionless time* t*, for the parameters indicated in (c) and (e) respectively.*

the radial coordinate r, is similar to the one of the pressure field in the rigid case p_{rigid}. Additionally, the reference pressure field in the rigid case p_{rigid} diverges close to contact. When adding the EHD coupling and the soft wall, the pressure is released compared to the reference, rigid case. In summary, if the unrealistic deformation field generated by the pressure field in the rigid case p_{rigid} is efficiently computed, then, the more realistic deformation field generated by the pressure field p, with the EHD coupling and the soft wall, can be computed too.

Discretization scheme of the full model: The thin-film equation as written in Eq. (5.38) is discretized with a half-implicit-half-explicit [272] scheme in time, and a centered finite-difference scheme in space [77, 273]. We first define the flux term $\mathcal{F}(r)$, as:

$$\mathcal{F}(r) = rh^3 \frac{\partial p}{\partial r}, \tag{5.63}$$

such that the thin-film equation (5.38) is written as:

$$\frac{\partial h}{\partial t} = \frac{1}{12r} \frac{\partial \mathcal{F}}{\partial r}. \tag{5.64}$$

The flux term $\mathcal{F}$ is discretized on a dual grid in r, which means in between two points of the main grid. The non-linear terms are expressed at the current time step t^n (half-explicit scheme), while the linear ones are expressed at the next time step t^{n+1} (half-implicit scheme). The latter choice enables to write a linear equation on the pressure field p^{n+1} at the next time step t^{n+1}, using powers of the fluid gap h^n at the current time step t^n as known coefficients. We denote $\mathcal{F}_{i+1/2}^{n+1}$ the flux term expressed at the dual point $r_{i+1/2} = (r_i + r_{i+1})/2$, and at the time step t^{n+1} (based on the unknown pressure at the next time step p^{n+1}), which reads:

$$\mathcal{F}_{i+1/2}^{n+1} = \frac{r_i + r_{i+1}}{2} \left[\frac{h_{i+1}^n + h_i^n}{2} \right]^3 \frac{p_{i+1}^{n+1} - p_i^{n+1}}{\Delta r}. \tag{5.65}$$

The radial derivative of the flux term at point r_i, and at time step t^{n+1}, is defined using a finite-difference scheme, as:

$$\left[\frac{\partial \mathcal{F}}{\partial r} \right]_i^{n+1} = \frac{\mathcal{F}_{i+1/2}^{n+1}. - \mathcal{F}_{i-1/2}^{n+1}}{\Delta r}. \tag{5.66}$$

Finally, we discretize the time derivative of the fluid gap h at point r_i with a finite-difference scheme, and we use the Euler method to integrate the thin-film equation in time. The discretized thin-film equation reads:

$$\frac{h_i^{n+1} - h_i^n}{\Delta t} = \frac{1}{12 r_i} \frac{\mathcal{F}_{i+1}^{n+1}. - \mathcal{F}_{i-1/2}^{n+1}}{\Delta r}. \tag{5.67}$$

Combining Eqs. (5.65) and (5.67), we can write the pressure field and the fluid gap at the next time step t^{n+1}, as functions of the fluid gap at the current time step t^n:

$$\begin{aligned} h_i^{n+1} - \frac{1}{192 r_i} \frac{\Delta t}{\Delta r^2} \Big[& (r_i + r_{i+1}) \left(h_{i+1}^n + h_i^n \right)^3 p_{i+1}^{n+1} \\ & - \left\{ (r_i + r_{i+1}) \left(h_{i+1}^n + h_i^n \right)^3 + (r_i + r_{i-1}) \left(h_{i-1}^n + h_i^n \right)^3 \right\} p_i^{n+1} \\ & + (r_i + r_{i-1}) \left(h_{i-1}^n + h_i^n \right)^3 p_{i-1}^{n+1} \Big] = h_i^n. \end{aligned} \tag{5.68}$$

The geometrical equation, the force balance equation and the deformation profile, as written respectively in Eqs. (5.36), (5.39) and (5.59) are discretized and expressed at the next time step t^{n+1}, as:

$$h_i^{n+1} = 1 - t^{n+1} + r_i^2 + w_i^{n+1} + \delta^{n+1}, \tag{5.69a}$$

$$\delta^{n+1} = \kappa_0 \Delta r \sum_{j=0}^{N_r - 1} r_j p_j^{n+1}, \tag{5.69b}$$

$$w_i^{n+1} = \epsilon_0 \Delta r \sum_{j=0}^{N_r - 1} r_j p_j^{n+1} \mathcal{K}_{\tau_0, \nu, ij}. \tag{5.69c}$$

Equations (5.68), (5.69b), (5.69c) and (5.69a) form a coupled system of $3N_r + 1$ linear equations with $3N_r + 1$ unknowns, being h_i^{n+1}, p_i^{n+1}, w_i^{n+1} and δ^{n+1}. In the following we describe the linear-algebra path that solves the system.

Boundary conditions: The boundary conditions in $r = 0$ are specified by Eqs. (5.32), which state that the gradients of all fields at the center should vanish, as a consequence of axisymmetry. The discretized boundary conditions on the pressure field and the fluid gap, at the current time step t^n, are expressed as:

$$h_0^n = h_1^n, \tag{5.70a}$$
$$p_0^n = p_1^n. \tag{5.70b}$$

Similarly, the boundary condition at $r \to \infty$ on the pressure field prescribes that the extra pressure compared to the atmospheric pressure should vanish far from the center. Thus, the discretized version of Eq. (5.33a) reads:

$$p_{N_r-1}^n = 0. \tag{5.71}$$

Algebraic resolution: The three equations given in Eqs. (5.69) are first combined into a single one by injecting Eq. (5.69b) and Eq. (5.69c) in Eq. (5.69a). Writing on the left side the unknown terms and on the right side the known ones, we get:

$$h_i^{n+1} - \Delta r \sum_{j=0}^{N_r-1} \left[\kappa_0 \delta_{ij} + \epsilon_0 \mathcal{K}_{\tau_0,\nu,ij}\right] r_j p_j^{n+1} = 1 - t^{n+1} + r_i^2, \tag{5.72}$$

with δ_{ij} the Kronecker symbol. We combine the components of the pressure field p_i^{n+1} and the fluid gap h_i^{n+1} at the next time t^{n+1} in the vector $\mathcal{V}^{n+1}$, defined as:

$$\mathcal{V}_i^{n+1} = \begin{cases} p_i^{n+1} & \text{for } i \in [\![0; N_r - 1]\!], \\ h_i^{n+1} & \text{for } i \in [\![N_r; 2N_r - 1]\!]. \end{cases} \tag{5.73}$$

Equations (5.68) and (5.72) can then be written as a matrix equation, taking into account the boundary conditions given in Eqs. (5.70) and (5.71), as:

$$\mathcal{M}^n \cdot \mathcal{V}^{n+1} = \mathcal{R}\mathcal{H}\mathcal{S}^n, \tag{5.74}$$

with $\mathcal{V}^{n+1}$ the vector to solve for and $\mathcal{M}^n$ a matrix to invert. The upper half of the matrix $\mathcal{M}^n$ transcripts the discretized thin-film equation given in Eq. (5.68). Thus, for $i \in [\![1; N_r - 2]\!]$, the matrix $\mathcal{M}^n$ is defined as:

$$\begin{cases} \mathcal{M}_{i,i+1}^n &= -\dfrac{1}{192 r_i} \dfrac{\Delta t}{\Delta r^2} \left(r_i + r_{i-1}\right) \left(h_{i-1}^n + h_i^n\right)^3, \\ \mathcal{M}_{i,i}^n &= \dfrac{1}{192 r_i} \dfrac{\Delta t}{\Delta r^2} \left\{ \left(r_i + r_{i+1}\right) \left(h_{i+1}^n + h_i^n\right)^3 + \left(r_i + r_{i-1}\right) \left(h_{i-1}^n + h_i^n\right)^3 \right\}, \\ \mathcal{M}_{i,i+1}^n &= -\dfrac{1}{192 r_i} \dfrac{\Delta t}{\Delta r^2} \left(r_i + r_{i+1}\right) \left(h_{i+1}^n + h_i^n\right)^3, \\ \mathcal{M}_{i,N_r+i}^n &= 1. \end{cases} \tag{5.75}$$

The lower half transcripts the combined geometrical equation given in Eq. (5.72). Thus, for $i \in [\![N_r; 2N_r - 1]\!]$, the matrix $\mathcal{M}^n$ is defined as:

$$\mathcal{M}_{i,i}^n = 1, \tag{5.76a}$$
$$\mathcal{M}_{i,j}^n = -\Delta r \left[\kappa_0 \delta_{ij} + \epsilon_0 \mathcal{K}_{\tau_0,\nu,ij}\right] r_j. \tag{5.76b}$$

At the edges in $i = 0$ and $i = N_r - 1$, the boundary conditions are:

$$\begin{cases} \mathcal{M}^n_{0,0} & = 1, \\ \mathcal{M}^n_{0,1} & = -1, \\ \mathcal{M}^n_{N_r-1,N_r-1} & = 1. \end{cases} \tag{5.77}$$

The right-hand-side vector $\mathcal{RHS}^n$ is known. It is computed from the pressure field and the fluid gap expressed at time step t^n. The upper half transcripts the right-hand-side of Eq. (5.68), thus for $i \in [\![1; N_r - 2]\!]$, $\mathcal{RHS}^n$ is expressed as:

$$\mathcal{RHS}^n_i = h^n_i. \tag{5.78}$$

The lower half represents the right-hand-side of Eq. (5.72), thus for $i \in [\![N_r; 2N_r - 1]\!]$:

$$\mathcal{RHS}^n_i = 1 - t^n + r_i^2. \tag{5.79}$$

The boundary conditions are transcripted on the edges, for $i = 0$ and $i = N_r - 1$, as:

$$\mathcal{RHS}^n_0 = \mathcal{RHS}^n_{N_r-1} = 0. \tag{5.80}$$

The matrix $\mathcal{M}^n$ can be inverted numerically. Thus, by solving Eq. (5.74), the pressure field and the fluid gap are computed at the next time step t^{n+1}, as:

$$\mathcal{V}^{n+1} = \mathcal{RHS}^n \cdot (\mathcal{M}^n)^{-1}. \tag{5.81}$$

Then, the deformation profile and the spring compression are computed using Eqs. (5.69b) and (5.69c). Finally, the force can be computed by integrating the pressure field over the surface of the sphere. Using a Riemann summation, the discretized force at the next time step t^{n+1} is computed as:

$$F^{n+1} = 2\pi\Delta r \sum_{i=0}^{N_r-1} r_i p_i^{n+1}. \tag{5.82}$$

Initialization: We consider that the simulation starts during the experimental, initial linear regime, when the sphere is far from the elastic substrate. Thus, the EHD coupling between the sphere and the substrate is weak, and the initial substrate deformation $w(r, t = 0)$ is small compared to the vertical length scale H. The sphere moves in the fluid at a constant velocity equal to the command velocity imposed at the back of the spring. The resulting force applied on the sphere is the Stokes drag, that generates an initial compression of the spring $\delta(0)$. The order of magnitude of this initial spring compression is calculated in Sec. 5.1.4.1 ($\delta(0) \sim 10^{-5}$ nm). As a result, the initial spring compression is negligible compared to the initial fluid gap ($h(0) \sim 1\,\mu$m)

With both the initial spring compression and substrate deformation being small, the initial fluid gap $h(r, t = 0)$ and pressure field $p(r, t = 0)$ are approximated by the ones computed in the rigid case, $h_{\text{rigid}}(r, t = 0)$ and $p_{\text{rigid}}(r, t = 0)$, respectively, given is Eqs. (5.45a) and (5.47) respectively. The initial spring compression $\delta(t = 0)$, deformation profile $w(r, t = 0)$ and finally the force $F(t = 0)$ are then computed from the initial,

rigid pressure field. In summary, for $i \in [\![0, N_r - 1]\!]$ a simulation is initialized as follow:

$$p_i^0 = p_{\text{rigid}}(r_i, t = 0), \tag{5.83a}$$

$$h_i^0 = h_{\text{rigid}}(r_i, t = 0), \tag{5.83b}$$

$$\delta^0 = \kappa_0 \Delta r \sum_{j=0}^{N_r-1} r_j p_j^0, \tag{5.83c}$$

$$w_i^0 = \epsilon_0 \Delta r \sum_{j=0}^{N_r-1} r_j p_j^0 \mathcal{K}_{\tau_0,\nu,ij}, \tag{5.83d}$$

$$F^0 = 2\pi \Delta r \sum_{j=0}^{N_r-1} r_j p_j^0. \tag{5.83e}$$

Numerical simulation for SFA experiments: The numerical parameters ϵ_0, κ_0, τ_0 and ν are first calculated based on experimental characteristics. A choice has to be made for the vertical distance scale H. The latter is directly related to the resolution of the simulation, as both the time and the vertical length are scaled by H (see Eq. (5.35)). Essentially, the H parameter acts as a zoom factor on a distance-time representation. The matrix of the kernel $\mathcal{K}_{\tau_0,\nu}$ is computed once for all at the beginning. Then, the numerical resolution of the full model presented in this subsection consists of calculating the initial pressure field p_i^0, fluid gap h_i^0, deformation profile w_i^0, and spring compression δ^0 based on the initialization step described above. The initial force F^0 is computed too. From quantities expressed at the initial time step t^0, all fields and quantities at the next time step t^1 are computed, following the algebraic resolution presented above. The operation is repeated $N_t - 1$ times by default. Eventually, the simulation is stopped when showing unphysical results (*e.g.* a negative fluid gap at $r = 0$, a negative spring compression or a fluid gap at $r = 0$ greater than its initial value...).

When performing SFA experiments, the measured quantity $D(t)$ is the distance between the two glass surfaces, which means the distance from the bottom of the elastic coating up to the surface of the sphere, at the center in $r = 0$. This distance includes the layer of deformed gel and the fluid gap. Thus, to link the experimental quantity $D(t)$ to the theoretical ones (with dimensions), we write:

$$D(t) = \tau - w(r = 0, t) + h(r = 0, t). \tag{5.84}$$

We introduce the dimensionless experimental distance $\tilde{D} = D/H$. In dimensionless writing, the latter equation reads:

$$\tilde{D}(\tilde{t}) = \tau_0 \sqrt{\frac{2R}{H}} - \tilde{w}(0, \tilde{t}) + \tilde{h}(0, \tilde{t}). \tag{5.85}$$

Finally, as the output of the simulation, the distance D is discretized and numerically computed as:

$$D^n = \tau_0 \sqrt{\frac{2R}{H}} - w_0^n + h_0^n. \tag{5.86}$$

To be compared to experimental data with dimension, the dimensionless, numerical distance D is finally multiplied by the distance H (defined in the simulation parameters).

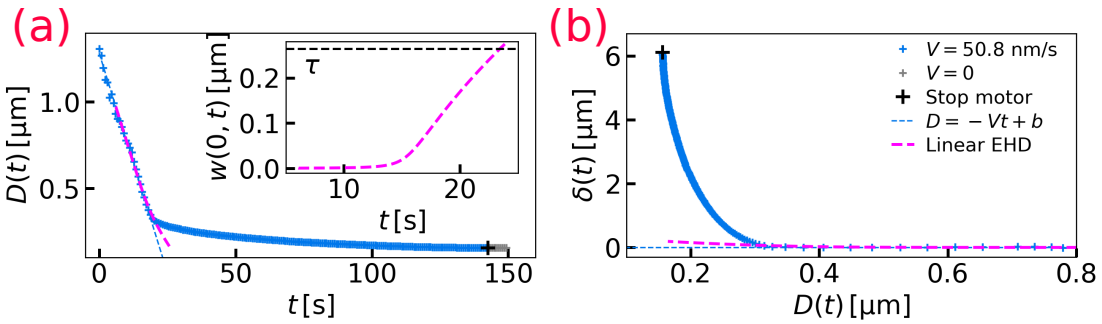

FIG. 5.13. **Linear elastic model for a sphere approaching a gel with an EHD coupling.** *(a): Distance between the two glass surfaces D as a function of time t, as an example of SFA data explained by modeling the gel as a linear elastic solid. The simulation is performed for a Young's modulus of* 5 kPa *and a Poisson ratio of* $\nu = 0.2$. *The initial, linear regime is recalled to exhibit the deviation of the simulated curve from a purely linear behavior in time. Inset: Deformation as a function of time, predicted by the numerical simulation. (b): Spring compression computed from the data of (a), as a function of the distance between the two glass surfaces D.*

5.2.2.5 Results

In Fig. 5.13 is shown a numerical simulation of a SFA approach in lubrication conditions, together with experimental data. The distance between the two glass surfaces D is shown as a function of time in Fig 5.13(a). In Fig. 5.13(b), the spring compression δ is shown as a function of the distance D between the two glass surfaces. The simulation presented here was performed for the following numerical parameters: $H = 0.25\,\mu$m, $\epsilon_0 = 6.51$, $\kappa_0 = 8.64.10^{-3}$, $\tau_0 = 1.97.10^{-3}$ and a Poisson ratio of $\nu = 0.2$. These numerical parameters were calculated from known and previously estimated physical parameters, except the Young's modulus that was adjusted at 5 kPa. The numerical curve was also adjusted to match the linear fit performed on the initial regime. An adjustment was necessary, to catch the deviation from the linear regime. Thus only one fitting parameter acting as an offset in time (and thus in distance D) was used.

First, we observe in both representations that the simulation exhibits a deviation from the initial, linear regime, as a result of the vicinity of the soft substrate. This deviation catches the experimental data better than the linear regime, on a small portion of the curve, during the five seconds before the main inflection point. Thus, when an interaction between the spherical probe and the hydrogel becomes measurable, the hydrogel can be described as a purely elastic and compressible layer, for a few seconds. Yet, the model does not predict the position of the inflection point at $t \approx 20$ s. The gel is modeled as a compressible elastic solid, whose mechanical behavior is described by a linear stress-strain relationship. Such an elasticity law supposes small deformations. As the sphere approaches the soft hydrogel, one can expect the deformations of the gel to increase, enough to break the hypothesis of small deformations. Indeed, as shown in the inset of Fig. 5.13(a), the predicted deformation at the center increases with time, and the hypothesis of small deformation is broken. In the following subsection, we propose an *ad-hoc* non-linear elasticity law that takes into account the finite thickness of the gel.

5.2.3 Lubrication regime at large deformations

In this subsection, the SFA experiment is modeled as in the previous subsection and the schematic of the experiment presented in Fig. 5.8 still holds. However, the hydrogel is

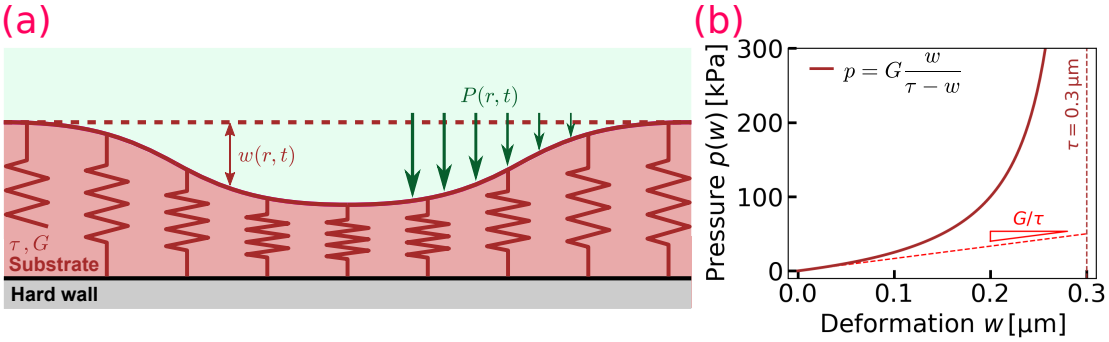

FIG. 5.14. **Non-linear elastic model for a largely deformed hydrogel.** *(a): Schematic of the situation. The hydrogel is considered as an elastic layer of thickness τ and shear modulus G, which is modeled as a mattress of springs, characteristic of a Winkler-like model. An external pressure field $p(r,t)$ is applied and generates a deformation profile $w(r,t)$.(b): Ad-hoc elasticity law describing the mechanical response of the hydrogel, computed with Eq. (5.87), for a gel of thickness $\tau = 0.3\,\mu$m and of shear modulus $G = 50\,$MPa.*

modeled differently.

5.2.3.1 Non-linear elasticity

Model: Here we present a simple, *ad-hoc* elastic model used to describe the mechanical behavior of the gel when larger deformations are encountered, taking into account its finite thickness. Two main hypotheses are taken into account. (i) Similarly to the rigid case, in which the pressure field diverges when the sphere touches the rigid boundary, here we consider that the pressure field should diverge when the deformation amplitude of the soft layer reaches its thickness, *e.g.* when the free surface of the gel touches the rigid boundary underneath. (ii) Similarly to Winkler's foundation model, the gel is described by a mattress of independent springs, as illustrated by Fig. 5.14(a). Thus, we neglect any contribution of the pressure field applied at a given position r to the deformation profile at another position r'. As a consequence of (i) and (ii), we postulate the following pressure-deformation relationship:

$$p(r,t) = G\frac{w(r,t)}{\tau - w(r,t)}, \tag{5.87}$$

with G the shear modulus. The pressure as a function of the deformation is plotted in Fig. 5.14(b), with Eq. (5.87), for a thickness of $\tau = 0.3\,\mu$m and a shear modulus of $G = 50\,$MPa. We recover the standard Winkler's foundation model when writing a Taylor development of the latter expression at order one in w/τ:

$$p(r,t) \simeq G\frac{w}{\tau}\left(1 + \frac{w}{\tau} + \left(\frac{w}{\tau}\right)^2\right). \tag{5.88}$$

The geometrical equation (5.20), the thin-film equation (5.21) and the force-balance equation (5.24), introduced in the previous section 5.2.2.2, are conserved. However, Eq. (5.30b) is replaced by:

$$w(r,t) = \tau\frac{p(r,t)}{G + p(r,t)}, \tag{5.89}$$

which is obtained by isolating $w(r,t)$ in Eq. (5.87). The boundary conditions are kept identical.

Non-dimensionalization: Using the scalings introduced in the previous section, we write Eq. (5.89) under a dimensionless form, as:

$$\tilde{w}(\tilde{r},\tilde{t}) = \epsilon_0 \tau_0 \frac{\tilde{p}(\tilde{r},\tilde{t})}{1+\epsilon_0\sqrt{\frac{H}{2R}}\tilde{p}(\tilde{r},\tilde{t})}, \tag{5.90}$$

with ϵ_0 and τ_0 being defined in Eqs. (5.44b) and (5.44a), respectively. We recall the three other equations (5.36), (5.38) and (5.39) written under a dimensionless form:

$$\tilde{h}(\tilde{r},\tilde{t}) \simeq 1 - \tilde{t} + \tilde{w}(\tilde{r},\tilde{t}) + \tilde{\delta}(\tilde{t}) + \tilde{r}^2, \tag{5.91a}$$

$$\frac{\partial \tilde{h}}{\partial \tilde{t}} = \frac{1}{12\tilde{r}}\frac{\partial}{\partial \tilde{r}}\left[\tilde{r}\tilde{h}^3\frac{\partial \tilde{p}}{\partial \tilde{r}}\right], \tag{5.91b}$$

$$\tilde{\delta}(t) = \kappa_0 \int_0^\infty \mathrm{d}\tilde{r}\,\tilde{r}\tilde{p}(\tilde{r},\tilde{t}). \tag{5.91c}$$

In the following paragraphs, to lighten the notation, we omit the tilde symbol ($\tilde{}$) on dimensionless quantities.

5.2.3.2 Numerical resolution

To solve numerically the model presented in this section, we use the iterative Newton-Raphson method [273, 274], which is known to be adapted for highly non-linear problems. Knowing the solution for the fields at the current time step t^n, the solution at the next time step t^{n+1} is computed by iteration.

Discretization scheme: The thin-film equation as written in Eq. (5.38) is discretized using an implicit scheme in time, and the same finite-difference scheme in space as in the previous section. Every quantity is expressed at the next time step t^{n+1}. The flux term as defined in Eq. (5.63) is again discretized on the dual grid. We write the flux at point $r_{i+1/2}$ and at the next time step t^{n+1}, as:

$$\mathcal{F}_{i+1/2}^{n+1} = \frac{r_i + r_{i+1}}{2}\left[\frac{h_{i+1}^{n+1} + h_i^{n+1}}{2}\right]^3 \frac{p_{i+1}^{n+1} - p_i^{n+1}}{\Delta r}. \tag{5.92}$$

Following then the same path as in the previous section, the radial derivative of the flux at the point r_i is given by Eq. (5.66), and the discretized thin-film equation is given by Eq. (5.67). We finally derive an equation over the pressure field and the fluid gap at the next time step t^{n+1}, as a function of the fluid gap at the current time step, as:

$$\begin{aligned} -192 r_i \frac{\Delta r^2}{\Delta t} h_i^{n+1} &+ (r_i + r_{i+1})\left(h_{i+1}^{n+1} + h_i^{n+1}\right)^3 p_{i+1}^{n+1} \\ &- \left\{(r_i + r_{i+1})\left(h_{i+1}^{n+1} + h_i^{n+1}\right)^3 + (r_i + r_{i-1})\left(h_{i-1}^{n+1} + h_i^{n+1}\right)^3\right\} p_i^{n+1} \\ &+ (r_i + r_{i-1})\left(h_{i-1}^{n+1} + h_i^{n+1}\right)^3 p_{i-1}^{n+1} = -192 r_i \frac{\Delta r^2}{\Delta t} h_i^n. \end{aligned} \tag{5.93}$$

The geometrical equation, the force-balance equation and the deformation profile, as written respectively in Eqs. (5.91a), (5.91c) and (5.90) are discretized as Eqs. (5.69),

and thus read:

$$h_i^{n+1} = 1 - t^{n+1} + r_i^2 + w_i^{n+1} + \delta^{n+1}, \tag{5.94a}$$

$$\delta^{n+1} = \kappa_0 \Delta r \sum_{j=0}^{N_r-1} r_j p_j^{n+1}, \tag{5.94b}$$

$$w_i^{n+1} = \epsilon_0 \tau_0 \frac{p_i^{n+1}}{1 + \epsilon_0 \sqrt{\frac{H}{2R}} p_i^{n+1}}. \tag{5.94c}$$

Equations (5.93), (5.94b), (5.94c) and (5.94a) form a coupled system of $3N_r + 1$ non-linear equations with $3N_r + 1$ unknowns, namely h_i^{n+1}, p_i^{n+1}, w_i^{n+1} and δ^{n+1}. In the following we describe how these equations are linearized with the Newton-Raphson method.

Boundary conditions: The boundary conditions in $r = 0$ and $r \to \infty$ on the pressure field p and the fluid gap h are the same as in the previous sections, and given by Eqs. (5.70) and (5.71).

Non-linear operator of the Newton-Raphson method: The three equations given in Eqs. (5.94) are first combined into a single by injecting Eq. (5.94b) and Eq. (5.94c) in Eq. (5.94a). Writing on the left side the unknown terms and on the right side the known ones, we get:

$$h_i^{n+1} - \kappa_0 \Delta r \sum_{j=0}^{N_r-1} r_j p_j^{n+1} - \epsilon_0 \tau_0 \frac{p_i^{n+1}}{1 + \epsilon_0 \sqrt{\frac{H}{2R}} p_i^{n+1}} = 1 - t^{n+1} + r_i^2. \tag{5.95}$$

As in the previous sections, we combine the components of the pressure field p_i^{n+1} and the fluid gap h_i^{n+1} at the next time t^{n+1} in the vector $\mathcal{V}^{n+1}$, defined as:

$$\mathcal{V}_i^{n+1} = \begin{cases} p_i^{n+1} & \text{for } i \in [\![0; N_r - 1]\!], \\ h_i^{n+1} & \text{for } i \in [\![N_r; 2N_r - 1]\!]. \end{cases} \tag{5.96}$$

Equations (5.93) and (5.95) can then be written under the form of a non-linear operator, applied on the vector $\mathcal{V}^{n+1}$, as:

$$\mathcal{OP}\left(\mathcal{V}^{n+1}\right) = \mathcal{RHS}^n, \tag{5.97}$$

with $\mathcal{RHS}^n$ the right-hand-side vector, being a known vector expressed with fields at the current time step t^n. The upper half of the non-linear operator $\mathcal{OP}$ transcripts the discretized thin-film equation given in Eq. (5.93). Thus, for $i \in [\![1; N_r - 2]\!]$, the operator $\mathcal{OP}(\mathcal{V}^{n+1})$ is expressed at a point r_i as:

$$\begin{aligned} \left[\mathcal{OP}(\mathcal{V}^{n+1})\right]_i = &-192 r_i \frac{\Delta r^2}{\Delta t} h_i^{n+1} + (r_i + r_{i+1}) \left(h_{i+1}^{n+1} + h_i^{n+1}\right)^3 p_{i+1}^{n+1} \\ &- \left\{ (r_i + r_{i+1}) \left(h_{i+1}^{n+1} + h_i^{n+1}\right)^3 + (r_i + r_{i-1}) \left(h_{i-1}^{n+1} + h_i^{n+1}\right)^3 \right\} p_i^{n+1} \\ &+ (r_i + r_{i-1}) \left(h_{i-1}^{n+1} + h_i^{n+1}\right)^3 p_{i-1}^{n+1}. \end{aligned} \tag{5.98}$$

The lower half transcripts the combined geometrical equation given in Eq. (5.95). Thus, for $i \in [\![N_r; 2N_r - 1]\!]$, the operator $\mathcal{OP}(\mathcal{V}^{n+1})$ is defined at point r_i as:

$$\left[\mathcal{OP}(\mathcal{V}^{n+1})\right]_i = h_i^{n+1} - \kappa_0 \Delta r \sum_{j=0}^{N_r-1} r_j p_j^{n+1} - \epsilon_0 \tau_0 \frac{p_i^{n+1}}{1 + \epsilon_0 \sqrt{\frac{H}{2R}} p_i^{n+1}}. \tag{5.99}$$

At the edges in $i = 0$ and $i = N_r - 1$, the boundary conditions are:

$$\begin{cases} \left[\mathcal{OP}(\mathcal{V}^{n+1})\right]_0 & = p_1^{n+1} - p_0^{n+1} \\ \left[\mathcal{OP}(\mathcal{V}^{n+1})\right]_{N_r-1} & = -p_{N_r-1}^{n+1}. \end{cases} \tag{5.100}$$

The right-hand-side vector $\mathcal{RHS}^n$ is known. The latter is computed from the fluid gap expressed at the current time step t^n. The upper half transcripts the right-hand-side of Eq. (5.93), thus for $i \in [\![1; N_r - 2]\!]$, $\mathcal{RHS}^n$ is expressed as:

$$\mathcal{RHS}_i^n = -192 r_i \frac{\Delta r^2}{\Delta t} h_i^n. \tag{5.101}$$

The lower half represents the right-hand-side of Eq. (5.95), thus for $i \in [\![N_r; 2N_r - 1]\!]$:

$$\mathcal{RHS}_i^n = 1 - t^n + r_i^2. \tag{5.102}$$

The boundary conditions are transcripted on the edges, for $i = 0$ and $i = N_r - 1$, as:

$$\mathcal{RHS}_0 = \mathcal{RHS}_{N_r-1} = 0. \tag{5.103}$$

Linearization and computation of an iteration: The principle of the Newton-Raphson method is to converge towards the solution $\mathcal{V}^{n+1}$ of the equation (5.97) by iterations. We consider then the current approximation $\tilde{\mathcal{V}}$ of the solution at the current iteration, and look for a better one, at the next iteration $\tilde{\mathcal{V}}^{\text{next}}$, such that:

$$\mathcal{OP}\left(\tilde{\mathcal{V}}^{\text{next}}\right) \approx \mathcal{OP}\left(\mathcal{V}^{n+1}\right) = \mathcal{RHS}^n. \tag{5.104}$$

To solve the system of equations represented by Eq. (5.104), for the approximated vector $\tilde{\mathcal{V}}^{\text{next}}$, one must linearize the non-linear operator $\mathcal{OP}$. Thus, we write a Taylor expansion around the current approximation $\tilde{\mathcal{V}}$ at order one in $\tilde{\mathcal{V}}^{\text{next}} - \tilde{\mathcal{V}}$, which reads:

$$\mathcal{OP}\left(\tilde{\mathcal{V}}^{\text{next}}\right) \approx \mathcal{OP}\left(\tilde{\mathcal{V}}\right) + \mathcal{J} \cdot \left[\tilde{\mathcal{V}}^{\text{next}} - \tilde{\mathcal{V}}\right] \approx \mathcal{RHS}^n, \tag{5.105}$$

with $\mathcal{J}$ the Jacobian matrix of the non-linear operator $\mathcal{OP}$, defined as:

$$\mathcal{J}_{ij}\left(\mathcal{V}\right) = \frac{\partial \left[\mathcal{OP}\left(\mathcal{V}\right)\right]_i}{\partial V_j}. \tag{5.106}$$

Equation (5.105) is solved by isolating $\mathcal{V}^{\text{next}}$:

$$\tilde{\mathcal{V}}^{\text{next}} \approx \mathcal{J}^{-1} \cdot \left[\mathcal{RHS}^n - \mathcal{OP}\left(\tilde{\mathcal{V}}\right)\right] + \tilde{\mathcal{V}}. \tag{5.107}$$

The difference $\mathcal{RHS}^n - \mathcal{OP}\left(\tilde{\mathcal{V}}\right)$ is called the residual. A condition to compute the next approximation $\tilde{\mathcal{V}}^{\text{next}}$ is then that the Jacobian $\mathcal{J}$ can be inverted. The next iteration is initialized by replacing $\tilde{\mathcal{V}}$ by $\tilde{\mathcal{V}}^{\text{next}}$, and the same process is repeated. The difference between two successive approximations $\tilde{\mathcal{V}}^{\text{next}} - \tilde{\mathcal{V}}$ should be asymptotically equal to zero with the increasing number of iterations, to ensure the convergence of the method. When the difference $\mathrm{d}\tilde{\mathcal{V}}$ passes below a prescribed threshold (which is set at 10^{-9} for the simulations presented here), or after a prescribed maximum number of iterations (which is set at 10 for the simulations presented here) if the latter threshold is not reached, the iterative process is stopped. The last approximation defines the solution at the next time step $\mathcal{V}^{n+1}$. The pressure field p^{n+1} and the fluid gap h^{n+1} at the next time step t^{n+1} are extracted from the vector $\mathcal{V}^{n+1}$. Finally, the deformation profile w^{n+1} and the spring compression δ^{n+1} can be computed using Eqs. (5.94c) and (5.94b), and the force is obtained by integrating the pressure field over the surface of the sphere, as:

$$F^{n+1} = 2\pi\Delta r \sum_{i=0}^{N_r-1} r_i p_i^{n+1}. \tag{5.108}$$

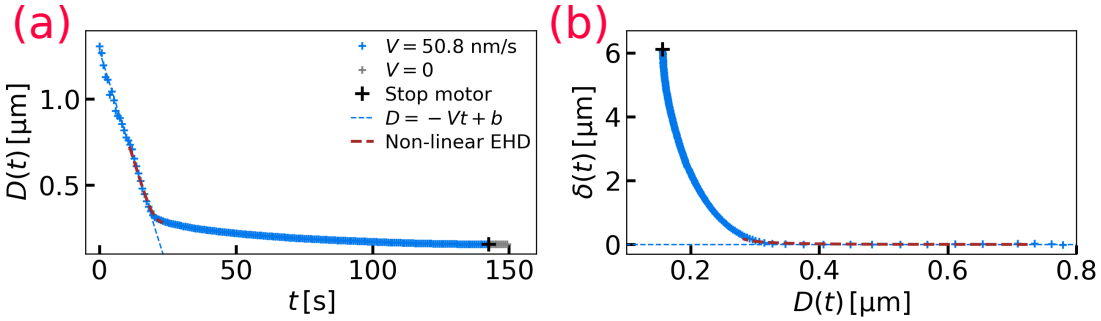

FIG. 5.15. **Non-linear elastic model for a sphere approaching a gel with an EHD coupling.** *(a): Distance between the two glass surfaces D as a function of time t, as an example of SFA data explained by modeling the gel as a mattress of non-linear springs. The simulation is performed for a Young's modulus of* 5 kPa *and a Poisson ratio of* $\nu = 0.2$*. The initial, linear regime is recalled to exhibit the deviation of the simulated curve from a purely linear behavior in time. (b): Spring compression computed from the data of (a), as a function of the distance between the two glass surfaces D.*

Initialization: Similarly to the previous section, the initialization of a given numerical simulation is done on the rigid case. The different fields and quantities are computed at time t^0 using Eqs. (5.83), except the deformation profile that is computed using Eq. (5.94c) expressed at time t^0, as:

$$w_i^0 = \epsilon_0 \tau_0 \frac{p_i^0}{1 + \epsilon_0 \sqrt{\frac{H}{2R}} p_i^0}. \tag{5.109}$$

The quantities are then computed at time step t^1 by iterations, as described in the previous paragraph, then at time t^2, *etc.* Finally, to compare the result of the numerical simulation to experimental data, we link the measured distance D^n between the two glass surfaces to the fluid gap h^n at time step t^n, with Eq. (5.86).

5.2.3.3 Results

In Fig. 5.15 we show a numerical simulation of a SFA approach in lubrication conditions, together with experimental data. As for the linear case, the distance between the two glass surfaces D is shown as a function of time in Fig 5.15(a). In Fig. 5.15(b), the spring compression δ is shown as a function of the distance D between the two glass surfaces. The numerical parameters ϵ_0, κ_0, τ_0 and the Poisson ratio ν are identical. The adjustment of the numerical curve on the experimental data, is still performed using an offset as a fitting parameter, and the latter is kept identical too.

As for the linear case, we observe in both representations that the numerical curve exhibits a deviation from the initial, linear regime, as a result of the vicinity of the substrate. This deviation catches the experimental data better than the linear regime, on the small portion of the curve, during the five seconds before the main inflection point of the experimental data. Furthermore, and in contrast to the linear model, the non-linear model catches the main inflection point of the experimental data at about $t \approx 20$ s. Thus, the gel can be modeled as a mattress of springs around the inflection point, whose mechanical behavior is described by a non-linear stress-strain relationship. Such a type of elasticity laws are often used to describe polymeric materials exhibiting a strain-hardening behavior, and experiencing large deformations [275–280].

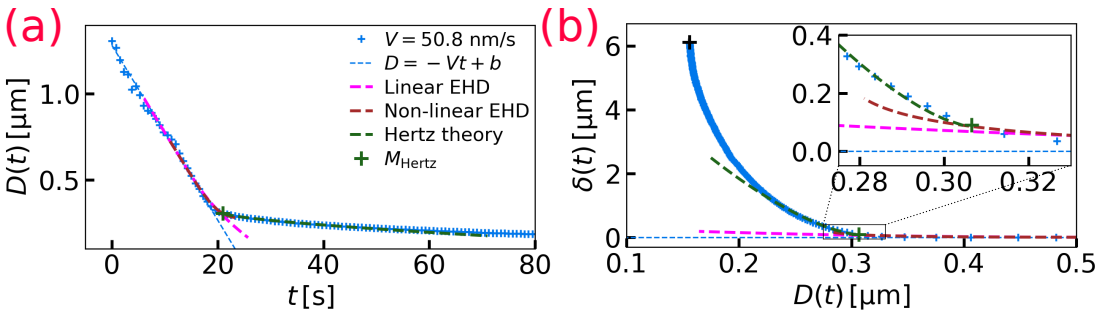

FIG. 5.16. **SFA experimental data compared to a succession of different models.** *(a): Distance between the two glass surfaces D as a function of time t. The experimental data is compared to different models, in the early-time, lubrication regime and in the late-time, contact regime, detailed in the legend. (b): Spring compression computed from the data of (a), as a function of the distance between the two glass surfaces D. The theoretical curves are detailed in the legend of (a). The inset shows a zoom on the region indicated by the gray rectangle, around the point M_{Hertz} and the transition between the lubricated and contact regimes.*

However, if the numerical computation of the SFA approaches exhibit a major inflection point using a strain-hardening type of elastic model, the calculation fails just after, as observed in Fig. 5.15 at $t \approx 23\,\text{s}$. The non-linear model presented in this section is adapted to describe an elastic layer encountering large deformations, in lubrication conditions. As the spherical probe approaches the sample, the deformation is larger and the contact is still lubricated, until the sphere touches the sample. When the contact is made, one can expect the model to break, as the lubrication layer thickness has vanished. To investigate why the numerical simulation breaks just after the inflection point, in the following, we gather results from the modeling of the contact problem and the lubrication problem.

5.3 Synthesis and discussion

5.3.1 Succession of different models

We gather the results of the modeling of the lubrication regime and the ones of the contact regime. In Fig. 5.16, we show one experimental approach together with the different models described in this Chapter. In the initial, linear regime in time (see Fig. 5.16(a)), the resulting force applied on the spherical probe approaching the soft substrate in water is the Stokes drag. The coupling between the probe and the gel is weak, thus, the extra spring compression δ is negligible (see Fig. 5.16(b)). Then, as the sphere approaches, the EHD coupling with the soft substrate increases and we observe a slight deviation from the linear regime, for $t = 17 - 20\,\text{s}$. This deviation is predicted by the EHD model based on a linear elastic response of the gel, in lubrication condition. Then, a major inflection point is observed in the experimental data, both on the distance-time and the compression-distance representations. The inflection point is furthermore predicted by the non-linear elasticity model, in lubrication conditions (see Fig. 5.16(b), inset). Then, the experimental data shows a slow relaxation of the distance D as a function of time t, and simultaneously the spring compression δ strongly increases. This regime is well-described by the Hertz theory, from only a few experimental points after the main inflection point. Finally, the experimental data reaches a constant and final value of distance D and the spring compression diverges. That last part is currently not

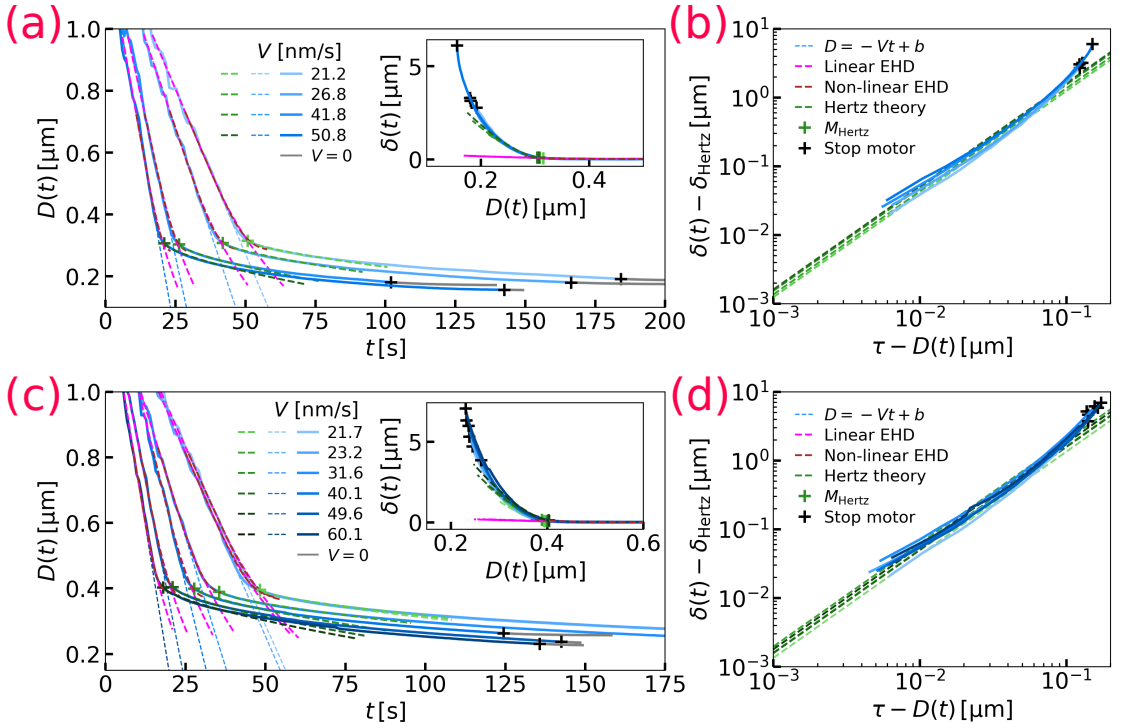

FIG. 5.17. **Summary of SFA experimental and modeling data.** *(a): Main panel: distance between the two glass surfaces D as a function of time t, for four different approach velocities V specified in the legend, corresponding to the first data set. The experimental data is compared to the different models described in this Chapter, for each velocity. Inset: Spring compression δ as a function of the distance D, from the experimental and numerical data of the main panel. (b): Spring compression δ as a function of the indentation $\tau - D$. The experimental data are fitted with Hertz contact theory. The legend indicates the different modeling elements represented in (a). (c): as for (a), for the second data set. (d): as for (b), for the second data set.*

described by a theory, but, an interesting perspective would be to build a contact model taking into account a non-linear elasticity of the substrate, in the large-deformation regime.

5.3.2 Comparison in velocities and reproducibility of the data

The modeling work presented in this Chapter exploits one single approach curve of a given SFA data set made on a given sample. SFA experiments are known to be difficult and delicate. Moreover, the synthesis of nanometric and ultra-clean hydrogel films is also a challenge. Yet, after numerous (about twenty) repetitions of the entire experimental process, two data sets were judged as valuable, composed of a total of ten approach curves. Therefore, the modeling work was repeated on these approach curves. In Fig. 5.17, we show a synthesis SFA experimental result, together with modelisation results. In Figs. 5.17(a) and (b), we show the results from the first data set, constituted of four approach curves, obtained by performing experiments on a sample of dry thickness $\tau_{\text{dry}} = 66\,\text{nm}$. In Figs. 5.17(c) and (d), we show the results from the second data set, composed of six approach curves, obtained by performing experiments on a similar sample of dry thickness $\tau_{\text{dry}} = 65\,\text{nm}$. In Figs. 5.17(a) and (c), we show on the main panel the distance between the two glass surfaces D as a function of time t, for the

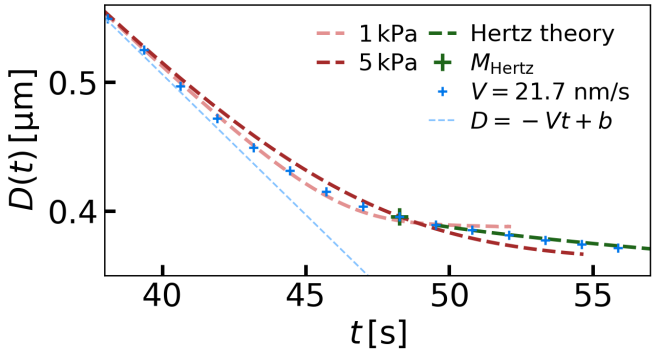

FIG. 5.18. **Comparison of numerical simulations with two different Young's Moduli to experimental data.** *Distance between the two glass surfaces D as a function of time t. The experimental data is compared to numerical simulations based on the non-linear EHD model, for two different values of the Young's modulus indicated in the legend.*

different approach velocities. The inset shows the spring compression δ as a function of the distance D. The initial, linear regime provides a measurement of the velocities. The numerical simulations based on the linear and non-linear EHD models are represented. Simulations were ran for a Young's modulus $E = 5\,\text{kPa}$, for both sets. Figures 5.17(b) and (d) show the late-time regime, fitted with the Hertz contact model. The points M_{Hertz} defined in Sec 5.2.1 are reported on panels (a) and (c) respectively, as well as the numerical computation of the distance as a function of time, based on the fitting parameters. We observe that these ten experimental approaches are well-described by the successive models. Thus the modeling work presented in the Chapter appears as robust to the variation of the velocity.

5.3.3 Estimation of the Young's modulus in lubricated regime

The numerical simulation performed based on both the linear and non-linear EHD models provide an estimate of the Young's modulus of the swollen PNIPAM gel. The computation time for a single curve, with a good resolution, is about 20 hours (on a powerful, experiment-dedicated computer, RAM 64 Go and processor *AMD Ryzen 3900X* 12 cores). Additionally, a numerical simulation enables to appreciate the relevance of a choice of Young's modulus, but does not provide the *best* value as a fit would do. The numerical simulations presented in this Chapter were performed for a Young's modulus $E = 5\,\text{kPa}$, the value for which the accordance between the numerical and experimental data is overall the best, among the tested values. For a matter of comparison, in Fig. 5.18, we show an experimental approach curve, together with two numerical curves, obtained by performing simulations based on the non-linear EHD model with two different values of Young's modulus: $E = 1\,\text{kPa}$ and $E = 5\,\text{kPa}$. The difference is particularly visible around the inflection point. In the following, we establish a systematic comparison.

Before the inflection point: A few seconds before the inflection point, the experimental data deviates from the initial, linear regime. In this portion of the data, the numerical simulation performed with a larger Young's modulus exhibit a larger deviation from the linear regime. In this part, the experimental data shown on Fig. 5.18 appears in between the two numerical curves, maybe closer to the one performed with $E = 1\,\text{kPa}$.

Inflection point: The numerical simulation performed with a smaller Young's modulus exhibits a sharper inflection point. Here, the inflection point shown by the experimental data is more spread out. Thus the simulation performed with $E = 5\,\text{kPa}$ may match better this experimental curve in particular.

After the inflection point: The numerical simulation performed with a smaller Young's modulus saturates faster, and results in a larger distance D. On that portion of the curve, the experimental data shown in Fig. 5.18 appears in between the two numerical curves, but does not saturates as fast as the simulation performed with $E = 1\,\text{kPa}$. The one performed with $E = 5\,\text{kPa}$ may match better the experimental data.

Estimation of E : In summary, the precise approach curve represented in Fig. 5.18 appears in between the two numerical curves, performed with $E = 1\,\text{kPa}$ and $E = 5\,\text{kPa}$. Extra numerical simulations could be ran to refine the estimation of the Young's modulus (taking $E \in [1; 5]$ kPa), for all the sets of curves, and would catch even better the experimental data.

5.3.4 Contact point and crossover between lubrication and contact regimes

The fitting of experimental data with the Hertz contact model enables to estimate the contact point. The point M_{Hertz} that was defined in Sec. 5.2.1 represents the moment from which Hertz model catches the data, and may be interpreted as the contact point. Figure 5.19 focuses on the point M_{Hertz} for a given approach curve. On Fig. 5.19(a) we show the distance D as a function of time, for reference. On Fig. 5.19(b) we show a zoom in the region around the point M_{Hertz}. We observe that precisely at the point M_{Hertz}, the non-linear elasticity model in lubrication condition describes still the experimental data for a few more experimental points. Additionally the Hertz model describes the experimental data from M_{Hertz}. Thus, when the lubrication-based model reaches its limit of validity, the contact-based one takes over. In this example, we observe then a crossover between the lubrication and the contact regimes, on a duration of about 7 s. In the following, we will refer to this window of $\approx 5 - 10\,\text{s}$ as the crossover region. For comparisons, zoomed figures on the region of M_{Hertz} are represented for each curve of Fig. 5.17 in Appendix B.

In the crossover region, the thickness of the fluid lubrication layer is decreasing, until reaching zero, which means the sphere enters in contact with the gel and no more solvent is present in the confined region in between. Thus the crossover region refers to a complex physical situation, and is of particular interest. To investigate in more detail this physical situation, and to refine the interpretation of M_{Hertz} as a contact point, we focus on the thickness of the lubrication layer. The numerical simulation based on the non-linear EHD model computes first the pressure field p and the fluid gap h, as explained in Sec. 5.2.3. Then, the deformation profile w as well as other quantities are computed from the pressure field and the fluid gap. The distance D corresponding to the experimentally measured distance is deduced afterwards. Thus, we extract the fluid gap h, computed by the numerical simulation used to catch the experimental data presented on Figs. 5.19(a) and (b). From the results of the numerical simulation based on the non-linear model, the deformation profile w is also extracted, and used to draw illustrations of the situation. Thus, in Figs. 5.19(c) and (d) we show illustrations of the situation, at scale, at two precise instants, respectively indicated as 1 and 2 on Fig 5.19(a). In the following, we describe these two instants.

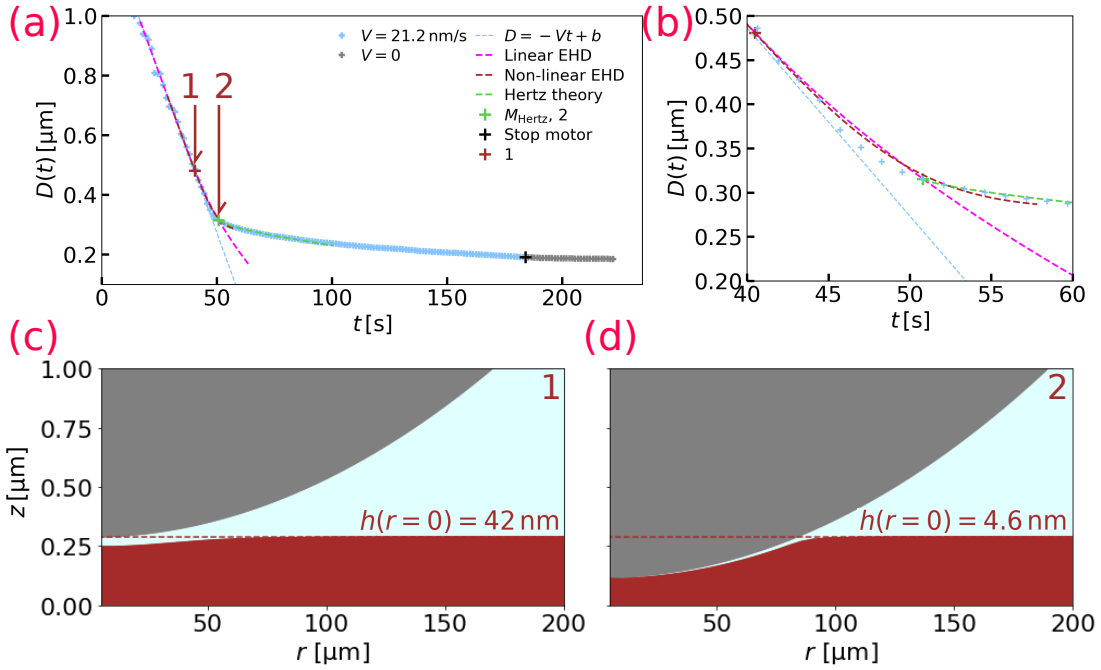

FIG. 5.19. **Crossover between lubrication and contact regimes.** *(a): Distance between the two glass surfaces D as a function of time, for a given approach velocity V. The different models described in the present Chapter are represented and indicated in the legend. (b): Zoom from panel (a), around the the point M_{Hertz}, where the Hertz contact model takes over on the non-linear EHD-based model. (c) and (d): At-scale schematic of the situation at two precise instants t_1 and t_2, indicated in panel (a), obtained from the numerical simulation performed with the non-linear EHD model, and used in panels (a) and (b).*

Instant 1: The instant 1 is defined as the instant when the surface of the sphere at the center $r = 0$ reaches the height of the undeformed surface of the substrate. For the experimental curve used in Fig. 5.19, this situation happens at $t_1 = 40.5\,\text{s}$. The numerical simulation based on the non-linear EHD model predicts a fluid gap at the center of $h(0, t_1) = 42\,\text{nm}$. As the sphere has reached the height of the undeformed surface, in this particular case the deformation is equal to the fluid gap at the center: $w(0, t_1) = h(0, t_1)$. First, the lubrication hypothesis still holds. Then, with the illustration presented in Fig. 5.19(c), we observe that the maximum deformation of the gel surface reaches approximately 15% of the thickness. At this point, the gel is still in a small-deformation regime. The linear model still holds, and indeed catches the experimental data (see Fig. 5.19(a)).

Instant 2: The instant 2 is defined by the point M_{Hertz}, as $t_2 = t_{\text{Hertz}}$. For the experimental curve used in Fig. 5.19, this situation happens at $t_1 = 50.8\,\text{s}$. The numerical simulation based on the non-linear EHD model predicts a fluid gap at the center of $h(0, t_1) = 4.6\,\text{nm}$, and a deformation of about 65% of the thickness. First, with a nanometric layer of fluid, the lubrication hypothesis becomes questionable for the following reasons. Lubrication theory relies on a continuum-mechanics-based description of matter. For $h \leq 1\,\text{nm}$, the continuum limit is crossed, thus the fluid phase can no longer be described as a continuous medium. Moreover, when the fluid gap is small compared to the deformation, the pressure field in the fluid converges towards the Hertz

pressure [217]. This picture defines the Hertz-like limit of soft-lubrication regimes, in which the fluid layer is completely squeezed between the sphere and the gel, forming thus an effective contact region [215, 281]. The force response of the material exhibits a continuous transition towards the Hertz response, as the fluid gap decreases [189, 213]. Additionally, a nanometric fluid gap means that the mechanical contact between the sphere and the surface of the gel is nearly reached. The latter statement may explain why the numerical simulation based on the non-linear EHD model fails a few seconds after the point M_{Hertz}: if the fluid gap is asymptotically zero, the pressure diverges. In summary, the schematic of the situation presented in Fig. 5.19(d) supports the fact that the Hertz contact model holds from M_{Hertz}.

Another information brought by the numerical simulation based on the non-linear EHD model, is the maximal gel deformation, which is about 65% of the gel thickness, as shown by the schematic presented in Fig. 5.19(d). Such an imposed strain expels the solvent present in the hydrogel matrix, and thus creates a partially dehydrated region. However, PNIPAM hydrogels become glassy upon drying, as discussed in Chapter 2. At 25°C, below a critical humidity rate of 30% ($m_{\text{PNIPAM}}/m_{\text{water}}$), (de)hydrated PNIPAM gels exhibit a dehydration-induced glass transition [107]. Using $\rho_{\text{PNIPAM}} = 1.1\,\text{g/cm}^3$ as the mass density of PNIPAM [282], the latter critical humidity rate corresponds to a solvent volume fraction of $\Phi_{\text{w,c}} = 0.25$ ($V_{\text{water}}/V_{\text{total}}$) at 25°C. The glass transition is characterized by a jump in Young's modulus, from a few tens of kPa to a few hundreds of MPa [243]. The local solvent volume fraction Φ_{w} and the maximal deformation w can be linked, as a function of time, as:

$$\Phi_{\text{w}}(t) = \frac{V_{\text{water}}}{V_{\text{tot}}} = \frac{\tau_{\text{swollen}} - w(0,t) - \tau_{\text{dry}}}{\tau_{\text{swollen}} - w(0,t)}, \tag{5.110}$$

with $\tau_{\text{swollen}} - w(0,t)$ giving the thickness of the deformed gel at a time t and at the center $r = 0$, and considering an uniaxial deformation. We consider a swelling ratio of $\tau_{\text{swollen}}/\tau_{\text{dry}} = 4$. Thus, we finally estimate that the critical deformation corresponding to the critical solvent fraction $\Phi_{\text{w,c}}$ at which the gel becomes glassy is $0.67\tau_{\text{swollen}}$. To conclude, the deformation amplitude of $\approx 0.65\tau_{\text{swollen}}$ that is predicted by the numerical simulation based on the non-linear EHD model at the point M_{Hertz} approximately corresponds to the critial one, at the onset of the glass transition.

In summary, a finer interpretation of the point M_{Hertz} would be that it marks the onset of the dehydration-induced glass transition of the PNIPAM hydrogel. Then, from the point M_{Hertz}, the value of the thin-film Young's modulus changes, and we should consider a typical value for glassy polymer films. Furthermore, Hertz fits provide an estimate of the reduced Young's modulus of the gel, which is $E^* = 266\,\text{MPa}$ for the approach presented in Fig. 5.19, perfectly consistent with the latter statement. In the next subsection, we will focus on the measurements of the Young's modulus in the glassy state.

5.3.5 Dependency of the Young's modulus on the approach velocity in the contact regime

The late-time, contact regime is fitted with the Hertz contact theory (see Sec. 5.2.1) and provides a measurement of the reduced Young's modulus of the glassy PNIPAM thin film. The fit is performed using the least-square method, which provides an estimate of the error on the reduced Young's modulus. In this subsection, we explore the consistency of that measurement among the different approach curves presented in the present Chapter. The reduced Young's modulus extracted from Hertz fits is referred to as *apparent*, for

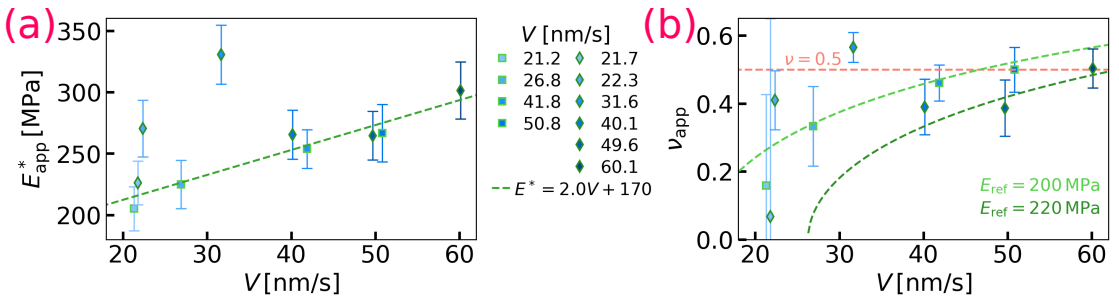

FIG. 5.20. **Dependency of the apparent Young's modulus of glassy PNIPAM on the approach velocity.** *(a): Apparent reduced Young's modulus E^*_{app} as a function of the approach velocity V, for two data sets. The apparent reduced Young's modulus is defined as $E^*_{app} = E/(1-\nu^2_{app})$ with ν_{app} the apparent Poisson ratio. The apparent reduced Young's modulus is computed from Hertz fits, based on Eq.* (5.14)*. The squares represent the first data set and the diamonds the second one. The linear fit represented by the green dashed line is computed over 8 out of 10 points. (b): Apparent Poisson ratio ν_{app} as a function of the approach velocity V, for the two data sets. The apparent Poisson ratio is computed with Eq.* (5.111)*, taking as a reference $E_{ref} = 200\,\text{MPa}$ and $E_{ref} = 225\,\text{MPa}$ for the first and the second data sets, respectively. The orange dashed line indicates the incompressible limit.*

reasons explained in the following. We note the apparent reduced Young's modulus as:

$$E^*_{app} = E_{ref}/(1-\nu^2_{app}), \tag{5.111}$$

with ν_{app} the apparent Poisson ratio, E_{ref} the "true" Young's modulus that should be independent on the velocity in a typical elasticity theory, and V the approach velocity. In Fig. 5.20(a) we show the apparent reduced Young's modulus for the two data sets. First, we observe that the apparent reduced Young's modulus slightly depends on the approach velocity. Such a dependency is the signature of dissipative effects in the gel. Indeed, a few molecules of solvent may be still present in the glassy gel, as the critical solvent volume fraction below which PNIPAM turns glassy is not zero, but $\Phi_{w,c} = 0.25$. Furthermore, we observe that the apparent Young's modulus increases with the velocity. Thus, at slow imposed indentation, the gel appears softer, and at fast imposed indentation, the gel appears stiffer.

The latter feature is reminiscent of the time-dependent poroelastic response that we highlighted in Chapter 3. Indeed, in the short-time limit, a poroelastic material behaves as an incompressible, purely elastic solid, whereas in the long-time limit, it behaves as a compressible, purely elastic solid. For any time, a porelastic material shows a mechanical response which features are in between these two asymptotic regimes. In the present case, when the velocity of approach V is smaller, the external time scale that is imposed to the system is longer. Thus, the solvent has more time to flow inside the porous matrix. The exhibited response is then closer to the one of a purely elastic and compressible material, and the measured reduced Young's modulus appears as lower. On the contrary, when the approach velocity V is larger, the external time scale that is imposed to the system is smaller. Thus, the solvent has less time to flow inside the porous matrix. The exhibited response is then closer to the one of a purely elastic and incompressible material, and the measured reduced Young's modulus appears as larger.

From Eq. (5.111), we can try to extract an apparent Poisson ratio ν_{app}, by estimating the value of the *true* Young's modulus noted as E_{ref}, that should be independent on the velocity of approach (but can be sample-dependent). In Fig. 5.20(b) we show the

apparent Poisson ratio ν_{app} as a function of the approach velocity V for the two data sets, taking $E_{\text{ref}} = 200\,\text{MPa}$ and $E_{\text{ref}} = 225\,\text{MPa}$ as references for the first and the second data sets, respectively. The incompressible limit ν_{app} is recalled, and the values of E_{ref} are chosen such that the apparent Poisson ratio ν_{app} does not exceed 0.5 at high velocities. We observe that the apparent Poisson ratio increases with the velocity, which constitutes a signature of poroelasticity, ranging from $\nu_{\text{app}} \approx 0.1$ to $\nu_{\text{app}} = 0.5$. However, the known Poisson ratio of swollen PNIPAM hydrogels is about $0.2 - 0.25$ [239, 240]. Thus, the two experimental points at the lowest velocities exhibit a too low value of Poisson ratio. Except these, the estimated values of the apparent Poisson ratio are in a physically possible range, and show a part of the transition from a purely elastic and compressible response to an incompressible one, with increasing velocities.

In summary, in the late-time, contact regime, the thin hydrogel film is dehydrated enough to be glassy, but still exhibits a velocity-dependent mechanical response. A quick qualitative analysis shows that the low, but non-zero, volume fraction of solvent in the gel generates a response that is typical of poroelastic matter. However, this quick analysis is based on values of the Young's modulus extracted using the Hertz contact model, which holds for purely elastic matter. Thus, an interesting perspective would be to develop a Hertz model for a poroelastic material, and compare it quantitatively to experimental data in the late-time regime.

5.4 Conclusion

In this Chapter, we presented SFA experiments in sphere-plane geometry, performed on a PNIPAM hydrogel thin film, in approach mode. The experiment enables to probe various regimes with increasing indentation, from no resolvable interaction between the probe and the gel, to the complete compression with expulsion of the solvent, passing mainly by a first lubricated regime, and a second, contact regime. We presented different models describing different parts of the data, showing that a succession of different descriptions enables to understand an experimental curve almost all along. The lubrication-based models were complemented with numerical simulations, whereas numerical fittings were performed based on the Hertz contact model. We showed that modeling efforts enable to estimate the Young's modulus of the swollen PNIPAM film, both in the lubricated regime ($E \approx 5\,\text{kPa}$) and in the contact regime (E$\approx 200\,\text{kPa}$). We thus showed that the imposed indentation of the probe expels enough solvent from the polymeric matrix to provoke a dehydration-induced glass transition, and we resolved the point at which the transition happens. Finally, we explored the dynamical response of the gel in the glassy state, and interpreted the velocity-dependency of the apparent Young's modulus as a signature of poroelasticity.

Perspectives could be proposed for several aspects of this work. First, the estimation of the Young's modulus in the lubricated regime results from a guessed value used as a parameter of numerical simulations. With time, tables of ready-to-use numerical approaches could be created, in order to estimate faster, with a better precision, the Young's modulus. Second, the contact regime is modeled using Hertz theory for elastic and compressible materials. Using the poroelastic response theory developed in Chapter 3, we could build a Hertz-like theory for poroelastic materials, and compare it to experimental data. Furthermore, within this framework, the discussion about the velocity-dependent Young's modulus as a signature of poroelasticity would be quantitatively founded. Finally, the last, almost constant part (in distance-time representation) of the experimental data is not caught by Hertz theory. Indeed, as the indentation

increases, the finite-size aspect of the thin film becomes more important. Some theoretical works were already developed taking into account corrections to the original Hertz model, to include finite-size effects [268, 283]. However, such a model assumes conditions on the length ratio between the sphere radius and the indentation, or on the ratio between the indentation and the thickness. These conditions were not matching our experimental situation, therefore the model would not be used. Thus a perspective would be to develop a model that takes into account finite-size effects, with non-linear elasticity as the deformation gets close to the thickness, like we did in the lubrication regime.

Complementary experiments based on other techniques could be used to confirm the observations and results described in the present Chapter. For instance, a simple measurement of the Young's modulus by AFM, in a closed chamber with a controlled humidity rate, could confirm that the results of Ref. [107] on the onset of the glass transition at room temperature apply to our samples. Additionally, AFM-based indentation experiments would be of great interest as a matter of comparison. Indeed, the experiment principle is similar, except that the sphere radius changes ($R \sim 10\,\mu$m in colloidal-probe AFM). Thus, the hydrodynamic radius changes, and the resulting force changes. By choosing carefully the cantilever stiffness, we could again tune an AFM-based experiment that probes all the different regimes described in this Chapter, from zero sphere-gel interaction to the dehydration-induced glass transition of the polymeric gel. Finally, as a "negative control", the same SFA experiments could be tested on hydrogel thin films made from a rubber-like polymer. For instance, Polyacrylamide (PAA) hydrogels should not exhibit a dehydration-induced glass transition. Thus, the Hertz contact modeling should provide a much softer Young's modulus. Such an experiment could support our interpretation and conclusion on PNIPAM hydrogels.

A longer-term project could consist in adapting the work presented in Chapter 3 on the poroelastic response to the approach case in lubrication conditions, after it has been done for the harmonic case in Chapter 4. Such a powerful tool would surely be a key to investigate soft hydrogels in SFA, as well as in AFM. Here we could model the gel as a purely elastic and compressible system (with no memory, thus simpler than a poroelastic system) in the lubricated regime, because the experimental conditions were such that only the late-time limit was explored. Yet, when changing material (*e.g.* using Polyacrylamide) or setup (*e.g.* using AFM), this may not be true any longer. Thus, the theoretical framework of a poroelastic and finite-size layer approached by a sphere would constitute the general tool, robust to time considerations, useful to describe approach and indentation experiments on soft and porous matter.

Conclusion

In this thesis, we have studied the mechanical response of PNIPAM hydrogel films from several aspects. Here, we gather the main conclusions, and we deepen the perspectives of this work.

In Chapter 2 we have shown swelling-induced surface instabilities on grafted PNIPAM films, resulting from swelling and drying processes. Different morphologies have been investigated by AFM. In the swollen state, a creased pattern has been observed, while in the dried state, two types of morphologies have been reported depending on the swollen thickness of the film. In particular, we have exhibited a new pattern shape, compared to patterns already reported in literature. The *volcano* pattern is observed at the surface of dried and thick PNIPAM films, characterized by a sinusoidal surface shape with small creases present on upper regions. Then, quantitative features such as the wavelength and the amplitude have been studied as functions of the thickness of the films. Comparisons of such characteristics between the swollen and the dried states have led to the proposition of a mechanism to explain the observation of the volcano pattern. We have suggested that drying makes a stiff, skin layer appearing at the surface of the already-creased surface of a polymer hydrogel. The latter skin layer applies a sufficient compressive stress to trigger a wrinkling instability [125, 151, 163], which results in the formation of the volcano pattern. To pursue this work and validate the latter hypothesis, an estimation of the skin layer thickness is required. Finally, such an unexplored morphology may present considerable advantages in the context of the fabrication of pattern-designed materials, for various application such as cellular culture or optically-switchable devices.

Chapter 3 has established the theoretical framework of the mechanical response of a permeable and poroelastic substrate, to an external axisymmetric pressure field. Based on linear poroelasticity, the point-force response in terms of deformation has been derived first, both in the infinitely-thick case and taking into account finite-size effects. Then, the latter solution has been generalized to any external pressure field exhibiting the same symmetry properties. We have shown that the poroelastic response is characterized by a transition from the limit of a purely elastic and incompressible response to the one of a purely elastic and compressible response. The propensity of the poroelastic response to be more similar to one limit or the other is determined by comparing the intrinsic response time scale of the material to the one imposed by the external excitation. This theoretical work can be applied to any situation involving a poroelastic material with an axial symmetry, as demonstrated in the two following Chapters. An experimental validation of the presented modeling work could be provided by any experimental technique able to track the deformed surface of a soft and porous material immersed in a solvent. Additionally, a similar theoretical framework could be used to compute the mechanical response of a poroelastic and permeable material to a point-force pressure field, in the case of a planar symmetry. By applying the same generalization principle, a direct perspective would be to theoretically address the poroelastic lift force in lubrication condition [188, 198, 211].

In Chapter. 4, the framework established in Chapter 3 has been directly applied to the case of a vertically-oscillating sphere, close to a poroelastic medium in lubrication conditions. In the first part of this Chapter, we have derived theoretically the loss and

storage components of the resulting force on the sphere, with complementing numerical simulations. In the second part of this Chapter, we have presented colloidal-probe AFM-based experiments on a swollen PNIPAM hydrogel thick film, and compared the results to the theory established in the first part. In summary, contactless, colloidal-probe techniques appear as good candidates to investigate soft and fragile materials without risks of damaging. However, the porosity appears as a minor feature of the response, which expands on a narrow range, from the limit of a purely elastic and incompressible behavior, to the one of a purely elastic and compressible behavior. Essentially, the porosity results in an effective compressibility. A natural perspective would be to compare the obtained experimental data with classical rheology data, or to go to non-linear modelling and large indentations. To conclude, we have demonstrated the efficiency of contactless colloidal-probe methods to investigate soft and fragile samples. Such a type of experimental techniques could be applied to any similar materials such as living systems, or multilayered viscous liquids.

In the last Chapter. 5, we have presented SFA experimental results in sphere-on-flat mode, performed on thin PNIPAM hydrogel films in lubrication conditions. The situation is similar to the one explored in Chapter. 4. However, the ratio between the probe radius and the sample thickness is completely different, and the experiment has been realized in approach mode until contact. Several different regimes of mechanical responses of the sample are highlighted, from small deformations in lubrication conditions to the dehydration-induced glass transition. Finally, describing the glassy, dehydrated PNIPAM film as a purely elastic material, we have measured an elastic modulus that depends of the driving approach velocity. We have rationalized the latter observation by the presence of solvent traces still flowing inside the polymeric network. Thus, an interesting perspective would be to model the glassy film as a poroelastic material, since a purely elastic description highlights dynamics. Furthermore, a last regime where the glassy film is physically in contact with the probe that imposes large deformations is still to describe. Finally, complementary experiments could be performed to validate our observation of a dehydration-induced glass transition, such as a study of the elastic properties as a function of the humidity rate, in AFM. Additionally, similar approach experiments could be tried in colloidal-probe AFM, which would change the length scales compared to SFA. Finally, the theoretical framework developed in Chapter. 3 could be adapted to describe approach experiments on poroelastic materials.

Summary in French

Chapter 6

Résumé substantiel en français

Dans cette partie en français, l'introduction et la conclusion de la thèse sont traduites. Ainsi le contexte général des recherches est présenté dans l'introduction, et les principaux résultats obtenus sont résumés chapitre par chapitre dans la conclusion. La figure 3.10 présente dans la conclusion du chapitre 3 est également ajoutée. Le contenu du chapitre préliminaire 1 n'est pas retranscrit, puisqu'il ne traite pas de résultats obtenus dans le cadre de cette thèse mais rassemble des notions spécifiques du domaine, utiles pour aborder les quatre chapitres suivants.

6.1 Introduction (traduite)

La matière molle et spongieuse est omniprésente dans la nature, à toute échelle. Quelques exemples emblématiques sont donnés par des systèmes vivants, comme les bactéries ou les éponges de mer, tandis que d'autres par des systèmes inertes, comme la boue et l'argile. D'autres exemples peuvent être trouvés dans des objets du quotidien fabriqués par l'homme, comme les éponges à vaisselle, ou encore au sein de matériaux synthétiques complexes, comme les mousses ou les réseaux polymériques. Ces exemples sont illustrés par la Fig. 6.1. D'un point de vue de physicien, de tels systèmes sont des matériaux poroélastiques. Ils ont la capacité d'être déformés et de retrouver ensuite leur forme initiale, comme signature de leur élasticité, d'absorber un solvant et d'héberger des courants de fluides, comme signature de leur porosité. Sous cet angle, les hydrogels de polymères réticulés sont des systèmes fascinants qui montrent particulièrement bien leur signature poroélastique. En particulier, la capacité du poly-N-isopropylacrylamide (PNIPAM) à gonfler d'un facteur 4 dans l'eau à température ambiante [1] a été largement exploitée en science fondamentales. L'hydrogel ainsi formé est caractérisé par une transition en température, d'un comportement hydrophile à température ambiante à un comportement hydrophobe pour des températures supérieures à 32°C. Lorsqu'il est greffé sur un substrat [2], ce polymère sensible à la température est utilisé dans le design de valves microfluidiques [3, 4], dans des disciplines biomédicales comme le piège de cellule unique [5], pour des analyses médicales ou la délivrance de substances médicamenteuses [6], et finalement dans le domaine de la culture cellulaire [7, 8], ce qui exploite sa biocompatibilité.

Malgré un intérêt croissant pour les hydrogels de polymères et leurs applications, leur comportement mécanique fondamental constitue toujours un sujet peu couvert de la littérature. Les premiers travaux sur la matière poroélastique ont été conduit par Biot [10], dans le contexte de la mécanique de sédimentation des sols. Tandis que les effets de la viscoélasticité ont été investigués récemment [11–13], la poroélasticité reste à explorer en plus amples détails [14–17]. La complexité intrinsèque de ces types de matéri-

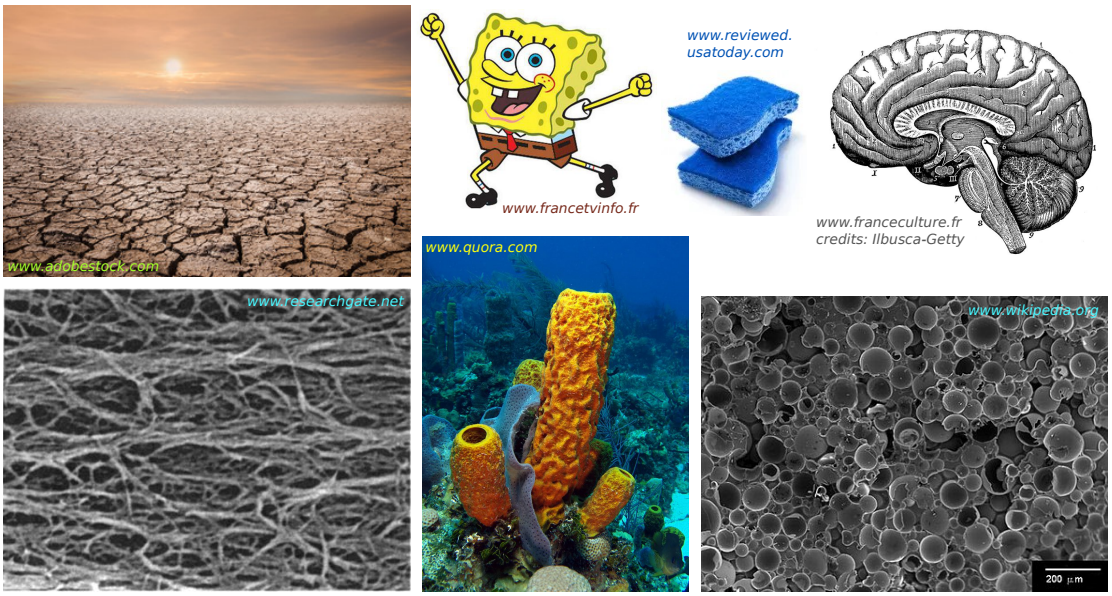

FIG. 6.1. **Exemples de systèmes souples et poreux.** *Une photo de boue craquelée prise en Irlande ; Bob l'éponge ; des éponges à vaisselle ; un dessin de cerveau humain ; une photo prise en microscopie électronique à balayage (SEM) d'un réseau de polymère ; des éponges de mer ; une photo prise en SEM d'une mousse synthétique. Le réseau de polymères photographié en SEM est à l'origine publié dans [9].*

aux composites engendre des couplages poroélastique et/ou élastohydrodynamique, donc leur réponse mécanique dépend de leur interaction avec leur environnement. De plus, les hydrogels de polymères sont formés par gonflement, et sont constitués d'un mélange de différentes espèces caractérisées par leur affinité [18]. Si la mécanique du gonflement a été explorée pour les gels de polymères [19–21] et celle du séchage bien documentée pour les gouttes de liquides complexes [22–25] et les films [26–29], la littérature sur la mécanique de dégonflement des gels est moins fournie. Qui-plus-est, le processus de gonflement et dégonflement présente des aspects asymétriques [19, 20, 30].

Dans cette thèse, le comportement mécanique de matériaux poroélastiques est étudié lorsque qu'ils sont immergés dans un solvant à la fois de façon théorique et expérimentale. Ce manuscrit est organisé comme suit. Un premier chapitre présente le contexte global de la thèse, allant des bases de mécanique des fluides, de mécanique des milieux continus et de physique des polymères, au contexte scientifique spécifique de la thèse. Le deuxième chapitre fait état d'instabilités de surface qui peuvent surgir à la surface d'hydrogels suite à leur gonflement et à celle de films de polymères suite à leur séchage. Une nouvelle morphologie qui n'est pas documentée dans la littérature (à la connaissance des auteurs) est mise en évidence. Dans le troisième chapitre, le cadre théorique de la réponse mécanique poroélastique à une force ponctuelle est établi. Le profil de déformation qui résulte est calculé en fonction du temps pour un milieu poroélastique perméable, à la fois dans le cas d'une épaisseur semi-infinie et dans celui d'une épaisseur finie. Dans le quatrième chapitre, cette théorie est appliquée au cas d'un gel indenté doucement par une sphère oscillante en conditions de lubrification. Les résultats théoriques obtenus sont comparés à des expériences préliminaires conduites sur des hydrogels de PNIPAM, en utilisant un système développé sur place et basé sur de la Microscopie à Force Atomique (AFM). Il est démontré que ce type de montage expérimental est approprié pour sonder des matériaux souples et fragiles, dans un mode sans contact, sans risque d'endommager les échantillons. Cependant la porosité de l'hydrogel gonflé apparaît seulement comme

un aspect discret de la réponse mécanique, sous la forme d'une compressibilité effective. Le dernier chapitre est dédié à l'étude de films minces d'hydrogel de PNIPAM avec un Appareil à Forces de Surface (SFA), en mode approche. Différents régimes de réponses mécaniques sont mis en exergue, allant d'un régime en faibles déformations à la transition vitreuse du film de polymères indenté, déclenchée par déshydratation. Globalement, il est démontré à travers différentes situations que la réponse poroélastique est caractérisée par une transition en fonction du temps allant du comportement d'un matériau purement élastique et incompressible à celui d'un matériau purement élastique et compressible.

6.2 Conclusion (traduite)

Dans cette thèse, la réponse mécanique de films d'hydrogels de PNIAPM a été étudiée sous plusieurs angles. A présent, les principales conclusions sont rassemblées, et les perspectives de ces travaux sont approfondies.

Au cours du chapitre 2, des instabilités de surface induites par gonflement ont été montrées, sur des films de PNIPAM greffés, qui résultent des processus de gonflement et de séchage. Différentes morphologies ont été explorées en AFM. A l'état gonflé, un motif comprenant des failles nettes a été observé, tandis qu'à l'état séché, deux types de morphologies, dépendants de l'épaisseur du film gonflé, ont été rapportés. En particulier, une nouvelle forme de motif a été observée, par comparaison aux formes déjà rapportées dans la littérature. Le motif *volcan* est observé en surface de films séchés et épais de PNIPAM, et est caractérisé par une forme de surface sinusoïdale, avec de petites failles sur les hauteurs. Ensuite, des aspects quantitatifs comme la longueur d'onde et l'amplitude des motifs ont été étudiés en fonction de l'épaisseur des films. Ces caractéristiques ont été comparées entre les états séchés et gonflés, ce qui a conduit à la proposition d'un mécanisme visant à expliquer l'observation du motif volcan. Il a été suggéré que le séchage fait apparaître une peau rigide et mince sur la surface préalablement déstabilisée de l'hydrogel de polymère. Cette couche de peau engendre une contrainte compressive suffisante pour déclencher une instabilité en forme de rides régulières [125, 151, 163], dont le motif volcan résulte. Pour poursuivre ce travail et valider cette dernière hypothèse, une estimation de l'épaisseur de la couche de peau est nécessaire. Enfin, une telle morphologie jusqu'à présent inexplorée pourrait présenter de considérables avantages dans le cadre de la fabrication de matériaux dont on dessine les motifs, avec des applications variées, telles que la culture cellulaire ou la création de dispositifs commutables optiquement.

Dans le chapitre 3 est établi le cadre théorique de la réponse mécanique d'un substrat perméable et poroélastique, à un champ de pression axisymétrique externe. Dans le cadre de la poroélasticité linéaire, la réponse en termes de déformation à une force ponctuelle a d'abord été établie, à la fois dans le cas d'un substrat semi-infini et dans celui prenant en compte les effets de taille finie. Ensuite, ce résultat a été généralisé à tout champ de pression externe ayant les mêmes propriétés de symétrie. Il a été montré qu'une réponse poroélastique est caractérisée par une transition entre la limite d'une réponse purement élastique et incompressible à celle d'une réponse purement élastique et compressible, comme illustré par la figure 6.2. La propension de la réponse poroélastique à être plus proche d'une limite ou l'autre est déterminée en comparant l'échelle de temps

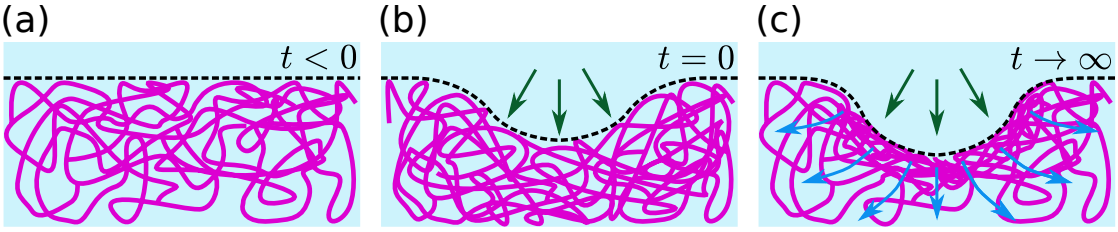

FIG. 6.2. **Matrice réticulée de polymère gorgée de solvant.** *(a) : Un gel réticulé non déformé est gonflé dans un solvant, et forme un système poroélastique idéal. Pour les temps négatifs, le champ de concentration en solvant est considéré comme homogène et fixé à c_0. Le champ de potentiel chimique est homogène à l'équilibre et fixé à μ_0. (b) : Quand un champ de pression est soudainement appliqué à $t = 0$, le champ de concentration en solvant c est toujours isotrope, du fait du caractère incompressible du liquide, mais des gradients non nuls de potentiel chimique μ apparaissent. Le matériau répond comme un solide élastique et incompressible. (c) : Dans la limite des temps longs, le solvant a eu le temps de couler, dirigé par les gradients de potentiel chimique. Le champ de concentration en solvant c est inhomogène mais le potentiel chimique a retrouvé sa valeur d'équilibre μ_0. Le matériau répond comme un solide élastique et compressible.*

propre et intrinsèque à la réponse, à celle qui est imposée par l'excitation externe. Ce cadre théorique peut être appliqué à n'importe quelle situation impliquant un matériau poroélastique dans une symétrie axiale, comme fait dans les deux chapitres suivants. Une validation expérimentale du travail de modélisation présenté dans ce chapitre pourrait être apportée par n'importe quelle technique expérimentale permettant de suivre la surface déformée d'un matériau souple et poreux immergé dans un solvant. Qui plus est, un cadre théorique similaire pourrait être utilisé pour calculer la réponse mécanique d'un matériau perméable et poroélastique à un champ de pression ponctuel, dans le cas d'une symétrie par rapport à un plan. En appliquant le même principe de généralisation, une perspective directe serait d'aborder le problème de la force de portance poroélastique en conditions de lubrification [188, 198, 211].

Au chapitre 4, le cadre théorique posé au cours du chapitre 3 a été directement appliqué au cas d'une sphère oscillant verticalement au voisinage d'un milieu poroélastique, en conditions de lubrification. Dans la première partie de ce chapitre, les composantes de conservation et de perte de la résultante des forces sur la sphère ont été établies théoriquement, avec des simulations numériques complémentaires. Dans la deuxième partie de ce chapitre, des résultats expérimentaux basés sur de l'AFM en sonde colloïdale, obtenus sur des films épais et gonflés de PNIPAM, ont été présentés puis comparés à la théorie établie lors de la première partie. En résumé, les techniques sans contact et en sonde colloïdale se présentent comme de bonnes candidates pour explorer des matériaux souples et fragiles, sans courir le risque de les abîmer. Cependant, la porosité apparaît comme un trait discret de la réponse, qui s'étend sur une gamme restreinte allant de la limite du comportement d'un matériau purement élastique et incompressible, à celle du comportement d'un matériau purement élastique et compressible. La porosité se traduit donc par une compressibilité effective. Une perspective naturelle serait de comparer les données expérimentales obtenues avec des données de rhéologie classique. Pour conclure, nous avons démontré l'efficacité d'une méthode sans contact et en sonde colloïdale pour explorer des échantillons souples et fragiles. Des techniques expérimentales de ce type

pourraient être appliquées à n'importe quel matériau similaire tel qu'un système vivant ou des liquides visqueux en couches multiples.

Dans le dernier chapitre 5, nous avons présenté des résultats expérimentaux de SFA en géométrie sphère/plan, obtenus sur des films minces d'hydrogel de PNIPAM, en conditions de lubrification. La situation est similaire à celle introduite au chapitre 4 à deux exceptions près : le ratio entre le rayon de la sphère et l'épaisseur du gel est complètement différent et l'expérience a été réalisée en mode approche jusqu'à atteindre le contact. Plusieurs régimes différents de réponse mécanique de l'échantillon ont été mis en valeur, allant de faibles déformations en conditions de lubrification à une transition vitreuse induite par la déshydratation. Enfin, en décrivant le film déshydraté et vitreux de PNIPAM comme un matériau purement élastique, un module élastique qui dépend de la vitesse d'approche a été mesuré. Cette observation a été expliquée par la présence de traces résiduelles de solvant toujours en train de couler dans le réseau polymérique. En conséquence, une perspective intéressante serait de modéliser le film vitreux comme un matériau poroélastique, puisqu'une description purement élastique révèle une réponse dynamique. En outre, un dernier régime reste à modéliser, celui où le film est physiquement en contact avec la sonde, qui lui impose de larges déformations. Enfin, des expériences complémentaires pourraient être réalisées pour valider les observations d'une transition vitreuse induite par la déshydratation, telles que l'étude des propriétés élastiques en fonction du taux d'humidité en AFM. Egalement, des expériences similaires en mode approche pourraient être testées en AFM en sonde colloïdale, ce qui changerait les échelles de longueur. Enfin, le cadre théorique établi au chapitre 3 pourrait être adapté pour décrire des expériences d'approche sur des matériaux poroélastiques.

Appendix

Appendix A

Analysis of experimental data

A.1 Treatment of AFM images

In the present section we detail the treatment process that is realized on raw AFM imaging data, using the software *Gwyddion* `http://gwyddion.net/`.In Fig. A.1, we show the main steps of treatment that are systematically applied. A raw AFM image is usually difficult to read, as shown for example on Fig. A.1(a). The sample is usually slightly tilted compared to the perfect horizontal plane. A first step of treatment consists in correcting the planar tilt, as indicated by the schematic below the image. Then, we obtain the image shown in Fig. A.1(b). To realize a topography measure, the AFM head moves laterally along a first line, from left to right, then measures the second line (just above or just below the first one), moving from right to left, then the third one from left to right, *etc.* A gap in height may appear between two successive lines. Then, the next step of treatment consists in correcting the gap between successive lines, as schematized below, to obtain the image shown in Fig. A.1(c). Finally, for a more convenient reading, the mean plane is subtracted. As a consequence, the legend color scale indicating the measured height in each point is centered at zero. On the final image that is shown in Fig. A.1(d), the color scale was also adapted to the height distribution, so as to improve the contrast and ease the reading.

Additionally, if the AFM image has a defect, such as the one we show in Fig. A.1, a

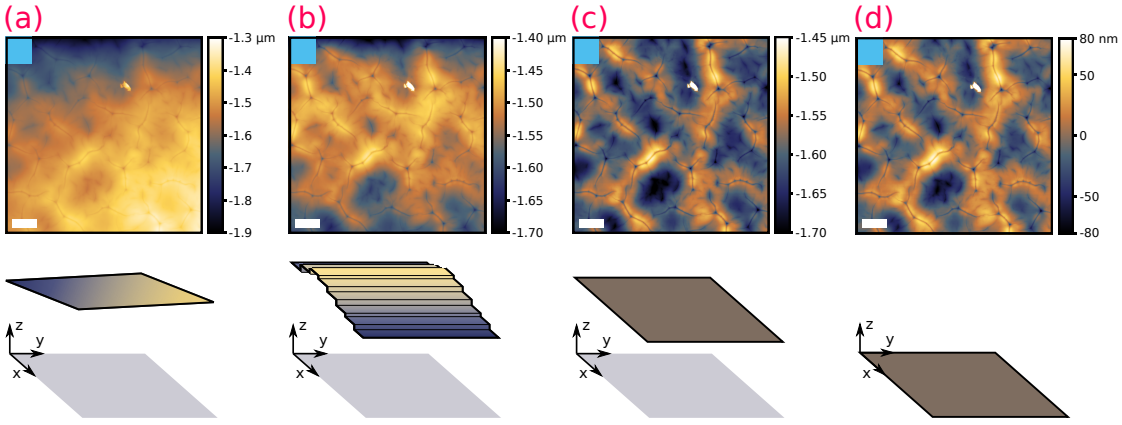

FIG. A.1. **Treatment of raw AFM images.** *Image et different steps of treatment and schematic of the defect to correct. (a): Raw image obtained after a topography measurement. (b): After correction of the planar tilt. (c): After correction of the gap between successive lines. (d): After subtracting the mean plane.*

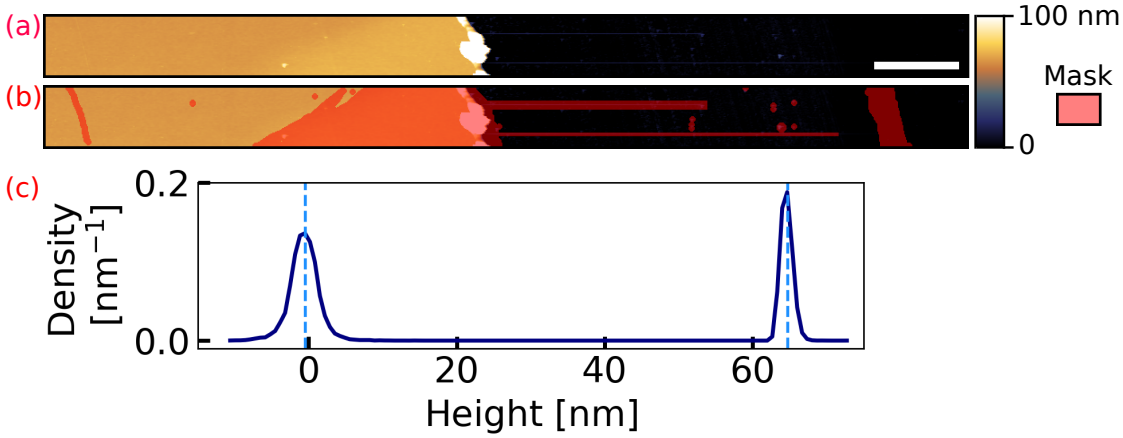

FIG. A.2. **AFM image of a scratch in a hydrogel thin film.** *(a): AFM image of the scratch. On the left we can see the gel surface, on the right the glass substrate. The white rectangle represents* $5\,\mu$m*. (b): Same image than in (a). The red color indicates the masked regions (imperfections, AFM artefacts, accumulation of matter close to the cliff...), that are not taken into account in the analysis. (c): Distribution of heights, based on (b). The gap between the two maxima define the thickness of the gel.*

mask can be drawn by hand on the concerned region, such that the calculation involved in data treatment does not take into account the defect. For instance, here the defect consists in a sharp roughness at the surface of the image, that is beautiful apart from that. Such a defect would introduce an error in the calculation of the tilted plane at step (a), and/or when computing the correspondence between successive lines at step (b), or a shift of the mean plane height upwards at step (c). Finally, other treatments may be useful depending on the image, such as a correction of grains, effect of adhesion... Yet the best is to have a nice image from the start.

A.2 Measurement of a hydrogel thickness by AFM

In this section we describe how the thickness of a dry gel is typically measured by AFM. A scratch is made on the gel with a scalpel, in an only gesture, such that the glass substrate underneath the polymer is discovered. Then, the topography of the scratched region is measured by AFM, in tapping mode, with a standard sharp tip (*Nanosurf, Dyn190Al*, nominal stiffness $k_{\text{nom}} = 48\,\text{N/m}$ and nominal resonance frequency $k_{\text{nom}} = 190\,\text{kHz}$). An exploitable image should show equally both the gel surface and the glass substrate. The “cliff" should appear vertically (perpendicularly to the scanning direction), in the middle of the image, and be as sharp as possible. In Fig A.2(a) we show such an AFM image of a scratch performed on a flat PNIPAM gel.After discarding irrelevant defects as shown in Fig. A.2(b), the distribution of heights is extracted from the image and is shown in Fig. A.2(c). Two planes are visible, and the difference of height between them provides a measurement of the thickness of the gel. In the example presented here, we measure a thickness of $65 \pm 2\,\text{nm}$. The present method is used to measure the thickness of thin and flat samples, as well as patterned ones, in both dry and wet conditions. In the case of a patterned sample, the averaged height of the surface of the gel is taken as the highest plane, within a larger error. In the case of a soft and swollen gel, the AFM image is done in contact mode with a low set-point (3 nN or less) and a specific probe (*Nanosensors, qp-BioAC*, softest cantilever, nominal stiffness $k_{\text{nom}} = 0.06\,\text{N/m}$ and nominal resonance

frequency $k_{\text{nom}} = 30\,\text{kHz}$).

A.3 Differentiating patterns

A.3.1 Height distributions of patterned samples

In this subsection we show how to differentiate creased pattern (*e.g.* brain-like patterns in the dry state) from volcano pattern, using the height distributions. In Fig. A.3, we show two AFM images of the surface topography of two samples. The first one, shown in Fig. A.3(a) is a swollen PNIPAM hydrogel of dry thickness $\tau_{\text{dry}} = 950\,\text{nm}$ (thus of swollen thickness $\tau_{\text{wet}} \approx 3.5 - 4\tau_{\text{dry}}$) exhibiting creases. The second one, shown in Fig. A.3(b) is a dried PNIPAM hydrogel of dry thickness $\tau_{\text{dry}} = 2.95\,\mu\text{m}$.

The height distributions are extracted from the both AFM images, and plotted below each image respectively. We observe that for creases, the distribution exhibit a shift towards the greater heights z, while for volcano pattern, the distribution exhibit a shift towards the smaller heights z. Thus, looking at distribution of heights constitutes a quick mean to identify a pattern type.

A.3.2 Minkovski functions

In this subsection, we compute the Minkovski functionals [284, 285] from the two AFM measurements of the surface topography of the two samples shown in the previous subsection, and show a quantitative and systematic method to classify pattern types. Considering a non-flat surface $\mathcal{S}$ of an object and $\delta\mathcal{S}$ its boundary, the Minkovsky functionals are defined as:

$$M_0(\mathcal{S}) = \int_{\mathcal{S}} \mathrm{d}s, \tag{A.1a}$$

$$M_1(\mathcal{S}) = \frac{1}{2\pi} \int_{\delta\mathcal{S}} \mathrm{d}c, \tag{A.1b}$$

$$M_2(\mathcal{S}) = \frac{1}{2\pi^2} \int_{\delta\mathcal{S}} \left[\frac{1}{R}\right] \mathrm{d}c, \tag{A.1c}$$

with $\mathrm{d}s$ being a surface element, dc a circumference element, R the radius of the local curvature. Then, the Minkovski surface area $\mathcal{A}_{\text{Mink}}$, perimeter $\mathcal{P}_{\text{Mink}}$, and connectivity χ_{Mink} are defined as :

$$\mathcal{A}_{\text{Mink}} = M_0(\mathcal{S}), \tag{A.2a}$$

$$\mathcal{P}_{\text{Mink}} = 2\pi M_1(\mathcal{S}), \tag{A.2b}$$

$$\chi_{\text{Mink}} = \pi M_2(\mathcal{S}). \tag{A.2c}$$

The Minkowski area A_{Mink}, perimeter P_{Mink}, and connectivity χ_{Mink} correspond respectivey to the area enclosed by an isocontour, the total length of the isocontours, and number of connected components in an isocontour. Minkowski functionals provide a method of distinguishing 3D patterns with different morphologies [286], since morphologically-equivalent patterns exhibit the same functional dependence on surface height. The Minkovski surface area, perimeter and connectivity were computed as a function of height z, using a special package of *Python* [287], whose documentation is available at `https://boeleman.github.io/quantimpy/index.html`. In Fig. A.3(c), we show the Minkowski area $\mathcal{A}_{\text{Mink}}$, perimeter $\mathcal{P}_{\text{Mink}}$, and connectivity χ_{Mink} as a function of the heights z, normalized by the amplitude of the surface topography A_{p}. We observe that these three quantities constitute an efficient way to clearly distinguish a pattern

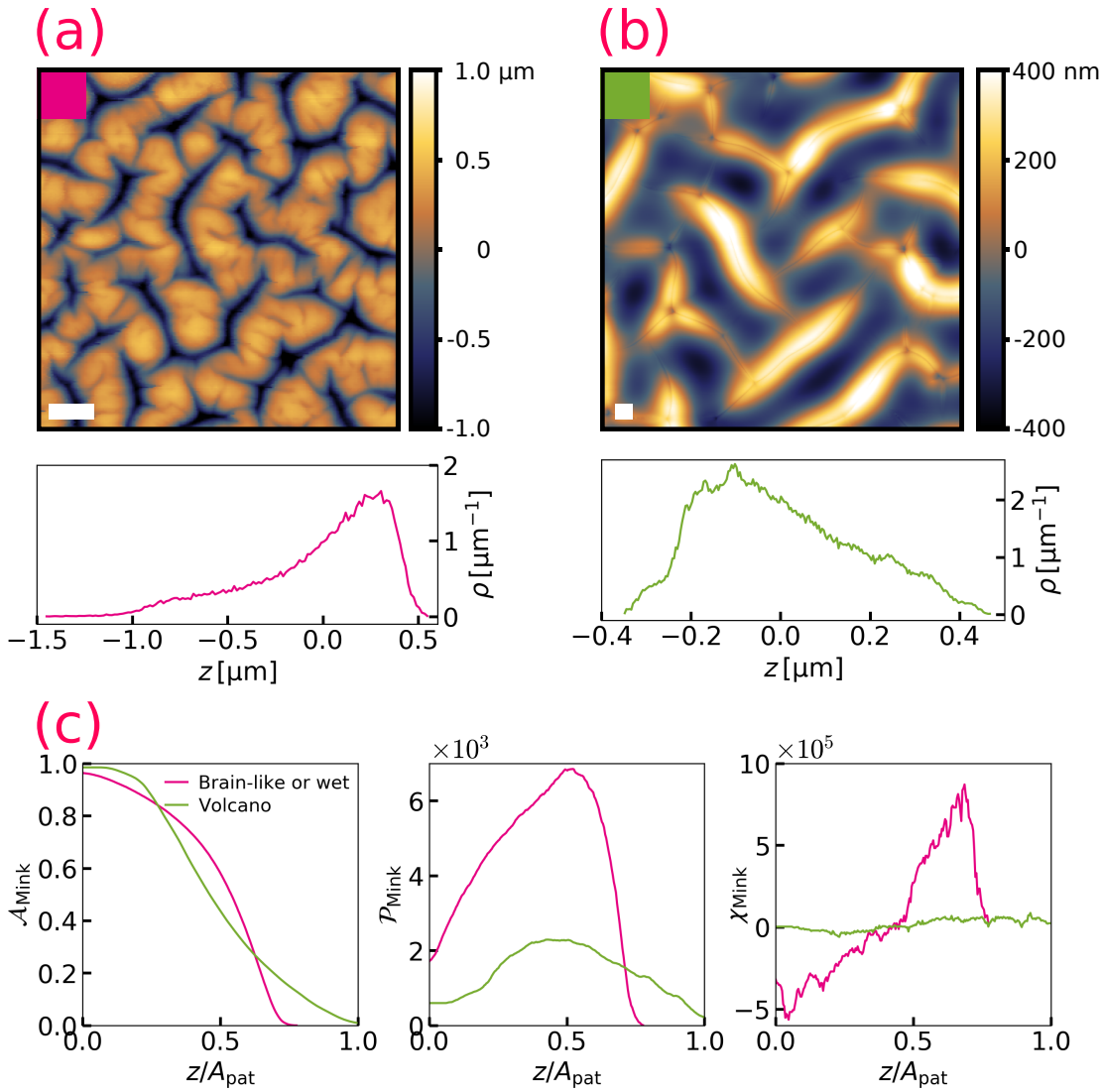

FIG. A.3. **Height distribution for different patterns.** *(a): Surface topography measured by AFM of a swollen PNIAPM film, fabricated using a spin-coating speed of* $\omega_{\text{spin}} = 2500\,\text{rpm}$ *and a polymer solution concentration at* $c_{\text{PNIPAM}} = 5\,\%$*. The thickness in the dried state is measured at* $\tau_{\text{dry}} = 950\,\text{nm}$*. The height distribution is extracted from the AFM image and shown below. (b): same as in (a), with a dried sample fabricated using a spin-coating speed of* $\omega_{\text{spin}} = 1000\,\text{rpm}$ *and a polymer solution concentration at* $c_{\text{PNIPAM}} = 10\,\%$*. The thickness in the dried state is measured at* $\tau_{\text{dry}} = 2.95\,\mu\text{m}$*. (c): Minkovski area* $\mathcal{A}_{\text{Mink}}$*, perimeter* $\mathcal{P}_{\text{Mink}}$ *and connectivity* χ_{Mink} *as a function of the heights* z*, normalized by the amplitude of the surface topography* A_{p}

type from another. In particular, the asymmetry of the perimeter distribution $\mathcal{P}_{\text{Mink}}$ gives a simple criteria to classify patterns.

A.4 Measurement of Young's modulus by AFM

A.4.1 Processing the raw data

From raw spectroscopy data to force-distance curves: In the present section we detail the analysis process of raw spectroscopy data [225, 226]. In practice, the

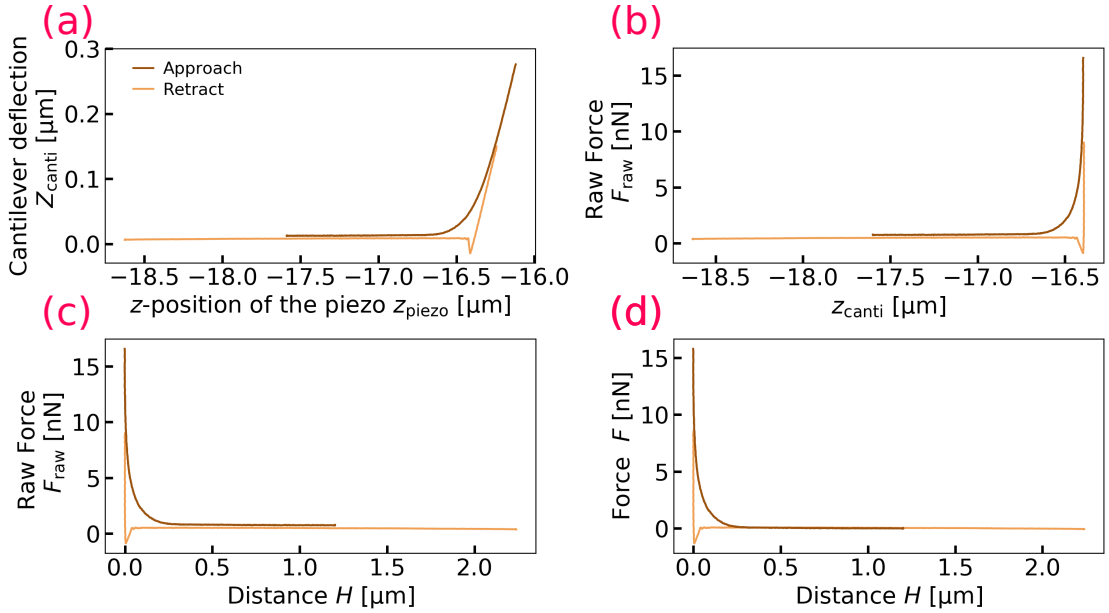

FIG. A.4. **Treatment steps of raw AFM spectroscopy data.** *(a): Cantilever deflection Z_{canti} as a function the piezo position z_{piezo}, as raw spectroscopy data. (b): Raw force F_{raw} as a function of the position of the cantilever z_{canti} as defined by Eq.* (A.3)*. (c): Raw force F_{raw} as a function of the distance between the probe and the sample, as defined by Eq.* (A.4)*. (d): After removing the baseline, we obtain the force F as a function of the sample-probe distance H.*

treatment in done using the software *AtomicJ* [241]. In Fig. A.4 we show the main steps of treatment that are systematically applied. A raw spectroscopy curve corresponds to the cantilever deflection Z_{canti} as a function of the z-position of the piezo element z_{piezo}. In Fig. A.4(a) we show an example of a raw spectroscopy curve (we know the deflection sensitivity DS, thus the cantilever deflection is expressed in distance). A first step is to compute the position of the cantilever z_{canti}, in the same frame as the one of the piezo, as:

$$z_{\text{canti}} = z_{\text{piezo}} - Z_{\text{canti}}. \tag{A.3}$$

Thus, knowing the spring constant k_{canti}, in Fig. A.4(b) we show the raw force F_{raw} as a function of the position of the cantilever z_{canti}. A second step is to convert the cantilever position z_{canti} into the sample-probe distance H. The latter distance is defined as:

$$H = z_{\text{div}} - z_{\text{canti}}, \tag{A.4}$$

with z_{div} the distance at which the force diverges, which gives the maximum indentation of the sample that is reached. Thus, in Fig. A.4(c) we show the raw force F_{raw} as a function of the sample-probe H. Finally, the baseline, which is the offset in force, is subtracted. The latter offset may result of a non-perfect alignment of the laser on the four-quadrant photodiode. In Fig. A.4(d) we show the resulting force F as a function of the distance H.

Fitting force-distance curves Then, force-distance curves can be exploited depending on (i) the probe used to investigate the sample and (ii) the mechanical response of the sample.

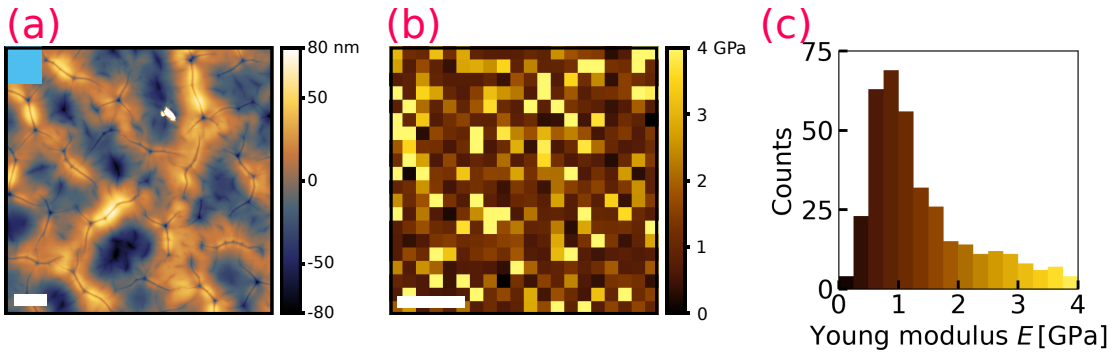

FIG. A.5. **Measurement of the Young's modulus of dry PNIPAM films.** *(a): Typical AFM image of the investigated sample. The PNIPAM film shown here was fabricated using a spin-coating speed of* $\omega_{\text{spin}} = 2500\,\text{rpm}$ *and a polymer solution concentration of* $c_{\text{PNIPAM}} = 5\,\%$*. The resulting dry thickness is measured at* $\tau_{\text{dry}} = 950\,\text{nm}$*. The white bar represents* $5\,\mu\text{m}$ *(b): Measured Young's modulus* E *as a function of the* x, y*-position of the measurement, on a* $20 \times 20\,\mu\text{m}$ *window. (c): Histogram of the measured values of Young's modulus* E*. We retain* $E = 700 \pm 100\,\text{MPa}$*.*

(i) The geometry of the probe determines how the contact between the probe and the sample is achieved. The software *AtomicJ* takes into account the shape of the tip (cone, pyramid, sphere, blunt tip...) and its dimensions (radius of curvature, half-angle...).

(ii) The model applied to describe the contact with the sample takes into account mechanical properties of the latter.The Hertz model is often used as a reference [216], however models taking into account adhesion may also be used [288, 289]. Finally, in relevant cases, electrostatic forces are taken into account [290].

A.4.2 Young's modulus of dry PNIPAM films

The process to extract the Young's modulus from force-distance curves is automatized using the software *AtomicJ* [241]. An example of the measurement is shown in Fig. A.5. In Fig. A.5(a) we show a typical AFM image of the investigated sample, that exhibit a pattern. In Fig. A.5(b) we show the measured Young's modulus, as a function of the x, y position of the measurement. We observe that the measured Young's modulus is independent of the pattern. Finally, on Fig. A.5(c) we show an histogram of the measured values of Young's modulus. We retain $E = 700 \pm 100\,\text{GPa}$, which is the most represented value in the histogram.

A.5 Enforcement of the period-doubling hypothesis

In Sec. 2.3.2, we performed a fit of experimental data, which are the expected wavelength in the swollen state of patterns observed at the surface of PNIPAM hydrogels, $\lambda_{\text{p}}^{\text{wet}}$, as a function of the expected swollen thickness τ_{wet}. The model on which the data are fitted is developped by *Dervaux and Ben Amar* [143]. The fit was done on two fitting parameters α_1 and α_2, that correspond respectively to a prefactor and the dry elastocapillary length $l\text{cap}^{\text{dry}}$, as given by Eq. (2.12). The wet expected wavelength is defined by the period doubling hypothesis, formulated in Eq. (2.7).

In the present section we question the factor 2 between the wavelength in dried and swollen states in the thin-film regime. We perform the same fit, but with a third fitting parameter, which corresponds to the factor between the wavelengths. Thus, the model

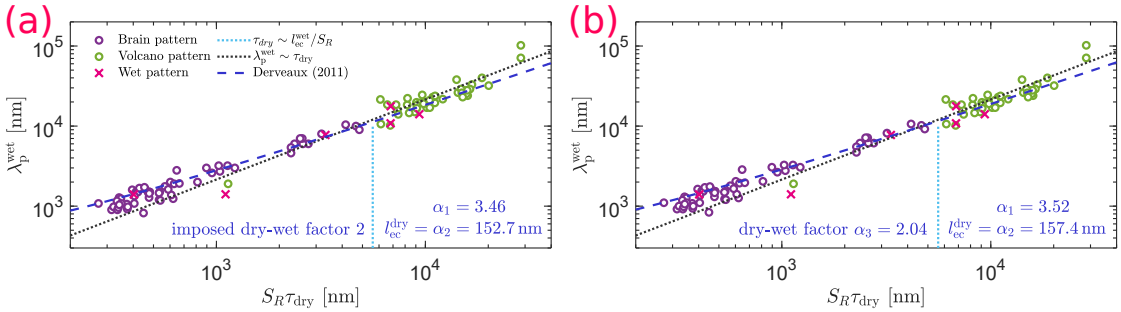

FIG. A.6. **Fit of the ratio between swollen and dried wavelength in the thin-film regime.** *Expected wavelength λ_{wet} when swollen as a function of expected swollen thickness $\tau_{wet} = S_R\tau_{dry}$. The experimental data are fitted with the model of Dervaux and Ber Amar. (a): With two fitting parameters α_1 and α_2, imposing the ratio between the swollen and dried wavelength in the thin-film regime. (b): With three parameters, α_1 α_2 and α_3, the ratio between the swollen and dried wavelength in the thin-film regime being kept as a fitting parameter.*

on which the experimental data are fitted reads:

$$\lambda_p^{wet} = \alpha_1 \frac{4\pi\tau_{dry}}{\log\left[\frac{44.953\tau_{dry}}{\alpha_2}\right]}, \tag{A.5}$$

$$\begin{cases} \lambda_p^{wet} = \alpha_3\lambda_p^{dry}, & \text{for} \quad \tau_{dry} \leq \tau_{dry,c} \\ \lambda_p^{wet} = \lambda_p^{dry}, & \text{for} \quad \tau_{dry} \geq \tau_{dry,c}. \end{cases} \tag{A.6}$$

The results are shown in Fig. A.6. In panel (a) we show the same data as in Fig. 2.14(a), for reference, with the best fit line established with two fitting parameters. In Fig. A.6(b), we show the experimental data fitted with three fitting parameters, based on Eqs. (A.5) and (A.6). We obtained a prefactor and an elastocapillary length from the fitting parameters α_1 and α_2 respectively, that are similar to the one obtained with a two-parameters fit, within $2-3\,\%$. Finally, we obtain from the third fitting parameter α_3 the ratio between the swollen and dried wavelengths in the thin-film regime, as $\alpha_3 = 2.04$, instead of the precise value of 2 that is imposed in the two-parameter fit. In conclusion, the hypothesis of the period doubling holds, within a $2\,\%$ error, which is small considering the dispersion of the data.

A.6 Finding centers on SFA images

In this section we detail how the center of an interference image is found numerically. The raw image is first divided by the background image. A typical obtained image is shown in Figs. A.7(a) and (b). A first guess of the center position is given manually on the last image of the series (we analyze from the closest distance D, thus we start with the last image). The coordinates of the center (x_0, y_0) being guessed, each pixel of the image is associated to cartesian coordinates (x, y), then to polar coordinates (r, θ). In Fig. A.7(c) the same image is shown, in polar coordinates.

The position of the center is numerically optimized from the first guess introduced manually, by working on the image in polar coordinates. We discretize linearly the azimuth axis in N points with a angle step $\Delta\theta$, and we note $\theta_i = i\Delta\theta$. For a given column j (corresponding to a given r_j), the following loss function on the intensity I (in

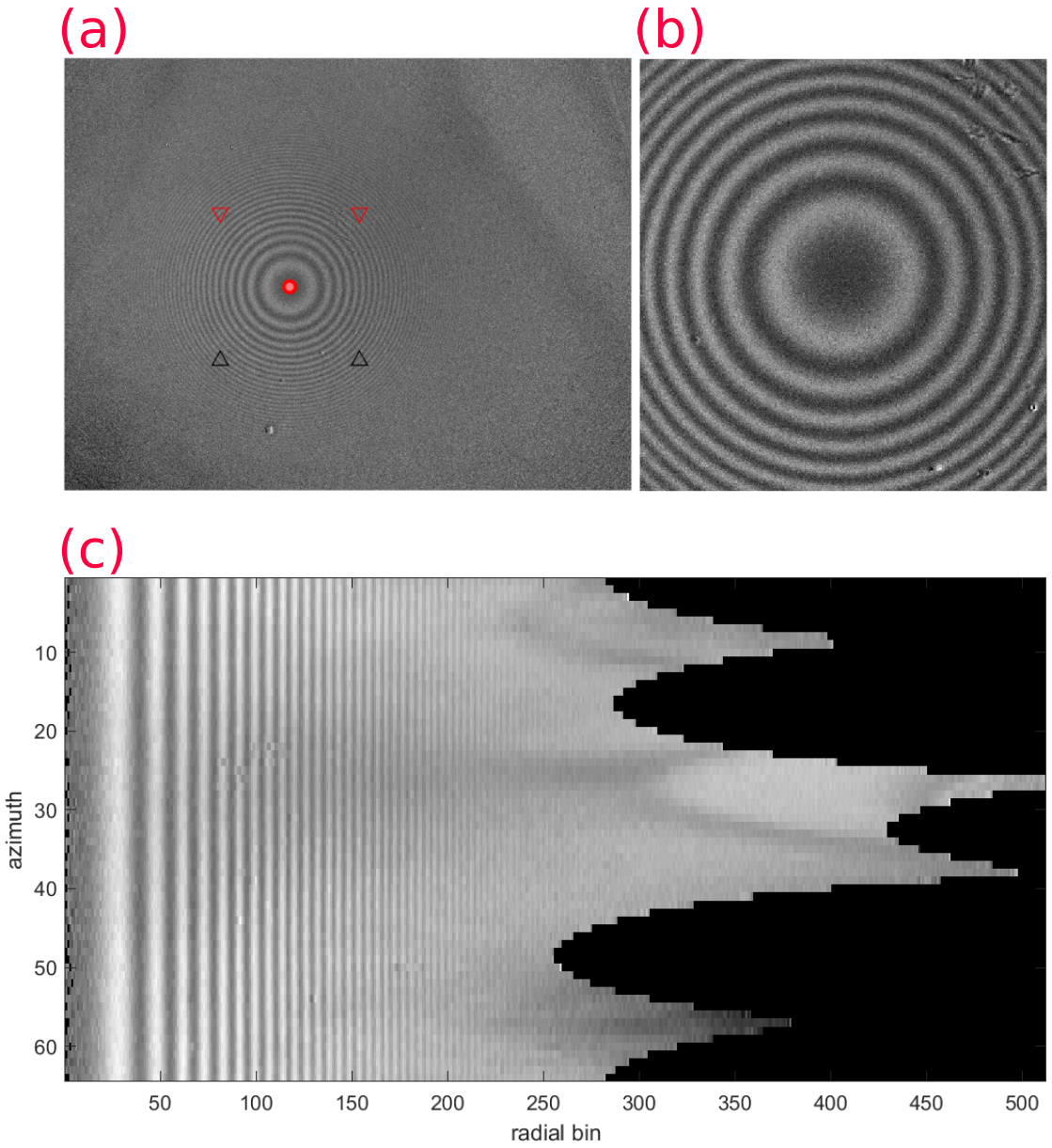

FIG. A.7. **Numerical search for the center of the Newton's rings.** *(a): Large plan of an interference image, after division by the background image. (b): Zoom on the center of the rings. (c): Conversion of the image into polar coordinates. The light intensity is plotted as a function of the radial coordinate r (horizontal axis) and the azimuths θ (vertical axis).*

grey scale) is computed:

$$\mathcal{L}(r_j) = \sum_{i=0}^{N-1} \left(I(r_j, \theta_i) - \bar{I}(r_j) \right)^2 , \tag{A.7}$$

with $\bar{I}(r_j)$ being the intensity averaged over a column. Then, the position of the center $(x_0,\ y_0)$ is optimized so as to minimize the function $\mathcal{L}$. Finally, the coordinates are obtained with a precision smaller than a pixel.

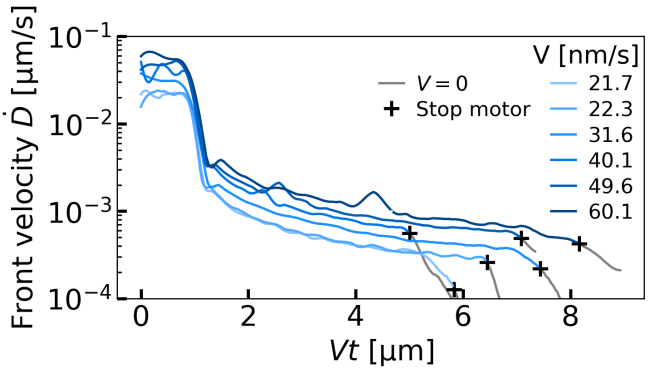

FIG. A.8. **Front velocity of the spherical probe in SFA.** *From the data of Fig. 5.6(b), the time-derivative of the distance D between the two glass interfaces is computed and plotted as a function of Vt, the traveling distance imposed at the back of the spring.*

A.7 Front velocity of the spherical probe in SFA experiments

In this section we compute the time-derivative of the distance D measured between the two glass interfaces in SFA experiments. We use the experimental data shown in Fig. 5.6(b). The experimental data are first filtered using a Savitsky Golay filter of order 3, on a 15-points window (see Appendix C.2.4). Then the time derivative is computed. The obtained velocity is filtered again, with a Savitsy Golay filter of order 3 on a 15-points window. In Fig. A.8 we show the front velocity of the spherical probe, $\dot{D}$, as a function of the traveling distance imposed at the back of the spring, Vt. We observe a first plateau regime for each command velocity, which correspond to the early-time regime, characterized by a constant velocity of the sphere in water. Then a second regime appears for $Vt \geq 1.5\,\mu$m, characterized by a slow decrease of each individual velocity, with front velocities on the order of $\dot{D} \approx 1\,$nm/s.

Appendix B

Crossover between lubrication and contact regimes in SFA experiments

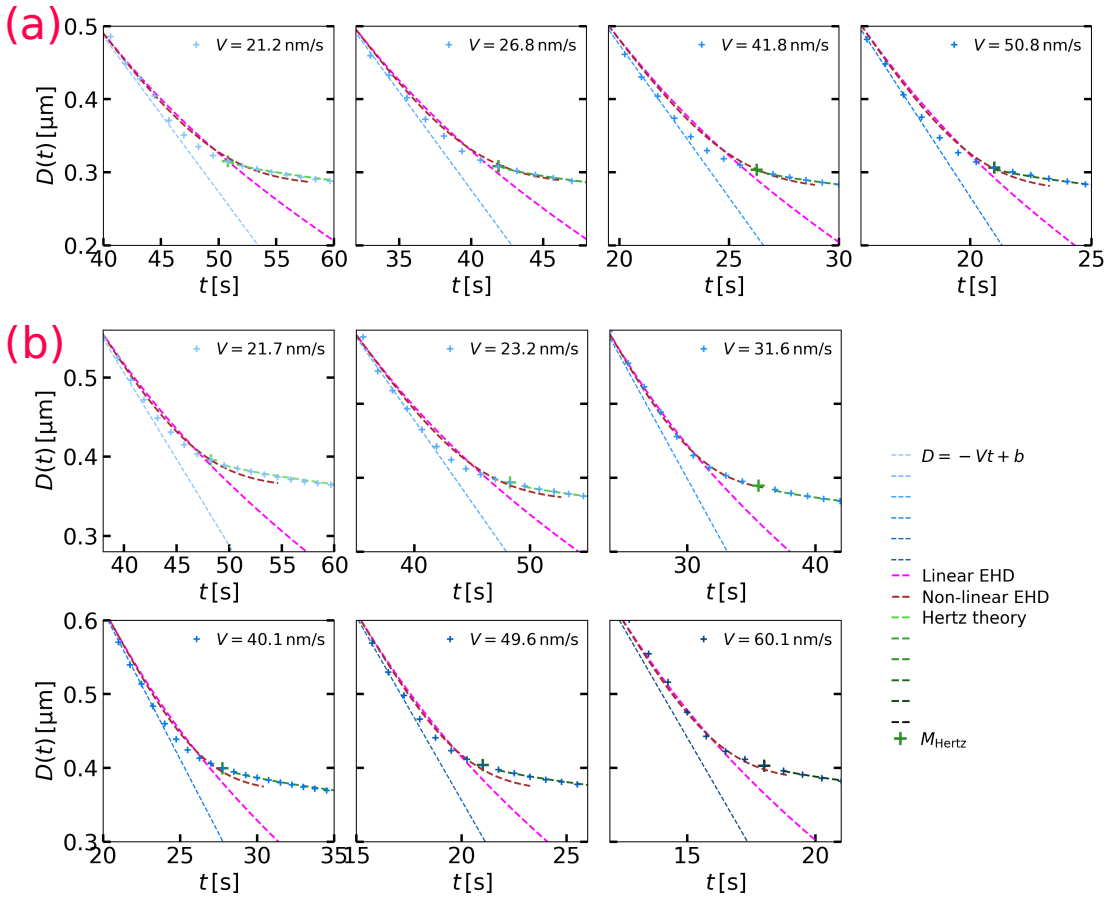

FIG. B.1. **Zoom around the inflection point in distance-time representation.** *Distance D between the two glass interfaces as a function of time, zoomed around the inflection point, for each of the ten approach curves shown in the Chapter 5. (a): First data set, made of four curves. (b): Second data set, made of six curves.*

Appendix C

Numerical Techniques

In reciprocal spaces, expressions were plotted using a logarithmic discretization of the spectral axis s, with a total number of points $N_s = 500$, on a range of $s \in [10^{-3}; 10^{3}]$. For the finite case, numerical errors are seen for values of q lower than 1.

C.1 Laplace inverse transforms

Laplace backward transform is formally expressed by the Bromwich intergral as in complex space:

$$X(t) = \frac{1}{2\pi i} \int_{\gamma - i\infty}^{\gamma + i\infty} \mathrm{d}q \, \hat{X}(q) e^{qt}. \tag{C.1}$$

Talbot's algorithm is used to compute numerically the inverse Laplace transform [255]. The inverse transform is approximated by:

$$X(t) = \frac{2}{5t} \sum_{k=0}^{M-1} \mathrm{Re}\left(w_k \hat{X}\left(\frac{\alpha_k}{t} \right) \right), \tag{C.2}$$

with the nodes given by:

$$\alpha_0 = \frac{2M}{5}, \quad \alpha_k = \frac{2k\pi}{5}\left(\coth(\frac{k\pi}{M}) + i \right) \quad 1 \leq k < M, \tag{C.3}$$

and the weight by:

$$w_0 = \frac{e^{\alpha_0}}{2}, \quad w_k = \left[1 + i\frac{k\pi}{M}\left(1 + \coth(\frac{k\pi}{M})^2 \right) - i\coth(\frac{k\pi}{M}) \right] e^{\alpha_k} \quad 1 \leq k < M. \tag{C.4}$$

A precision of $M = 24$ is chosen, and the time axis is linearly discretized.

A requirement of Talbot's algorithm is that the function to invert should be explicit in Laplace space. As such, Laplace backward transforms are always computed first on explicit functions in reciprocal space. Then, Hankel backward transforms are computed on real-time expressions.

C.2 Hankel inverse transforms

C.2.1 Riemann summation

In the figures shown in this chapter, the backward Hankel transforms were computed with Riemman summation over a finite domain. We recall the backward transform of order 0:

$$X(r) = \int_0^{\infty} \mathrm{d}s \, \hat{X}(s) J_0(sr) s. \tag{C.5}$$

For the semi-infinite case, a linear discretization scheme was used, with a fixed space step both in spectral and real domains, respectively $\mathrm{d}s$ and $\mathrm{d}r$, using N_s and N_r points. The integral is approximated by a Riemann summation so that the backward transform, expressed at the point $r_i = i * \mathrm{d}r$, reads:

$$X(r_i) = \sum_{j=0}^{N_s-1} \hat{X}(s_j) J_0(s_j r_i) s_j \mathrm{d}s. \tag{C.6}$$

The numerical parameters chosen are $N_s = N_r = 200\,000$ and $\mathrm{d}r = 0.005$, on a finite reciprocal domain $s \in [10^{-3}; 10^3]$.

C.2.2 Gauss-Legendre quadrature method

For the finite case, a non-linear, more adapted discretization scheme is chosen to increase the precision. The integral is computed using Gauss-Legendre quadrature method. The integral of an expression f on an interval $x \in [-1; 1]$ is approximated by:

$$\int_{-1}^{1} \mathrm{d}x\, f(x) \approx \sum_{j=0}^{N} w_j f(x_j), \tag{C.7}$$

with x_j the j-th zero of the Legendre polynomial of order n P_n and w_j the associated weight, given by:

$$w_j = \frac{2}{(1 - x_j^2)\left[P_n'(x_j)\right]^2}. \tag{C.8}$$

A mapping of the s axis on $[-1; 1]$ is performed using a linear change of variable and leads to the following discretization of the reciprocal axis:

$$s_j = \frac{s_{N_s-1} - s_{N_0}}{2} x_j + \frac{s_{N_s-1} + s_{N_0}}{2}, \tag{C.9}$$

such that the backward transform expressed at the point r_i reads:

$$X(r_i) = \sum_{j=0}^{N_s-1} \hat{X}(s_j) J_0(s_j r_i) s_j w_j. \tag{C.10}$$

The numerical parameters chosen are $N_s = N_r = 200\,000$ and $\mathrm{d}r = 0.05$, on a finite reciprocal domain $s \in [10^{-4}; 10^2]$.

C.2.3 Fourier-Bessel series

Another method based on Fourier-Bessel serie was explored to numerically compute inverse Hankel transfoms on a finite domains [291]. Let us denote j_k the k-th root of the Bessel function of order 0 J_0, and respectively s_N and r_N the upper bounds of the reciprocal and real domains. The reciprocal axis s and the real axis r are discretized on a total of N points, as:

$$s_m = \frac{j_m}{r_N} = \frac{j_m s_N}{j_N} \quad 1 \leq m \leq N, \tag{C.11a}$$

$$r_k = \frac{j_k r_N}{j_N} = \frac{j_k}{s_N} \quad 1 \leq k \leq N. \tag{C.11b}$$

The forward Hankel transform is approximated by:

$$\hat{X}(s_m) = \sum_{k=1}^{N} \frac{2}{s_N^2 J_1^2(j_k)} X(r_k) J_0\left(\frac{j_k j_m}{j_N}\right). \tag{C.12}$$

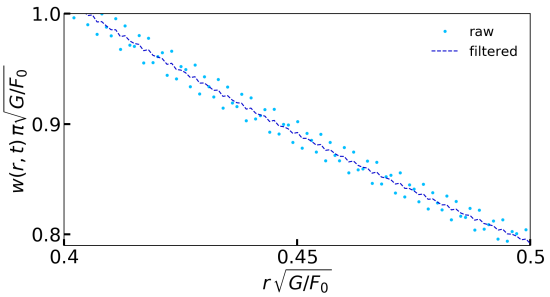

FIG. C.1. **Effect of a Savitsky-Golay filter of order 3.** *A Savitsky-Golay filter of order 3 is applied on a 9-points wide sliding window, for a total of* 200 000 *points.*

The backward Hankel transform is approximated by:

$$X(r_k) = \sum_{m=1}^{N} \frac{2}{r_N J_1^2(j_m)} \hat{X}(s_m) J_0\left(\frac{j_m j_k}{j_N}\right). \tag{C.13}$$

This method is claimed to be efficient to reduce numerical errors due to the truncation of the integral at a finite value s_N, yet it adds constraints on the sampling in both reciprocal and real space, such as $s_N r_N = j_N$.

C.2.4 Savitsky-Golay filter

After having applied both backward Laplace and Hankel transforms, a few residual oscillations remain on the numerical result. Curves are smoothened using a polynomial Savitsky-Golay filter of order 3, on a 9 points-wide sliding window, for a total of 100 000 (finite-sized case) or 200 000 (semi-infinite case) points. Fig.C.1 shows that when an effect of smoothening is obtained, residual oscillations due to numerical challenges are erased, and results are more lisible. For our purpose no information is lost in the process.

C.2.5 Numerical calculation of the finite-thickness poroelastic Green's function in reciprocal space

When computing large numbers with *Python*, fatal errors occur ("OverFlowError") and the software does not end the computation. To avoid this problem, the calculation is made as follows:

$$\hat{w}_\tau(s,q) = \begin{cases} \dfrac{F_0}{4\pi G s q} \dfrac{N_1+N_2+N_3}{D_1+D_2+D_3} & \text{with Eqs. (3.42) and (3.43), for} \quad s\sqrt{\dfrac{F_0}{G}} \leq 100 \\ \dfrac{F_0}{4\pi G s q} \dfrac{1}{1+\Lambda\frac{\mathcal{D}_{\mathrm{pe}}s^2}{q}\left(1-\sqrt{1+\frac{q}{\mathcal{D}_{\mathrm{pe}}s^2}}\right)} & \text{with Eq. (3.35), for} \quad s\sqrt{\dfrac{F_0}{G}} > 100 \end{cases} \tag{C.14}$$

C.3 Numerical resolution of the Fredholm integral

In this section we detail the numerical resolution of the Fredholm integral of the second kind used in Sec. 4.1.5. We first recall the integro-differential equation of the Fredholm

integral:

$$p^*(k) = -\frac{3ik}{4}K_1(k) - \frac{3i}{2k}\left(\frac{H_\mathrm{c}}{H}\right)^{3/2}\int_0^\infty \mathrm{d}s\,\mathcal{G}^*(s)p^*(s)\mathcal{K}(s,k), \tag{C.15}$$

with the variables s, k, the complex pressure field p^* and the Green's function $\mathcal{G}$ in reciprocal space being dimensionless. The kernel $\mathcal{K}$ of the Fredholm equation has an analytical solution [261], given by Eq. (4.30). The integral is evaluated with Gauss-Legendre quadrature method described in Appendix C.2.2. The s-axis is discretized in N points, we denote s_j the j-th point being the j-th zero of the Legendre polynomial of order N and w_j the associated weight. We denote the complex pressure field p^* expressed at the discrete point k_j: $p^*_j = p^*(k_j)$, and the kernel $\mathcal{K}$ expressed at the discrete points s_l and k_j: $\mathcal{K}_{l,j} = \mathcal{K}(s_l, k_j)$. The discretized version of Eq. (C.15) reads:

$$p^*_j = -\frac{3ik_j}{4}K_1(k_j) - \frac{3i}{2k_j}\left(\frac{H_\mathrm{c}}{H}\right)^{3/2}\sum_{l=0}^{N-1} w_l\mathcal{G}^*(s_l)p^*_l\mathcal{K}_{l,j}. \tag{C.16}$$

We can write the latter equation under the form of a matrical system:

$$\mathcal{M}.\mathcal{P} = \mathcal{RHS}, \tag{C.17}$$

with $\mathcal{P}$ the vector to solve for, $\mathcal{RHS}$ a known vector and $\mathcal{M}$ a matrix to invert, the expressions of which are given by:

$$\mathcal{P}_l = p^*_l, \quad l \in [\![0; N-1]\!], \tag{C.18a}$$

$$\mathcal{RHS}_j = -ik_jK_1(k_j), \quad j \in [\![0; N-1]\!], \tag{C.18b}$$

$$\mathcal{M}_{j,l} = \frac{4}{3}\delta_{l,j} - \frac{2i}{k_j}\left(\frac{H_\mathrm{c}}{H}\right)^{3/2} w_l\mathcal{G}^*(s_l)\mathcal{K}_{l,j}, \quad l,j \in [\![0; N-1]\!], \tag{C.18c}$$

with $\delta_{l,j}$ the Kronecker symbol. The matrix $\mathcal{M}$ can be numerically inverted, such that the complex pressure field is given in reciprocal space by:

$$\mathcal{P} = \mathcal{M}^{-1}.\mathcal{RHS}. \tag{C.19}$$

The discretized complex pressure field at a point k_l is then given by:

$$p^*_l = \mathcal{P}_l = \left(\mathcal{M}^{-1}\right)_{l,j}\mathcal{RHS}_j, \quad l \in [\![0; N-1]\!]. \tag{C.20}$$

C.4 Calculation of the finite-thickness poroelastic Green's function with *Mathematica*

In this section is given a *Mathematica* code that computes formally the poroelastic Green's function for a finite-thickness layer in reciprocal spaces. To make the output display, one can erase the punctuation sign ";" at the end of a line.

```
chi[s_, q_] = Dpe * s^2 / q;
beta[s_, q_] = Sqrt[1 + 1 / chi[s, q]];
zeta[s_] = s * tau;

RHS[s_, q_] = {0, -F0 / (4 Pi G * s^2 q), 0, 0, 0, 0};

BigMatrix[s_, q_] = {{0, 0, 1, beta[s, q], -1, -beta[s, q]}, {-1 / s, 1 / s, 1, 1, 1, 1},
    {1 / s, -1 / s, 0, 1 / (Lambda * chi[s, q]), 0, 1 / (Lambda * chi[s, q])},
    {-tau * Exp[-zeta[s]], -tau * Exp[zeta[s]], Exp[-zeta[s]],
     Exp[-zeta[s] * beta[s, q]], Exp[zeta[s]], Exp[zeta[s] * beta[s, q]]},
    {(1 + zeta[s]) / s * Exp[-zeta[s]], (1 - zeta[s]) / s * Exp[zeta[s]],
     -Exp[-zeta[s]], beta[s, q] * Exp[-zeta[s] * beta[s, q]], Exp[zeta[s]],
     beta[s, q] * Exp[zeta[s] * beta[s, q]]}, {1 / s * Exp[-zeta[s]], 1 / s * Exp[zeta[s]],
     0, beta[s, q] / (Lambda * chi[s, q]) * Exp[-zeta[s] * beta[s, q]],
     0, -beta[s, q] / (Lambda * chi[s, q]) * Exp[zeta[s] * beta[s, q]]}};

InvBigMatrix[s_, q_] = Inverse[BigMatrix[s, q]];

CoeffAB[s_, q_] = InvBigMatrix[s, q].RHS[s, q];

A1[s_, q_] = Part[CoeffAB[s, q], 1];
A2[s_, q_] = Part[CoeffAB[s, q], 2];
B1[s_, q_] = Part[CoeffAB[s, q], 3];
B2[s_, q_] = Part[CoeffAB[s, q], 4];
B3[s_, q_] = Part[CoeffAB[s, q], 5];
B4[s_, q_] = Part[CoeffAB[s, q], 6];

Apotential[s_, z_, q_] = A1[s, q] * Exp[s * z] + A2[s, q] * Exp[-s * z];
Bpotential[s_, z_, q_] = B1[s, q] * Exp[s * z] + B2[s, q] * Exp[s * z * beta[s, q]] +
    B3[s, q] * Exp[-s * z] + B4[s, q] * Exp[-s * z * beta[s, q]];

Uz[s_, z_, q_] =
  z * D[Apotential[s, z, q], z] - Apotential[s, z, q] + D[Bpotential[s, z, q], z];

GreenPoroElastic[s_, q_] = Uz[s, 0, z];
```

Appendix D

Green's functions

D.1 Introduction to Green's function: resolution of a diffusion equation

In this section, we detail the classical path that is used to solve a three-dimensional diffusion equation. We take the opportunity of solving a simple standard diffusion equation to present the calculation method, which scope is much more general. This method is generally used to solve more complex systems of partial differential equations. Let us consider the following diffusion equation over a concentration field c:

$$\frac{\partial c}{\partial t} = \mathcal{D}\boldsymbol{\nabla}^2 c. \tag{D.1}$$

The diffusion equation is first solved in one dimension, along the x axis, for simplicity. First, a fundamental solution denoted $\mathcal{G}$ is desired, *i.e.* a solution that satisfies the following initial condition:

$$c(x, t = 0) = c_0\delta(x) \tag{D.2}$$

We introduce the spatial Fourier transform of the concentration field c, as:

$$\hat{c}(q, t) = \frac{1}{\sqrt{2\pi}} \int_{-\infty}^{\infty} \mathrm{d}x\, c(x, t) e^{-iqt}. \tag{D.3}$$

Thus, the diffusion equation (D.1) and the initial condition given in Eq. (D.2) are expressed in Fourier space, as:

$$\frac{\partial \hat{c}}{\partial t} = -\mathcal{D}q^2\hat{c} \tag{D.4a}$$

$$\hat{c}(q, t = 0) = c_0. \tag{D.4b}$$

The solution to Eqs. (D.4) in Fourier space is called the fundamental solution or the Green's function of the diffusion equation (1.16), and reads:

$$\hat{\mathcal{G}}(q, t) = c_0 \exp\left(\mathcal{D}q^2 t\right). \tag{D.5}$$

By applying the inverse Fourier transform, the Green's function is expressed in real space, as:

$$\mathcal{G}(x, t) = \frac{c_0}{\sqrt{4\pi\mathcal{D}t}} \exp\left(-\frac{x^2}{4\mathcal{D}t}\right). \tag{D.6}$$

We consider now the three-dimensional diffusion equations written in Eq. (D.1), associated to the fundamental initial condition, as:

$$c(\boldsymbol{x}, t = 0) = c_0\delta^3(\boldsymbol{x}). \tag{D.7}$$

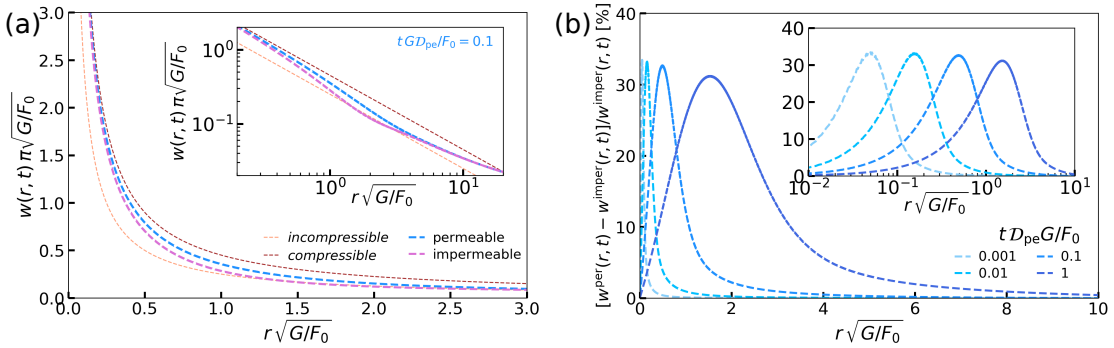

FIG. D.1. **Comparison between the point-force solutions of the permeable and impermeable cases.** *(a): Normalized surface deformation as a function of the radial coordinate at the noted time, using* $\nu = 0.1$. *The point-force solutions for permeable and impermeable boundary conditions are shown, computed from the inverse transforms of Eqs.* (3.35) *and* (D.11). *The orange and red dashed lines correspond to the inverse transforms of Eqs.* (3.36a) *and* (3.36b). *The inset shows the same data on logarithmic scales. (b): Relative difference between the surface deformation in the permeable and impermeable cases, as a function of the radial coordinate, for the noted dimensionless times. The inset shows the same data in semi-logarithmic scale.*

The fundamental solution of the problem, or the three-dimensional Green's function, is the product of the Green's functions in one dimension, as written in Eq. (D.6). The resulting Green's function in three dimension reads:

$$\mathcal{G}(\boldsymbol{x}, t) = \frac{c_0}{\sqrt{4\pi\mathcal{D}t}^3} \exp\left(-\frac{\boldsymbol{x}^2}{4\mathcal{D}t}\right). \tag{D.8}$$

Finally, by applying the superposition principle, the solution to the diffusion equation (1.16) associated with any initial condition is computed by convolution to the Green's function $\mathcal{G}$, as:

$$c(\boldsymbol{x}, t) = \iiint_{\mathbb{R}^3} \mathrm{d}^3\boldsymbol{x}\, \mathcal{G}(\boldsymbol{x} - \boldsymbol{y}, t) c(\boldsymbol{y}, t = 0), \tag{D.9}$$

with $c(\boldsymbol{x}, t = 0)$ the initial condition.

D.2 Point-force solution for a semi-inifinite impermeable gel and comparison to the permeable case

Here, we discuss the effect of surface permeability on the point-force response. In this chapter, the focus is made on permeable-interface case, we assumed that the gel is in contact with a bath of its own solvent, which fixes the chemical potential of the solvent at the surface to its reference value, at all times. If the gel is in contact with an other kind of medium (*e.g.* air, solid surface, or immiscible liquid), the description should be modified, in particular by incorporating drying. If one considers time scales smaller than the drying time, we can neglect the solvent exchange at the interface. In that case, we suppose the solvent flux vanishes at the surface, allowing us to impose the *impermeable* boundary condition at $z = 0$:

$$\mathbf{J} \cdot \mathbf{n} = \frac{\partial \mu}{\partial z}(r, z = 0, t) = 0. \tag{D.10}$$

We can use the same method as the one described in section 3.3.1.1, in order to derive the point-force response of a semi-infinite, permeable medium:

$$\hat{w}^{\text{imper}}(s,q) = -\frac{1}{2Gsq}\frac{1}{1+\Lambda\frac{\mathcal{D}_{\text{pe}}s^2}{q}\left(\frac{1}{\sqrt{1+\frac{q}{s^2\mathcal{D}_{\text{pe}}}}}-1\right)}, \tag{D.11}$$

where the superscript "imper" stands for the impermeable condition. We thus recover the solution derived in Ref. [110]. The diffusive-like self-similarity discussed in the main text, holds as well here.

The point-force responses with impermeable and permeable boundary conditions are compared in Fig.D.1(a). Both solutions appear to be qualitatively similar, and display the same short-term and long-term behaviors. Nevertheless, at a given time $t = 0.1F_0/(G\mathcal{D}_{\text{pe}})$, we observe that the surface deformation in the impermeable case is smaller than the one in the permeable case. Also, the permeable solution relaxes faster than the impermeable one towards the long-time purely elastic compressible limit. Quantitatively, for a Poisson ratio $\nu = 0.1$, we observe a relative difference between the two solutions up to 35%, where the maximum difference is located at a radial position $\sim \sqrt{\mathcal{D}_{\text{pe}}t}$, as shown in Fig. D.1 (b).

D.3 Derivation of the semi-infinite, poroelastic Green's function in steady-state

In chapter 3 we derive the deformation profile of a semi-infinite poroelastic layer submitted to any axisymmetrical, external pressure field, in the general case.

D.3.1 Linear poroelastic theory

In this section we focus on the particular case of a periodic pressure field p, and we thus invoke the linear response theory, we write a field X as:

$$X(r,t) = \text{Re}[X^*(r)e^{i\omega t}], \tag{D.12}$$

where * indicates complex variables, $i^2 = -1$, and Re is the real part. We recall the set of two coupled equations Eqs. (3.8) on the concentration field and the chemical potential that govern the problem, and write them in complex variables:

$$\nabla^2\left[\mu^* - 2G\Omega^2\frac{1-\nu}{1-2\nu}c^*\right] = 0, \tag{D.13a}$$

$$\mathcal{D}_{\text{pe}}\nabla^2 c^* - i\omega c^* = 0. \tag{D.13b}$$

At the solvent-gel interface in the steady-state regime, a pressure field $p^*(r)$ is applied, thus Eq. (3.10) becomes in complex variable:

$$\sigma^*_{zz} = -p^*(r), \quad \sigma^*_{rz} = 0. \tag{D.14}$$

We consider the solvent-gel interface to be permeable as in section 3.2.1.2, which sets the surface chemical potential to its reference and constant value. In the steady-state regime, the constant disappears:

$$\mu^*(r, z=0) = 0. \tag{D.15}$$

The poroelastic layer is considered infinitely thick. In the limit $z \to \infty$, the stress and strain fields vanish. The complex solvent concentration c^* and chemical potential μ^* fields go to 0 in the steady-state regime.

D.3.2 Resolution

Following the method introduced by McNamee & Gibson [117, 252–254], we use the same change of variables as in chapter 3, section 3.3.1 which consists of the introduction of two displacement potentials $A^*(r,z)$ and $B^*(r,z)$, in steasy-state regime, defined by:

$$u_r^* = z\frac{\partial A^*}{\partial r} + \frac{\partial B^*}{\partial r}, \tag{D.16a}$$

$$u_z^* = z\frac{\partial A^*}{\partial z} - A^* + \frac{\partial B^*}{\partial z}, \tag{D.16b}$$

with u_r^* and u_z^* being the two components of the complex displacement field $\mathbf{u}^*$. The potentials A^* and B^* satisfy the following equations:

$$\nabla^2 A^* = 0, \tag{D.17a}$$

$$\nabla^2 B^* = \Omega c^*, \tag{D.17b}$$

$$2G\Omega\frac{\partial A^*}{\partial z} = \mu^* - 2G\Omega^2\frac{1-\nu}{1-2\nu}c^*, \tag{D.17c}$$

$$\mathcal{D}_{\mathrm{pe}}\nabla^4 B^* = i\omega\nabla^2 B^*. \tag{D.17d}$$

Given the axisymmetry of the situation, to solve Eqs. (D.17), we reconsider the problem in spatial spectral domain. We introduce the Hankel transform of i-th order, with $i \in \{0,1\}$. In such a framwork, a given field $X^*(r)$is transformed into:

$$\hat{X}^*(s) = \int_0^\infty \mathrm{d}r\, X^*(r) r J_i(sr), \tag{D.18}$$

where J_0 is the Bessel function of the first kind and zeroth order. The inversion formula reads:

$$X^*(r) = \int_0^\infty \mathrm{d}s\, \hat{X}^*(s) s J_i(sr). \tag{D.19}$$

Then, the calculation path detailed in section 3.3.1 applies for the calculation in the steady-state regime, substituing the temporal frequency q in Laplace domain by $i\omega$ in the steady-state description. Expressing Eqs. (D.17) in spectral domain, we get the following ordinary differential equations on the transformed potentials $\hat{A}^*(s,z)$ and $\hat{B}^*(s,z)$:

$$\left(\frac{\partial^2}{\partial z^2} - s^2\right)\hat{A}^* = 0, \tag{D.20a}$$

$$\left(\frac{\partial^2}{\partial z^2} - s^2 - \frac{i\omega}{\mathcal{D}_{\mathrm{pe}}}\right)\left(\frac{\partial^2}{\partial z^2} - s^2\right)\hat{B}^* = 0. \tag{D.20b}$$

The solutions to Eqs. (D.20a) and (D.20b) that vanish at $z \to -\infty$ read:

$$\hat{A}^* = a_1 e^{sz}, \tag{D.21a}$$

$$\hat{B}^* = b_1 e^{sz} + b_2 e^{z\sqrt{s^2 + i\omega/\mathcal{D}_{\mathrm{pe}}}}, \tag{D.21b}$$

where a_1, b_1, b_2 are integration constants, that depend on the spectral variable s and the frequency ω. Expressing the stress and chemical-potential boundary conditions of Eqs. (D.14) and (D.15) in reciprocal spaces in terms of the potentials, we obtain under a matricial form:

$$\begin{pmatrix} 0 \\ -\frac{\hat{p}^*(s)}{2Gs^2} \\ 0 \end{pmatrix} = \begin{pmatrix} 0 & 1 & \beta \\ -\frac{1}{s} & 1 & 1 \\ \frac{1}{s} & 0 & \frac{1}{\Lambda\chi} \end{pmatrix} . \begin{pmatrix} a_1 \\ b_1 \\ b_2 \end{pmatrix}, \tag{D.22}$$

with:

$$\chi = -i\frac{\mathcal{D}_{\mathrm{pe}}s^2}{\omega}, \quad \beta = \sqrt{1+\frac{i\omega}{\mathcal{D}_{\mathrm{pe}}s^2}} = \sqrt{1+\frac{1}{\chi}}, \quad \Lambda = \frac{1-2\nu}{1-\nu}. \tag{D.23}$$

Solving Eq. (D.22), we can compute a_1, b_1 and b_2. Using Eqs. (D.16), (D.21) and (D.22), we finally express the deformation profile in the steady-state regime:

$$\hat{w}^*(s) = -\hat{u}_z^*(s, z=0) = \frac{\hat{p}^*(s)}{2Gs}\,\frac{1}{1-i\Lambda\frac{\mathcal{D}_{\mathrm{pe}}s^2}{\omega}\left(1-\sqrt{1+\frac{i\omega}{\mathcal{D}_{\mathrm{pe}}s^2}}\right)}\,. \tag{D.24}$$

The Green's function of the problem in the steady-state regime reads:

$$\hat{\mathcal{G}}^*(s) = \frac{1}{2Gs}\,\frac{1}{1-i\Lambda\frac{\mathcal{D}_{\mathrm{pe}}s^2}{\omega}\left(1-\sqrt{1+\frac{i\omega}{\mathcal{D}_{\mathrm{pe}}s^2}}\right)}\,. \tag{D.25}$$

D.4 Derivation of the finite-thickness, purely elastic Green's function

In chapter 3 we derive the deformation profile of a semi-infinite poroelastic layer submitted to any axisymmetrical, external pressure field, in the general case.

D.4.1 Linear elastic theory

D.4.1.1 Description of a purely elastic medium

In this section we focus on a purely elastic and compressible finite-size layer. There is no solvent flux inside the elastic matrix, thus, the chemical potential is fixed to its reference value μ_0, and the permeability k and the solvent flux bmJ are set to zero. We recall the definition of the strain tensor $\boldsymbol{\epsilon}$, as written in Eq. (3.1):

$$\boldsymbol{\epsilon} = \frac{1}{2}\left[\boldsymbol{\nabla}\mathbf{u} + (\boldsymbol{\nabla}\mathbf{u})^T\right], \tag{D.26}$$

where $\mathbf{u}$ denotes the displacement field with respect to the reference state. We suppose again the stress-strain relationship to be linear. The stress tensor $\boldsymbol{\sigma}$ given by Eq. (3.5), in the absence of any flow, reads:

$$\boldsymbol{\sigma} = 2G\Big[\boldsymbol{\epsilon} + \frac{\nu}{1-2\nu}\mathrm{Tr}(\boldsymbol{\epsilon})\mathbf{I}\Big], \tag{D.27}$$

where $\mathbf{I}$ is the identity tensor. In the absence of body force, the mechanical equilibrium is expressed by Navier's closure equation, given in Eq. (3.6), by:

$$\boldsymbol{\nabla}\cdot\boldsymbol{\sigma} = \mathbf{0}. \tag{D.28}$$

D.4.1.2 Equation governing the displacement field

Combining the last three equations, we get and equation on the displacement field $\mathbf{u}$:

$$\boldsymbol{\nabla}^2\mathbf{u} + \frac{1}{1-2\nu}\boldsymbol{\nabla}\left(\boldsymbol{\nabla}\cdot\mathbf{u}\right) = 0. \tag{D.29}$$

Finally, we take the divergence of Eq. (D.29), and get:

$$\boldsymbol{\nabla}^2\left(\boldsymbol{\nabla}\cdot\mathbf{u}\right) = 0. \tag{D.30}$$

In the general case of a compressible material, the divergence of the displacement field is not zero:

$$\boldsymbol{\nabla}\cdot\mathbf{u} \neq 0. \tag{D.31}$$

D.4.2 Boundary conditions

Following the calculation path given in Chap. 3, we first describe the free interface. For times $t \leq 0$, we suppose that the gel is in the undeformed reference state with strain- and stress-free conditions. For $t = 0$, an axisymmetric pressure field $p(r)$ is applied on the surface. At the interface *i.e.* $z = 0$ in the reference state), the stress boundary condition is therefore given in Eq. (3.10), by:

$$\boldsymbol{\sigma} \cdot \mathbf{e}_z = -p(r)\mathbf{e}_z, \tag{D.32}$$

where $\delta(\mathbf{r})$ denotes the Dirac distribution. At the interface with the substrate, located at $z = -\tau$, we consider that the elastic layer is fixed to the rigid boundary. Thus, the displacement field is set at zero, as expressed by Eq. (3.14), which reads:

$$\mathbf{u}(z = -\tau) = \mathbf{0}. \tag{D.33}$$

D.4.3 Resolution

D.4.3.1 Expression in terms of potential functions

We follow the same calculation path as in Chapter 3. Then, we introduce the same displacement functions $A(r, z, t)$ and $B(r, z, t)$, defined in Eq. (3.16), as:

$$u_r = z\frac{\partial A}{\partial r} + \frac{\partial B}{\partial r}, \tag{D.34a}$$

$$u_z = z\frac{\partial A}{\partial z} - A + \frac{\partial B}{\partial z}, \tag{D.34b}$$

and that satisfy the following equations:

$$\boldsymbol{\nabla}^2 A = 0, \tag{D.35a}$$

$$\nabla^2 B = \boldsymbol{\nabla} \cdot \mathbf{u}, \tag{D.35b}$$

$$\frac{\partial A}{\partial z} = \frac{1-\nu}{1-2\nu}\boldsymbol{\nabla} \cdot \mathbf{u}, \tag{D.35c}$$

$$\boldsymbol{\nabla}^4 B = 0. \tag{D.35d}$$

Using Eqs. (D.35), we can write a last one that links A and B:

$$\frac{\partial A}{\partial z} - \frac{1-\nu}{1-2\nu}\nabla^2 B = 0. \tag{D.36}$$

Using Eqs. (D.27), (D.34) and (D.35), we recall the components of the stress tensor, as given in Eqs. (3.19), by:

$$\sigma_{rr} = 2G\left(z\frac{\partial^2 A}{\partial r^2} - \frac{\partial A}{\partial z} + \frac{\partial^2 B}{\partial r^2} - \Delta B\right), \tag{D.37a}$$

$$\sigma_{zz} = 2G\left(z\frac{\partial^2 A}{\partial z^2} - \frac{\partial A}{\partial z} + \frac{\partial^2 B}{\partial z^2} - \Delta B\right), \tag{D.37b}$$

$$\sigma_{rz} = 2G\left(\frac{\partial^2 B}{\partial r \partial z} + z\frac{\partial^2 A}{\partial z \partial r}\right). \tag{D.37c}$$

D.4.3.2 Mathematical transforms

As in Chapter. 3, we reconsider the problem in the spectral domain. We recall the Hankel transform, introduced by Eq. (3.20), which reads:

$$\hat{X}(s) = \int_0^\infty \mathrm{d}r \; X(r,t) r J_j(sr), \tag{D.38}$$

with $j \in \{0,1\}$ being the order of the Hankel transform in space. By applying Eq. (D.38) on Eqs. (D.35), we get the following ordinary differential equations on the transformed potentials $\hat{A}(s,z)$ and $\hat{B}(s,z)$:

$$\left(\frac{\partial^2}{\partial z^2} - s^2\right)\hat{A} = 0, \tag{D.39a}$$

$$\left(\frac{\partial^2}{\partial z^2} - s^2\right)^2 \hat{B} = 0. \tag{D.39b}$$

For clarity, we write the expressions of the transformed components of the displacement field and the stress tensor, as:

$$\hat{u}_s = sz\hat{A} + s\hat{B}, \tag{D.40a}$$

$$\hat{u}_z = z\frac{\partial \hat{A}}{\partial z} - \hat{A} + \frac{\partial \hat{B}}{\partial z}, \tag{D.40b}$$

$$\hat{\sigma}_{sz} = sz\frac{\partial \hat{A}}{\partial z} + s\frac{\partial \hat{B}}{\partial z}, \tag{D.40c}$$

$$\hat{\sigma}_{zz} = z\frac{\partial^2 \hat{A}}{\partial z^2} + \frac{\nu}{1-2\nu}\left(\frac{\partial^2 \hat{B}}{\partial z^2} - s^2\hat{B}\right) + \frac{\partial^2 \hat{B}}{\partial z^2}. \tag{D.40d}$$

Finally, the transformed Eq. (D.36) reads:

$$\frac{\partial \hat{A}}{\partial z} + \frac{1-\nu}{1-2\nu}\left(\frac{\partial^2 \hat{B}}{\partial z^2} - s^2\hat{B}\right) = 0. \tag{D.41}$$

D.4.3.3 Solutions for a finite-size layer

The solutions to Eqs. (D.39) read:

$$\hat{A} = a_1 e^{sz} + a_2 e^{-sz}, \tag{D.42a}$$

$$\hat{B} = (b_1 + zb_2)e^{sz} + (b_3 + zb_4)e^{-sz}, \tag{D.42b}$$

where $a_1, a_2, b_1, b_2, b_3, b_4$ are integration constants, that depend on the spectral variable s. Combining Eqs. (D.41) and (D.42), we derive the following expressions of the integration constants a_1 and a_2:

$$a_1 = -2\frac{1-\nu}{1-2\nu}b_2, \tag{D.43a}$$

$$a_2 = -2\frac{1-\nu}{1-2\nu}b_4, \tag{D.43b}$$

which reduces the problem from 6 to 4 integration constants to solve. We use an auxiliary function as introduced in Chapter 3, which reads:

$$\zeta = s\tau. \tag{D.44}$$

Then, combining the transformed stress tensor and displacement field given in Eqs. (D.40), together with the boundary conditions given in Eqs. (D.32) and (D.33), we obtain:

$$\hat{\sigma}_{sz}(s, z=0, q) = \quad 0 \quad = 2G\left[s(b_1 - b_3) + b_2 + b_4\right], \tag{D.45a}$$

$$\hat{\sigma}_{zz}(s, z=0, q) = -\hat{p}(s) = 2Gs\left[s(b_1 + b_3) + \frac{2(1-\nu)}{1-2\nu}(b_2 - b_4)\right], \tag{D.45b}$$

$$\hat{u}_s(s, z=-\tau) = \quad 0 \quad = s\left[b_1 e^{-\zeta} + b_3 e^{\zeta}\right] + \frac{\zeta}{1-2\nu}\left[b_2 e^{-\zeta} + b_4 e^{\zeta}\right], \tag{D.45c}$$

$$\hat{u}_z(s, z=-\tau) = \quad 0 \quad = s\left[b_1 e^{-\zeta} - b_3 e^{\zeta}\right] + \frac{1}{1-2\nu}\left[(3 - 4\nu + \zeta) b_2 e^{-\zeta} + (3 - 4\nu - \zeta) b_4 e^{\zeta}\right]. \tag{D.45d}$$

Equations (D.45) can be written under the form of a matrix equation, with division by the factors $2G$ and $2Gs$, on the first two lines, respectively, as:

$$\begin{pmatrix} 0 \\ -\frac{\hat{p}(s)}{2Gs} \\ 0 \\ 0 \end{pmatrix} = \begin{pmatrix} s & 1 & -s & 1 \\ s & \frac{2(1-\nu)}{1-2\nu} & s & -\frac{2(1-\nu)}{1-2\nu} \\ se^{-\zeta} & \frac{\zeta}{1-2\nu}e^{-\zeta} & se^{\zeta} & \frac{\zeta}{1-2\nu}e^{\zeta} \\ se^{-\zeta} & \frac{3-4\nu+\zeta}{1-2\nu}e^{-\zeta} & -se^{\zeta} & \frac{3-4\nu-\zeta}{1-2\nu}e^{\zeta} \end{pmatrix} \cdot \begin{pmatrix} b_1 \\ b_2 \\ b_3 \\ b_4 \end{pmatrix}. \tag{D.46}$$

Using the formal calculation software *Mathematica*, the four coefficients b_1, b_2, b_3, b_4 are computed, then, the two $a - 1$, and a_2. The vertical displacement field $\hat{u}_z$ is computed. By taking the opposite of its value in $z = 0$, we obtain the deformation profile of a finite-size, purely elastic and compressible layer, as:

$$\hat{w}_\tau^{\text{comp}}(s) = -\hat{u}_z(s, z=0) = \frac{\hat{p}(s)(1-\nu)}{Gs} \frac{2\zeta - (4\nu - 3)\sinh(2\zeta)}{5 + 4\nu(2\nu - 3) + 2\zeta^2 - (4\nu - 3)\cosh(2\zeta)}, \tag{D.47}$$

and the Green's function of the problem reads:

$$\hat{\mathcal{G}}_\tau^{\text{comp}}(s) = \frac{1-\nu}{Gs} \frac{2\zeta - (4\nu - 3)\sinh(2\zeta)}{5 + 4\nu(2\nu - 3) + 2\zeta^2 - (4\nu - 3)\cosh(2\zeta)}, \tag{D.48}$$

as given in Eq. (3.45) and in [203], and derived in [212].

Appendix E

Mechanical response of a thick poroelastic gel in contactless colloidal-probe rheology

In this section we reproduce the published work from which Chapters. 3 and 4 are inspired [251], for reference.

PROCEEDINGS A

royalsocietypublishing.org/journal/rspa

Research

Cite this article: Kopecz-Muller C, Bertin V, Raphaël E, McGraw JD, Salez T. 2023 Mechanical response of a thick poroelastic gel in contactless colloidal-probe rheology. *Proc. R. Soc. A* **479**: 20220832.
https://doi.org/10.1098/rspa.2022.0832

Received: 14 December 2022
Accepted: 3 February 2023

Subject Areas:
mechanical engineering, chemical physics, fluid mechanics

Keywords:
gels, colloidal probe, soft lubrication, poroelasticity, rheology

Authors for correspondence:
Vincent Bertin
e-mail: v.l.bertin@utwente.nl
Joshua D. McGraw
e-mail: joshua.mcgraw@cnrs.fr
Thomas Salez
e-mail: thomas.salez@cnrs.fr

Mechanical response of a thick poroelastic gel in contactless colloidal-probe rheology

Caroline Kopecz-Muller[1,2,3], Vincent Bertin[4], Elie Raphaël[1], Joshua D. McGraw[1,2] and Thomas Salez[3]

[1]Univ. Bordeaux, CNRS, LOMA, UMR 5798, 33400 Talence, France
[2]Gulliver, CNRS UMR 7083, ESPCI Paris, Université PSL, 75005 Paris, France
[3]Institut Pierre-Gilles de Gennes, ESPCI Paris, Université PSL, 75005 Paris, France
[4]Physics of Fluids, Faculty of Sciences and Technology, University of Twente, 7500AE Enschede, The Netherlands

TS, 0000-0001-6111-8721

When a rigid object approaches a soft material in a viscous fluid, hydrodynamic stresses arise in the lubricated contact region and deform the soft material. The elastic deformation modifies in turn the flow, hence generating a soft-lubrication coupling. Moreover, soft elastomers and gels are often porous. These materials may be filled with solvent or uncrosslinked polymer chains, and might be permeable to the surrounding fluid, which further complexifies the description. Here, we derive the point-force response of a semi-infinite and permeable poroelastic substrate. Then, we use this fundamental solution in order to address the specific poroelastic lubrication coupling associated with contactless colloidal-probe methods. In particular, we derive the conservative and dissipative components of the force associated with the oscillating vertical motion of a sphere close to the poroelastic substrate. Our results may be relevant for dynamic surface force apparatus and contactless colloidal-probe atomic force microscopy experiments on soft, living and/or fragile materials, such as swollen hydrogels and biological membranes.

THE ROYAL SOCIETY PUBLISHING

1. Introduction

Modern synthesis techniques and observation methods at small scales have fostered intense research activity on soft materials and their interfaces [1]. Many of these materials are elastomers and gels, deform considerably under small stress, and are commonly found in biological and technological systems. Stimuli-responsive hydrogels, for example, are candidate materials in novel devices for the detection of diseases by isolation of cells [2]. Elastomers and gels are typically made of synthetic or natural polymers that are crossed-linked to form a network. When immersed in a favourable solvent, the polymer matrix swells as described by Flory–Huggins theory [3,4]. For such gels, the material may eventually contain a large proportion of solvent molecules with a volume increase up to a factor five, for example [5], or more.

Solvent molecules inside a gel can diffuse through the inter-chain regions of the polymer matrix. Therefore, when a load is applied to a gel, material deformations are time-dependent. This dynamic response arises since the chains are restrained from unbounded displacements by elasticity while the solvent motion implies viscous dissipation. The latter mechanism is called poroelasticity, which has been extensively used to describe the mechanical properties of gels. The first poroelastic theory was introduced by Biot to model the consolidation of soils [6]. Since then, additional features have been added such as nonlinear elasticity [7,8], viscoelasticity [9] or surface stresses [10–12], and instabilities have been considered [13]. Notably, the mechanical response of a gel depends on the interactions between the gel and its environment. If the gel is indented by a rigid object, as in the emblematic example of contact mechanics [14–19], solvent molecules do not flow across the interface between the gel and the indenter, which is thus impermeable. By contrast, if the gel is immersed in its own solvent, then the solvent molecules can be transported across the gel–solvent interface, which is thus permeable. In the case of a spherical indenter in contact with the probed gel, impermeability should be considered in the central contact region while permeability should be considered in the coronal, contact-free region around the indenter.

In addition to the permeability boundary condition above, when a rigid object moves in a viscous fluid near a soft surface, it generates hydrodynamic stresses [20] that, despite the lack of direct contact, may deform the soft surface. In turn, the deformation of the soft surface modifies the flow which generates so-called soft-lubrication couplings, that are at the heart of the recent development of gentle, contactless rheological methods for soft materials [21–29]. These methods have been employed to measure the rheology of diverse surfaces such as elastomers [30], gels [31,32], glasses [33], living cells [34] and liquid–air interfaces with impurities [35,36]. They typically involve colloidal-probe atomic force microscopy [37,38], dynamical surface force apparati [39–41] or tuning-fork microscopes [42]. The underlying principle involves driving a spherical probe near a soft surface of interest (see figure 1*b*), and to combine the measured force and the soft-lubrication model in order to infer the material rheology.

Another interesting aspect of soft-lubrication couplings is the emergence of inertial-like forces at zero Reynolds number, such as the lift force for transverse driving [43–52]. As a direct consequence, the effective friction between two objects in respective sliding motion can be strongly reduced [53–56], as compared to the classical rigid lubrication case. This might have important practical implications, in physiology for instance, since the friction between bones in mammalian joints [57,58] may be strongly reduced through the presence of poroelastic cartilages between the solid bones and the synovial lubricant. In the same way, the wet contact between the eyelid and the eyeball is complemented by a stratification of polymer-like and gel-like layers, that may offer better sliding when blinking [59].

Despite the above interest in soft materials and their rheology measured from contactless methods, it is interesting to realize that only simple linear elastic-like constitutive responses have been addressed in the context of soft-lubrication theory. While the effects of viscoelasticity have been recently investigated in more detail [60–62], the effects of poroelasticity remain scarcely and partially addressed [63–65] and certainly at a too basic level to address the more complex

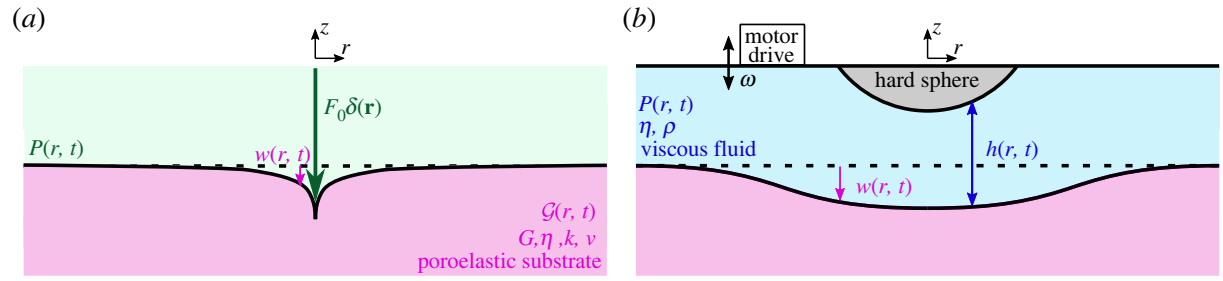

Figure 1. Semi-infinite permeable poroelastic medium deformed by two different external axisymmetric pressure fields. (*a*) A point-force pressure field $P(r, t) = F_0\delta(\mathrm{r})$ is suddenly applied at $t = 0$ on the poroelastic substrate, and generates a surface deformation $w(r, t)$. The latter is directly related to the Green's function $\mathcal{G}(r, t)$. We denote G, ν and k, the effective shear elastic modulus, effective Poisson ratio and porosity of the substrate, respectively, as well as η the viscosity of the solvent flowing in the porous material. (*b*) In contactless colloidal-probe rheological methods, a micrometric sphere is oscillating at angular frequency ω normally to the substrate in a liquid (identical to the solvent in the gel here) of dynamic shear viscosity η and density ρ. The hydrodynamic lubrication pressure field $P(r, t)$ generated by the associated flow deforms the gel surface, leading to a deformed liquid-gap profile $h(r, t)$.

and subtle responses of nonlinear functionalized materials [66]. Early works on purely porous substrates suggest an equivalent description involving effective slippage at the interface, with either the slip length considered to be on the order of the pore size [67], or a full slip boundary condition [68], while more recent work suggests a key role of the permeability boundary conditions [69].

In this article, in view of the identified gap in the literature noted above, we derive a model to characterize the mechanical response of thick poroelastic gels in the framework of contactless colloidal-probe rheological methods. Since we are interested in describing gels in contact with a reservoir of solvent, a full permeability boundary condition at the gel–solvent interface is considered. Our focus contrasts with a previous study in the impermeable case [10,70], that is more relevant to methods involving direct solid contact. In the first part, we obtain the surface deformation of a semi-infinite, permeable, poroelastic layer under the action of an arbitrary pressure field. We use the formalism of Green's functions in axisymmetric conditions, as was done for purely elastic media in the context of soft lubrication [24,25,29,71,72], or for a poroelastic but impermeable soft substrate [10]. In the second part, we apply this formalism to the canonical situation for contactless colloidal-probe rheology, namely the soft-lubricated motion of a sphere oscillating vertically near a poroelastic gel, and we characterize the substrate deformation and resulting normal force in detail.

2. Mechanical response to an external pressure field

(a) Linear poroelastic theory

The considered system is shown in figure 1*a*. It consists of a gel that occupies the half-space defined by $z \leq 0$. We suppose that the mechanics of the gel is described by the linear poroelastic theory. As mentioned in the introduction, this model was first established by Biot [6], and was adapted to model the migration of solvent in elastomeric gels [10,15,70]. We take as a reference state a swollen gel, with a homogeneous solvent concentration c_0, and where the chemical potential of the solvent inside the gel is μ_0. The elastic deformation of the gel is characterized by the strain tensor $\boldsymbol{\epsilon}$. The latter is defined as the symmetric part of the displacement field gradient tensor, as

$$\boldsymbol{\epsilon} = \frac{1}{2}[\boldsymbol{\nabla}\mathbf{u} + (\boldsymbol{\nabla}\mathbf{u})^T], \tag{2.1}$$

where $\mathbf{u}$ denotes the displacement field with respect to the reference state. The solvent mass being conserved, the molar concentration c satisfies the continuity equation:

$$\frac{\partial c}{\partial t} + \nabla \cdot \mathbf{J} = 0, \tag{2.2}$$

where the flux of solvent inside the gel is denoted $\mathbf{J}$. The linear poroelastic theory assumes that the solvent flow is driven by the gradient of solvent chemical potential μ, through the Darcy law:

$$\mathbf{J} = -\left(\frac{k}{\eta \Omega^2}\right)\nabla \mu. \tag{2.3}$$

Here, η and Ω are the viscosity and molecular volume of the solvent, respectively, and k is the permeability that is on the order of the pore surface area of the swollen polymeric network—but with a prefactor depending on the specific network architecture. The solvent and the polymer network are both supposed to be incompressible. As a consequence, the local variations of volume of the polymer network are due to the local changes in solvent concentration, which sets the condition:

$$\mathrm{Tr}(\boldsymbol{\epsilon}) = \nabla \cdot \mathbf{u} = (c - c_0)\Omega, \tag{2.4}$$

where Tr is the trace. As discussed in [17], we expect that the free energy density $\mathcal{U}$ of the gel is a function of the strain tensor and the concentration field. The work done on a gel element is given by $\delta \mathcal{U} = \sigma_{ij}\delta\epsilon_{ij} + (\mu - \mu_0)\delta c$, where σ is the mechanical stress tensor. Nevertheless, because of the incompressibility condition in equation (2.4), the solvent concentration is no longer an independent variable, and the free energy density only depends on strain. The latter is supposed to follow the standard linear-elastic energy density, i.e. $\mathcal{U} = G[\boldsymbol{\epsilon} : \boldsymbol{\epsilon} + (\nu/(1-2\nu))\mathrm{Tr}^2(\boldsymbol{\epsilon})]$, where G and ν are the effective shear elastic modulus and Poisson ratio at equilibrium, respectively. The stress tensor is then given by [17]

$$\boldsymbol{\sigma} = 2G\left[\boldsymbol{\epsilon} + \frac{\nu}{1-2\nu}\mathrm{Tr}(\boldsymbol{\epsilon})\mathbf{I}\right] - \frac{\mu - \mu_0}{\Omega}\mathbf{I}, \tag{2.5}$$

where $\mathbf{I}$ is the identity tensor. The difference in chemical potentials per molecular volume appears as a hydrostatic pressure, often called *pore pressure*, and is obtained by enforcing the incompressibility condition with a Lagrange multiplier. In the absence of body force, the mechanical equilibrium is expressed by Navier's closure equation:

$$\nabla \cdot \boldsymbol{\sigma} = \mathbf{0}. \tag{2.6}$$

Combining the two last equations leads to:

$$G\Omega\left(\nabla^2 \mathbf{u} + \frac{\Omega}{1-2\nu}\nabla(c - c_0)\right) = \nabla(\mu - \mu_0). \tag{2.7}$$

Invoking equation (2.3), equations (2.2), (2.4) and (2.7) form a closed system of five equations for the five fields μ, c and the three components of $\mathbf{u}$. Combining the latter equations reduces the problem to a set of two coupled equations on the concentration field c and chemical potential μ, as

$$\nabla^2\left[(\mu - \mu_0) - 2G\Omega^2\frac{1-\nu}{1-2\nu}(c - c_0)\right] = 0 \tag{2.8a}$$

and

$$\frac{\partial c}{\partial t} = \mathcal{D}_{\mathrm{pe}}\nabla^2 c, \tag{2.8b}$$

where we have introduced an effective, poroelastic diffusion coefficient

$$\mathcal{D}_{\mathrm{pe}} = \frac{2(1-\nu)}{1-2\nu}\frac{Gk}{\eta}. \tag{2.9}$$

Equation (2.8*a*) couples the chemical potential with the concentration, as the flow of solvent is driven by gradients of chemical potential (or equivalently, gradients of pore pressure). Equation (2.8*b*) describes the diffusion of solvent through the porous matrix, with $\mathcal{D}_{\mathrm{pe}}$ of equation (2.9)

constructed using macroscopic material parameters. An osmotic modulus, $2(1-\nu)/(1-2\nu)$, arises in the expression of the diffusion coefficient $\mathcal{D}_{\mathrm{pe}}$. We note lastly, however, that even while $\mathcal{D}_{\mathrm{pe}}$ is constructed from these macroscopic parameters, one can recover a molecular-scale diffusion coefficient. To make the correspondence, we use the Stokes–Einstein relation for molecular diffusion, $\mathcal{D}_\mu \sim k_{\mathrm{B}}T/(\eta a)$, with $k_{\mathrm{B}}T$ and $a \approx \Omega^{1/3}$ the thermal energy and monomer size, respectively. Estimating furthermore the typical polymeric modulus $G \sim k_{\mathrm{B}}T/(Na^3)$, and the permeability $k \sim Na^2$, where N is a typical number of monomers between crosslinks in the network, we find $\mathcal{D}_{\mathrm{pe}} \sim \mathcal{D}_\mu$ upon substitution into equation (2.9).

(b) Point-force driving

We now derive the response of the gel to a spatially delta-distributed force density applied to the surface of the gel. Prior to the application of such a force, i.e. for times $t \leq 0$, we suppose that the gel is in the (swollen) reference state with strain- and stress-free conditions. For $t \geq 0$, a point-force pressure source of magnitude F_0 is suddenly applied on the surface. This forcing drives a deformation of the gel surface, and solvent flow within the polymer matrix. At the interface (i.e. $z = 0$ in the reference state), the stress boundary condition is, therefore, given by

$$\boldsymbol{\sigma} \cdot \mathbf{e}_z = -F_0 \delta(\mathbf{r}) H(t) \mathbf{e}_z, \tag{2.10}$$

where $H(t)$ denotes the Heaviside step function and $\delta(\mathbf{r})$ the Dirac distribution.

In the limit $z \to -\infty$, the stress and strain fields vanish and the solvent concentration field reaches its reference equilibrium value c_0. At infinitesimally small times after the point force has been applied, the solvent did not have time to flow, so that the solvent concentration is the same as the one at $t < 0$, i.e.:

$$c(r, z, t = 0) = c_0. \tag{2.11}$$

We suppose that the gel is in contact with a reservoir of solvent molecules, which sets the surface chemical potential to the reference equilibrium value μ_0. Such a permeability condition allows for solvent exchange between the gel and the outer reservoir, and is relevant to situations where the gel is immersed in a liquid phase (e.g. its own solvent) with some affinity between the two. Thus, the boundary condition on the chemical potential at the undeformed interface of the gel reads:

$$\mu(r, z = 0, t) = \mu_0. \tag{2.12}$$

(i) Resolution

To determine the surface deformation $w(r, t)$ associated with the pressure source of equation (2.10) (see figure 1*a*), we follow the method introduced by Liu *et al.* [11], McNamme & Gibson [73,74] and Gibson et al. [75]. The key ingredient of that method is the introduction of two displacement potentials $A(r, z, t)$ and $B(r, z, t)$, defined by

$$u_r = z\frac{\partial A}{\partial r} + \frac{\partial B}{\partial r} \tag{2.13a}$$

and

$$u_z = z\frac{\partial A}{\partial z} - A + \frac{\partial B}{\partial z}, \tag{2.13b}$$

and that satisfy the following equations:

$$\boldsymbol{\nabla}^2 A = 0, \tag{2.14a}$$

$$\nabla^2 B = \Omega(c - c_0), \tag{2.14b}$$

$$2G\Omega\frac{\partial A}{\partial z} = (\mu - \mu_0) - 2G\Omega^2\frac{1-\nu}{1-2\nu}(c - c_0) \tag{2.14c}$$

and

$$\frac{\partial \boldsymbol{\nabla}^2 B}{\partial t} = \mathcal{D}_{\mathrm{pe}}\boldsymbol{\nabla}^4 B. \tag{2.14d}$$

Substituting the strain tensor $\boldsymbol{\epsilon}$ in equation (2.5), using equations (2.1) and (2.4), the stress tensor $\boldsymbol{\sigma}$ can be written as a function of μ, c and $\mathbf{u}$. Using then equations (2.13), (2.14*b*) and (2.14*c*), the stress tensor can be expressed as a function of A and B, as

$$\sigma_{rr} = 2G\left(z\frac{\partial^2 A}{\partial r^2} - \frac{\partial A}{\partial z} + \frac{\partial^2 B}{\partial r^2} - \Delta B\right), \tag{2.15a}$$

$$\sigma_{zz} = 2G\left(z\frac{\partial^2 A}{\partial z^2} - \frac{\partial A}{\partial z} + \frac{\partial^2 B}{\partial z^2} - \Delta B\right) \tag{2.15b}$$

and

$$\sigma_{rz} = 2G\left(\frac{\partial^2 B}{\partial r \partial z} + z\frac{\partial^2 A}{\partial z \partial r}\right). \tag{2.15c}$$

We note that azimuthal stresses and displacements have not been considered here, given the axisymmetry of the problem.

To solve equation (2.14*b*), we reconsider the problem in the spectral domain. Specifically, we use the Hankel transform of zeroth order in space and the Laplace transform in time. In such a framework, a given field $X(r,t)$ is transformed into:

$$\hat{X}(s,q) = \int_0^\infty \mathrm{d}t\, \mathrm{e}^{-qt} \int_0^\infty \mathrm{d}r\, X(r,t) r J_0(sr), \tag{2.16}$$

where J_0 is the Bessel function of the first kind and zeroth order. The inversion formula reads:

$$X(r,t) = \frac{1}{2\pi \mathrm{i}} \int_{\gamma-\mathrm{i}\infty}^{\gamma+\mathrm{i}\infty} \mathrm{d}q\, \mathrm{e}^{qt} \int_0^\infty \mathrm{d}s\, \hat{X}(s,q) s J_0(sr), \tag{2.17}$$

where the inverse Laplace transform is written using the Bromwich integral. Then, expressing equation (2.14*b*) in the spectral domain and invoking the initial condition $\nabla^2 B(r,z,0) = 0$, we get the following ordinary differential equations on the transformed potentials $\hat{A}(s,z,q)$ and $\hat{B}(s,z,q)$:

$$\left(\frac{\partial^2}{\partial z^2} - s^2\right)\hat{A} = 0 \tag{2.18}$$

and

$$\left(\frac{\partial^2}{\partial z^2} - s^2 - \frac{q}{\mathcal{D}_{\mathrm{pe}}}\right)\left(\frac{\partial^2}{\partial z^2} - s^2\right)\hat{B} = 0. \tag{2.19}$$

The solutions to equations (2.18) and (2.19) that vanish at $z \to -\infty$ read:

$$\hat{A} = a_1 \mathrm{e}^{sz} \tag{2.20a}$$

and

$$\hat{B} = b_1 \mathrm{e}^{sz} + b_2 \mathrm{e}^{z\sqrt{s^2 + q/\mathcal{D}_{\mathrm{pe}}}}, \tag{2.20b}$$

where a_1, b_1, b_2 are integration constants, that depend on the spectral variables s and q. Expressing the stress and chemical-potential boundary conditions of equations (2.10) and (2.12) in terms of the potentials, we obtain:

$$\hat{\sigma}_{sz}(s, z=0, q) = 0 = -2Gs\left[b_1 s + b_2\sqrt{s^2 + \frac{q}{\mathcal{D}_{\mathrm{pe}}}}\right], \tag{2.21a}$$

$$\hat{\sigma}_{zz}(s, z=0, q) = -\frac{F_0}{2\pi q} = 2G[-a_1 s + (b_1 + b_2)s^2] \tag{2.21b}$$

and

$$\hat{\mu}(s, z=0, q) - \hat{\mu}_0 = 0 = 2G\Omega\left[\frac{1-\nu}{1-2\nu} b_2 \frac{q}{\mathcal{D}_{\mathrm{pe}}} + a_1 s\right]. \tag{2.21c}$$

Solving equations (2.21), we obtain a_1, b_1 and b_2.

(ii) Results and discussion

Having solved the poroelastic problem equations (2.8)–(2.12) for the potentials A, B defined in the previous section, we find the surface normal deformation of the gel $\hat{w}(s,q) = -\hat{u}_z(s, z=0, q)$ in reciprocal space (see equation (2.16)) by invoking equation (2.13*b*), as

$$\hat{w}(s,q) = \frac{F_0}{4\pi G s q} \frac{1}{1 + \Lambda(\mathcal{D}_{\rm pe} s^2/q)(1 - \sqrt{1 + (q/\mathcal{D}_{\rm pe} s^2)})}, \tag{2.22}$$

where the Poisson ratio appears in the compressiblity factor

$$\Lambda = \frac{1-2\nu}{1-\nu}. \tag{2.23}$$

We first note that if the gel is nearly incompressible, i.e. as $\nu \to 1/2$, then $\Lambda \to 0$ and the poroelasticity does not affect the surface deformation as revealed in equation (2.22). In such a case, the poroelastic medium responds as a purely elastic and incompressible one, at all times. Similarly, if the permeability is small, i.e. as $k \to 0$, the diffusion constant $\mathcal{D}_{\rm pe}$ of the solvent vanishes and the medium again behaves as an incompressible elastic material. In the opposite limit of large permeability, the solvent can diffuse almost instantaneously and the stress is immediately relaxed, so that the response is one of a compressible elastic material at all times.

In figure 2*a* is shown $\hat{w}(s,q)$ plotted as a function of s for various q. We choose a value $\nu = 0.1$, a typical value for swollen gels and giving finite Λ. The vertical normalization is chosen such that dimensionless values of s and q were used, length is normalized by $\sqrt{F_0/G}$ and time by $F_0/(G\mathcal{D}_{\rm pe})$. The results show parallel power-law decays in the small- and large-s limits, with a larger prefactor for large s (small distance). To explain this observation, we explore the temporal asymptotics of the governing equation (2.22). The initial and final value theorems can be used in the short- and long-time limits of the surface deformation. We thus find:

$$\hat{w}(s, t=0^+) = \lim_{q\to\infty} q\hat{w}(s,q) = \frac{F_0}{4\pi G s} \tag{2.24a}$$

and

$$\hat{w}(s, t\to\infty) = \lim_{q\to 0^+} q\hat{w}(s,q) = \frac{F_0(1-\nu)}{2\pi G s}, \tag{2.24b}$$

leading to the deformation in real space:

$$w(r, t=0^+) = \frac{F_0}{4\pi G r} = w^{\rm incomp}(r), \tag{2.25a}$$

and

$$w(r, t\to\infty) = \frac{F_0(1-\nu)}{2\pi G r} = w^{\rm comp}(r). \tag{2.25b}$$

Thus for both short and long times, we find spectral power-law decays of the surface deformation. The former expression is the point-force solution of a purely elastic, incompressible and semi-infinite medium of shear modulus G, denoted $w^{\rm incomp}(r)$. At long times, we have the point-force solution of a purely elastic and semi-infinite medium of shear modulus G and Poisson ratio ν, denoted $w^{\rm comp}(r)$. Equations (2.24) are plotted using dashed lines in figure 2*a*. These expressions thus form a link between poroelastic and elastic materials [45,76]: at large distances (small s), the solvent has no time to flow inside the porous matrix and the response is elastic-like, with an incompressibility condition due to the liquid fraction. At small distances (large s), the solvent does not flow anymore and the response recovers a steady elastic deformation, with compression (i.e. a concentration change) as compared to the initial state. In between the two asymptotic regimes, the surface deformation smoothly changes from the short-time (incompressible) to the long-time (compressible) elastic-like behaviours, as shown with blue lines and using finite q in figure 2*a*.

To connect the asymptotic inverse space and time responses, we note in equation (2.22) that at fixed Λ, a natural variable is an inverse, dimensionless diffusive one $\mathcal{D}_{\rm pe} s^2/q$. This is expected since the solvent concentration follows a diffusive-like law with a diffusion constant $\mathcal{D}_{\rm pe}$. In

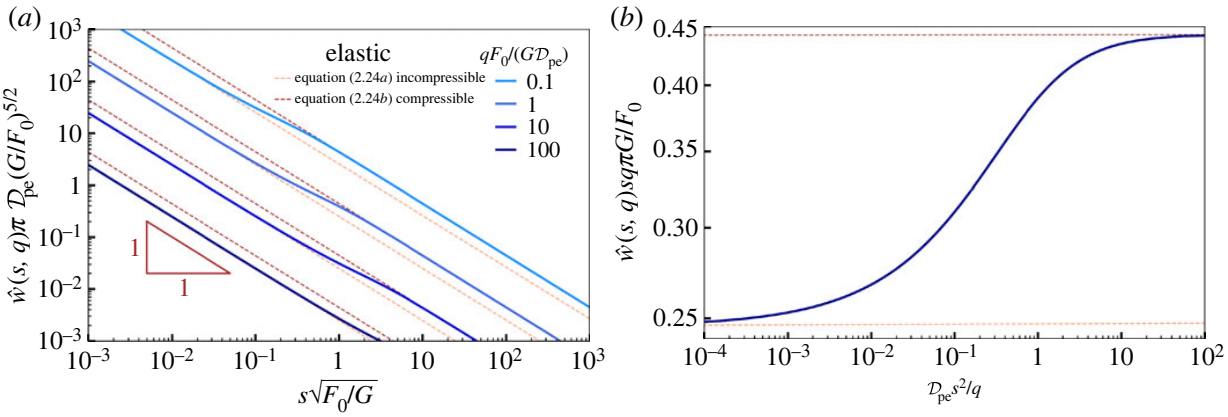

Figure 2. Surface deformation induced by a point-force pressure source in Hankel–Laplace space. (*a*) Dimensionless, reciprocal-space surface deformation $\hat{w}(s, q)$ as computed from equation (2.22), as a function of the scaled spatial frequency, s, for various temporal frequencies, q, normalized by $\mathcal{D}_{pe}G/F_0$, using $\nu = 0.1$. The orange and red dashed lines correspond to equations (2.24*a*) and (2.24*b*), respectively. (*b*) Normalized surface deformation in reciprocal space $\hat{w}(s, q)$, as a function of the variable $\mathcal{D}_{pe}s^2/q$, for $\nu = 0.1$, as computed from equation (2.22). The orange and red dashed lines as described in (*a*).

figure 2*b*, we thus plot the normalized surface deformation in reciprocal space, as a function of the normalized diffusive variable, having fixed the Poisson ratio and for the same q noted in figure 2*b*. Given the normalization and the form of equation (2.22), we find that a single curve describes the response in reciprocal space. Interpreting the response physically, we note that when the gel starts to be indented, it first exhibits an incompressible elastic-like response, as discussed above. Later, at a given time t, the solvent and stress have typically diffused over a radial distance $r_c \sim \sqrt{\mathcal{D}_{pe}t}$, giving a self-similar curve in reciprocal space.

To have a direct view on the spatial and temporal relaxations described above for reciprocal space, the inverse Laplace transform of equation (2.22) was numerically computed using the Talbot algorithm [77]. The inverse Hankel transform was computed with Riemann summation over a finite spectral domain. Numerical oscillations were first reduced by increasing the domain size and reducing the space step, in the limit of a reasonable computational time. Residual oscillations were then smoothed using a Savitzky–Golay filter of order 3 on a window of 9 points over the total 200 000 used in the linear discretization of the r, s axes. The results are presented in figure 3*a*, where the deformation in real space is plotted as a function of the radial coordinate for various times. For $r < r_c$ noted in the previous paragraph, the gel state has essentially relaxed and the response is compressible (red dashed line), while for $r > r_c$ the state and response are not modified with respect to the initial, incompressible elastic ones (orange dashed line). The transitions between compressible and incompressible deformations are also elucidated in the logarithmic representation of the data shown in the inset, where the short- and long-time asymptotic relaxations are shown.

In figure 3*b*, we quantitatively show the gel's relaxation to its final state, plotting the difference of the data in figure 3*a* with that of the asymptotic late-time limit in equation (2.25*b*) as a function of the radial coordinate. A continuous decay toward the late-time value is observed for all radii. Taking a few examples, we show in the inset of figure 3*b* the temporal decay toward the final state for the three radii noted by vertical dashed lines in the main part of the figure. For early times, we note a plateau at a value $F_0(1 - 2\nu)/(4\pi G)$, corresponding to the difference between the two asymptotic limits in equation (2.25). Remarkably, a temporal power law with exponent $-1/2$, characteristic of a diffusive process, is reached for all the radii at long times. In appendix A, the late-time $t^{-1/2}$ asymptotic power-law decay is demonstrated by expanding equation (2.22) at small q and transforming to real space. The intercept between the asymptotic decay law and the initial plateau value indicates its typical duration time, that scales with the diffusion time $r^2/\mathcal{D}_{pe}$.

Lastly, we note that in appendix B we compare the results of the present permeable description to the case of an impermeable surface. For the impermeable case, the solvent flux vanishes at the

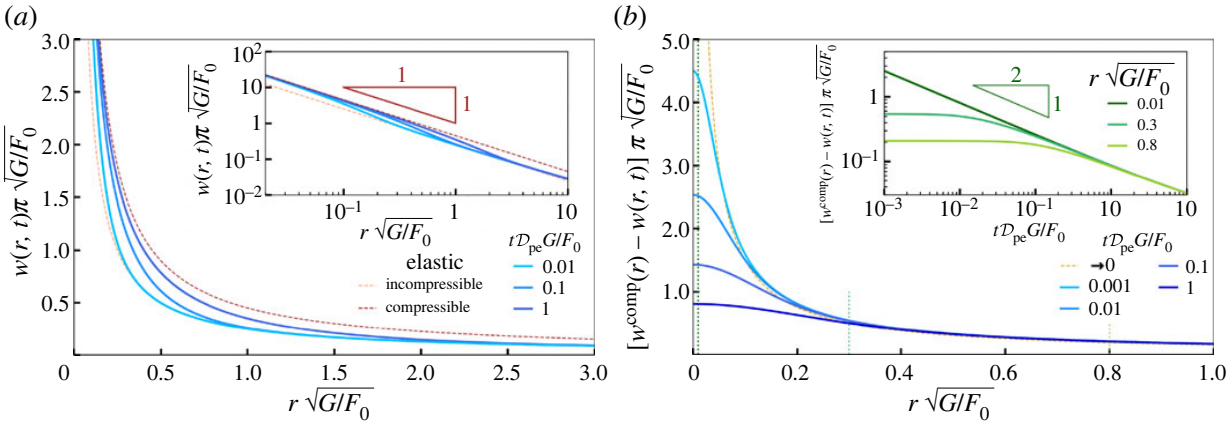

Figure 3. Surface deformation induced by a point-force pressure source. (*a*) Normalized surface deformation as a function of the radial coordinate, for the times noted in the legend, as computed from the inverse transform of equation (2.22) and using $\nu = 0.1$. The orange and red dashed lines correspond to the asymptotic limits in equations (2.25). The inset shows the same data on logarithmic scales. (*b*) Difference $w^{\mathrm{comp}}(r) - w(r,t)$ (normalized) between the surface deformation of a purely elastic compressible material (see equation (2.25*b*)) and the one of the poroelastic material, as a function of normalized radial coordinate, for the dimensionless times noted in the legend. The inset shows the same data, but as a function of time and for various radial positions (corresponding to the vertical dashed green lines in the main panel), using logarithmic scales. The −1/2 exponent of the asymptotic power-law behaviour is discussed in appendix A.

interface. This alternative boundary condition is relevant when the gel is not in contact with its own liquid solvent. Such a situation arises when a gel is indented by a rigid object [14–19], as well as in some configurations of soft wetting [10,78]. The surface deformations are found to adopt qualitatively similar shapes in the permeable and impermeable cases. However, the respective behaviours quantitatively differ, and the stress relaxation is in particular faster in the permeable case, due to the allowed exchange of solvent with the outer reservoir.

(c) Solution for an arbitrary pressure field

In real systems, gels are indented with probes that have finite size [16–19]. In these cases, the external load is not a point force, and the outer pressure field has a finite spatial extent. Additionally, the outer pressure field may exhibit temporal variations. Since the above model only involves linear operators, we can apply the superposition principle. Henceforth, the surface deformation generated by an arbitrary time-dependent and space-dependent pressure field $p(\mathbf{r}, t)$ is given by the convolution:

$$w(\mathbf{r},t) = \int_{-\infty}^{t} \mathrm{d}t' \int_{\mathbb{R}^2} \mathrm{d}^2\mathbf{r}'\, \mathcal{G}(|\mathbf{r}-\mathbf{r}'|, t-t')\, p(\mathbf{r}', t'), \tag{2.26}$$

where $\mathcal{G}$ is the Green's function of the problem, which is the surface deformation induced by a point force $\delta(\mathbf{r})\delta(t)$. The latter is directly related to equation (2.22), through:

$$\hat{\mathcal{G}}(s,q) = \frac{1}{4\pi G s} \frac{1}{1 + \Lambda \frac{\mathcal{D}_{\mathrm{pe}} s^2}{q} \left(1 - \sqrt{1 + (q/\mathcal{D}_{\mathrm{pe}} s^2)}\right)}, \tag{2.27}$$

and the inverse transform:

$$\mathcal{G}(r,t) = \frac{1}{2\mathrm{i}\pi} \int_{\gamma-\mathrm{i}\infty}^{\gamma+\mathrm{i}\infty} \mathrm{d}q\, \mathrm{e}^{qt} \int_0^\infty \mathrm{d}s\, \hat{\mathcal{G}}(s,q) s J_0(sr). \tag{2.28}$$

3. Application to contactless colloidal-probe rheology

In this section, we apply the general results of the previous one for a specific outer pressure field that is relevant to contactless colloidal-probe rheological methods. Specifically, we focus on the elastohydrodynamic coupling between a rigid sphere of radius R and a semi-infinite permeable poroelastic medium. For this purpose, we invoke the linear-response theory introduced by Leroy & Charlaix [22], and widely used in contactless measurements of the mechanical properties of soft surfaces [30–34,36,42].

(a) Soft-lubrication approximation

The above-mentioned sphere is placed at a distance D from the undeformed gel surface and oscillates vertically with angular frequency ω and amplitude h_0, as schematized in figure 1*b*. The ensemble is fully immersed in a Newtonian fluid (identical to the solvent in the gel here) of dynamic shear viscosity η and density ρ. We suppose that the sphere-plane distance is small with respect to the sphere radius, and can thus invoke the lubrication approximation [20]. The sphere profile can be approximated by a parabola in the lubricated contact region, and the liquid-film thickness profile is thus given by

$$h(r,t) \simeq D + h_0 \cos(\omega t) + w(r,t) + \frac{r^2}{2R}. \tag{3.1}$$

The Reynolds number is assumed to be small, so that the flow is laminar. Furthermore, we suppose that the typical viscous penetration depth $\sqrt{\eta/(\rho\omega)}$ is large compared to the liquid-gap thickness. Therefore, the flow can be described by the steady Stokes equations with no-slip boundary conditions at both the sphere and gel surfaces. This latter condition is assumed for simplicity since the typical slip length at poroelastic surfaces is comparable to the pore size $\sim\sqrt{k}$ [67,69], which is normally nanometric.

The liquid-film thickness profile follows the axisymmetric thin-film equation [79]:

$$\frac{\partial h}{\partial t} = \frac{1}{12\eta r}\frac{\partial}{\partial r}\left[rh^3\frac{\partial p}{\partial r}\right], \tag{3.2}$$

where p is the excess pressure field in the liquid with respect to the atmospheric pressure. In the lubrication approximation, the viscous shear stresses are negligible compared to the pressure. Therefore, the force balance at the gel surface takes the same form as in §2, and the surface deformation profile can be computed from equation (2.26).

(b) Linear-response theory

Following [22], we suppose that the oscillation amplitude is much smaller than the liquid-gap thickness. Hence, we invoke the linear-response theory, and write the fields as

$$w(r,t) = \mathrm{Re}[w^*(r)\mathrm{e}^{\mathrm{i}\omega t}], \quad p(r,t) = \mathrm{Re}[p^*(r)\mathrm{e}^{\mathrm{i}\omega t}], \tag{3.3}$$

where * indicates complex variables, $\mathrm{i}^2 = -1$, and Re is the real part. Equation (3.2) is then linearized, giving:

$$\mathrm{i}\omega\left(h_0 + w^*\right) = \frac{1}{12\eta r}\frac{\mathrm{d}}{\mathrm{d}r}\left[r\left(D + \frac{r^2}{2R}\right)^3\frac{\mathrm{d}p^*}{\mathrm{d}r}\right]. \tag{3.4}$$

Using the solution derived in §2c, we can obtain the surface deformation by injecting equation (3.3) into equation (2.26). The amplitude of the surface deformation in Hankel space reads:

$$\hat{w}^*(s) = \hat{p}^*(s)\hat{\mathcal{G}}^*(s) = \frac{\hat{p}^*(s)}{2Gs}\,\frac{1}{1 - \mathrm{i}\Lambda(\mathcal{D}_{\mathrm{pe}}s^2/\omega)\left(1 - \sqrt{1 + (\mathrm{i}\omega/\mathcal{D}_{\mathrm{pe}}s^2)}\right)}, \tag{3.5}$$

with:

$$\hat{w}^*(s) = \int_0^\infty \mathrm{d}r\, w^*(r) r J_0(sr) \quad \text{and} \quad \hat{p}^*(s) = \int_0^\infty \mathrm{d}r\, p^*(r) r J_0(sr). \tag{3.6}$$

Note that, in contrast to §2, the $\hat{}$ symbol now only refers to the Hankel transform, since there is no time dependence on the amplitudes and thus no Laplace transform. From equation (3.1), the contact length $\sqrt{2RD}$—i.e. the so-called hydrodynamic radius—sets a typical horizontal length scale. Besides, h_0 sets a typical vertical length scale. Thus, we introduce the following dimensionless variables:

$$\tilde{r} = \frac{r}{\sqrt{2RD}}, \quad \tilde{s} = s\sqrt{2RD}, \quad \tilde{w}^*(\tilde{r}) = \frac{w^*(r)}{h_0}. \tag{3.7}$$

From the horizontal projection of the Stokes equation, and the incompressibility condition, we find that the typical lubrication pressure scale is $2\eta R\omega h_0/D^2$. Thus, we introduce the following dimensionless pressure field:

$$\tilde{p}^*(\tilde{r}) = \frac{D^2 p^*(r)}{2\omega R\eta h_0}. \tag{3.8}$$

Injecting these new variables in equation (3.2), the dimensionless thin-film equation results:

$$\mathrm{i}(1+\tilde{w}^*) = \frac{1}{12\tilde{r}} \frac{\mathrm{d}}{\mathrm{d}\tilde{r}} \left[\tilde{r}\left(1+\tilde{r}^2\right)^3 \frac{\mathrm{d}\tilde{p}^*}{\mathrm{d}\tilde{r}} \right]. \tag{3.9}$$

Finally, we introduce two characteristic parameters. First, the critical distance at which the surface deformation and sphere oscillation amplitude are of the same order:

$$D_\mathrm{c} = 8R\left(\frac{\eta\omega}{2G}\right)^{2/3}. \tag{3.10}$$

Second, the critical poroelastic angular frequency at which solvent typically diffuses over the contact length at the critical distance during one oscillation:

$$\omega_\mathrm{c} = \frac{\mathcal{D}_\mathrm{pe}}{2RD_\mathrm{c}} = \frac{\mathcal{D}_\mathrm{pe}}{16R^2}\left(\frac{2G}{\eta\omega}\right)^{2/3}. \tag{3.11}$$

(c) Deformation profile and normal force

Using the dimensionless variables and critical parameters above, we can write equation (3.5) in dimensionless form, as

$$\hat{\tilde{w}}^*(s) = \frac{\hat{\tilde{p}}^*(s)}{8s} \frac{(D_\mathrm{c}/D)^{3/2}}{1 - \mathrm{i}\Lambda(\tilde{s}^2/(\omega D/(\omega_\mathrm{c} D_\mathrm{c})))\left(1 - \sqrt{1 + (\mathrm{i}\omega D/(\omega_\mathrm{c} D_\mathrm{c}))/\tilde{s}^2}\right)}. \tag{3.12}$$

Moreover, the amplitude F^* of the vertical elastohydrodynamic force exerted on the sphere is obtained by integrating the amplitude of the lubrication pressure field over the surface, as

$$F^* = 2\pi \int_0^\infty \mathrm{d}r\, r\, p^*(r) = \frac{8\pi\eta\omega h_0 R^2}{D_\mathrm{c}} \tilde{F}^*, \quad \text{with } \tilde{F}^* = \frac{D_\mathrm{c}}{D} \int_0^\infty \mathrm{d}\tilde{r}\, \tilde{r}\, \tilde{p}^*(\tilde{r}), \tag{3.13}$$

where we have noted the dimensionless force $\tilde{F}^*$, which depends on the dimensionless parameters, D/D_c, ω/ω_c and Λ.

Equations (3.9) and (3.12) can be solved numerically, as detailed in appendix C. Examples of the obtained surface deformation field are plotted in figure 4*a* for various sphere-substrate distances. In a contactless colloidal-probe rheological experiment; however, it is not the deformation amplitude that is typically measured. Rather, the sampled surface slowly approaches the oscillating spherical probe using a piezo stage, with the typical experimental outputs being the measured force amplitude and phase as functions of the sphere-substrate distance. The other parameters are kept constant. From the amplitude and phase, the real and imaginary components

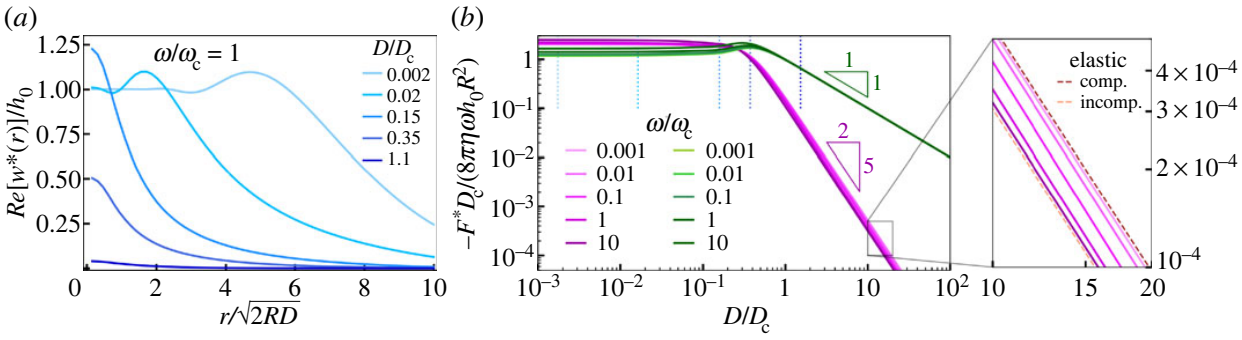

Figure 4. Mechanical response of a poroelastic gel in the contactless colloidal-probe configuration. (*a*) Normalized amplitude w^*/h_0 of the surface deformation profile as a function of the rescaled radial coordinate $r/\sqrt{2RD}$, for various normalized sphere-substrate distances, as computed from equation (3.12) with $\omega/\omega_c = 1$ and $\nu = 0.1$. (*b*) Real (pink) and imaginary (green) parts of the normalized force $F^*D_c/(8\pi\,\eta\omega h_0R^2)$ exerted on the spherical probe as functions of normalized sphere-substrate distance, for various reduced angular frequencies ω/ω_c, as computed from equation (3.13) with $\nu = 0.1$. The vertical dashed blue lines correspond to the distances at which the surface deformation profiles are plotted in (*a*). The zoomed inset shows in addition the purely elastic incompressible case (orange) and the purely elastic compressible case (red).

of the complex force can be evaluated. These force components can be evaluated theoretically using equation (3.13), while the amplitude of the pressure field can also be obtained numerically.

Therefore, in figure 4*b*, we plot the dimensionless force amplitudes as a function of the dimensionless distance, for various oscillation angular frequencies. Two regimes can be observed. At large distance, i.e. $D/D_c \gg 1$, the surface deformation is small with respect to the oscillation amplitude (see figure 4*a*). As a result, the elastohydrodynamic coupling is weak, and the force is dominated by the viscous dissipation in the liquid film. In the far-field asymptotic regime, we recover the classical lubrication Stokes drag $F^* = -6i\pi\,\eta R^2 h_0\omega/D$, which can be obtained by integrating equation (3.2) in the absence of substrate deformation. The real part of the force amplitude in the far field is much smaller than the imaginary part, but it displays a signature of the elasticity of the substrate through an asymptotic decay with the distance as $\sim (D/D_c)^{-5/2}$. The exact prefactor of this scaling law can be obtained by expanding the solution in (D_c/D) [22,36]. At small distance, i.e. $D/D_c \ll 1$, the substrate deformation saturates and scales with the oscillation amplitude (see figure 4*a*). As a consequence, the real and imaginary parts of the force amplitude saturate as well to values that do not depend on the distance. Besides, at all distances (see e.g. inset of figure 4*b*, at large distance), we recover the qualitative feature discussed in the previous part: at small frequency, the elastohydrodynamic coupling is similar to that of a purely elastic compressible layer; conversely, at large frequency, the elastohydrodynamic coupling is similar to the one of a purely elastic incompressible layer.

Finally, in these rescaled variables, we observe a small influence of the solvent diffusion in the gel on the elastohydrodynamic coupling, despite the diffusion constant being varied over 4 orders of magnitude (via the critical frequency). Therefore, from our model, it appears that contactless colloidal-probe rheological methods in the linear-response regime are not appropriate to robustly measure the effects of the solvent diffusion through the gel network. By contrast, such methods appear to be well suited for measuring the effective shear elastic moduli and Poisson ratios of gels.

4. Conclusion

We theoretically addressed the mechanical response of a semi-infinite and permeable, linear poroelastic substrate to an external axisymmetric pressure field. The point-force response was first computed. By convolution of the latter to any outer pressure field, the surface deformation profile can be computed. Motivated by the recent development of contactless colloidal-probe rheological experiments on soft and complex materials, we applied our general results to the specific case

of a sphere oscillating vertically near a gel, within an outer fluid identical to the solvent present in the polymeric matrix. The complex amplitude of the force exerted on the spherical probe was numerically computed and studied. As a result, contactless colloidal-probe methods in the linear-response regime appear as good candidates to robustly measure the effective elastic properties of gels and biological membranes, without risks of wear and adhesion. Going beyond linear response, and incorporating large deformations as well as a polymeric description of the gel architecture seem to be the next steps towards modelling further the complex response of gels and measuring their specific poroelastic behaviours.

Data accessibility. The data presented in this article are accessible from the authors upon reasonable request.

Authors' contributions. C.K.-M.: formal analysis, investigation, visualization, writing—original draft, writing—review and editing; V.B.: formal analysis, investigation, software, supervision, writing—review and editing; E.R.: validation, writing—review and editing; J.D.M.: conceptualization, funding acquisition, methodology, project administration, resources, supervision, writing—review and editing; T.S.: conceptualization, funding acquisition, methodology, project administration, resources, supervision, writing—review and editing.

All authors gave final approval for publication and agreed to be held accountable for the work performed therein.

Conflict of interest declaration. We declare we have no competing interests.

Funding. The authors acknowledge financial support from the European Union through the European Research Council under EMetBrown (ERC-CoG-101039103) grant, as well as the Agence Nationale de la Recherche under CoPinS (ANR-19-CE06-0021), EMetBrown (ANR-21-ERCC-0010-01), Softer (ANR-21-CE06-0029) and Fricolas (ANR-21-CE06-0039) grants. The authors also acknowledge financial support from Institut Pierre-Gilles de Gennes (Equipex ANR-10-EQPX-34 and Labex ANR-10-LABX-31).

Acknowledgements. The authors thank Elisabeth Charlaix, Abdelhamid Maali, Zaicheng Zhang and Yvette Tran, for interesting discussions. They also thank the Soft Matter Collaborative Research Unit, Frontier Research Center for Advanced Material and Life Science, Faculty of Advanced Life Science at Hokkaido University, Sapporo, Japan.

Appendix A. Long-term asymptotic deformation

In order to rationalize the $t^{-1/2}$ power law observed in the inset of figure 3*b*, the point-force solution obtained in the main text, equation (2.22), can be expanded at small temporal frequency q (or similarly at large time t), as

$$\begin{aligned}\hat{w}(s,q) &\approx \frac{F_0}{4\pi G s q}\,\frac{1}{1+((1-2\nu)/(1-\nu))(\mathcal{D}_{\mathrm{pe}}s^2/q)(1-[1+(1/2)(q/s^2\mathcal{D}_{\mathrm{pe}})-(1/8)(q/s^2\mathcal{D}_{\mathrm{pe}})^2])}\\ &= \frac{F_0(1-\nu)}{2\pi G s q}\,\frac{1}{1+((1-2\nu)q/4\mathcal{D}_{\mathrm{pe}}s^2)}.\end{aligned} \tag{A 1}$$

Taking the inverse Laplace transform, we get:

$$\hat{w}(s,t) \approx \frac{F_0(1-\nu)}{2\pi G s}\left[1-\exp\left(-\frac{4\mathcal{D}_{\mathrm{pe}}ts^2}{1-2\nu}\right)\right]. \tag{A 2}$$

Finally taking the inverse Hankel transform, we get:

$$\begin{aligned}w(r,t) &= \frac{F_0(1-\nu)}{2\pi G r}\left[1-\frac{r}{\sqrt{\mathcal{D}_{\mathrm{pe}}t/\pi(1-2\nu)}}I_0\left(-\frac{(1-2\nu)r^2}{32\mathcal{D}_{\mathrm{pe}}t}\right)\exp\left(-\frac{(1-2\nu)r^2}{32\mathcal{D}_{\mathrm{pe}}t}\right)\right]\\ &\simeq \frac{F_0(1-\nu)}{2\pi G r}-\frac{F_0(1-\nu)\sqrt{(1-2\nu)\pi}}{2\pi G\sqrt{16\mathcal{D}_{\mathrm{pe}}t}},\end{aligned} \tag{A 3}$$

where I_0 is a modified Bessel function of the first kind, of order 0, and the last expansion is obtained by taking the long-time limit. The first term of the right-hand side gives the purely elastic and compressible response of the material at long time. The second term corresponds to the long-term correction to the latter, as plotted in figure 3*b*. The decay does not depend on r and scales as $\sim 1/\sqrt{\mathcal{D}_{\mathrm{pe}}t}$, as recovered through the asymptotic $-1/2$ exponent in the inset of figure 3*b*.

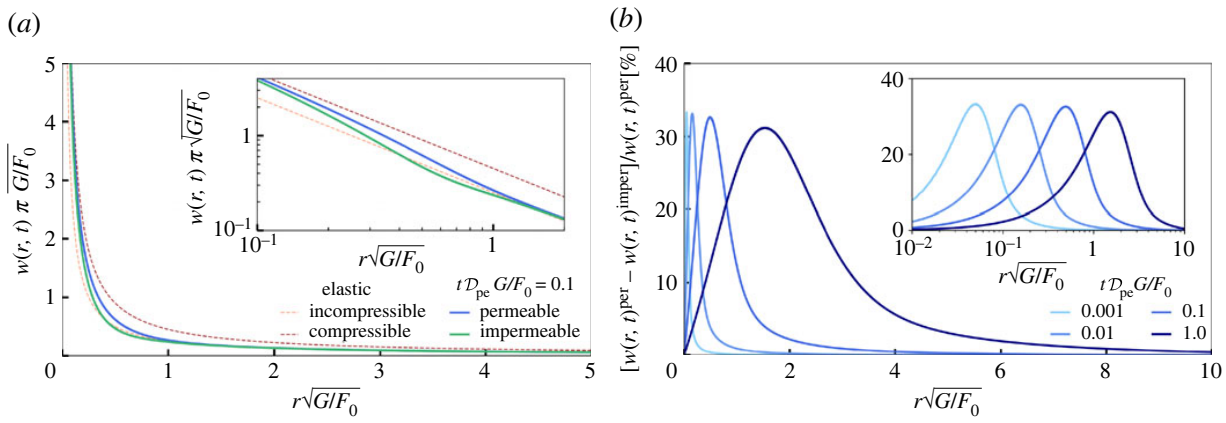

Figure 5. Comparison between the point-force solutions of the permeable and impermeable cases. (*a*) Normalized surface deformation as a function of the radial coordinate at the noted time, using $\nu = 0.1$. Shown are the point-force solutions for permeable and impermeable boundary conditions, computed from the inverse transforms of equations (2.22) and (B 2). The orange and red dashed lines correspond to the inverse transforms of equations (2.24*a*) and (2.24*b*). The inset shows the same data on logarithmic scales. (*b*) Relative difference between the surface deformation in the permeable and impermeable cases, as a function of the radial coordinate, for the noted dimensionless times. The inset shows the same data in semi-logarithmic scale.

Appendix B. Point-force solution for an impermeable gel and comparison to the permeable case

Here, we discuss the effect of surface permeability on the point-force response. In the model presented in the main text, we assumed that the gel is in contact with a bath of its own solvent, which fixes the chemical potential of the solvent at the surface to its reference value, at all times. If the gel is in contact with another kind of medium (e.g. air, solid surface or immiscible liquid), the description should be modified, and incorporate drying in particular. If one considers time scales smaller than the drying time, we can neglect the solvent exchange at the interface. In that case, we suppose the solvent flux vanishes at the surface, allowing us to impose the *impermeable* boundary condition at $z = 0$:

$$\mathbf{J} \cdot \mathbf{n} = \frac{\partial \mu}{\partial z} = 0. \tag{B 1}$$

We can use the same method as the one used in the main text, in order to derive the point-force response:

$$\hat{w}^{\mathrm{imper}}(s,q) = -\frac{1}{2Gsq} \frac{1}{1 + \Lambda(\mathcal{D}_{\mathrm{pe}} s^2/q)\left((1/(\sqrt{1 + (q/s^2\mathcal{D}_{\mathrm{pe}})})) - 1\right)}, \tag{B 2}$$

where the superscript 'imper' stands for the impermeable condition. We thus recover the solution derived in [10]. The diffusive-like self-similarity discussed in the main text also holds here.

The point-force responses with impermeable and permeable boundary conditions are compared in figure 5*a*. Both solutions appear to be qualitatively similar, and display the same short-term and long-term behaviours. Nevertheless, at a given time $t = 0.1F_0/(G\mathcal{D}_{\mathrm{pe}})$, we observe that the surface deformation in the impermeable case is smaller than the one in the permeable case. Also, the permeable solution relaxes faster than the impermeable one towards the long-time purely elastic compressible limit. Quantitatively, for a Poisson ratio $\nu = 0.1$, we observe a relative difference between the two solutions up to 35%, where the maximum difference is located at a radial position $\sim \sqrt{\mathcal{D}_{\mathrm{pe}} t}$, as shown in figure 5*b*.

Appendix C. Numerical computation of the normal force

Here, we detail how equations (3.9), (3.12) and (3.13) are numerically solved. All variables are dimensionless in this section for simplicity and the ˜ symbol is omitted. The normalized deformation in reciprocal spaces reads according to equation (3.12):

$$\hat{w}^*(s) = \frac{\hat{p}^*(s)}{8}\left(\frac{D_c}{D}\right)^{3/2}\hat{\mathcal{G}}^*(s) \text{ with } \hat{\mathcal{G}}^*(s) = \frac{1}{s}\frac{1}{1 - i\Lambda\frac{s^2}{\omega D/(\omega_c D_c)}\left(1 - \sqrt{1 + ((i\omega D/(\omega_c D_c))/s^2)}\right)}. \quad (C\,1)$$

By integrating equation (3.9) between 0 and r, and invoking equation (C 1), we obtain the following equation for the pressure:

$$\frac{dp^*}{dr} = \frac{6ir}{(1+r^2)^3} + \frac{3i}{2(1+r^2)^3}\left(\frac{D_c}{D}\right)^{3/2}\int_0^\infty ds\, J_1(sr)\hat{\mathcal{G}}^*(s)\hat{p}^*(s). \quad (C\,2)$$

Finally, by performing a first-order Hankel transform of the latter equation, we obtain the Fredholm equation of the second kind:

$$\hat{p}^*(s) = -\frac{3is}{4}K_1(s) - \frac{3i}{2}\left(\frac{D_c}{D}\right)^{3/2}\int_0^\infty dk\hat{\mathcal{G}}^*(k)\hat{p}^*(k)\int_0^\infty dr\frac{rJ_1(kr)J_1(sr)}{s(1+r^2)^3}, \quad (C\,3)$$

where K_n is the modified Bessel function of the second kind with index n. The kernel of the Fredholm equation has an analytical solution [31], given by

$$\begin{aligned}\int_0^\infty dr\,\frac{rJ_1(kr)J_1(sr)}{(1+r^2)^3} &= \frac{k^2+s^2}{8}I_1(s)K_1(k) - sk\frac{I_2(s)K_2(k)}{4} \quad \text{for } s < k,\\ &= \frac{k^2+s^2}{8}I_1(k)K_1(s) - sk\frac{I_2(k)K_2(s)}{4} \quad \text{for } k < s, \end{aligned} \quad (C\,4)$$

where I_n is the modified Bessel function of the first kind with index n. Integrals are numerically evaluated with the Gauss–Legendre-quadrature method. The discretized version of equation (C 3) is a linear algebraic problem and can be numerically solved. Finally, the dimensionless force can be computed as in equation (3.13) by

$$F^* = \frac{D_c}{D}\hat{p}^*(s=0). \quad (C\,5)$$

References

1. Andreotti B, Bäumchen O, Boulogne F, Daniels KE, Dufresne ER, Perrin H, Salez T, Snoeijer JH, Style RW. 2016 Solid capillarity: when and how does surface tension deform soft solids? *Soft Matter* **12**, 2993–2996. (doi:10.1039/C5SM03140K)
2. d'Eramo L *et al.* 2018 Microfluidic actuators based on temperature-responsive hydrogels. *Microsyst. Nanoeng.* **4**, 1–7. (doi:10.1038/micronano.2017.69)
3. Flory PJ. 1953 *Principles of polymer chemistry*. Ithaca, NY: Cornell University Press.
4. de Gennes P-G. 1979 *Scaling concepts in polymer physics*. Ithaca, NY: Cornell University Press.
5. Li M, Bresson B, Cousin F, Fretigny C, Tran Y. 2015 Submicrometric films of surface-attached polymer network with temperature-responsive properties. *Langmuir* **31**, 11 516–11 524. (doi:10.1021/acs.langmuir.5b02948)
6. Biot MA. 1941 General theory of three-dimensional consolidation. *J. Appl. Phys.* **12**, 155–164. (doi:10.1063/1.1712886)
7. Hong W, Zhao X, Zhou J, Suo Z. 2008 A theory of coupled diffusion and large deformation in polymeric gels. *J. Mech. Phys. Solids* **56**, 1779–1793. (doi:10.1016/j.jmps.2007.11.010)
8. Bouklas N, Huang R. 2012 Swelling kinetics of polymer gels: comparison of linear and nonlinear theories. *Soft Matter* **8**, 8194–8203. (doi:10.1039/c2sm25467k)
9. Hu Y, Suo Z. 2012 Viscoelasticity and poroelasticity in elastomeric gels. *Acta Mech. Solida Sin.* **25**, 441–458. (doi:10.1016/S0894-9166(12)60039-1)

10. Zhao M, Dervaux J, Narita T, Lequeux F, Limat L, Roché M. 2018 Geometrical control of dissipation during the spreading of liquids on soft solids. *Proc. Natl Acad. Sci. USA* **115**, 1748–1753. (doi:10.1073/pnas.1712562115)
11. Liu Z, Bouklas N, Hui C-Y. 2020 Coupled flow and deformation fields due to a line load on a poroelastic half space: effect of surface stress and surface bending. *Proc. R. Soc. A* **476**, 20190761. (doi:10.1098/rspa.2019.0761)
12. Ang I, Liu Z, Kim J, Hui C-Y, Bouklas N. 2020 Effect of elastocapillarity on the swelling kinetics of hydrogels. *J. Mech. Phys. Solids* **145**, 104132. (doi:10.1016/j.jmps.2020.104132)
13. Dervaux J, Amar MB. 2012 Mechanical instabilities of gels. *Annu. Rev. Condens. Matter Phys.* **3**, 311–332. (doi:10.1146/annurev-conmatphys-062910-140436)
14. Johnson KL. 1987 *Contact mechanics*. Cambridge, UK: Cambridge University Press. (doi:10.1017/CBO9781139171731)
15. Hui C-Y, Lin YY, Chuang F-C, Shull KR, Lin W-C. 2006 A contact mechanics method for characterizing the elastic properties and permeability of gels. *J. Polym. Sci. B: Polym. Phys.* **44**, 359–370. (doi:10.1002/polb.20613)
16. Hu Y, Zhao X, Vlassak JJ, Suo Z. 2010 Using indentation to characterize the poroelasticity of gels. *Appl. Phys. Lett.* **96**, 121904. (doi:10.1063/1.3370354)
17. Hu Y, Chen X, Whitesides GM, Vlassak JJ, Suo Z. 2011 Indentation of polydimethylsiloxane submerged in organic solvents. *J. Mater. Res.* **26**, 785–795. (doi:10.1557/jmr.2010.35)
18. Delavoipiere J, Tran Y, Verneuil E, Chateauminois A. 2016 Poroelastic indentation of mechanically confined hydrogel layers. *Soft Matter* **12**, 8049–8058. (doi:10.1039/C6SM01448H)
19. Degen GD, Chen Y-T, Chau AL, Månsson LK, Pitenis AA. 2020 Poroelasticity of highly confined hydrogel films measured with a surface forces apparatus. *Soft Matter* **16**, 8096–8100. (doi:10.1039/D0SM01312A)
20. Reynolds O. 1886 Iv. On the theory of lubrication and its application to mr. beauchamp tower's experiments, including an experimental determination of the viscosity of olive oil. *Phil. Trans. R. Soc.* **177**, 157–234. (doi:10.1098/rstl.1886.0005)
21. Vakarelski IU, Manica R, Tang X, O'Shea SJ, Stevens GW, Grieser F, Dagastine RR, Chan DY. 2010 Dynamic interactions between microbubbles in water. *Proc. Natl Acad. Sci. USA* **107**, 11 177–11 182. (doi:10.1073/pnas.1005937107)
22. Leroy S, Charlaix E. 2011 Hydrodynamic interactions for the measurement of thin film elastic properties. *J. Fluid Mech.* **674**, 389–407. (doi:10.1017/S0022112010006555)
23. Dowson D, Higginson GR. 2014 *Elasto-hydrodynamic lubrication: international series on materials science and technology*. Oxford, UK: Elsevier.
24. Kaveh F, Ally J, Kappl M, Butt H-J. 2014 Hydrodynamic force between a sphere and a soft, elastic surface. *Langmuir* **30**, 11 619–11 624. (doi:10.1021/la502328u)
25. Wang Y, Dhong C, Frechette J. 2015 Out-of-contact elastohydrodynamic deformation due to lubrication forces. *Phys. Rev. Lett.* **115**, 248302. (doi:10.1103/PhysRevLett.115.248302)
26. Wang Y, Tan MR, Frechette J. 2017 Elastic deformation of soft coatings due to lubrication forces. *Soft Matter* **13**, 6718–6729. (doi:10.1039/C7SM01061C)
27. Wang Y, Pilkington GA, Dhong C, Frechette J. 2017 Elastic deformation during dynamic force measurements in viscous fluids. *Curr. Opin. Colloid Interface Sci.* **27**, 43–49. (doi:10.1016/j.cocis.2016.09.009)
28. Wang Y, Frechette J. 2018 Morphology of soft and rough contact via fluid drainage. *Soft Matter* **14**, 7605–7614. (doi:10.1039/C8SM00884A)
29. Karan P, Das SS, Mukherjee R, Chakraborty J, Chakraborty S. 2020 Flow and deformation characteristics of a flexible microfluidic channel with axial gradients in wall elasticity. *Soft Matter* **16**, 5777–5786. (doi:10.1039/D0SM00333F)
30. Leroy S, Steinberger A, Cottin-Bizonne C, Restagno F, Léger L, Charlaix E. 2012 Hydrodynamic interaction between a spherical particle and an elastic surface: a gentle probe for soft thin films. *Phys. Rev. Lett.* **108**, 264501. (doi:10.1103/PhysRevLett.108.264501)
31. Guan D, Barraud C, Charlaix E, Tong P. 2017 Noncontact viscoelastic measurement of polymer thin films in a liquid medium using long-needle atomic force microscopy. *Langmuir* **33**, 1385–1390. (doi:10.1021/acs.langmuir.6b04066)
32. Zhang Z, Arshad M, Bertin V, Almohamad S, Raphaël E, Salez T, Maali A. 2022 Contactless rheology of soft gels over a broad frequency range. *Phys. Rev. Applied* **17**, 064045. (doi:10.1103/PhysRevApplied.17.064045)

33. Villey R, Martinot E, Cottin-Bizonne C, Phaner-Goutorbe M, Léger L, Restagno F, Charlaix E. 2013 Effect of surface elasticity on the rheology of nanometric liquids. *Phys. Rev. Lett.* **111**, 215701. (doi:10.1103/PhysRevLett.111.215701)
34. Guan D, Charlaix E, Qi RZ, Tong P. 2017 Noncontact viscoelastic imaging of living cells using a long-needle atomic force microscope with dual-frequency modulation. *Phys. Rev. Appl.* **8**, 044010. (doi:10.1103/PhysRevApplied.8.044010)
35. Wang Y, Zeng B, Alem HT, Zhang Z, Charlaix E, Maali A. 2018 Viscocapillary response of gas bubbles probed by thermal noise atomic force measurement. *Langmuir* **34**, 1371–1375. (doi:10.1021/acs.langmuir.7b03857)
36. Bertin V, Zhang Z, Boisgard R, Grauby-Heywang C, Raphael E, Salez T, Maali A. 2021 Contactless rheology of finite-size air-water interfaces. *Phys. Rev. Res.* **3**, L032007. (doi:10.1103/PhysRevResearch.3.L032007)
37. Cappella B, Dietler G. 1999 Force-distance curves by atomic force microscopy. *Surf. Sci. Rep.* **34**, 1–104. (doi:10.1016/S0167-5729(99)00003-5)
38. Butt H-J, Cappella B, Kappl M. 2005 Force measurements with the atomic force microscope: technique, interpretation and applications. *Surf. Sci. Rep.* **59**, 1–152. (doi:10.1016/j.surfrep.2005.08.003)
39. Israelachvili JN, Adams G. 1976 Direct measurement of long range forces between two mica surfaces in aqueous KNO_3 solutions. *Nature* **262**, 774–776. (doi:10.1038/262774a0)
40. Israelachvili J *et al.* 2010 Recent advances in the surface forces apparatus (SFA) technique. *Rep. Prog. Phys.* **73**, 036601. (doi:10.1088/0034-4885/73/3/036601)
41. Kristiansen K *et al.* 2019 Multimodal miniature surface forces apparatus (μSFA) for interfacial science measurements. *Langmuir* **35**, 15 500–15 514. (doi:10.1021/acs.langmuir.9b01808)
42. Lainé A, Jubin L, Canale L, Bocquet L, Siria A, Donaldson SH, Niguès A. 2019 Micromegascope based dynamic surface force apparatus. *Nanotechnology* **30**, 195502. (doi:10.1088/1361-6528/ab02ba)
43. Sekimoto K, Leibler L. 1993 A mechanism for shear thickening of polymer-bearing surfaces: elasto-hydrodynamic coupling. *Europhys. Lett.* **23**, 113. (doi:10.1209/0295-5075/23/2/006)
44. Beaucourt J, Biben T, Misbah C. 2004 Optimal lift force on vesicles near a compressible substrate. *Europhys. Lett.* **67**, 676. (doi:10.1209/epl/i2004-10103-0)
45. Skotheim J, Mahadevan L. 2005 Soft lubrication: the elastohydrodynamics of nonconforming and conforming contacts. *Phys. Fluids* **17**, 092101. (doi:10.1063/1.1985467)
46. Urzay J, Llewellyn Smith SG, Glover BJ. 2007 The elastohydrodynamic force on a sphere near a soft wall. *Phys. Fluids* **19**, 103106. (doi:10.1063/1.2799148)
47. Snoeijer JH, Eggers J, Venner CH. 2013 Similarity theory of lubricated hertzian contacts. *Phys. Fluids* **25**, 101705. (doi:10.1063/1.4826981)
48. Salez T, Mahadevan L. 2015 Elastohydrodynamics of a sliding, spinning and sedimenting cylinder near a soft wall. *J. Fluid Mech.* **779**, 181–196. (doi:10.1017/jfm.2015.425)
49. Vialar P, Merzeau P, Giasson S, Drummond C. 2019 Compliant surfaces under shear: elastohydrodynamic lift force. *Langmuir* **35**, 15605–15613. (doi:10.1021/acs.langmuir.9b02019)
50. Zhang Z, Bertin V, Arshad M, Raphael E, Salez T, Maali A. 2020 Direct measurement of the elastohydrodynamic lift force at the nanoscale. *Phys. Rev. Lett.* **124**, 054502. (doi:10.1103/PhysRevLett.124.054502)
51. Bertin V, Amarouchene Y, Raphael E, Salez T. 2022 Soft-lubrication interactions between a rigid sphere and an elastic wall. *J. Fluid Mech.* **933**, A23. (doi:10.1017/jfm.2021.1063)
52. Bureau L, Coupier G, Salez T. 2022 Lift at zero reynolds number. (http://arxiv.org/abs/2207.04538).
53. Bouchet A-S, Cazeneuve C, Baghdadli N, Luengo GS, Drummond C. 2015 Experimental study and modeling of boundary lubricant polyelectrolyte films. *Macromolecules* **48**, 2244–2253. (doi:10.1021/acs.macromol.5b00151)
54. Saintyves B, Jules T, Salez T, Mahadevan L. 2016 Self-sustained lift and low friction via soft lubrication. *Proc. Natl Acad. Sci. USA* **113**, 5847–5849. (doi:10.1073/pnas.1525462113)
55. Davies HS, Débarre D, El Amri N, Verdier C, Richter RP, Bureau L. 2018 Elastohydrodynamic lift at a soft wall. *Phys. Rev. Lett.* **120**, 198001. (doi:10.1103/PhysRevLett.120.198001)
56. Rallabandi B, Oppenheimer N, Ben Zion MY, Stone HA. 2018 Membrane-induced hydroelastic migration of a particle surfing its own wave. *Nat. Phys.* **14**, 1211–1215. (doi:10.1038/s41567-018-0272-z)
57. Hou J, Mow VC, Lai W, Holmes M. 1992 An analysis of the squeeze-film lubrication mechanism for articular cartilage. *J. Biomech.* **25**, 247–259. (doi:10.1016/0021-9290(92)90024-U)

58. Jahn S, Seror J, Klein J. 2016 Lubrication of articular cartilage. *Annu. Rev. Biomed. Eng.* **18**, 235–258. (doi:10.1146/annurev-bioeng-081514-123305)
59. Cher I. 2008 A new look at lubrication of the ocular surface: fluid mechanics behind the blinking eyelids. *Ocul. Surf.* **6**, 79–86. (doi:10.1016/S1542-0124(12)70271-9)
60. Pandey A, Karpitschka S, Venner CH, Snoeijer JH. 2016 Lubrication of soft viscoelastic solids. *J. Fluid Mech.* **799**, 433–447. (doi:10.1017/jfm.2016.375)
61. Kargar-Estahbanati A, Rallabandi B. 2021 Lift forces on three-dimensional elastic and viscoelastic lubricated contacts. *Phys. Rev. Fluids* **6**, 034003. (doi:10.1103/PhysRevFluids.6.034003)
62. Hui C-Y, Wu H, Jagota A, Khripin C. 2021 Friction force during lubricated steady sliding of a rigid cylinder on a viscoelastic substrate. *Tribol. Lett.* **69**, 1–17. (doi:10.1007/s11249-020-01396-5)
63. Delavoipière J, Tran Y, Verneuil E, Heurtefeu B, Hui CY, Chateauminois A. 2018 Friction of poroelastic contacts with thin hydrogel films. *Langmuir* **34**, 9617–9626. (doi:10.1021/acs.langmuir.8b01466)
64. Ciapa L, Delavoipière J, Tran Y, Verneuil E, Chateauminois A. 2020 Transient sliding of thin hydrogel films: the role of poroelasticity. *Soft Matter* **16**, 6539–6548. (doi:10.1039/D0SM00641F)
65. Cuccia NL, Pothineni S, Wu B, Méndez Harper J, Burton JC. 2020 Pore-size dependence and slow relaxation of hydrogel friction on smooth surfaces. *Proc. Natl Acad. Sci. USA* **117**, 11 247–11 256. (doi:10.1073/pnas.1922364117)
66. Eddine MA, Belbekhouche S, de Chateauneuf-Randon S, Salez T, Kovalenko A, Bresson B, Monteux C. 2022 Large and nonlinear permeability amplification with polymeric additives in hydrogel membranes. *Macromolecules* **55**, 9841–9850. (doi:10.1021/acs.macromol.2c01462)
67. Beavers GS, Joseph DD. 1967 Boundary conditions at a naturally permeable wall. *J. Fluid Mech.* **30**, 197–207. (doi:10.1017/S0022112067001375)
68. Meeker SP, Bonnecaze RT, Cloitre M. 2004 Slip and flow in pastes of soft particles: direct observation and rheology. *J. Rheol.* **48**, 1295–1320. (doi:10.1122/1.1795171)
69. Knox D, Duffy B, McKee S, Wilson S. 2017 Squeeze-film flow between a curved impermeable bearing and a flat porous bed. *Phys. Fluids* **29**, 023101. (doi:10.1063/1.4974521)
70. Van de Velde P, Dervaux J, Protière S, Duprat C. 2022 Spontaneous localized fluid release on swelling fibres. *Soft Matter* **18**, 4565–4571. (doi:10.1039/D2SM00460G)
71. Hughes B, White L. 1979 'soft' contact problems in linear elasticity. *Q. J. Mech. Appl. Math.* **32**, 445–471. (doi:10.1093/qjmam/32.4.445)
72. Essink MH, Pandey A, Karpitschka S, Venner CH, Snoeijer JH. 2021 Regimes of soft lubrication. *J. Fluid Mech.* **915**, A49. (doi:10.1017/jfm.2021.96)
73. McNamee J, Gibson R. 1960 Plane strain and axially symmetric problems of the consolidation of a semi-infinite clay stratum. *Q. J. Mech. Appl. Math.* **13**, 210–227. (doi:10.1093/qjmam/13.2.210)
74. McNamee J, Gibson R. 1960 Displacement functions and linear transforms applied to diffusion through porous elastic media. *Q. J. Mech. Appl. Math.* **13**, 98–111. (doi:10.1093/qjmam/13.1.98)
75. Gibson R, Schiffman R, Pu S. 1970 Plane strain and axially symmetric consolidation of a clay layer on a smooth impervious base. *Q. J. Mech. Appl. Math.* **23**, 505–520. (doi:10.1093/qjmam/23.4.505)
76. Hariprasad DS, Secomb TW. 2012 Motion of red blood cells near microvessel walls: effects of a porous wall layer. *J. Fluid Mech.* **705**, 195–212. (doi:10.1017/jfm.2012.102)
77. Abate J, Whitt W. 2006 A unified framework for numerically inverting laplace transforms. *INFORMS J. Comput.* **18**, 408–421. (doi:10.1287/ijoc.1050.0137)
78. Xu Q, Wilen LA, Jensen KE, Style RW, Dufresne ER. 2020 Viscoelastic and poroelastic relaxations of soft solid surfaces. *Phys. Rev. Lett.* **125**, 238002. (doi:10.1103/PhysRevLett.125.238002)
79. Guyon E. 2001 *Physical Hydrodynamics*. Oxford, UK: Oxford University Press.

Bibliography

1. Li, M., Bresson, B., Cousin, F, Fretigny, C. & Tran, Y. Submicrometric films of surface-attached polymer network with temperature-responsive properties. *Langmuir* **31,** 11516–11524 (2015).
2. Russell, T. Surface-responsive materials. *Science* **297,** 964–967 (2002).
3. Beebe, D. J. *et al.* Functional hydrogel structures for autonomous flow control inside microfluidic channels. *Nature* **404,** 588–590 (2000).
4. Idota, N., Kikuchi, A., Kobayashi, J., Sakai, K. & Okano, T. Microfluidic valves comprising nanolayered thermoresponsive polymer-grafted capillaries. *Advanced Materials* **17,** 2723–2727 (2005).
5. d'Eramo, L. *et al.* Microfluidic actuators based on temperature-responsive hydrogels. *Microsystems & Nanoengineering* **4,** 1–7 (2018).
6. Peppas, N. A., Hilt, J. Z., Khademhosseini, A. & Langer, R. Hydrogels in biology and medicine: from molecular principles to bionanotechnology. *Advanced materials* **18,** 1345–1360 (2006).
7. Bearinger, J. *et al.* P (AAm-co-EG) interpenetrating polymer networks grafted to oxide surfaces: Surface characterization, protein adsorption, and cell detachment studies. *Langmuir* **13,** 5175–5183 (1997).
8. Eslahi, N., Abdorahim, M. & Simchi, A. Smart polymeric hydrogels for cartilage tissue engineering: a review on the chemistry and biological functions. *Biomacromolecules* **17,** 3441–3463 (2016).
9. Fung, Y. *et al.* Polymer networks formed in liquid crystal. *Liquid Crystals* **19,** 797–801 (Dec. 1995).
10. Biot, M. A. General theory of three-dimensional consolidation. *Journal of applied physics* **12,** 155–164 (1941).
11. Pandey, A., Karpitschka, S., Venner, C. H. & Snoeijer, J. H. Lubrication of soft viscoelastic solids. *Journal of fluid mechanics* **799,** 433–447 (2016).
12. Kargar-Estahbanati, A. & Rallabandi, B. Lift forces on three-dimensional elastic and viscoelastic lubricated contacts. *Physical Review Fluids* **6,** 034003 (2021).
13. Hui, C.-Y., Wu, H., Jagota, A. & Khripin, C. Friction force during lubricated steady sliding of a rigid cylinder on a viscoelastic substrate. *Tribology Letters* **69,** 1–17 (2021).
14. Eddine, M. A. *et al.* Large and Nonlinear Permeability Amplification with Polymeric Additives in Hydrogel Membranes. *Macromolecules* (2022).
15. Delavoipière, J. *et al.* Friction of poroelastic contacts with thin hydrogel films. *Langmuir* **34,** 9617–9626 (2018).
16. Ciapa, L., Delavoipière, J., Tran, Y., Verneuil, E. & Chateauminois, A. Transient sliding of thin hydrogel films: the role of poroelasticity. *Soft Matter* **16,** 6539–6548 (2020).
17. Cuccia, N. L., Pothineni, S., Wu, B., Méndez Harper, J. & Burton, J. C. Pore-size dependence and slow relaxation of hydrogel friction on smooth surfaces. *Proceedings of the National Academy of Sciences* **117,** 11247–11256 (2020).
18. Flory, P. J. *Principles of polymer chemistry* (Cornell university press, 1953).
19. Bertrand, T., Peixinho, J., Mukhopadhyay, S. & MacMinn, C. W. Dynamics of swelling and drying in a spherical gel. *Physical Review Applied* **6,** 064010 (2016).
20. Etzold, M. A., Linden, P. F. & Worster, M. G. Transpiration through hydrogels. *Journal of Fluid Mechanics* **925,** A8 (2021).
21. Engelsberg, M & Barros Jr, W. Free-evolution kinetics in a high-swelling polymeric hydrogel. *Physical Review E* **88,** 062602 (2013).

22. Deegan, R. D. Pattern formation in drying drops. *Physical review E* **61,** 475 (2000).

23. Zang, D., Tarafdar, S., Tarasevich, Y. Y., Choudhury, M. D. & Dutta, T. Evaporation of a Droplet: From physics to applications. *Physics Reports* **804,** 1–56 (2019).

24. Ozawa, K., Nishitani, E. & Doi, M. Modeling of the drying process of liquid droplet to form thin film. *Japanese journal of applied physics* **44,** 4229 (2005).

25. Pauchard, L & Allain, C. Stable and unstable surface evolution during the drying of a polymer solution drop. *Physical Review E* **68,** 052801 (2003).

26. De Gennes, P. G. Instabilities during the evaporation of a film: Non-glassy polymer+ volatile solvent. *The European Physical Journal E* **6,** 421–424 (2001).

27. De Gennes, P. G. Solvent evaporation of spin cast films:"crust" effects. *The European Physical Journal E* **7,** 31–34 (2002).

28. Routh, A. F. Drying of thin colloidal films. *Reports on Progress in Physics* **76,** 046603 (2013).

29. Okuzono, T., Ozawa, K. & Doi, M. Simple model of skin formation caused by solvent evaporation in polymer solutions. *Physical review letters* **97,** 136103 (2006).

30. Yoon, J., Kim, J. & Hayward, R. C. Nucleation, growth, and hysteresis of surface creases on swelled polymer gels. *Soft Matter* **6,** 5807–5816 (2010).

31. Navier, C. L. M. H. Mémoire sur les lois du Mouvement des Fluides. *Mémoires de l'Académie Royale des Sciences de l'Institut de France,* 389–440 (1823).

32. Reynolds, O. IV. On the theory of lubrication and its application to Mr. Beauchamp tower's experiments, including an experimental determination of the viscosity of olive oil. *Philosophical transactions of the Royal Society of London,* 157–234 (1886).

33. GENNES, P. Viscometric flows of tangled polymers. *Comptes Rendus Hebdomadaires Des Seances De L Academie Des Sciences Serie B* **288,** 219–220 (1979).

34. Léger, L, Hervet, H, Massey, G & Durliat, E. Wall slip in polymer melts. *Journal of Physics: Condensed Matter* **9,** 7719 (1997).

35. Mhetar, V. & Archer, L. Slip in entangled polymer melts. 1. General features. *Macromolecules* **31,** 8607–8616 (1998).

36. Huang, D. M., Sendner, C., Horinek, D., Netz, R. R. & Bocquet, L. Water slippage versus contact angle: A quasiuniversal relationship. *Physical review letters* **101,** 226101 (2008).

37. Bocquet, L. & Charlaix, E. Nanofluidics, from bulk to interfaces. *Chemical Society Reviews* **39,** 1073–1095 (2010).

38. Poiseuille, J. L. Experimental research on the movement of liquids in tubes of very small diameters. *Mémoires presentés par divers savants a l'Académie Royale des Sciences de l'Institut de France, IX,* 433–544 (1846).

39. Duprat, C. & Shore, H. A. *Fluid-structure interactions in low-Reynolds-number flows* (Royal Society of Chemistry, 2016).

40. Stone, H. A., Stroock, A. D. & Ajdari, A. Engineering flows in small devices: microfluidics toward a lab-on-a-chip. *Annu. Rev. Fluid Mech.* **36,** 381–411 (2004).

41. Whitesides, G. M. The origins and the future of microfluidics. *nature* **442,** 368–373 (2006).

42. Squires, T. M. & Quake, S. R. Microfluidics: Fluid physics at the nanoliter scale. *Reviews of modern physics* **77,** 977 (2005).

43. Kaoui, B., Ristow, G., Cantat, I., Misbah, C. & Zimmermann, W. Lateral migration of a two-dimensional vesicle in unbounded Poiseuille flow. *Physical Review E* **77,** 021903 (2008).

44. Bruus, H. *Theoretical microfluidics* (Oxford university press, 2007).

45. Wheeler, A. R. *et al.* Microfluidic device for single-cell analysis. *Analytical chemistry* **75,** 3581–3586 (2003).

46. Yin, H. & Marshall, D. Microfluidics for single cell analysis. *Current opinion in biotechnology* **23,** 110–119 (2012).

47. Zare, R. N. & Kim, S. Microfluidic platforms for single-cell analysis. *Annual review of biomedical engineering* **12,** 187–201 (2010).

48. Vilquin, A. *et al.* Nanoparticle Taylor dispersion near charged surfaces with an open boundary. *Physical Review Letters* **130,** 038201 (2023).

49. Vilquin, A. *et al.* Time dependence of advection-diffusion coupling for nanoparticle ensembles. *Physical Review Fluids* **6,** 064201 (2021).

50. Santiago, J. G., Wereley, S. T., Meinhart, C. D., Beebe, D. & Adrian, R. J. A particle image velocimetry system for microfluidics. *Experiments in fluids* **25,** 316–319 (1998).

51. Chin, C. D. *et al.* Microfluidics-based diagnostics of infectious diseases in the developing world. *Nature medicine* **17,** 1015–1019 (2011).

52. Sackmann, E. K., Fulton, A. L. & Beebe, D. J. The present and future role of microfluidics in biomedical research. *Nature* **507,** 181–189 (2014).

53. Benzaquen, M., Salez, T. & Raphaël, E. Intermediate asymptotics of the capillary-driven thin-film equation. *The European Physical Journal E* **36,** 1–7 (2013).

54. Oron, A., Davis, S. H. & Bankoff, S. G. Long-scale evolution of thin liquid films. *Reviews of modern physics* **69,** 931 (1997).

55. Happel, J. & Brenner, H. *Low Reynolds number hydrodynamics: with special applications to particulate media* (Springer Science & Business Media, 1983).

56. Dowson, D. & Higginson, G. R. *Elasto-hydrodynamic lubrication: international series on materials science and technology* (Elsevier, 2014).

57. Venner, C. H. & Lubrecht, A. A. *Multi-level methods in lubrication* (Elsevier, 2000).

58. Brodsky, E. E. & Kanamori, H. Elastohydrodynamic lubrication of faults. *Journal of Geophysical Research: Solid Earth* **106,** 16357–16374 (2001).

59. Campbell, C. S. Self-lubrication for long runout landslides. *The Journal of Geology* **97,** 653–665 (1989).

60. Huerre, A. *et al.* Droplets in microchannels: dynamical properties of the lubrication film. *Physical review letters* **115,** 064501 (2015).

61. Baroud, C. N., Gallaire, F. & Dangla, R. Dynamics of microfluidic droplets. *Lab on a Chip* **10,** 2032–2045 (2010).

62. Dangla, R., Kayi, S. C. & Baroud, C. N. Droplet microfluidics driven by gradients of confinement. *Proceedings of the National Academy of Sciences* **110,** 853–858 (2013).

63. Abbyad, P., Dangla, R., Alexandrou, A. & Baroud, C. N. Rails and anchors: guiding and trapping droplet microreactors in two dimensions. *Lab on a Chip* **11,** 813–821 (2011).

64. Guyon, E., Hulin, J.-P., Petit, L. & de Gennes, P. G. *Hydrodynamique physique* (EDP sciences Les Ulis, 2001).

65. Landau, L. D. & Lifshitz, E. M. *Fluid Mechanics: Landau and Lifshitz: Course of Theoretical Physics, Volume 6* (Elsevier, 2013).

66. Lovalenti, P. M. & Brady, J. F. The force on a bubble, drop, or particle in arbitrary time-dependent motion at small Reynolds number. *Physics of Fluids A: Fluid Dynamics* **5,** 2104–2116 (1993).

67. Brenner, H. The slow motion of a sphere through a viscous fluid towards a plane surface. *Chemical engineering science* **16,** 242–251 (1961).

68. Basset, A. B. A Treatise on Hydrodynamics, vol. 1 (1888).

69. Proudman, I. & Pearson, J. Expansions at small Reynolds numbers for the flow past a sphere and a circular cylinder. *Journal of Fluid Mechanics* **2,** 237–262 (1957).

70. Lovalenti, P. M. & Brady, J. F. The hydrodynamic force on a rigid particle undergoing arbitrary time-dependent motion at small Reynolds number. *Journal of Fluid Mechanics* **256,** 561–605 (1993).

71. Brenner, H & Cox, R. The resistance to a particle of arbitrary shape in translational motion at small Reynolds numbers. *Journal of Fluid Mechanics* **17,** 561–595 (1963).

72. Loudon, C. & Tordesillas, A. The use of the dimensionless Womersley number to characterize the unsteady nature of internal flow. *Journal of theoretical biology* **191,** 63–78 (1998).

73. Rohlf, K & Tenti, G. The role of the Womersley number in pulsatile blood flow: a theoretical study of the Casson model. *Journal of biomechanics* **34,** 141–148 (2001).

74. Fick, A. Ueber diffusion. *Annalen der Physik* **170,** 59–86 (1855).

75. Duhamel, J. M. C. *Éléments de calcul infinitésimal* (Mallet-Bachelier, 1860).

76. Ettlinger, H. A Simple Form of Duhamel's Theorem and Some New Applications. *The American Mathematical Monthly* **29,** 239–250 (1922).

77. Crank, J. *The mathematics of diffusion* (Oxford university press, 1979).

78. Einstein, A. Über die von der molekularkinetischen Theorie der Wärme geforderte Bewegung von in ruhenden Flüssigkeiten suspendierten Teilchen. *Annalen der physik* **4** (1905).

79. Sutherland, W. LXXV. A dynamical theory of diffusion for non-electrolytes and the molecular mass of albumin. *The London, Edinburgh, and Dublin Philosophical Magazine and Journal of Science* **9,** 781–785 (1905).

80. Von Smoluchowski, M. Zur kinetischen theorie der brownschen molekularbewegung und der suspensionen. *Annalen der physik* **326,** 756–780 (1906).

81. Miller, C. C. The Stokes-Einstein law for diffusion in solution. *Proceedings of the Royal Society of London. Series A, Containing Papers of a Mathematical and Physical Character* **106,** 724–749 (1924).

82. Perrin, J. *Mouvement brownien et réalité moléculaire* in *Annales de Chimie et de Physique* **18** (1909), 1–114.

83. Kubo, R. The fluctuation-dissipation theorem. *Reports on progress in physics* **29,** 255 (1966).

84. Marconi, U. M. B., Puglisi, A., Rondoni, L. & Vulpiani, A. Fluctuation–dissipation: response theory in statistical physics. *Physics reports* **461,** 111–195 (2008).

85. Landau, L. D. & Lifshitz, E. M. *Statistical Physics: Landau and Lifshitz: Course of Theoretical Physics, Volume 5* (Elsevier, 2013).

86. Onuki, A. Theory of phase transition in polymer gels. *Responsive Gels: Volume Transitions I,* 63–121 (2005).

87. Darcy, H. Les fontaines publiques de Dijon (1856).

88. Biot, M. A. General solutions of the equations o elasticity and consolidation for a porous material, 91–96 (1956).

89. Terzaghi, K. *Theoretical soil mechanics* (1943).

90. Beavers, G. S. & Joseph, D. D. Boundary conditions at a naturally permeable wall. *Journal of fluid mechanics* **30,** 197–207 (1967).

91. Wang, H. *Theory of linear poroelasticity with applications to geomechanics and hydrogeology* (Princeton university press, 2000).

92. Rice, J. R. & Cleary, M. P. Some basic stress diffusion solutions for fluid-saturated elastic porous media with compressible constituents. *Reviews of Geophysics* **14,** 227–241 (1976).

93. Sarfati, R., Calderon, C. P. & Schwartz, D. K. Enhanced diffusive transport in fluctuating porous media. *ACS nano* **15,** 7392–7398 (2021).

94. Knox, D., Duffy, B., McKee, S & Wilson, S. Squeeze-film flow between a curved impermeable bearing and a flat porous bed. *Physics of Fluids* **29,** 023101 (2017).

95. Brochard, F. & de Gennes, P.-G. Dynamical scaling for polymers in theta solvents. *Macromolecules* **10,** 1157–1161 (1977).

96. Jones, R. A. *Soft condensed matter* (Oxford University Press, 2002).

97. De Gennes, P.-G. *Scaling concepts in polymer physics* (Cornell university press, 1979).

98. Cahn, J. W. On spinodal decomposition. *Acta metallurgica* **9,** 795–801 (1961).

99. Archer, A. J. & Evans, R. Dynamical density functional theory and its application to spinodal decomposition. *The Journal of chemical physics* **121,** 4246–4254 (2004).

100. Doi, M. *Soft matter physics* (Oxford University Press, USA, 2013).

101. Doi, M. & Onuki, A. Dynamic coupling between stress and composition in polymer solutions and blends. *Journal de Physique II* **2,** 1631–1656 (1992).

102. Lee, D. *et al.* Physical, mathematical, and numerical derivations of the Cahn–Hilliard equation. *Computational Materials Science* **81,** 216–225 (2014).

103. Huang, C., de La Cruz M., O. & W., S. B. Phase separation of ternary mixtures: Symmetric polymer blends. *Macromolecules* **28,** 7996–8005 (1995).

104. Butler, M. D. & Montenegro-Johnson, T. D. The swelling and shrinking of spherical thermo-responsive hydrogels. *Journal of Fluid Mechanics* **947,** A11 (2022).

105. Cummings, J., Lowengrub, J. S., Sumpter, B. G., Wise, S. M. & Kumar, R. Modeling solvent evaporation during thin film formation in phase separating polymer mixtures. *Soft Matter* **14,** 1833–1846 (2018).

106. Sierra-Martin, B, Laporte, Y, South, A., Lyon, L. A. & Fernández-Nieves, A. Bulk modulus of poly (N-isopropylacrylamide) microgels through the swelling transition. *Physical Review E* **84,** 011406 (2011).

107. Bar, A., Ramon, O., Cohen, Y. & Mizrahi, S. Shrinkage behaviour of hydrophobic hydrogel during dehydration. *Journal of food engineering* **55,** 193–199 (2002).

108. Landau, L. D., Lifshitz, E. M., Kosevich, A. M. & Pitaevskii, L. P. *Theory of elasticity: Landau and Lifshitz: Course of Theoretical Physics, volume 7* (Elsevier, 1986).

109. Love, A. E. H. *A treatise on the mathematical theory of elasticity* (Cambridge university press, 2013).

110. Zhao, M. *et al.* Geometrical control of dissipation during the spreading of liquids on soft solids. *Proceedings of the National Academy of Sciences* **115,** 1748–1753 (2018).

111. Van de Velde, P., Dervaux, J., Protière, S. & Duprat, C. Spontaneous localized fluid release on swelling fibres. *Soft Matter* **18,** 4565–4571 (2022).

112. Hu, Y., Zhao, X., Vlassak, J. J. & Suo, Z. Using indentation to characterize the poroelasticity of gels. *Applied Physics Letters* **96,** 121904 (2010).

113. Delavoipiere, J., Tran, Y., Verneuil, E. & Chateauminois, A. Poroelastic indentation of mechanically confined hydrogel layers. *Soft Matter* **12,** 8049–8058 (2016).

114. Hong, W., Zhao, X., Zhou, J. & Suo, Z. A theory of coupled diffusion and large deformation in polymeric gels. *Journal of the Mechanics and Physics of Solids* **56,** 1779–1793 (2008).

115. Bouklas, N. & Huang, R. Swelling kinetics of polymer gels: comparison of linear and nonlinear theories. *Soft Matter* **8,** 8194–8203 (2012).

116. Hu, Y. & Suo, Z. Viscoelasticity and poroelasticity in elastomeric gels. *Acta Mechanica Solida Sinica* **25,** 441–458 (2012).

117. Liu, Z., Bouklas, N. & Hui, C.-Y. Coupled flow and deformation fields due to a line load on a poroelastic half space: effect of surface stress and surface bending. *Proceedings of the Royal Society A* **476,** 20190761 (2020).

118. Ang, I., Liu, Z., Kim, J., Hui, C.-Y. & Bouklas, N. Effect of elastocapillarity on the swelling kinetics of hydrogels. *Journal of the Mechanics and Physics of Solids* **145,** 104132 (2020).

119. Dervaux, J. & Amar, M. B. Mechanical instabilities of gels. *Annu. Rev. Condens. Matter Phys.* **3,** 311–332 (2012).

120. Engler, A. J., Richert, L., Wong, J. Y., Picart, C. & Discher, D. E. Surface probe measurements of the elasticity of sectioned tissue, thin gels and polyelectrolyte multilayer films: correlations between substrate stiffness and cell adhesion. *Surface science* **570,** 142–154 (2004).

121. Davies, H. S. *et al.* Elastohydrodynamic lift at a soft wall. *Physical review letters* **120,** 198001 (2018).

122. Trujillo, V., Kim, J. & Hayward, R. C. Creasing instability of surface-attached hydrogels. *Soft Matter* **4,** 564–569 (2008).

123. Hong, W., Zhao, X. & Suo, Z. Formation of creases on the surfaces of elastomers and gels. *Applied Physics Letters* **95** (2009).

124. Ortiz, O., Vidyasagar, A., Wang, J. & Toomey, R. Surface instabilities in ultrathin, cross-linked poly (N-isopropylacrylamide) coatings. *Langmuir* **26,** 17489–17494 (2010).

125. Chen, D., Yoon, J., Chandra, D., Crosby, A. J. & Hayward, R. C. Stimuli-responsive buckling mechanics of polymer films. *Journal of Polymer Science Part B: Polymer Physics* **52,** 1441–1461 (2014).

126. Ciarletta, P. Matched asymptotic solution for crease nucleation in soft solids. *Nature communications* **9,** 496 (2018).

127. Cai, S., Chen, D., Suo, Z. & Hayward, R. C. Creasing instability of elastomer films. *Soft Matter* **8,** 1301–1304 (2012).

128. Hohlfeld, E. & Mahadevan, L. Unfolding the sulcus. *Physical review letters* **106,** 105702 (2011).

129. Chen, D., Cai, S., Suo, Z. & Hayward, R. C. Surface energy as a barrier to creasing of elastomer films: An elastic analogy to classical nucleation. *Physical review letters* **109,** 038001 (2012).

130. Suematsu, N., Sekimoto, K. & Kawasaki, K. Three-dimensional computer modeling for pattern formation on the surface of an expanding polymer gel. *Physical Review A* **41,** 5751 (1990).

131. Li, B., Cao, Y.-P., Feng, X.-Q. & Gao, H. Mechanics of morphological instabilities and surface wrinkling in soft materials: a review. *Soft Matter* **8,** 5728–5745 (2012).

132. Weiss, F. *et al.* Creases and wrinkles on the surface of a swollen gel. *Journal of Applied Physics* **114** (2013).

133. Sheppard, S. & Elliott, F. The reticulation of gelatine. *Journal of the Franklin Institute* **187,** 227 (1919).

134. Southern, E & Thomas, A. Effect of constraints on the equilibrium swelling of rubber vulcanizates. *Journal of Polymer Science Part A: General Papers* **3,** 641–646 (1965).

135. Tanaka, T. *et al.* Mechanical instability of gels at the phase transition. *Nature* **325,** 796–798 (1987).

136. Tanaka, H., Tomita, H., Takasu, A., Hayashi, T. & Nishi, T. Morphological and kinetic evolution of surface patterns in gels during the swelling process: Evidence of dynamic pattern ordering. *Physical review letters* **68,** 2794 (1992).

137. Brau, F. *et al.* Multiple-length-scale elastic instability mimics parametric resonance of nonlinear oscillators. *Nature Physics* **7,** 56–60 (2011).

138. Ghatak, A. & Das, A. L. Kink instability of a highly deformable elastic cylinder. *Physical review letters* **99,** 076101 (2007).

139. Chen, D., Jin, L., Suo, Z. & Hayward, R. C. Controlled formation and disappearance of creases. *Materials Horizons* **1,** 207–213 (2014).

140. Jin, L., Chen, D., Hayward, R. C. & Suo, Z. Creases on the interface between two soft materials. *Soft Matter* **10,** 303–311 (2014).

141. Guvendiren, M., Burdick, J. A. & Yang, S. Solvent induced transition from wrinkles to creases in thin film gels with depth-wise crosslinking gradients. *Soft Matter* **6,** 5795–5801 (2010).

142. Drummond, W. R., Knight, M. L., Brannon, M. L. & Peppas, N. A. Surface instabilities during swelling of pH-sensitive hydrogels. *Journal of controlled release* **7,** 181–183 (1988).

143. Dervaux, J. & Amar, M. B. Buckling condensation in constrained growth. *Journal of the Mechanics and Physics of Solids* **59,** 538–560 (2011).

144. Amar, M. B. & Ciarletta, P. Swelling instability of surface-attached gels as a model of soft tissue growth under geometric constraints. *Journal of the Mechanics and Physics of Solids* **58,** 935–954 (2010).

145. Cerda, E. & Mahadevan, L. Geometry and physics of wrinkling. *Physical review letters* **90,** 074302 (2003).

146. Allen, H. G. *Analysis and design of structural sandwich panels: the commonwealth and international library: structures and solid body mechanics division* (Elsevier, 2013).

147. Bowden, N., Huck, W. T., Paul, K. E. & Whitesides, G. M. The controlled formation of ordered, sinusoidal structures by plasma oxidation of an elastomeric polymer. *Applied physics letters* **75,** 2557–2559 (1999).

148. Bowden, N., Brittain, S., Evans, A. G., Hutchinson, J. W. & Whitesides, G. M. Spontaneous formation of ordered structures in thin films of metals supported on an elastomeric polymer. *nature* **393,** 146–149 (1998).

149. Davis, C. S. & Crosby, A. J. Mechanics of wrinkled surface adhesion. *Soft Matter* **7,** 5373–5381 (2011).

150. Niven, J. F., Chowdhry, G., Sharp, J. S. & Dalnoki-Veress, K. The emergence of local wrinkling or global buckling in thin freestanding bilayer films. *The European Physical Journal E* **43,** 1–7 (2020).

151. Kodio, O., Griffiths, I. M. & Vella, D. Lubricated wrinkles: Imposed constraints affect the dynamics of wrinkle coarsening. *Physical Review Fluids* **2,** 014202 (2017).

152. Genzer, J. & Groenewold, J. Soft matter with hard skin: From skin wrinkles to templating and material characterization. *Soft Matter* **2,** 310–323 (2006).

153. Breid, D. & Crosby, A. J. Surface wrinkling behavior of finite circular plates. *Soft Matter* **5,** 425–431 (2009).

154. Kim, P., Abkarian, M. & Stone, H. A. Hierarchical folding of elastic membranes under biaxial compressive stress. *Nature materials* **10,** 952–957 (2011).

155. Biot, M. A. Surface instability of rubber in compression. *Applied Scientific Research, Section A* **12,** 168–182 (1963).

156. Mora, S., Abkarian, M., Tabuteau, H & Pomeau, Y. Surface instability of soft solids under strain. *Soft matter* **7,** 10612–10619 (2011).

157. Hohlfeld, E. B. *Creasing, point-bifurcations, and the spontaneous breakdown of scale-invariance* (Harvard University, 2008).

158. Liu, Q., Ouchi, T., Jin, L., Hayward, R. & Suo, Z. Elastocapillary crease. *Physical review letters* **122,** 098003 (2019).

159. Cao, Y. & Hutchinson, J. W. From wrinkles to creases in elastomers: the instability and imperfection-sensitivity of wrinkling. *Proceedings of the Royal Society A: Mathematical, Physical and Engineering Sciences* **468,** 94–115 (2012).

160. Wong, W., Guo, T., Zhang, Y. & Cheng, L. Surface instability maps for soft materials. *Soft Matter* **6,** 5743–5750 (2010).

161. Kim, J., Yoon, J. & Hayward, R. C. Dynamic display of biomolecular patterns through an elastic creasing instability of stimuli-responsive hydrogels. *Nature materials* **9,** 159–164 (2010).

162. Yoon, J., Bian, P., Kim, J., McCarthy, T. J. & Hayward, R. C. Local switching of chemical patterns through light-triggered unfolding of creased hydrogel surfaces. *Angewandte Chemie* **29,** 7258–7261 (2012).

163. Tallinen, T., Biggins, J. S. & Mahadevan, L. Surface sulci in squeezed soft solids. *Physical review letters* **110,** 024302 (2013).

164. Van Limbeek, M. A., Essink, M. H., Pandey, A., Snoeijer, J. H. & Karpitschka, S. Pinning-induced folding-unfolding asymmetry in adhesive creases. *Physical review letters* **127,** 028001 (2021).

165. Deegan, R. D. *et al.* Contact line deposits in an evaporating drop. *Physical review E* **62,** 756 (2000).

166. Hennessy, M. G., Ferretti, G. L., Cabral, J. T. & Matar, O. K. A minimal model for solvent evaporation and absorption in thin films. *Journal of Colloid and Interface Science* **488,** 61–71 (2017).

167. Deegan, R. D. *et al.* Capillary flow as the cause of ring stains from dried liquid drops. *Nature* **389,** 827–829 (1997).

168. Poulard, C & Damman, P. Control of spreading and drying of a polymer solution from Marangoni flows. *Europhysics Letters* **80,** 64001 (2007).

169. Hu, H. & Larson, R. G. Analysis of the effects of Marangoni stresses on the microflow in an evaporating sessile droplet. *Langmuir* **21,** 3972–3980 (2005).

170. Tsoumpas, Y., Dehaeck, S., Rednikov, A. & Colinet, P. Effect of Marangoni flows on the shape of thin sessile droplets evaporating into air. *Langmuir* **31,** 13334–13340 (2015).

171. Barash, L. Y. Marangoni convection in an evaporating droplet: Analytical and numerical descriptions. *International Journal of Heat and Mass Transfer* **102,** 445–454 (2016).

172. Pauchard, L & Allain, C. Buckling instability induced by polymer solution drying. *Europhysics Letters* **62,** 897 (2003).

173. Talini, L. & Lequeux, F. Formation of glassy skins in drying polymer solutions: approximate analytical solutions. *Soft Matter* **19,** 5835–5845 (2023).

174. Larson, R. G. Transport and deposition patterns in drying sessile droplets. *AIChE Journal* **60,** 1538–1571 (2014).

175. Hu, H. & Larson, R. G. Analysis of the microfluid flow in an evaporating sessile droplet. *Langmuir* **21,** 3963–3971 (2005).

176. Pauchard, L. & Allain, C. Mechanical instability induced by complex liquid desiccation. *Comptes Rendus Physique* **4,** 231–239 (2003).

177. Zhou, J., Man, X., Jiang, Y. & Doi, M. Structure Formation in Soft-Matter Solutions Induced by Solvent Evaporation. *Advanced Materials* **29,** 1703769 (2017).

178. Chen, L. & Evans, J. R. Arched structures created by colloidal droplets as they dry. *Langmuir* **25,** 11299–11301 (2009).

179. McGraw, J. D., Li, J., Tran, D. L., Shi, A.-C. & Dalnoki-Veress, K. Plateau-Rayleigh instability in a torus: formation and breakup of a polymer ring. *Soft Matter* **6,** 1258–1262 (2010).

180. McGraw, J. D., Rowe, I. D., Matsen, M. & Dalnoki-Veress, K. Dynamics of interacting edge defects in copolymer lamellae. *The European Physical Journal E* **34,** 1–7 (2011).

181. Zhang, Y., Qian, Y., Liu, Z., Li, Z. & Zang, D. Surface wrinkling and cracking dynamics in the drying of colloidal droplets. *The European Physical Journal E* **37,** 1–7 (2014).

182. Wang, X. & Christov, I. C. Theory of the flow-induced deformation of shallow compliant microchannels with thick walls. *Proceedings of the Royal Society A* **475,** 20190513 (2019).

183. Davis, R. H., Serayssol, J.-M. & Hinch, E. The elastohydrodynamic collision of two spheres. *Journal of Fluid Mechanics* **163,** 479–497 (1986).

184. Hughes, B. & White, L. 'Soft'contact problems in linear elasticity. *The Quarterly Journal of Mechanics and Applied Mathematics* **32,** 445–471 (1979).

185. Dowson, D. Elastohydrodynamic and micro-elastohydrodynamic lubrication. *Wear* **190,** 125–138 (1995).

186. Dowson, D & Ehret, P. Past, present and future studies in elastohydrodynamics. *Proceedings of the institution of mechanical engineers, part J: journal of engineering tribology* **213,** 317–333 (1999).

187. Skotheim, J. & Mahadevan, L. Soft lubrication. *Physical review letters* **92,** 245509 (2004).

188. Skotheim, J. & Mahadevan, L. Soft lubrication: The elastohydrodynamics of nonconforming and conforming contacts. *Physics of Fluids* **17,** 092101 (2005).

189. Essink, M. H., Pandey, A., Karpitschka, S., Venner, C. H. & Snoeijer, J. H. Regimes of soft lubrication. *Journal of fluid mechanics* **915** (2021).

190. Weekley, S., Waters, S. & Jensen, O. Transient elastohydrodynamic drag on a particle moving near a deformable wall. *The Quarterly Journal of Mechanics and Applied Mathematics* **59,** 277–300 (2006).

191. Temizer, I & Stupkiewicz, S. Formulation of the Reynolds equation on a time-dependent lubrication surface. *Proceedings of the Royal Society A: Mathematical, Physical and Engineering Sciences* **472,** 20160032 (2016).

192. Jahn, S., Seror, J. & Klein, J. Lubrication of articular cartilage. *Annual review of biomedical engineering* **18,** 235–258 (2016).

193. Hou, J., Mow, V. C., Lai, W. & Holmes, M. An analysis of the squeeze-film lubrication mechanism for articular cartilage. *Journal of biomechanics* **25,** 247–259 (1992).

194. Cher, I. A new look at lubrication of the ocular surface: fluid mechanics behind the blinking eyelids. *The ocular surface* **6,** 79–86 (2008).

195. Gipson, I. K. & Argueso, P. Role of mucins in the function of the corneal and conjunctival epithelia. *Int Rev Cytol* **231,** 1–49 (2003).

196. Hariprasad, D. S. & Secomb, T. W. Motion of red blood cells near microvessel walls: effects of a porous wall layer. *Journal of fluid mechanics* **705,** 195–212 (2012).

197. Zhang, Z. *et al.* Contactless Rheology of Soft Gels over a Broad Frequency Range. *arXiv preprint arXiv:2202.04386* (2022).

198. Salez, T. & Mahadevan, L. Elastohydrodynamics of a sliding, spinning and sedimenting cylinder near a soft wall. *Journal of Fluid Mechanics* **779,** 181–196 (2015).

199. Zhang, Z. *et al.* Direct measurement of the elastohydrodynamic lift force at the nanoscale. *Physical review letters* **124,** 054502 (2020).

200. Saintyves, B., Jules, T., Salez, T. & Mahadevan, L. Self-sustained lift and low friction via soft lubrication. *Proceedings of the National Academy of Sciences* **113,** 5847–5849 (2016).

201. Rallabandi, B., Oppenheimer, N., Ben Zion, M. Y. & Stone, H. A. Membrane-induced hydroelastic migration of a particle surfing its own wave. *Nature Physics* **14,** 1211–1215 (2018).

202. Karan, P., Das, S. S., Mukherjee, R., Chakraborty, J. & Chakraborty, S. Flow and deformation characteristics of a flexible microfluidic channel with axial gradients in wall elasticity. *Soft Matter* **16,** 5777–5786 (2020).

203. Leroy, S. & Charlaix, E. Hydrodynamic interactions for the measurement of thin film elastic properties. *Journal of Fluid Mechanics* **674,** 389–407 (2011).

204. Leroy, S. *et al.* Hydrodynamic interaction between a spherical particle and an elastic surface: a gentle probe for soft thin films. *Physical review letters* **108,** 264501 (2012).

205. Wang, Y., Pilkington, G. A., Dhong, C. & Frechette, J. Elastic deformation during dynamic force measurements in viscous fluids. *Current opinion in colloid & interface science* **27,** 43–49 (2017).

206. Wang, Y. & Frechette, J. Morphology of soft and rough contact via fluid drainage. *Soft Matter* **14,** 7605–7614 (2018).

207. Wang, Y., Tan, M. R. & Frechette, J. Elastic deformation of soft coatings due to lubrication forces. *Soft Matter* **13,** 6718–6729 (2017).

208. Kaveh, F., Ally, J., Kappl, M. & Butt, H.-J. Hydrodynamic force between a sphere and a soft, elastic surface. *Langmuir* **30,** 11619–11624 (2014).

209. Wang, Y., Dhong, C. & Frechette, J. Out-of-contact elastohydrodynamic deformation due to lubrication forces. *Physical review letters* **115,** 248302 (2015).

210. Vialar, P., Merzeau, P., Giasson, S. & Drummond, C. Compliant surfaces under shear: elastohydrodynamic lift force. *Langmuir* **35,** 15605–15613 (2019).

211. Bertin, V., Amarouchene, Y., Raphael, E. & Salez, T. Soft-lubrication interactions between a rigid sphere and an elastic wall. *Journal of Fluid Mechanics* **933** (2022).

212. Li, J. & Chou, T.-W. Elastic field of a thin-film/substrate system under an axisymmetric loading. *International Journal of Solids and Structures* **34,** 4463–4478 (1997).

213. Wu, H., Moyle, N., Jagota, A. & Hui, C.-Y. Lubricated steady sliding of a rigid sphere on a soft elastic substrate: hydrodynamic friction in the Hertz limit. *Soft Matter* **16,** 2760–2773 (2020).

214. Hui, C.-Y., Lin, Y. Y., Chuang, F.-C., Shull, K. R. & Lin, W.-C. A contact mechanics method for characterizing the elastic properties and permeability of gels. *Journal of Polymer Science Part B: Polymer Physics* **44,** 359–370 (2006).

215. Snoeijer, J. H., Eggers, J & Venner, C. H. Similarity theory of lubricated Hertzian contacts. *Physics of fluids* **25** (2013).

216. Hertz, H. Ueber die Berührung fester elastischer Körper. (1882).

217. Johnson, K. L. *Contact mechanics* (Cambridge university press, 1987).

218. Meeker, S. P., Bonnecaze, R. T. & Cloitre, M. Slip and flow in pastes of soft particles: Direct observation and rheology. *Journal of Rheology* **48,** 1295–1320 (2004).

219. Xu, Q., Wilen, L. A., Jensen, K. E., Style, R. W. & Dufresne, E. R. Viscoelastic and poroelastic relaxations of soft solid surfaces. *Physical Review Letters* **125,** 238002 (2020).

220. Webber, J. J. & Worster, M. G. A linear-elastic-nonlinear-swelling theory for hydrogels. Part 1. Modelling of super-absorbent gels. *Journal of Fluid Mechanics* **960,** A37 (2023).

221. Hu, Y., Chen, X., Whitesides, G. M., Vlassak, J. J. & Suo, Z. Indentation of polydimethylsiloxane submerged in organic solvents. *Journal of Materials Research* **26,** 785–795 (2011).

222. Degen, G. D., Chen, Y.-T., Chau, A. L., Månsson, L. K. & Pitenis, A. A. Poroelasticity of highly confined hydrogel films measured with a surface forces apparatus. *Soft Matter* **16,** 8096–8100 (2020).

223. Abdorahim, M. *High throughput compartmentalization with thermosensitive hydrogel. Application to bacteria studies* PhD thesis (Université Paris sciences et lettres, 2021).

224. Binnig, G., Quate, C. F. & Gerber, C. Atomic force microscope. *Physical review letters* **56,** 930 (1986).

225. Butt, H.-J., Cappella, B. & Kappl, M. Force measurements with the atomic force microscope: Technique, interpretation and applications. *Surface science reports* **59,** 1–152 (2005).

226. Cappella, B. & Dietler, G. Force-distance curves by atomic force microscopy. *Surface science reports* **34,** 1–104 (1999).

227. Ducker, W. A., Senden, T. J. & Pashley, R. M. Direct measurement of colloidal forces using an atomic force microscope. *Nature* **353,** 239–241 (1991).

228. Sader, J. E., Larson, I., Mulvaney, P. & White, L. R. Method for the calibration of atomic force microscope cantilevers. *Review of Scientific Instruments* **66,** 3789–3798 (1995).

229. Sader, J. E. Frequency response of cantilever beams immersed in viscous fluids with applications to the atomic force microscope. *Journal of applied physics* **84,** 64–76 (1998).

230. Sader, J. E., Chon, J. W. & Mulvaney, P. Calibration of rectangular atomic force microscope cantilevers. *Review of scientific instruments* **70,** 3967–3969 (1999).

231. Sader, J. E. *et al.* Spring constant calibration of atomic force microscope cantilevers of arbitrary shape. *Review of Scientific Instruments* **83** (2012).

232. Neumeister, J. M. & Ducker, W. A. Lateral, normal, and longitudinal spring constants of atomic force microscopy cantilevers. *Review of scientific instruments* **65,** 2527–2531 (1994).

233. Hoffmann, Á, Jungk, T & Soergel, E. Cross-talk correction in atomic force microscopy. *Review of scientific instruments* **78** (2007).

234. Onal, C. D., Sümer, B. & Sitti, M. Cross-talk compensation in atomic force microscopy. *Review of scientific instruments* **79** (2008).

235. Li, Y., Li, C. & Hu, Z. Pattern formation of constrained acrylamide/sodium acrylate copolymer gels in acetone/water mixture. *The Journal of chemical physics* **100,** 4637–4644 (1994).

236. Li, C., Hu, Z. & Li, Y. Temperature and time dependencies of surface patterns in constrained ionic N-isopropylacrylamide gels. *The Journal of chemical physics* **100,** 4645–4652 (1994).

237. Gérardin, H, Buguin, A & Brochard-Wyart, F. Pattern formation in anti-fog and anti-frost polymer coatings. *preprint* (2009).

238. Durie, K., Razavi, M. J., Wang, X. & Locklin, J. Nanoscale surface creasing induced by post-polymerization modification. *ACS nano* **9,** 10961–10969 (2015).

239. Hirotsu, S. Softening of bulk modulus and negative Poisson's ratio near the volume phase transition of polymer gels. *The Journal of chemical physics* **94,** 3949–3957 (1991).

240. Boon, N. & Schurtenberger, P. Swelling of micro-hydrogels with a crosslinker gradient. *Physical Chemistry Chemical Physics* **19,** 23740–23746 (2017).

241. Hermanowicz, P., Sarna, M., Burda, K. & Gabryś, H. AtomicJ: an open source software for analysis of force curves. *Review of Scientific Instruments* **85** (2014).

242. Gilmour, I., Trainor, A & Haward, R. Elastic moduli of glassy polymers at low strains. *Journal of Applied Polymer Science* **23,** 3129–3138 (1979).

243. Haq, M. A., Su, Y. & Wang, D. Mechanical properties of PNIPAM based hydrogels: A review. *Materials Science and Engineering: C* **70,** 842–855 (2017).

244. Hashmi, S. M. & Dufresne, E. R. Mechanical properties of individual microgel particles through the deswelling transition. *Soft Matter* **5,** 3682–3688 (2009).

245. Shibayama, M., Morimoto, M. & Nomura, S. Phase separation induced mechanical transition of poly (N-isopropylacrylamide)/water isochore gels. *Macromolecules* **27,** 5060–5066 (1994).

246. Zhang, J. & Pelton, R. The surface tension of aqueous poly (N-isopropylacrylamide-co-acrylamide). *Journal of Polymer Science Part A: Polymer Chemistry* **37,** 2137–2143 (1999).

247. Jin, L., Cai, S. & Suo, Z. Creases in soft tissues generated by growth. *Europhysics Letters* **95,** 64002 (2011).

248. Sun, J.-Y., Xia, S., Moon, M.-W., Oh, K. H. & Kim, K.-S. Folding wrinkles of a thin stiff layer on a soft substrate. *Proceedings of the Royal Society A: Mathematical, Physical and Engineering Sciences* **468,** 932–953 (2012).

249. Pocivavsek, L. *et al.* Stress and fold localization in thin elastic membranes. *Science* **320,** 912–916 (2008).

250. Stafford, C. M. *et al.* A buckling-based metrology for measuring the elastic moduli of polymeric thin films. *Nature materials* **3,** 545–550 (2004).

251. Kopecz-Muller, C., Bertin, V., Raphael, E., raw, J. D. & Salez, T. Mechanical response of a thick poroelastic gel in contactless colloidal-probe rheology. *Proceedings of the Royal Society A* **479,** 20220832 (2023).

252. McNAMEE, J. & Gibson, R. Plane strain and axially symmetric problems of the consolidation of a semi-infinite clay stratum. *The Quarterly Journal of Mechanics and Applied Mathematics* **13,** 210–227 (1960).

253. McNamee, J. & Gibson, R. Displacement functions and linear transforms applied to diffusion through porous elastic media. *The Quarterly Journal of Mechanics and Applied Mathematics* **13,** 98–111 (1960).

254. Gibson, R., Schiffman, R. & Pu, S. Plane strain and axially symmetric consolidation of a clay layer on a smooth impervious base. *The Quarterly Journal of Mechanics and Applied Mathematics* **23,** 505–520 (1970).

255. Abate, J. & Whitt, W. A unified framework for numerically inverting Laplace transforms. *INFORMS Journal on Computing* **18,** 408–421 (2006).

256. Prieve, D. C. & Frej, N. A. Total internal reflection microscopy: a quantitative tool for the measurement of colloidal forces. *Langmuir* **6,** 396–403 (1990).

257. Axelrod, D. Total internal reflection fluorescence microscopy in cell biology. *Traffic* **2,** 764–774 (2001).

258. Prieve, D. C. Measurement of colloidal forces with TIRM. *Advances in Colloid and Interface Science* **82,** 93–125 (1999).

259. Villey, R. *et al.* Effect of surface elasticity on the rheology of nanometric liquids. *Physical review letters* **111,** 215701 (2013).

260. Guan, D., Charlaix, E., Qi, R. Z. & Tong, P. Noncontact viscoelastic imaging of living cells using a long-needle atomic force microscope with dual-frequency modulation. *Physical Review Applied* **8,** 044010 (2017).

261. Guan, D., Barraud, C., Charlaix, E. & Tong, P. Noncontact viscoelastic measurement of polymer thin films in a liquid medium using long-needle atomic force microscopy. *Langmuir* **33,** 1385–1390 (2017).

262. Lainé, A. *et al.* MicroMegascope based dynamic surface force apparatus. *Nanotechnology* **30,** 195502 (2019).

263. Bertin, V. *et al.* Contactless rheology of finite-size air-water interfaces. *Physical Review Research* **3,** L032007 (2021).

264. Cleveland, J., Manne, S., Bocek, D & Hansma, P. A nondestructive method for determining the spring constant of cantilevers for scanning force microscopy. *Review of scientific instruments* **64,** 403–405 (1993).

265. Kristiansen, K. *et al.* Multimodal miniature surface forces apparatus (μSFA) for interfacial science measurements. *Langmuir* **35,** 15500–15514 (2019).

266. Heavens, O. Optical properties of thin films. *Reports on Progress in Physics* **23,** 1 (1960).

267. Lhermerout, R. & Perkin, S. Nanoconfined ionic liquids: Disentangling electrostatic and viscous forces. *Physical Review Fluids* **3,** 014201 (2018).

268. Dimitriadis, E. K., Horkay, F., Maresca, J., Kachar, B. & Chadwick, R. S. Determination of elastic moduli of thin layers of soft material using the atomic force microscope. *Biophysical journal* **82,** 2798–2810 (2002).

269. Rackauckas, C. A comparison between differential equation solver suites in matlab, r, julia, python, c, mathematica, maple, and fortran. *Authorea Preprints* (2023).

270. Sofroniou, M. & Spaletta, G. Precise numerical computation. *The Journal of Logic and Algebraic Programming* **64,** 113–134 (2005).

271. Sofroniou, M., Spaletta, G., *et al.* Extrapolation methods in mathematica. *JNAIAM J. Numer. Anal. Indust. Appl. Math* **3,** 105–121 (2008).

272. Duchemin, L. & Eggers, J. The explicit–implicit–null method: Removing the numerical instability of PDEs. *Journal of Computational Physics* **263,** 37–52 (2014).

273. Press, W. H., Teukolsky, S. A., Vetterling, W. T. & Flannery, B. P. *Numerical recipes 3rd edition: The art of scientific computing* (Cambridge university press, 2007).

274. Ypma, T. J. Historical development of the Newton–Raphson method. *SIAM review* **37,** 531–551 (1995).

275. Le Menn, F.-M. *Micromechanics of cavitation in confined soft polymer layers* PhD thesis (Université Paris sciences et lettres, 2022).

276. Rubinstein, M & Colby, R. Polymer Physics Oxford University Press. *New York* (2003).

277. Treloar, L. The elasticity and related properties of rubbers. *Reports on progress in physics* **36,** 755 (1973).

278. Yeoh, O. H. & Fleming, P. A new attempt to reconcile the statistical and phenomenological theories of rubber elasticity. *Journal of Polymer Science Part B: Polymer Physics* **35,** 1919–1931 (1997).

279. Gent, A. N. A new constitutive relation for rubber. *Rubber chemistry and technology* **69,** 59–61 (1996).

280. Rivlin, R. S. & Saunders, D. Large elastic deformations of isotropic materials VII. Experiments on the deformation of rubber. *Philosophical Transactions of the Royal Society of London. Series A, Mathematical and Physical Sciences* **243,** 251–288 (1951).

281. Bissett, E. The line contact problem of elastohydrodynamic lubrication-I. Asymptotic structure for low speeds. *Proceedings of the Royal Society of London. A. Mathematical and Physical Sciences* **424,** 393–407 (1989).

282. Sbeih, S., Mohanty, P. S., Morrow, M. R. & Yethiraj, A. Structural parameters of soft PNIPAM microgel particles as a function of crosslink density. *Journal of colloid and interface science* **552,** 781–793 (2019).

283. Chadwick, R. S. Axisymmetric indentation of a thin incompressible elastic layer. *SIAM Journal on Applied Mathematics* **62,** 1520–1530 (2002).

284. Mecke, K. R. Integral geometry in statistical physics. *International Journal of Modern Physics B* **12,** 861–899 (1998).

285. Mecke, K. R. in *Statistical Physics and Spatial Statistics: The art of analyzing and modeling spatial structures and pattern formation* 111–184 (Springer, 2000).

286. Scholz, C., Schröder-Turk, G. E. & Mecke, K. Pattern-fluid interpretation of chemical turbulence. *Physical Review E* **91,** 042907 (2015).

287. Boelens, A. M. & Tchelepi, H. A. QuantImPy: Minkowski functionals and functions with Python. *SoftwareX* **16,** 100823. ISSN: 2352-7110. `https://www.sciencedirect.com/science/article/pii/S2352711021001151` (2021).

288. Johnson, K. L., Kendall, K. & Roberts, a. Surface energy and the contact of elastic solids. *Proceedings of the royal society of London. A. mathematical and physical sciences* **324,** 301–313 (1971).

289. Derjaguin, B. V., Muller, V. M. & Toporov, Y. P. Effect of contact deformations on the adhesion of particles. *Journal of Colloid and interface science* **53,** 314–326 (1975).

290. London, F. The general theory of molecular forces. *Transactions of the Faraday Society* **33,** 8b–26 (1937).

291. Baddour, N. & Chouinard, U. Theory and operational rules for the discrete Hankel transform. *JOSA A* **32,** 611–622 (2015).

Mecanique de films d'hydrogels : instabilités induites par le gonflement, effets de taille finie, de la rhéologie sans contact à une déshydratation induite par indentation

Résumé : Dans ce manuscrit, nous étudions la réponse mécanique de films minces d'hydrogel sous plusieurs angles, incluant celui d'instabilités de la surface libre, d'indentation de la surface au moyen d'un fluide et de situations proches du contact de Hertz. Un premier chapitre préliminaire est consacré à la présentation des concepts de base utilisés dans cette thèse. Ensuite, dans une première partie, nous nous intéressons à des instabilités de surface induites par gonflement, que l'on observe à la fois sur des hydrogels gonflés et sur des films séchés. Nous analysons la formation de motifs comme le résultat d'un important gonflement anisotrope des films qui sont attachés à une surface, suivi du séchage de la surface libre de l'hydrogel de polymères, d'ores et déjà déstabilisée. Dans une deuxième partie, nous développons un modèle poroélastique pour décrire la réponse mécanique d'un hydrogel perméable soumis à un quelconque champ de pression possédant une symétrie axiale, dans un cas général. Aussi bien le cas d'une épaisseur infinie que les effets de taille finie sont étudiés et comparés. Dans une troisième partie, nous utilisons ce cadre théorique pour aborder le problème spécifique du couplage entre poroélasticité et lubrification, rencontré dans le cadre de techniques en sonde colloïdale et sans contact. Nous aboutissons théoriquement aux composantes dissipative et conservative de la force résultant du mouvement vertical d'une sphère au voisinage du substrat poroélastique. Ces résultats théoriques sont confrontés à des résultats expérimentaux de Microscopie à Force Atomique (AFM) en sonde colloïdale, obtenus sur un hydrogel épais et gonflé. Dans une dernière partie, nous mettons en évidence une succession de réponses mécaniques de la part d'hydrogels gonflés, avec des expériences d'Appareil à Forces de Surface (SFA). Partant d'un régime dénué d'interactions entre la sonde et le gel, la surface de l'hydrogel subit d'abord une faible déformation, dans un régime en lubrification. Enfin, nous montrons qu'à température ambiante la contrainte mécanique imposée déclenche par déshydratation la transition vitreuse du polymère. Dans l'ensemble, les résultats obtenus montrent que la réponse poroélastique est caractérisée par une transition dans le temps allant d'un comportement purement élastique et incompressible à un comportement purement élastique et compressible.
Mots-clés : Hydrogels, poroelasticité, lubrification souple, elastohydrodynamique, motifs de surface, rhéologie.

Mechanics of hydrogel films: swelling-induced instabilities, finite-size effects, and contactless rheology to indentation-induced dehydration

Abstract: In this manuscript, we study the mechanical response of hydrogel thin films from different perspectives, including free-surface instability, fluid-mediated surface indentation and Hertz-like contact situations. A first, preliminary Chapter is deduced to the introduction of basic concepts used is this thesis. Then, in a first part, we focus on swelling-induced surface instabilities that are observed on both swollen hydrogels and dried polymer films. The different observed morphologies are characterized by shape and spacing. We analyse the pattern formation as the result of an important anisotropic swelling of surface-attached films, and a subsequent drying of the already-destabilized free surface of polymer hydrogel. In a second part, we develop a poroelastic model to describe the mechanical response of a permeable hydrogel to any axially-symmetric pressure field, in a general case. Both the infinite-thickness case and finite-size effects are studied and compared. In a third part, we use the latter theoretical framework to address the specific poroelastic lubrication coupling associated with contactless colloidal-probe methods. We derive theoretically the conservative and dissipative components of the force associated with the oscillating vertical motion of a sphere close to the poroelastic substrate. We confront our theoretical results to colloidal-probe Atomic Force Microscopy (AFM) experiments performed on a thick and swollen hydrogel. In a last part, we highlight a succession of several mechanical responses of swollen hydrogels, with Surface Force Apparatus (SFA) experiments. From a regime with no gel-probe interaction, the hydrogel first undergoes a gentle deformation of its surface in a lubricated regime. Then, the indentation of the probe in a contact regime forces the expulsion of the solvent from the polymer matrix. We finally show that, at room temperature, the imposed mechanical load triggers the dehydration-induced glass transition of the polymer. Overall, our results show that the poroelastic response is characterized by a transition in time from a purely elastic and incompressible behaviour to a purely elastic and compressible one.
Keywords: Hydrogels, poroelasticity, soft lubrication, elastohydrodynamic, patterning, rheology.

Laboratoire Ondes et Matière d'Aquitaine, Université de Bordeaux, UMR 5798 CNRS
351 cours de la libération, 33405 Talence Cedex